

GEOLOGICA ULTRAIECTINA

**MEDEDELINGEN VAN DE
FACULTEIT GEOWETENSCHAPPEN
UNIVERSITEIT UTRECHT**

NO. 235

**DIRECT INTERCALIBRATION OF
RADIO-ISOTOPIC AND ASTRONOMICAL TIME
IN THE MEDITERRANEAN NEOGENE**

KLAUDIA KUIPER

The investigations were supported by the Netherlands Council for Earth and Life Sciences (ALW) with financial aid from the Netherlands Organisation for Scientific Research (NWO), project number 750-198-02.

ISBN 90-5744-094-6

**DIRECT INTERCALIBRATION OF
RADIO-ISOTOPIC AND ASTRONOMICAL TIME
IN THE MEDITERRANEAN NEOGENE**

Directe intercalibratie van radio-isotopische
en astronomische tijdsbepalingen in het Neogeen van het
Middellandse Zee gebied

(met een samenvatting in het Nederlands)

PROEFSCHRIFT

ter verkrijging van de graad van doctor aan de Universiteit Utrecht
op gezag van de Rector Magnificus, Prof. Dr. W.H. Gispen,
ingevolge het besluit van het College voor Promoties
in het openbaar te verdedigen op

donderdag 6 november 2003 des ochtends te 10.30 uur

door

KLAUDIA FINETTE KUIPER

geboren op 29 april 1974 te Steenwijkerwold

PROMOTORES

Prof. Dr. J.E. Meulenkamp
*Faculty of Geosciences, Utrecht University
Utrecht, The Netherlands*

Prof. Dr. P.A.M. Andriessen
*Faculty of Earth and Life Sciences, Vrije Universiteit
Amsterdam, The Netherlands*

CO-PROMOTORES

Dr. F.J. Hilgen
*Faculty of Geosciences, Utrecht University
Utrecht, The Netherlands*

Dr. J.R. Wijbrans
*Faculty of Earth and Life Sciences, Vrije Universiteit
Amsterdam, The Netherlands*

The research for this thesis was carried out at the

Department of Isotope Geochemistry, Faculty of Earth and Life Sciences, Vrije Universiteit
Amsterdam, De Boelelaan 1085, 1081 HV Amsterdam, The Netherlands.
<http://www.geo.vu.nl/users/kuik>

Institute of Paleoenvironments and Paleoclimate of Utrecht University (IPPU),
Budapestlaan 4, 3584 CD Utrecht, The Netherlands.
http://www.geo.uu.nl/Research/Strat_Paleontology/

MEMBERS OF THE DISSERTATION COMMITTEE

Prof. Dr. D. Kroon

*Faculty of Earth and Life Sciences, Vrije Universiteit
Amsterdam, The Netherlands*

Prof. Dr. C.G. Langereis

*Faculty of Geosciences, Utrecht University
Utrecht, The Netherlands*

Dr. P.R. Renne

*Berkeley Geochronology Center
Berkeley, United States of America*

M. Villeneuve

*Geological Survey of Canada
Ottawa, Canada*

Prof. Dr. G.J. van der Zwaan

*Faculty of Geosciences, Utrecht University
Utrecht, The Netherlands*

"...metiri me tempora. itane metior et quid metiar nescio"

"...I measure time, do I then measure and know not what it is that I am measuring?"

Aurelius Augustinus, Confessiones

11-26-33

CONTENTS

BIBLIOGRAPHY		9
GENERAL INTRODUCTION AND SUMMARY		11
INTRODUCTIE EN SAMENVATTING (SUMMARY IN DUTCH)		15
CHAPTER 1	Theoretical background, application and development of the $^{40}\text{Ar}/^{39}\text{Ar}$ dating technique at the VUA.	21
CHAPTER 2	Astronomical dating technique and its application in accurately determining the absolute age of Neogene volcanic ash layers in the Mediterranean.	61
CHAPTER 3	$^{40}\text{Ar}/^{39}\text{Ar}$ ages of tephras intercalated in astronomical tuned Neogene sedimentary sequences in the Eastern Mediterranean.	75
CHAPTER 4	Messinian astrochronology of the Melilla Basin: stepwise restriction of the Mediterranean-Atlantic connection through Morocco.	101
CHAPTER 5	$^{40}\text{Ar}/^{39}\text{Ar}$ dating of tephra layers intercalated in astronomically tuned marine, Upper Miocene sedimentary sequences in the western Mediterranean.	123
CHAPTER 6	Systematic discrepancies between $^{40}\text{Ar}/^{39}\text{Ar}$ and astronomical dating in the Middle Miocene?	147
CHAPTER 7	Intercalibration of the $^{40}\text{Ar}/^{39}\text{Ar}$ and U/Pb isotope systems with astronomical time: an example from the Pliocene Ptolemais Formation, N-Greece.	167
CHAPTER 8	Direct intercalibration of astronomical and isotopic time in the Mediterranean Neogene: a synthesis.	187
REFERENCES		195
ACKNOWLEDGEMENTS / DANKWOORD		206
CURRICULUM VITAE		209
APPENDICES		211

BIBLIOGRAPHY

CHAPTER 3

K.F. Kuiper, F.J. Hilgen, J. Steenbrink and J.R. Wijbrans, $^{40}\text{Ar}/^{39}\text{Ar}$ ages of tephras intercalated in astronomical tuned Neogene sedimentary sequences in the Eastern Mediterranean, *Submitted to Earth and Planetary Science Letters*.

CHAPTER 4

E. van Assen, K.F. Kuiper, N. Barhoun, W. Krijgsman and F.J. Sierro, in press, Messinian astrochronology of the Melilla Basin: stepwise restriction of the Mediterranean-Atlantic connection through Morocco. *Palaeogeography, Palaeoclimatology, Palaeoecology*.

CHAPTER 5

K.F. Kuiper, E. van Assen, N. Barhoun, F.J. Hilgen, W. Krijgsman, F.J. Sierro and J.R. Wijbrans, Intercalibration of isotopic ($^{40}\text{Ar}/^{39}\text{Ar}$) and astronomical dating methods. *In preparation for Earth and Planetary Science Letters*.

K.F. Kuiper, W. Krijgsman, M. Garcés and J.R. Wijbrans, in press, Revised isotopic ($^{40}\text{Ar}/^{39}\text{Ar}$) age for the lamproite volcano of Cabezos Negros, Fortuna Basin (Eastern Betics, SE Spain). *Palaeogeography, Palaeoclimatology, Palaeoecology*.

The following Chapters were co-authored by

CHAPTER 1 K.F. Kuiper and J.R. Wijbrans

CHAPTER 2 K.F. Kuiper and F.J. Hilgen

CHAPTER 6 K.F. Kuiper, J.R. Wijbrans and F.J. Hilgen

CHAPTER 7 K.F. Kuiper, F.J. Hilgen, J.R. Wijbrans and M. Villeneuve

CHAPTER 8 K.F. Kuiper, F. Hilgen and J.R. Wijbrans

INTRODUCTION AND SUMMARY

As accurate measurement of geological time is the key to understanding processes that occurred in the Earth's history, development and testing of time scales is a first order problem in the geological sciences. Increasingly precise and accurate dating methods are imperative to understand processes governing the evolution of our planet in increasing detail. One of the most versatile dating methods for the younger part of the Earth's history is undoubtedly $^{40}\text{Ar}/^{39}\text{Ar}$ dating. This study was initiated to build an extensive set of high quality $^{40}\text{Ar}/^{39}\text{Ar}$ data for volcanic ash layers intercalated in Mediterranean Neogene sedimentary successions for which an excellent time control exists based on the astronomical dating technique. This database will allow a rigorous and direct intercalibration of radio-isotopic and astronomical time with the aim to provide an independent test of the accuracy of conventional K/Ar ages of mineral dating standards and to investigate the potential of providing an astronomically dated $^{40}\text{Ar}/^{39}\text{Ar}$ standard. On the other hand, a rigorous intercalibration over an extended segment of the time scale will serve in the future as an independent test for the reliability of the astronomical tuning for older intervals. In a broader perspective, intercalibration of isotopic and astronomical time scales will allow precise ($^{40}\text{Ar}/^{39}\text{Ar}$) dating of volcanic layers that cannot be dated directly with the astronomical time scale.

The factors presently limiting the accuracy in $^{40}\text{Ar}/^{39}\text{Ar}$ dating are the age uncertainty of the neutron fluence monitors (mineral dating standards) and uncertainties in decay constants (e.g., Min et al., 2000 and references therein). These uncertainties outweigh typical analytical errors of modern $^{40}\text{Ar}/^{39}\text{Ar}$ analytical systems by at least one order of magnitude. For instance, published ages for Fish Canyon Tuff sanidine, one of the key dating standards for the younger part of the time scale, range from 27.5-28.5 Ma, introducing an error of $\sim 3\%$, although generally smaller intra-laboratory errors for FCT are used in age calculations (e.g., Lanphere and Baadsgaard, 2001; Renne et al., 1998; Schmitz and Bowring, 2001). One solution to reduce the uncertainty is to improve the quality of K/Ar ages of primary standards to which secondary standards (e.g., FCT) are intercalibrated. The amount of radiogenic ^{40}Ar in the primary standard can for example be improved by a more precise absolute calibration of a ^{38}Ar tracer (e.g., Lanphere and Dalrymple, 2000) and/or the amount of K in a primary standard can be determined more accurately (e.g., Renne et al., 1998) both using isotope dilution techniques. Other solutions focus on direct (U/Pb) dating of secondary standards (e.g., Schmitz and Bowring, 2001).

An alternative solution is to compare radio-isotopic ($^{40}\text{Ar}/^{39}\text{Ar}$, U/Pb) ages with ages that have been obtained independently by astronomical dating. This dating method is based on the correlation or tuning of cyclic variations in the geological record to computed astronomical time series of orbital variations. The astronomical dating technique was developed in the seventies for the late Pleistocene. More extensive application of this technique occurred simultaneously with new technical developments in the $^{40}\text{Ar}/^{39}\text{Ar}$ dating technique (e.g., single crystal laser fusion) in the late eighties, early nineties. This resulted in an avalanche of studies focusing on the comparison of astronomical ages of geomagnetic polarity reversals and their equivalent $^{40}\text{Ar}/^{39}\text{Ar}$ ages (e.g., Baksi, 1993; Baksi et al., 1992, 1993, 1995; Clement et al., 1997; Hall and Farrell, 1995; Izett and Obradovich, 1994; Renne et al., 1993; Singer and Pringle, 1996; Spell and McDougall, 1992; Tauxe et al., 1992; Turrin et al., 1994). All these studies showed a remarkable agreement between $^{40}\text{Ar}/^{39}\text{Ar}$ and astronomical ages. However, the applied methods ranged from $^{40}\text{Ar}/^{39}\text{Ar}$ dating of whole rock or groundmass of lava flows in or bracketing polarity reversals (Baksi, 1993; Baksi et al., 1992,

1993; Singer and Pringle, 1996; Singer et al., 1999), single crystal dating on sanidine from rhyolitic domes (Spell and McDougall, 1992; Izett and Obradovich, 1994; Turrin et al., 1994), to dating of minerals from volcanic layers intercalated in sediments with a reliable magnetostratigraphy (Hall and Farrell, 1995; Clement et al., 1997; Renne et al., 1993; Tauxe et al., 1992) and none involved direct application of both astronomical and isotopic dating on one sample. All these studies are subject to several assumptions like e.g. an excellently defined magnetostratigraphy (both in the studied section and the astronomically tuned reference section), correct correlations between the studied section and the Astronomical Polarity Time Scale (APTS) and/or linear inter- or extrapolation assuming constant sedimentation rates.

The first intercalibration study between the astronomical and $^{40}\text{Ar}/^{39}\text{Ar}$ system with the purpose to derive an astronomically calibrated $^{40}\text{Ar}/^{39}\text{Ar}$ standard was published by Renne et al. (1994). They recalculated published $^{40}\text{Ar}/^{39}\text{Ar}$ ages for 7 polarity reversals younger than 3.5 Ma to fit them to astronomical ages of the same reversals. The best fit was obtained when they adopted an age of 28.03 ± 0.09 Ma ($\pm 1\sigma$) for FCT sanidine. A disadvantage of their approach noted by Renne et al. (1994) is that the $^{40}\text{Ar}/^{39}\text{Ar}$ ages for 5 out of 7 reversals had to be calculated by linear interpolation of sediment accumulation rates between dated volcanic beds thereby assuming a constant sedimentation rate in depositional settings where this may not be justified. But although linear interpolation is an imperfect means of calculation, this should produce non-systematic errors that will be cancelled out in a sufficiently large data set. Another potential source of uncertainty is that the exact position of reversal boundaries is not always perfectly known due to lack of sample density and/or post depositional remagnetization (Van Hoof et al., 1993; Lourens et al., 1996). Such potential shortcomings are avoided by dating volcanic ash beds in sedimentary sequences that have been dated astronomically. This approach ensures $^{40}\text{Ar}/^{39}\text{Ar}$ ages to be compared directly with astronomical ages.

The Mediterranean Neogene provides one of the best places for research directed at the direct intercalibration of radio-isotopic and astronomical time. The latitudinal position in combination with the semi-enclosed, land-locked configuration makes the Mediterranean particularly sensitive to record astronomically induced oscillations in climate. This favorable setting resulted in a prominent and ubiquitously present sedimentary cyclicity which has been used to construct astronomically calibrated time scales for the last 13.5 Ma by tuning characteristic sedimentary cycle patterns to computed astronomical target curves, allowing timing of sequences to within 21 kyr (e.g., Hilgen et al., 1995, 2003; Lourens et al., 1996). But apart from being sensitive to record astronomically induced climatic changes, the Mediterranean marks the active convergent boundary between the African and Eurasian plates. This plate tectonic setting and associated widespread and frequently felsic volcanic activity is particularly favorable for the occurrence of primary ash fall horizons in -astronomically dated- sedimentary sequences.

The first preliminary attempts to use $^{40}\text{Ar}/^{39}\text{Ar}$ dating of ash beds in astronomically dated sequences for intercalibration with astronomical time were made by Krijgsman et al. (1997) and Hilgen et al. (1997). Dating of biotite and plagioclase from the Monte del Casino section (Upper Tortonian-Lower Messinian, northern Italy) resulted in ages that approximate the astronomical ages. Nevertheless they are less suitable for our intercalibration purpose because the isotopic ages do not perfectly match the stratigraphic order, their reproducibility is rather poor and they are affected by excess argon (Krijgsman et al., 1997; Laurenzi et al., 1997). Dating of biotite, plagioclase and sanidine obtained from ash beds in the Lower Messinian sections on Crete yielded results which were consistent with the stratigraphic order and more or less

equivalent to the astronomical age (Hilgen et al., 1997), but these data could not be reproduced (Steenbrink, unpublished results; this thesis) due to a less accurate analytical approach in Hilgen et al. (1997). $^{40}\text{Ar}/^{39}\text{Ar}$ experiments on sanidine from ash beds intercalated in Pliocene lacustrine sections in northern Greece yielded good to excellent results consistent with the stratigraphic order, sometimes even up to the level of successive precession controlled sedimentary cycles (Steenbrink et al., 1999). A remarkable discrepancy between $^{40}\text{Ar}/^{39}\text{Ar}$ and astronomical ages was observed where the isotopic ages tended to be younger with ~ 200 kyr. The disadvantage of Ptolemais is that astronomical ages were obtained via magnetostratigraphic calibration to the APTS and therefore some additional uncertainties are included. However, solving the discrepancy between the isotopic and astronomical ages in Ptolemais is evidently of crucial importance to establish a reliable age control based on one or both methods.

Therefore, we decided to continue the study of the Ptolemais and Cretan tephtras. But before analyzing these ash layers, we optimized the analytical conditions of the $^{40}\text{Ar}/^{39}\text{Ar}$ extraction system and mass spectrometer at the Vrije Universiteit Amsterdam (VUA). In chapter 1 the analytical procedures are described in detail. The chapter starts with a brief introduction of the theoretical background and the main issues regarding uncertainties in $^{40}\text{Ar}/^{39}\text{Ar}$ ages. The data reduction of the raw data to a final age is discussed, including improvement of the error propagation methods based on and extended from the study of Min et al. (2000). A newly derived error propagation method for intercalibration of the $^{40}\text{Ar}/^{39}\text{Ar}$ and astronomical dating methods is presented. To monitor the system performance, a new and more accurate method to monitor mass discrimination, which is a significant source of analytical uncertainty, is described in detail. To determine the accuracy of the analytical system over years, the results of intercalibration data on TCR sanidine and FCT sanidine will be presented and discussed in detail.

In chapter 2 the theoretical background of the astronomical dating is explained and potential uncertainties with regard to astronomical ages of volcanic ash layers are discussed. This chapter is mainly focussed on all uncertainties in the astronomical dating technique (e.g., what is the error in the astronomical solution?), although the uncertainties with regard to actual field observation and the tuning of cyclically bedded sediments are discussed in more detail in later chapters.

In chapter 3 the new data for the Cretan and Ptolemais ash layers are presented and discussed in detail. The Cretan ash layer A1 and the Ptolemais ash layers all contained sanidine, which is excellently suitable for $^{40}\text{Ar}/^{39}\text{Ar}$ dating. The improved analytical facilities reduced the discrepancy observed between astronomical and $^{40}\text{Ar}/^{39}\text{Ar}$ ages by Steenbrink et al. (1999), but the offset between both methods was not completely solved. The Ptolemais data could be divided into the upper (5) and lower (3) ashes, where the $^{40}\text{Ar}/^{39}\text{Ar}$ ages of the upper ashes were $\sim 2\%$ younger and the older ashes $\sim 1\%$ younger than their astronomical counterparts. The Cretan A1 showed the same systematic discrepancy of $\sim 1\%$ found for the lower Ptolemais ashes. In this thesis results of isotopic dating of tephtras will often be discussed as equivalent FCT ages. Using the astronomically determined age for the tephra and by assuming that age for the sanidine of the tephra an age can be calculated for the FCT fluence monitor used during irradiation of the samples as if it was an unknown. Intercalibration with FCT sanidine resulted in age of respectively 28.21 ± 0.04 Ma based on A1, 28.28 ± 0.21 Ma for the lower Ptolemais ashes and 28.61 ± 0.20 Ma based on the upper Ptolemais ashes.

Following the partially inconsistent results from our study in Ptolemais and Crete, this research was extended to the western Mediterranean Sorbas, Nijar and Melilla Basins. For the Melilla Basin no astronomical time control was available and the construction of an astronomical time frame is presented in chapter 4. Integrated magneto-, cyclo- and biostratigraphy allowed a detailed correlation to the astronomical target-curve, resulting in a high-resolution time frame for the Late Miocene evolution of the basin. Next to the potential for a direct comparison of isotopic and astronomical ages, we will show that the input of Atlantic waters through the Rifian Corridor became restricted after 6.85 Ma, and was minimized by 6.58 Ma. In the final period towards the Messinian Salinity Crisis (6.58-5.96 Ma), the Melilla Basin can be considered as a marginal basin of the Mediterranean.

In chapter 5 the $^{40}\text{Ar}/^{39}\text{Ar}$ data of the ash layers intercalated in the Sorbas, Nijar and Melilla Basins are presented. The major advantage of the Melilla ash layers, apart from a good astronomical time control, is the proximity of the source volcanoes and therefore large grainsizes of sanidine (and biotite) crystals allowing single crystal dating. Intercalibration of in total 183 experiments of 16 Melilla ash layers with astronomical time resulted in an age of 28.24 ± 0.01 Ma for FCT (1 standard error of the mean). This is in agreement with the lower Ptolemais and A1 ash layers. The single crystal analyses provided the opportunity to remove data of xenocrystic grains from the intercalibration dataset, making the data more ideal than e.g. the A1, which is based on multiple grain experiments. The three ash layers in the Sorbas / Nijar Basins did not contain high quality sanidine; instead the focus was on biotite experiments. The data provided reliable age spectra, but biotite ages tended to be older than the astronomical ages. The few ash layers with experiments on both sanidine and biotite show almost always consistently older ages for biotite.

In chapter 6 the research is extended to the Middle Miocene where we expected to see the same discrepancy between astronomical and isotopic ages. However, instead of being $\sim 1\%$ younger, the isotopic ages appeared to be equal (feldspar fractions) or older (biotite fractions) than the astronomical ages. Convincing arguments against the proposed intercalibration between astronomical and isotopic time based on the Melilla ash layers could not be given, because multiple grains in smaller grainsize fractions have been analyzed and xenocrystic contamination might go unnoticed. We observed indeed broadening of the age probability distributions, which might be explained by this effect.

In chapter 7 a first effort is made to intercalibrate the U/Pb system with the $^{40}\text{Ar}/^{39}\text{Ar}$ and astronomical methods. Following inspection of the samples, the upper Ptolemais ash layer (SR3M) was selected as one of the better candidates for U/Pb experiments. Dating of such young zircons required either a lot of material (TIMS) or is on the edge of practical limitations (SHRIMP). Unfortunately, the zircon of this ash layer seemed to be affected by an inherited component and no strong recommendations concerning intercalibration of the several systems could be made. Finally, in chapter 8 the implications of this research are described and a kick off for an astronomically intercalibrated standard in $^{40}\text{Ar}/^{39}\text{Ar}$ dating is given.

INTRODUCTIE EN SAMENVATTING

De ontwikkeling en het testen van tijdschalen is zeer belangrijk voor de aardwetenschappen, omdat het nauwkeurig meten van geologische tijd de sleutel is om processen te begrijpen in de geschiedenis van de aarde. Een grotere nauwkeurigheid en precisie van dateringsmethoden zijn nodig om de processen, die de ontwikkeling van onze planeet beheersen, in toenemende mate te begrijpen. De $^{40}\text{Ar}/^{39}\text{Ar}$ dateringsmethode is ongetwijfeld een van de meest veelzijdige dateringsmethoden voor het jongere deel van de geschiedenis van de aarde. De huidige studie is opgezet om een uitgebreide $^{40}\text{Ar}/^{39}\text{Ar}$ dataset van goede kwaliteit op te bouwen voor vulkanische aslagen in sediment opeenvolgingen van Neogene ouderdom in het Middellandse Zee gebied. Voor deze opeenvolgingen bestaat een uitstekende tijdscontrole gebaseerd op de astronomische dateringstechniek. De verzamelde gegevens maken een zorgvuldige en directe vergelijking van radiometrische met astronomische ouderdommen mogelijk. Hiermee kan de nauwkeurigheid van de conventionele K/Ar ouderdom van minerale dateringstandaarden worden getest en de mogelijkheid van een astronomisch gedateerde $^{40}\text{Ar}/^{39}\text{Ar}$ standaard worden onderzocht. Verder kan een zorgvuldige intercalibratie in de toekomst dienen als een onafhankelijke test voor de betrouwbaarheid van de astronomische calibratie van sedimentaire cycli voor oudere tijdsintervallen. Daarnaast kan deze intercalibratie nauwkeuriger ($^{40}\text{Ar}/^{39}\text{Ar}$) dateringen van vulkanische lagen opleveren, die niet direct met de astronomische methode gedateerd kunnen worden.

De factoren, die op dit moment de nauwkeurigheid van de $^{40}\text{Ar}/^{39}\text{Ar}$ dateringsmethode bepalen, zijn de onzekerheid in de ouderdom van de dateringstandaarden en de onzekerheid in de verval constanten. Deze onzekerheden zijn minimaal één orde groter dan de gemiddelde analytische fout in moderne $^{40}\text{Ar}/^{39}\text{Ar}$ dateringen. De gepubliceerde ouderdom van bijvoorbeeld de Fish Canyon Tuff, één van de belangrijkste dateringstandaarden voor het jongste deel van de tijdschaal, varieert van 27.5 tot 28.5 Ma, waardoor een fout van ~3% geïntroduceerd wordt. Echter, in het algemeen worden de veel kleinere intralaboratorium fouten voor FCT gebruikt in het berekenen van de ouderdom. Een oplossing om de onzekerheid in de $^{40}\text{Ar}/^{39}\text{Ar}$ methode te reduceren is de kwaliteit van de K/Ar ouderdom van primaire standaarden, waaraan secundaire standaarden (bijv. FCT) zijn geïntercalibreerd, te verbeteren. Zowel de hoeveelheid K als de hoeveelheid radiogeen ^{40}Ar in een primaire standaard kunnen bijvoorbeeld nauwkeuriger bepaald worden door verbeterde isotopen verdunningstechnieken te gebruiken. Andere oplossingen richten zich op directe (U/Pb) dateringen van secundaire standaarden.

Een alternatieve oplossing is het vergelijken van de radio-isotopen ($^{40}\text{Ar}/^{39}\text{Ar}$, U/Pb) ouderdom met de ouderdom die onafhankelijk verkregen is met de astronomische dateringsmethode. Deze laatste methode is gebaseerd op cyclische klimaatsveranderingen die het gevolg zijn van veranderingen in de hoeveelheid instraling van de zon, die op zijn beurt weer samenhangt met de stand van de aardas en de baan van de aarde rondom de zon. Deze klimaatsveranderingen worden vastgelegd in sediment afzettingen en patronen in die afzettingen kunnen gekoppeld worden aan een zgn. instralingcurve, waarmee de exacte ouderdom van de afzetting bepaald wordt. De astronomische dateringsmethode werd ontwikkeld in de zeventiger jaren (van de vorige eeuw) voor het laat Pleistoceen en uitgebreid naar het vroeg Pleistoceen. Grootschaliger toepassing van de astronomische dateringstechniek vond eind jaren tachtig, begin jaren negentig plaats gelijktijdig met nieuwe technische ontwikkelingen in de $^{40}\text{Ar}/^{39}\text{Ar}$ dateringstechniek (bijv. laser dateringen van individuele kristallen). Dit resulteerde in een groot aantal studies gericht op de

vergelijking van $^{40}\text{Ar}/^{39}\text{Ar}$ en astronomische ouderdommen voor geomagnetische polariteitomkeringen. Al deze studies lieten een opmerkelijke overeenkomst tussen de $^{40}\text{Ar}/^{39}\text{Ar}$ en astronomische ouderdommen zien. De toegepaste methoden varieerden echter van $^{40}\text{Ar}/^{39}\text{Ar}$ dateringen op het volledige gesteente of de grondmassa van lavastromen in of rondom een polariteitomkering, dateringen van individuele sanidien kristallen van rhyolitische lichamen, tot dateringen van mineralen van vulkanische aslagen in sedimenten met een betrouwbare magnetostratigrafie. Geen van de studies hield zich bezig met directe astronomisch en isotopen dateringen op één en hetzelfde monster. Al deze studies waren afhankelijk van een aantal aannamen zoals een betrouwbare magnetostratigrafie (in zowel de bestudeerde sectie als de astronomische gedateerde referentie secties), juiste correlaties tussen de bestudeerde sectie en de Astronomische Polariteit Tijd Schaal (APTS) en/of lineaire inter- en extrapolatie uitgaande van een constante sedimentatie snelheid.

De eerste studie met betrekking tot intercalibratie van de astronomische en $^{40}\text{Ar}/^{39}\text{Ar}$ dateringssystemen met het doel een astronomisch gecalibreerde $^{40}\text{Ar}/^{39}\text{Ar}$ dateringstandaard te ontwikkelen werd gepubliceerd door Renne et al. (1994). Zij herberekenden de gepubliceerde $^{40}\text{Ar}/^{39}\text{Ar}$ ouderdommen van 7 polariteitomkeringen jonger dan 3.5 Ma door deze aan te passen aan de astronomische ouderdom voor dezelfde omkeringen. De beste overeenkomst werd bereikt, wanneer een ouderdom van 28.03 ± 0.09 Ma ($\pm 1\sigma$) voor FCT sanidien werd gebruikt. Een nadeel van de benadering van Renne et al. (1994) is dat de $^{40}\text{Ar}/^{39}\text{Ar}$ ouderdom voor 5 van de 7 omkeringen berekend moesten worden met behulp van lineaire interpolatie van de sedimentatie snelheid tussen de gedateerde vulkanische lagen waarbij een constante snelheid verondersteld wordt. Maar hoewel lineaire interpolatie niet een perfect middel voor deze berekening is, zou deze methode moeten resulteren in fouten die niet systematisch zijn en tegen elkaar opwegen in een voldoende grote dataset. Een andere mogelijke bron van onzekerheid is dat de exacte positie van de omkeringen niet altijd bekend is door een te lage monsterdichtheid en/of remagnetisatie na afzetting (Van Hoof et al., 1993; Lourens et al., 1996). Zulke mogelijke onzekerheden kunnen worden vermeden door het direct dateren van vulkanische aslagen in sedimentaire afzettingen, die astronomisch gedateerd zijn. Deze benadering verzekert ons dat de $^{40}\text{Ar}/^{39}\text{Ar}$ ouderdommen direct met de astronomische ouderdommen vergeleken kunnen worden.

Het Neogeen van het Middellandse Zee gebied is één van de beste plaatsen voor onderzoek gericht op de directe vergelijking van radiometrische en astronomische tijd. Het Middellandse Zee gebied is bijzonder gevoelig voor de registratie van astronomisch geïnduceerde schommelingen in het klimaat vanwege zijn paleolatitudo en het vrijwel afgesloten karakter van het bekken. Deze gunstige omstandigheden resulteerden in een prominente cycliciteit in de sedimenten, welke gebruikt is om een astronomisch gecalibreerde tijdschaal voor de laatste 13.5 Ma te maken. Dit gebeurde door karakteristieke patronen in de sedimentaire cycli te correleren naar astronomische curves voor de veranderingen in de aardbaan en de stand van de aardas. Hierdoor wordt de ouderdomsbepaling van opeenvolgingen mogelijk met een oplossend vermogen van minder dan 21.000 jaar. Maar behalve de gevoeligheid voor de registratie van astronomisch geïnduceerde klimaat schommelingen, wordt het Middellandse Zee gebied ook gekenmerkt door een actieve grens tussen de Afrikaanse en Euraziatische plaat. Deze plaattektonische setting, waarmee wijdverbreid en veelvuldig felsisch vulkanisme is geassocieerd, is bijzonder gunstig voor het voorkomen van primaire asregens in lagen in -astronomisch gedateerde- sedimentaire afzettingen.

De eerste pogingen om $^{40}\text{Ar}/^{39}\text{Ar}$ ouderdommen te bepalen van aslagen afkomstig uit astronomisch gedateerde afzettingen dateren van eind jaren negentig (Krijgsman et al., 1997; Hilgen et al., 1997). Dateringen van biotiet en plagioklaas van de Monte del Casino sectie (Laat Tortonien - Vroeg Messinien, Noord Italië) kwamen ongeveer overeen met de astronomische ouderdom. Desondanks waren deze aslagen minder geschikt voor onze intercalibratie studie, omdat de $^{40}\text{Ar}/^{39}\text{Ar}$ ouderdommen niet perfect overeen kwamen met de stratigrafische volgorde, de reproduceerbaarheid nogal laag was en de ouderdom beïnvloed werd door een argon component, die al in het mineraal aanwezig was. Dateringen van biotiet, plagioklaas en sanidien verkregen uit aslagen van Messinien secties op Kreta resulteerden in data die consistent waren met de stratigrafische volgorde en min of meer gelijk aan de astronomische ouderdom. Deze data konden echter niet worden gereproduceerd (Steenbrink, ongepubliceerde data; dit proefschrift) wat verklaard kon worden door een minder nauwkeurige analytische benadering in Hilgen et al. (1997). $^{40}\text{Ar}/^{39}\text{Ar}$ experimenten op sanidien van aslagen afkomstig uit het Pliocene, lacustrien Ptolemais bekken in Noord Griekenland leverden goede tot uitstekende resultaten op die consistent waren met de stratigrafische volgorde (Steenbrink et al., 1999). Een opmerkelijke discrepantie tussen de $^{40}\text{Ar}/^{39}\text{Ar}$ en astronomische ouderdommen werd echter gesignaleerd waarbij de $^{40}\text{Ar}/^{39}\text{Ar}$ ouderdommen ongeveer 200.000 jaar jonger zijn. Het nadeel van Ptolemais is dat de astronomische tijdscontrole verkregen werd door calibratie van de magnetostratigrafie aan de APTS en daardoor enige extra onzekerheden heeft. Het oplossen van de discrepantie tussen de isotopen en astronomische ouderdom in Ptolemais is dan ook van fundamenteel belang voor de ontwikkeling van een betrouwbare tijdschaal gebaseerd op beide methoden.

Om die reden zijn de analytische omstandigheden van het $^{40}\text{Ar}/^{39}\text{Ar}$ extractie systeem en de massa spectrometer aan de Vrije Universiteit Amsterdam (VUA) geoptimaliseerd. In hoofdstuk 1 worden de analytische procedures in detail beschreven. Dit hoofdstuk begint met een korte introductie van de theoretische achtergrond en de belangrijkste kwesties op het gebied van de onzekerheden in een $^{40}\text{Ar}/^{39}\text{Ar}$ ouderdom. Het terugbrengen van de ruwe data tot een uiteindelijke ouderdom wordt bediscussieerd, waarbij een verbeterde methode voor het doorberekenen van fouten wordt gepresenteerd. Verder wordt een nieuwe methode voor het doorberekenen van fouten beschreven voor de intercalibratie van de $^{40}\text{Ar}/^{39}\text{Ar}$ en astronomische dateringmethoden. Een nieuwe en nauwkeuriger methode om de massa discriminatie te bepalen, wordt in detail beschreven. Dit dient om de werking van het analytische systeem te registreren en omdat de massa discriminatie een significante bron van analytische onzekerheid kan zijn. Verder worden de resultaten van de intercalibratie van twee vaak gebruikte dateringstandaarden (TCR sanidien en FCT sanidien) bediscussieerd om de nauwkeurigheid van het analytische systeem over de afgelopen jaren te controleren.

In hoofdstuk 2 wordt de theoretische achtergrond van de astronomische dateringmethode uiteengezet en worden de mogelijke onzekerheden met betrekking tot de astronomische ouderdom van vulkanische aslagen bediscussieerd. Dit hoofdstuk richt zich hoofdzakelijk op alle onzekerheden die betrekking hebben op de astronomische dateringstechniek (bijv. wat is de fout in de astronomische oplossing?) en op de feitelijke waarnemingen in het veld.

In hoofdstuk 3 worden de nieuwe data voor de aslagen van Kreta en Ptolemais gepresenteerd en in detail bediscussieerd. De Kretenzische aslaag A1 en de Ptolemais aslagen bevatten alle sanidien, dat uitermate geschikt is voor $^{40}\text{Ar}/^{39}\text{Ar}$ dateringen. De verbeterde analytische faciliteiten leidden tot een afname van de

eerder waargenomen discrepantie tussen de astronomische en $^{40}\text{Ar}/^{39}\text{Ar}$ ouderdommen van Steenbrink et al. (1999), maar het verschil bleef bestaan. De Ptolemais gegevens konden worden verdeeld over de bovenste (5) en onderste (3) aslagen, waarbij de $^{40}\text{Ar}/^{39}\text{Ar}$ ouderdommen van de bovenste aslagen $\sim 2\%$ en van de onderste aslagen $\sim 1\%$ jonger zijn dan de astronomische ouderdommen. De Kretenzische A1 laat dezelfde discrepantie van 1% zien als de onderste aslagen in Ptolemais. De resultaten worden eveneens weergegeven als een astronomisch geijkte FCT ouderdom. Dat houdt in dat de astronomische ouderdom van een aslaag in combinatie met de veronderstelling dat deze ouderdom de ouderdom van de sanidien in deze aslaag is, kan worden gebruikt om een ouderdom te berekenen voor de FCT standaard, als ware de standaard een onbekende. Intercalibratie met FCT sanidien resulteerde in een ouderdom van respectievelijk 28.21 ± 0.04 Ma gebaseerd op A1, 28.28 ± 0.21 Ma voor de onderste Ptolemais aslagen en 28.61 ± 0.20 Ma voor de bovenste Ptolemais aslagen.

Naar aanleiding van de inconsistentie in de uitkomst van onze studie in Ptolemais en Kreta is het onderzoek uitgebreid naar de Sorbas, Nijar en Melilla Bekkens in het westelijk Middellandse Zee gebied. Het opstellen van een astronomische tijdscontrole voor de sedimentaire afzettingen in het Melilla Bekken wordt beschreven in hoofdstuk 4. Een geïntegreerde magneto-, cyclo- en biostratigrafie maken een gedetailleerde correlatie van de sedimentaire cycli naar een astronomische instralingscurve mogelijk. Dit resulteert in een tijdskader met een hoog oplossend vermogen voor de Laat Miocene ontwikkeling van het bekken. Naast de mogelijkheid om de isotopen en astronomische ouderdom direct met elkaar te vergelijken, wordt aannemelijk gemaakt dat de toevoer van Atlantisch water door de Rif Straat werd beperkt na 6.85 Ma, en zo goed als onmogelijk werd rond 6.58 Ma. In de laatste periode voor de "Messinien Salinity Crisis" (6.58-5.96 Ma), is het Melilla bekken een marginaal bekken van de Middellandse Zee geworden.

In hoofdstuk 5 worden de $^{40}\text{Ar}/^{39}\text{Ar}$ data van de aslagen in de Sorbas, Nijar en Melilla Bekkens gepresenteerd. Het grote voordeel van het Melilla bekken is, behalve de betrouwbare astronomische tijdscontrole, de aangrenzende vulkaan, die hoogstwaarschijnlijk de bron is van de aslagen. Daarom zijn de sanidien (en biotiet) kristallen groot genoeg om individuele kristallen te dateren. Intercalibratie met de astronomische ouderdom van in totaal 183 experimenten op 16 aslagen resulteerde in een ouderdom van 28.24 ± 0.01 Ma voor FCT (± 1 "standaard fout van het gemiddelde"). Dit is in overeenstemming met de Kretenzische A1 en de onderste Ptolemais aslagen. Het dateren van individuele kristallen biedt de mogelijkheid om data van xenokristen te verwijderen uit de dataset. Daardoor zijn de Melilla data geschikter voor intercalibratie dan bijvoorbeeld de A1, waarvan de ouderdom gebaseerd is op experimenten op meerdere kristallen. De drie aslagen in de Sorbas en Nijar Bekkens bevatten geen sanidien van hoge kwaliteit en daarom werden de experimenten voornamelijk op biotiet uitgevoerd. De biotiet ouderdommen, gebaseerd op betrouwbare ouderdomspectra, tonen consequent hogere ouderdommen in vergelijking met sanidien, en met de astronomische ouderdom.

In hoofdstuk 6 wordt het onderzoek uitgebreid naar het Midden Mioceen, waar we dezelfde discrepantie tussen de astronomische en isotopen ouderdom verwachtten aan te treffen. We vonden echter dat de isotopen ouderdommen gelijk (veldspaat fracties) of ouder (biotiet fracties) bleken te zijn dan de astronomische ouderdommen in plaats van 1% jonger. Overtuigende argumenten tegen de in hoofdstuk 5 voorgestelde intercalibratie van de astronomische en isotopen methoden kunnen niet worden gegeven, aangezien de dateringen op meerdere kristallen tegelijk zijn uitgevoerd, waardoor contaminatie met

INTRODUCTIE EN SAMENVATTING

xenokristen onopgemerkt blijft. Wij zien inderdaad een verbreding van de cumulatieve waarschijnlijkheidsverdeling van de ouderdom, die mogelijk door dit effect verklaard kan worden.

In hoofdstuk 7 is een eerste poging ondernomen om de U/Pb methode met de $^{40}\text{Ar}/^{39}\text{Ar}$ én de astronomische methode te intercalibreren. Na inspectie van de monsters werd één van de bovenste aslagen in Ptolemais (SR3M) geselecteerd als een van de beste kandidaten voor U/Pb experimenten. Dateren van zulke jonge zirkonen vereist óf een enorme hoeveelheid materiaal (TIMS), óf is op de rand van de praktische beperkingen (SHRIMP). Helaas lijkt de zirkoon van deze aslaag een oudere component te bevatten en kunnen geen duidelijke aanbevelingen worden gedaan met betrekking tot de intercalibratie van de verschillende systemen.

Hoofdstuk 8 sluit af met de beschrijving van de implicaties van het onderzoek en geeft een overtuigende aanzet voor het invoeren van een astronomische gedateerde $^{40}\text{Ar}/^{39}\text{Ar}$ standaard.

CHAPTER 1

**THEORETICAL BACKGROUND, APPLICATION AND
DEVELOPMENT OF THE $^{40}\text{Ar}/^{39}\text{Ar}$ DATING TECHNIQUE
AT THE DUA.**

INTRODUCTION

The $^{40}\text{Ar}/^{39}\text{Ar}$ variant of the K/Ar dating technique is a widely applied versatile method to determine ages of geological material from the origin of the Earth until recent and is one of the fundamentals in this thesis. Because the intercalibration of two completely independent methods (astronomical dating versus $^{40}\text{Ar}/^{39}\text{Ar}$ geochronology) is the main aim of this thesis a substantial component of methodology with respect to $^{40}\text{Ar}/^{39}\text{Ar}$ dating (this chapter) and astronomical dating (chapter 2) will be discussed. This chapter is divided into three parts. The first part describes the theoretical basis of the $^{40}\text{Ar}/^{39}\text{Ar}$ dating technique and focuses on potential sources of systematic errors. The absolute ages of neutron fluence monitors and the values of the decay constants are for example two parameters dominating the absolute error (e.g., Min et al., 2000) and are assessed in more detail. In the second part of this chapter the implementation of the $^{40}\text{Ar}/^{39}\text{Ar}$ technique at the Vrije Universiteit Amsterdam (VUA) will be addressed with a focus on optimizing accuracy and precision of the method. This includes the process of error propagation in age determinations, because the evaluation of systematic and random uncertainties is important for demonstrating where improvements in the dating technique can be made. The development of error propagation methods is continued for the case of intercalibration of secondary standards with astronomical dated volcanic ash layers instead of the commonly used intercalibration with a primary K/Ar dated standard. The third part of this chapter describes two aspects that are able to monitor the performance of the analytical system: the mass fractionation and intercalibration of two standards in several irradiation batches. This part of the chapter is based on data, which have been obtained during the data collection of chapters 3, 5 and 6.

PART I: THEORETICAL BACKGROUND AND SYSTEMATIC ERRORS IN $^{40}\text{Ar}/^{39}\text{Ar}$ DATING

THEORETICAL BACKGROUND OF THE $^{40}\text{Ar}/^{39}\text{Ar}$ METHOD

Potassium is one of the eight most abundant elements in the crust of the earth and is a major constituent in rock-forming minerals. Potassium has three naturally occurring isotopes with an abundance of $93.2581 \pm 0.0029\%$ for ^{39}K , $0.01167 \pm 0.00004\%$ for ^{40}K and $6.7302 \pm 0.0029\%$ of ^{41}K (Garner et al., 1975). The radioactive ^{40}K isotope decays to stable ^{40}Ar by electron capture and positron decay and to ^{40}Ca by electron emission. When the quantities of the parent and daughter element in a sample and the decay constant are known, an age of a sample since closure of the system can be calculated.

The $^{40}\text{Ar}/^{39}\text{Ar}$ method developed from the K/Ar method (e.g., Merrihue and Turner, 1966). Instead of measuring the amount of parent (^{40}K) and daughter (^{40}Ar) isotopes on different sample splits using different analytical methods, parent and daughter could be measured simultaneously. Advantages were the smaller sample sizes required for the analyses, better analytical precision, avoidance of problems with sample heterogeneity and no need for elemental abundance measurements (Dalrymple and Lanphere, 1971). Also techniques like incremental heating and spot fusion with a laser became available for the $^{40}\text{Ar}/^{39}\text{Ar}$ dating technique allowing us to unravel geological histories of rocks. Disadvantage of the $^{40}\text{Ar}/^{39}\text{Ar}$ technique is that the samples are radioactive which requires special laboratory facilities and the need to quantify undesired isotopic interferences and gradients in the neutron flux during irradiation. In a nuclear reactor ^{39}K is transformed into ^{39}Ar by neutron capture. The concentration of ^{39}Ar produced from irradiation

is a function of ^{40}K , because the ratio of $^{40}\text{K}/^{39}\text{K}$ in terrestrial materials is assumed to be constant. The number of atoms ^{39}Ar atoms formed during the neutron bombardment can therefore be corrected by simultaneously irradiating unknowns and standards. A $^{40}\text{Ar}/^{39}\text{Ar}$ age can be calculated with

$$t = \frac{1}{\lambda} \ln \left(1 + J \frac{[^{40}\text{Ar}^*]}{[^{39}\text{Ar}_k]} \right) \quad (1.1)$$

where t is the age of the unknown, λ is the decay constant ($5.543 \pm 0.010 \times 10^{-10}$, Steiger and Jäger, 1977), J is the irradiation parameter determined by the measured $^{40}\text{Ar}^*/^{39}\text{Ar}_k$ ratio of a standard with a known age (in actuality the apparent age) and $^{40}\text{Ar}^*/^{39}\text{Ar}_k$ is the measured ratio of the unknown. For more a more detailed background on $^{40}\text{Ar}/^{39}\text{Ar}$ geochronology the reader is referred to textbooks of e.g. Faure (1986), Dickin (1997) and McDougall and Harrison (1999).

SYSTEMATIC ERRORS IN THE $^{40}\text{Ar}/^{39}\text{Ar}$ DATING TECHNIQUE

The absolute error in an age t consists of a combination of the reliability of a number of assumptions and the uncertainties in the decay constants, in the irradiation parameter J and the measured $^{40}\text{Ar}^*/^{39}\text{Ar}_k$ ratio of a sample. Hidden in the value of J is the uncertainty in the absolute age of the standard and that of the proportion of decays of ^{40}K to ^{40}Ar with respect to the total activity of ^{40}K . In many cases, this uncertainty is not propagated into the final age. Note that this uncertainty is systematic and not random. The discussion about the accuracy of $^{40}\text{Ar}/^{39}\text{Ar}$ dating presently concentrates on the accuracy of the ages of dating standards (e.g., Renne et al., 1998; Lanphere and Baadsgaard, 2001) and decay constants (e.g., Min et al., 2000; Dazé et al., 2003; Spell and McDougall, 2003). However, first the underlying basic assumptions of the $^{40}\text{Ar}/^{39}\text{Ar}$ (and K/Ar) method will be briefly discussed.

BASIC ASSUMPTIONS K/Ar AND $^{40}\text{Ar}/^{39}\text{Ar}$

The ^{40}K decay rate must be independent of its physical or chemical state and must be unaffected by variations of temperature or pressure. So far measurements on decay rates of ^{40}K in different substances under various circumstances do not show a detectable effect on its decay constant (McDougall and Harrison, 1999 and references therein). The $^{40}\text{K}/\text{K}$ ratio must be constant in nature and isotopic measurements on potassium of terrestrial and extraterrestrial samples support this assumption, at least no differences greater than $\sim 1.3\%$ have been reported (McDougall and Harrison, 1999). The radiogenic ^{40}Ar measured in a sample must be produced by in situ decay of ^{40}K . Corrections must be made for non-radiogenic ^{40}Ar present in the sample by assuming a constant $^{40}\text{Ar}/^{36}\text{Ar}$ ratio of the non-radiogenic atmospheric contaminant. One way to assess this assumption is the use of isochron diagrams (see McDougall and Harrison, 1999, for details). For the K/Ar method sample homogeneity is extremely important, because the ^{40}K and ^{40}Ar are measured on separate sample splits. Furthermore the system must have remained closed with respect to K and Ar since the event being dated. However, departures from this assumption are quite common especially in areas with complex geological histories, but incremental heating techniques enable us to assess this assumption. Apart from a good control on the irradiation parameter J it is important to correct for interfering nuclear reactions for the $^{40}\text{Ar}/^{39}\text{Ar}$ method. Experimental artifacts due to recoil of ^{39}Ar and ^{37}Ar may occur as a result of chemical or crystallographic inhomogeneities in a sample.

NUCLEAR INTERFERENCE CORRECTION FACTORS

A detailed discussion of correction factors is given in McDougall and Harrison (1999) and references therein. The most commonly used correction factors for interference reactions, atmospheric argon and optimization of irradiation conditions are summarized here. Corrections must be made for any contaminating atmospheric argon contained within the sample or contributed from the mass spectrometer or the vacuum system in which the gas is extracted from the samples. The correction can be made by assuming that all of the ^{36}Ar is of atmospheric origin after corrections of blanks and mass discrimination and minor amounts of neutron-induced ^{36}Ar have been carried out. Nuclear interference reactions of Ca-derived argon isotopes can be corrected by measuring the ratio of the different isotopes relative to $^{37}\text{Ar}_{\text{Ca}}$ in a zero age Ca-salt (CaF_2), because the yields of the $^{37}\text{Ar}_{\text{Ca}}$ producing reactions are negligible except for the $^{40}\text{Ca}(n,\alpha)^{37}\text{Ar}$ reaction. The abundance of ^{37}Ar in a sample is therefore a direct indication for the amount of Ca present in a sample. However, an additional correction for the decay of the radioactive ^{37}Ar has to be made ($T_{1/2} = 35.1$ days). To be able to apply a correction for Ca neutron interference reactions, samples must be analyzed within ~ 1 year after irradiation, otherwise most ^{37}Ar has decayed. A correction factor for the $^{42}\text{Ca}(n,\alpha)^{39}\text{Ar}$ interference reaction is derived by measurement of the $(^{39}\text{Ar}/^{37}\text{Ar})_{\text{Ca}}$ ratio on a pure zero age Ca-salt (no need for atmospheric correction) corrected for the radioactive decay of ^{37}Ar , ^{39}Ar ($T_{1/2} = 269.9$ yr), blanks and mass discrimination. A correction factor for the reaction $^{40}\text{Ca}(n,n\alpha)^{36}\text{Ar}$ is derived in a similar way by measurement of the $(^{36}\text{Ar}/^{37}\text{Ar})_{\text{Ca}}$ on the same Ca-salt corrected for the radioactive decay of ^{37}Ar , ^{39}Ar , atmospheric ^{36}Ar , blanks and mass discrimination.

A correction factor for interference reactions on potassium is generally determined by measurement of the isotope ratios of argon extracted from a pure potassium salt (e.g., K_2SO_4) that has been irradiated in the same facility utilized for $^{40}\text{Ar}/^{39}\text{Ar}$ dating. Another option is to use K-rich silicate glass synthesized from very high purity salts. Because no nuclear interference reaction is known which produces ^{36}Ar from potassium, all the measured ^{36}Ar in a zero-age K-salt or K-glass is attributed to atmospheric ^{36}Ar . Further, in a pure potassium salt or glass all the ^{39}Ar is derived from potassium. In this way a correction factor $(^{40}\text{Ar}/^{39}\text{Ar})_{\text{K}}$ for neutron-induced ^{40}Ar caused by the interference reaction $^{40}\text{K}(n,p)^{40}\text{Ar}$ and a correction factor $(^{38}\text{Ar}/^{39}\text{Ar})_{\text{K}}$ for the reaction of $^{41}\text{K}(n,\alpha)^{38}\text{Ar}$ can be derived, although this last reaction is of minor importance.

Irradiation conditions can be chosen such the influence of nuclear interference reactions is minimized. For accurate $^{40}\text{Ar}/^{39}\text{Ar}$ dating results samples and sample size must be chosen to provide sufficient $^{40}\text{Ar}^*$. Depending on the age and potassium content of a sample an estimate of the amount of sample necessary for an adequate analysis can be estimated. Further, the amount of ^{39}Ar produced during irradiation must be sufficient to enable its measurement relative to $^{40}\text{Ar}^*$ with an appropriate precision (the measured $^{40}\text{Ar}^*/^{39}\text{Ar}$ ratio must have an upper limit of ~ 300 as suggested by Turner (1971), for high precision results the $^{40}\text{Ar}^*/^{39}\text{Ar}$ ratio is preferably < 25). To minimize the influence of interfering nuclear reactions it is best to analyze samples with low Ca contents and to use Cd-shielding which prevents the occurrence of the reaction $^{40}\text{K}(n,p)^{40}\text{Ar}$, because of the reduction of thermal neutrons by Cd-shielding required for this reaction. Table 1.1 lists the correction factors as reported in literature for the Oregon TRIGA reactor used for irradiation of samples in this study. Correction factors of Steenbrink et al. (1999) are used throughout this thesis (table 1.1).

Publication	$(^{36}\text{Ar}/^{37}\text{Ar})_{\text{Ca}} \times 10^{-4} \pm \text{SD}$	$(^{39}\text{Ar}/^{37}\text{Ar})_{\text{Ca}} \times 10^{-4} \pm \text{SD}$	$(^{39}\text{Ar}/^{37}\text{Ar})_{\text{Ca}} \times 10^{-5} \pm \text{SD}$	$(^{39}\text{Ar}/^{37}\text{Ar})_{\text{Ca}} \times 10^{-5} \pm \text{SD}$	$(^{38}\text{Ar}/^{39}\text{Ar})_{\text{K}} \times 10^{-2} \pm \text{SD}$	$(^{40}\text{Ar}/^{39}\text{Ar})_{\text{K}} \times 10^{-4} \pm \text{SD}$	$(^{37}\text{Ar}/^{39}\text{Ar})_{\text{K}} \times 10^{-4} \pm \text{SD}$
Woldegabriel et al., 1994 (BGC)	2.6 ± 0.1	6.6 ± 2.4	-	2.20 ± 0.71	1.21 ± 0.01	51 ± 25	-
Renne et al., 1998 (BGC)	2.71 ± 0.10 2.73 ± 0.13	7.56 ± 0.43 7.60 ± 0.40	-	2.85 ± 1.54	1.24 ± 0.01 1.21 ± 0.01	1.4 ± 0.6 13.1 ± 11.1 4.5 ± 2.3	1.17 ± 0.83 1.87 ± 0.94 1.33 ± 2.80
	2.74 ± 0.14	7.08 ± 0.84	-	2.58 ± 1.62	-	-	-
	2.71 ± 0.04	6.90 ± 0.08	-	1.77 ± 0.13	1.21 ± 0.02	14.4 ± 2.3	5.00 ± 9.40
	2.67 ± 0.18	9.58 ± 1.08	-	2.70 ± 0.98	1.19 ± 0.02	39.7 ± 13.3	1.85 ± 0.69
	2.64 ± 0.05	7.30 ± 0.30	-	1.93 ± 0.34	1.23 ± 0.01	5.7 ± 4.5	1.89 ± 0.26
	2.52 ± 0.07	8.22 ± 0.65	-	2.16 ± 1.18	-	-	-
	2.61 ± 0.03	7.17 ± 0.09	-	1.72 ± 0.32	-	-	-
	2.59 ± 0.05	6.95 ± 0.23	-	1.84 ± 0.29	1.22 ± 0.01	3.4 ± 2.6	-
	-	-	-	-	1.23 ± 0.01	8.0 ± 1.2	1.63 ± 1.32
	2.66 ± 0.074	7.60 ± 0.85	-	2.19 ± 0.42	1.22 ± 0.01	6.6 ± 2.0	-
Simple mean	2.635 ± 0.018	7.061 ± 0.055	-	1.82 ± 0.10	1.218 ± 0.015	10.8 ± 11.7	2.11 ± 1.31
Weighted mean ± SE	2.705 ± 0.105 (A)	7.64 ± 0.56 (A)	-	-	1.221 ± 0.004	3.6 ± 0.5	1.82 ± 0.22
Karner and Renne, 1998 (BGC)	2.57 ± 0.06 (B)	6 ± 2 (B)	-	-	-	1.4 ± 0.6 (A)	-
	2.64 ± 0.02 (C)	6.73 ± 0.04 (C)	-	-	-	0 ± 0.02 (B)	-
	2.70 ± 0.06	6.59 ± 0.16	-	-	-	7 ± 3 (C)	-
Min et al., 2000 (BGC)	2.66 ± 0.07	7.35 ± 0.44	-	-	1.22 ± 0.02	6.3 ± 0.2	-
McDougall and Harrison (1999) based on Renne et al. (1998)	-	-	-	-	-	11 ± 12	-
Culler et al. (2000) based on Renne et al., (1998)	2.64 ± 0.02	7.04 ± 0.06	-	-	-	8 ± 3	-
Lelieveld (1995) (internal report) (VUA)	2.69 ± 0.04	7.09 ± 0.36	3.2 ± 1.8	3.2 ± 1.8	1.211 ± 0.003	8.58 ± 7.58	2.1 ± 2.1
Wijbrans et al., 1995 (based on Lelieveldt, 1995) (VUA)	2.69 ± 0.03	7.09 ± 0.36	-	-	-	16.5 ± 21.1	-
Steenbrink et al., 1999 (VUA)	2.64 ± 0.017	6.73 ± 0.037	-	-	-	8.6 ± 0.7	-
Odin et al., 2001	2.640 ± 0.017	6.730 ± 0.037	-	-	-	8.6 ± 2.3	-

Table 1.1 Compilation of the K and Ca factors for the OSU TRIGA CLICIT facility.

Published K and Ca correction factors for the OSU Triga CLICIT facility. Most of the correction factors are based on experiments performed in the Berkeley Geochronology Center. The rest is based on experiments performed at the VUA. Odin et al. (2001) did not mention if they determined the correction factors or used factors from another publication. Further, it is intriguing to see that two studies refer to the BGC data of Renne et al. (1998), but quote different factors and errors. McDougall and Harrison (1999) remarked that correction factors for Ca nuclear interference reactions did not differ enormously between different reactors, K corrections factor were more dependent on the reactor and reactor circumstances.

NEUTRON FLUENCE MONITORS

Fish Canyon Tuff sanidine (FCT) and the Taylor Creek Rhyolite sanidine (TCR) are used as neutron fluence monitors throughout this study. A brief background is given of the geological history of the two standards and potential heterogeneity due to different sample locations of different standard splits. Any single standard prepared from the FCT or TCR might be homogeneous in age. However, a standard based on samples taken from different locations of a welded tuff and different mineral separation procedures may not be identical in age. Further, an overview of published ages for FCT and TCR is given. Published ages are based on a range of methods and minerals resulting in an age range of 27.5 – 28.5 Ma for FCT and 27.9 – 28.4 Ma for TCR. The ~3% wide range in published data reveal the difficulty in establishing the “true” age of a standard. Though, as long as standards and standard ages are cited in publications as relative instead of absolute ages, results of different studies can be compared (unless we are dealing with heterogeneous standards).

GEOLOGICAL BACKGROUND OF FCT AND TCR

The San Juan volcanic field is located on the eastern margin of the Colorado Plateau in southwest Colorado and covers an area of ~25,000 km² with a total volume of ~40,000 km³ (figure 1.1). The volcanic activity in the San Juan Volcanic field began with a period of andesitic magmatism (~35-30 Ma) characterized by eruptions of numerous scattered central volcanoes onto eroded tectonically stable terrain (Lipman et al., 1970). Voluminous explosive activity began around ~29 Ma and at least 17 large silicic ash flow sheets and related post-collapse lavas were erupted during ~3 Ma from calderas clustered in the west, central and southeast part of the field. The caldera forming eruptions started in the west and southeast followed by eruptions in the central part. The FCT belongs to a series of 9 major ash flow tuffs and related lavas and erupted from the extremely productive central San Juan cluster and is the second and largest ignimbrite in the San Juan field (~5000 km³). In the early Miocene the character of volcanism changed to a largely bimodal association of basalt and high-silica alkali rhyolite related to the opening of the Rio Grande rift (Lipman et al., 1970). Three distinct phases of magmatic activity within the system occurred in a rapid succession around ~28 Ma. The first phase consisted of the eruptions of homogeneous crystal-rich dacite from an enormous magma reservoir. The second phase was the eruption of the FCT, a vast ignimbrite erupted during the formation of the 75 by 35 km² La Garita Caldera. The last phase was a post-resurgence lava-like unit of small volume (<1 km³) within the caldera (Bachmann et al., 2000). The eruptive history of the FCT magmatic system itself seems to be complex involving the emplacement of the magmatic body in the upper crust, cooling to a partly solidified crystal mush and remobilization and eruption due to the influx of new mafic magma (Bachmann et al., 2002).

Whitney and Stormer (1985) described the FCT as a phenocryst-rich, crystal vitric tuff, very even textured and massive in appearance. No large pumice blocks and a few recognizable lithic fragments were found. Within ash flow units there was no noticeable sorting and only minor and gradational variations in grain size. Phenocrysts consisted of plagioclase, sanidine, biotite hornblende, quartz and minor magnetite, ilmenite, zircon, sphene and apatite making up 35 to 50% of the rock. The matrix was composed of glass shards and small flattened pumice fragments. Plagioclase was the most abundant phenocryst comprising about 55% of the phenocryst assemblages. Other assemblage percentages were alkali feldspar (15%),

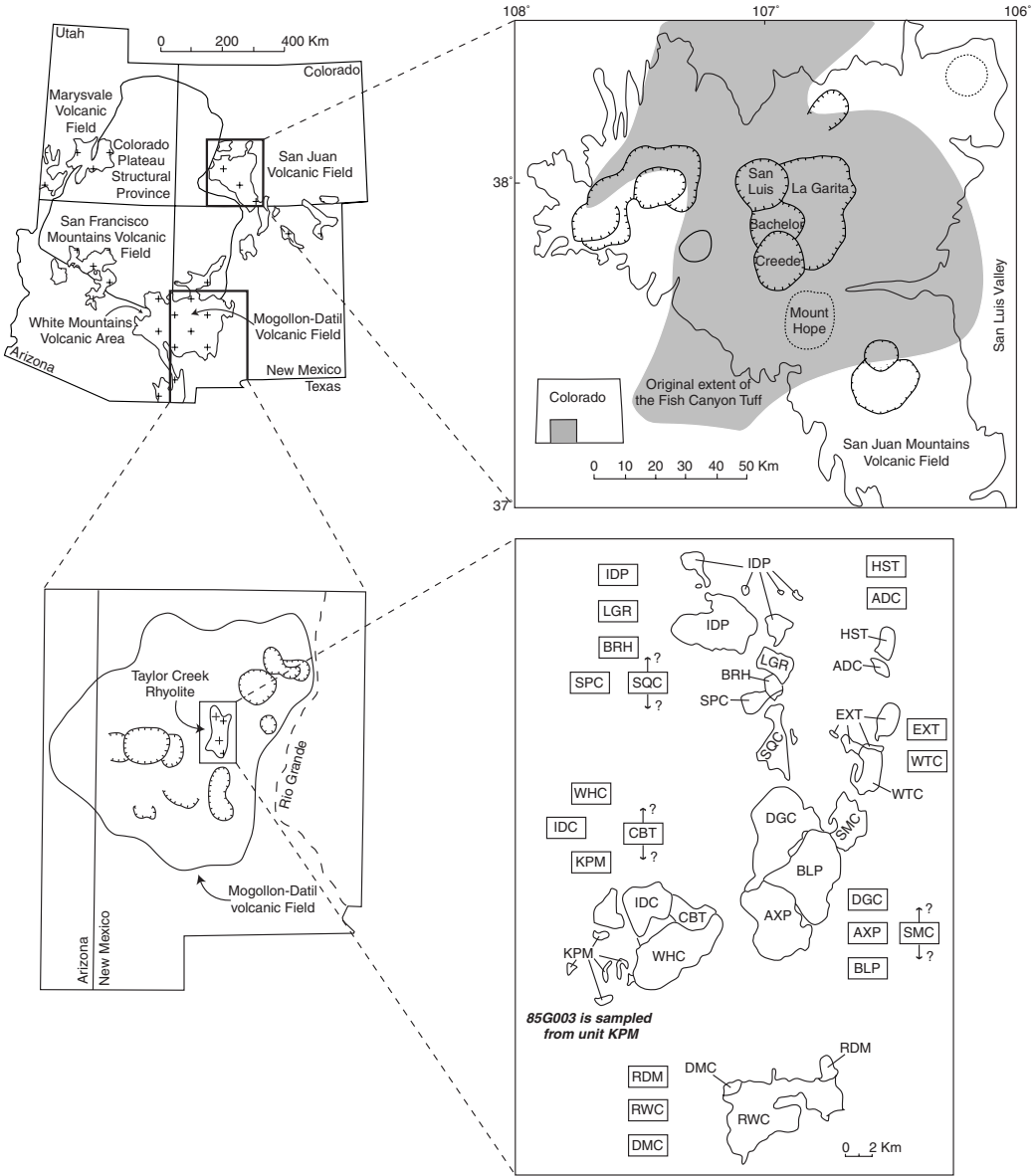


Figure 1.1 A location map of the Fish Canyon Tuff and Taylor Creek Rhyolite.

Location maps from the Fish Canyon Tuff (FCT) and Taylor Creek Rhyolite (TCR) reproduced from Ratté et al. (1984), Whitney and Stormer (1985) and Knesel et al. (1999). Hatched lines mark nearby calderas. The original extent of the FCT is shown in grey. For the TCR the eruptive units are identified by three letter codes and boxes summarize field stratigraphic relations (see for details Knesel et al., 1999). The sample split 85G003 (commonly used as standard) originates from eruptive units KPM.

quartz (5%), biotite (10%), hornblende (10%), sphene, oxides and apatite (5%). One of the important petrologic aspects is the occurrence of resorption textures, which were previously thought to be limited to quartz (Whitney and Stormer, 1985). The presence of plagioclase mantles on sanidine in unaltered volcanic rocks confirmed that rapakivi texture formed in high temperature magmatic environment (Stimac and Wark, 1992). According to Bachmann et al. (2002) resorption textures are also widespread in feldspar phenocrysts of FCT and evidence of grain boundary melting is also preserved when two feldspar phases are in contact. When these processes occur at conditions where the system is still open for Ar diffusion no effects on K/Ar or $^{40}\text{Ar}/^{39}\text{Ar}$ ages are expected. For the purpose of $^{40}\text{Ar}/^{39}\text{Ar}$ dating plagioclase mantle around sanidine can be removed with HF leaching.

In contrast to the FCT, the TCR does not form a single cooling unit. The Taylor Creek Rhyolite is a group of Oligocene lava flows and domes. This group is part of the Mogollon-Datil volcanic field of southwestern New Mexico (Figure 1.1). The many lavas and domes originate from multiple vents. The combined pre-erosion volume of lavas and pyroclastic deposits is conservatively estimated to be 100 km³. The rhyolite is for a large part uniform in appearance throughout the lava field, is flow foliated with a devitrified groundmass, and is porphyritic with a uniform suite of phenocrysts (12-38%). Most grains are between 2 mm and 4 mm. (Duffield and Dalrymple, 1990). The phenocryst assemblage is dominated by subequal amounts of quartz and sanidine. Quartz and sanidine occur as euhedral and subeuhedral grains. Most quartz and sanidine grains are partly rounded and many exhibit deep smooth-walled embayments. Many sanidine grains appear optically homogeneous whereas some show micropertthitic texture. Plagioclase and altered biotite and/or hornblende occur as minor yet ubiquitous phenocrysts.

THE AGE OF FISH CANYON TUFF?

Table 1.2 lists the ages, methods and minerals used for establishing an "absolute" age for FCT. Figure 1.2 visualizes the information of table 1.2. All ages have been (re)calculated with the Steiger and Jäger (1977) decay constants and all errors are reported at the 95% significance level (2σ) unless stated otherwise. Several methods were used to determine the absolute age of FCT: conventional K/Ar dating, fission track dating, Rb/Sr dating, $^{40}\text{Ar}/^{39}\text{Ar}$ measurement relative to a primary K/Ar dated standard, U/Pb dating and $^{40}\text{Ar}/^{39}\text{Ar}$ measurement relative to standards with ages based on techniques independent of radio isotopic methods.

Steven et al. published the first radio-isotopic ages for FCT in 1967. Since then a total of 18 K/Ar analyses were published by different authors on different minerals of FCT resulting in an age range of 27.2 – 27.9 Ma with relatively large uncertainties. Three publications report fission track ages ranging from 26.8 – 28.5 Ma, but with extremely large uncertainties. These large uncertainties in fission track dating compared to other methods make this method unsuitable for calibrating the K/Ar system to standards with fission track derived ages. The Rb/Sr isotopic system may also be used to obtain an "absolute" age for a standard. However, the large uncertainty in the ^{87}Rb decay constant (Renne et al., 1998) forces us to be careful to use the Rb/Sr system to calibrate the K/Ar system, i.e. it would seem rather pointless to intercalibrate a system with large uncertainty to another system with a relatively large uncertainty. Lanphere and Baadsgaard (2001) published a Rb/Sr FCT age (27.44 ± 0.16 Ma) excluding the error in the decay constant and ignore the ongoing discussion of the true value of the ^{87}Rb decay constant (e.g., Begemann et al., 2001). Further, the

reported regression error might underestimate the uncertainty of the estimated age. This age was based on an essentially two-point isochron of the 'best' biotite and feldspar.

Until now the most accepted method to derive an absolute age for the secondary FCT and TCR standards is intercalibration with a primary standard, whose age is determined by K/Ar. A series of primary standards (biotites SB-3 and GA1550, the hornblende MMhb-1 and the muscovite Be4M) was used for this purpose. Apart from the range of primary standards used for intercalibration, also no consensus exists about the K/Ar ages of the primary standards. All the ages for FCT relative to a primary K/Ar standard are cited in table 1.2 with the intercalibration and K/Ar ages as in the original publications. Later "updates" of ages of primary standards are ignored. Renne et al. (1998) published a frequently used age of 28.02 ± 0.32 Ma for FCT-sanidine. They re-measured the K content of the primary standard GA1550 by isotope dilution, which in combination with ⁴⁰Ar* content of McDougall and Roksandic (1974) resulted in an age of 98.79 ± 0.96 Ma for GA1550 compared to 97.9 ± 0.9 Ma previously reported by McDougall and Roksandic (1974). The uncertainty in the FCT age increases to 28.02 ± 0.56 Ma when the error represents the total external error including decay constant errors (errors from Beckinsale and Gale, 1969, as used in the compilation of Steiger and Jäger, 1977). Recently, a new data compilation of potassium measurements by flame photometry from 1968 to 2001 by Spell and McDougall (2003) became available, resulting in a K/Ar age of 98.5 ± 0.8 Ma for GA1550. Spell and McDougall (2003) give an FCT sanidine age of 28.10 ± 0.04 Ma (excluding decay constant uncertainties) using this GA1550 age in combination with their intercalibration factor between FC-s and GA1550. This FCT age decreases to 27.94 ± 0.28 Ma (including decay constant uncertainty) using the FC-s / GA1550 intercalibration factor of Renne et al. (1998). The USGS uses a significantly lower age for FCT based on their intercalibration with primary standard SB3 biotite (Lanphere and Baadsgaard, 2001).

The studies of Oberli et al. (1990), Lanphere and Baadsgaard (2001) and Schmitz and Bowring (2001) performed direct U/Pb experiments on zircon and/or titanite of the FCT. Lanphere and Baadsgaard (2001) show a distinctly younger age than the other U/Pb studies. However, Schmitz et al. (2003) commented on the potential problems inherent to the U/Pb results of Lanphere and Baadsgaard (2001). Apart from statistical problems with the ID-TIMS U/Pb multigrain fraction zircon data, the Lanphere and Baadsgaard data are most likely affected by inheritance and Pb loss (see Schmitz et al., 2003 for detailed discussion). Further, the SHRIMP U/Pb analyses of Lanphere and Baadsgaard (2001) show data which are all (except one) indistinguishable from an age of ~28.7 Ma or are essentially concordant Cretaceous to Proterozoic inherited grains. Arguments by Lanphere and Baadsgaard (2001) to discard these data are weak (Schmitz et al., 2003).

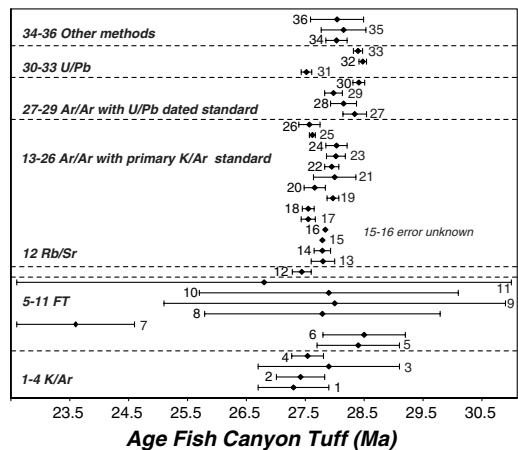


Figure 1.2 An overview of the published ages for Fish Canyon Tuff.

Error bars represent 2σ errors. See text for details. Numbers correspond to publications listed in table 1.2.

Publication	Ref. # figure	Sample information	Age $\pm 2\sigma$ (Ma)	Method
Schmitz and Bowring (2001)	(I) 32 (II) 33	(I) FC-2 zircon (distributed by the New Mexico Geochronology Research Laboratory) (II) FC-2 titanite	(I) 28.402 ± 0.023 Ma ($^{206}\text{Pb}/^{238}\text{U}$, MSWD 0.93) 28.529 ± 0.030 Ma ($^{207}\text{Pb}/^{235}\text{U}$, MSWD 0.74) Preferred age 28.476 ± 0.064 Ma ^a (II) 28.553 ± 0.050 Ma ($^{206}\text{Pb}/^{238}\text{U}$, MSWD 1.60) 28.87 ± 0.40 Ma ($^{207}\text{Pb}/^{235}\text{U}$, MSWD 3.18) Preferred age 28.395 ± 0.078 Ma ^a	(I) U-Pb: Concordia (II) U-Pb: $^{206}\text{Pb}/^{238}\text{U}$
Lanphere and Beadsgaard (2001)	(I) 31 (II) 25	FCT – different sample splits (I) zircon (II) sanidine, biotite	(I) 27.52 ± 0.09 Ma (II) 27.62 ± 0.05 Ma ^b	(I) U/Pb discordia age (of all less discordant data, i.e. $^{207}\text{Pb}/^{235}\text{U} < 0.040$) (II) $^{39}\text{Ar}/^{39}\text{Ar}$ total fusion ages relative to SB-3 of 162.9 ± 0.9 Ma (weighted mean calculated from data in publication)
Min et al. (2000)	(III) 26	(III) sanidine, biotite	(III) 27.57 ± 0.18 Ma (sanidine, biotite)	(III) $^{40}\text{Ar}-^{39}\text{Ar}$ plateau and isochron ages relative to SB-3 of 162.9 ± 0.9 Ma
Villeneuve et al. (2000)	(IV) 12 (V) 4	(IV) biotite, feldspar (V) 79COLES (biotite, hornblende)	(IV) 27.44 ± 0.16 Ma (biotite, feldspar) (V) 27.54 ± 0.27 Ma ^b	(IV) Rb-Sr isochron age (V) Weighted mean K-Ar age of 2 experiments
Bachmann et al. (2000)	27 (28) 29	FCT sanidine FCT biotite	28.34 ± 0.20 Ma (28.15 ± 0.22 Ma) ^c 27.98 ± 0.15 Ma	$^{40}\text{Ar}-^{39}\text{Ar}$ age relative to F239 Palisade Rhyolite sanidine with a zircon $^{207}\text{Pb}/^{235}\text{U}$ age of 1097.6 ± 5.3 Ma $^{40}\text{Ar}-^{39}\text{Ar}$ age relative to MAC-83 biotite with $^{207}\text{Pb}/^{235}\text{U}$ monazite age of 24.21 ± 0.10
Bachmann et al. (2000)	24	FCT sanidine	28.03 ± 0.18 Ma	Mean $^{40}\text{Ar}/^{39}\text{Ar}$ age of 11 total fusions relative to TCR 28.34 Ma
Renne and Min (1998)	36	FCT sanidine	28.04 ± 0.45 Ma	Sandstone of the eruption of Vesuvius 79 AD is used to calibrate Alder Creek Rhyolite. AC is calibrated to FC using the intercalibration factor of Renne et al., 1998
Renne et al. (1998)	23	FCT sanidine, BGC-split	28.02 ± 0.32 Ma	$^{40}\text{Ar}-^{39}\text{Ar}$ age relative to GA1550 biotite K/Ar age of 98.79 ± 0.96 Ma
Hilgen et al. (1997)	35	FCT-3 biotite	28.15 ± 0.38 Ma	$^{40}\text{Ar}-^{39}\text{Ar}$ age relative to tephra with an APTS age
Baksi et al. (1996)	(I) 20 (II) 21 (III) 22	(I) FCT-3 sanidine (II) FCT-3 biotite (III) FCT-3 biotite	(I) 27.66 ± 0.18 Ma ^e (II) 28.00 ± 0.36 Ma ^e (III) 27.95 ± 0.12 Ma (27.96 ± 0.06 Ma)	(I) Mean $^{40}\text{Ar}-^{39}\text{Ar}$ age relative to GA1550 of 97.8 Ma (II) Mean $^{40}\text{Ar}-^{39}\text{Ar}$ age relative to GA1550 of 97.8 Ma (III) Mean $^{40}\text{Ar}-^{39}\text{Ar}$ age relative to SB-3 of 162.9Ma (weighted mean age between brackets)
Van den Boogaard (1995)	19	FCT-3 biotite	27.97 ± 0.05 (1 σ , MSWD 1.3)	Weighted mean $^{40}\text{Ar}/^{39}\text{Ar}$ age of 17 multiple grain fusions relative to MMhb-1 of 520.4 ± 1.7 Ma
Renne et al. (1994)	34	FCT sanidine	28.03 ± 0.18 Ma	$^{40}\text{Ar}/^{39}\text{Ar}$ age relative to samples near geomagnetic reversals with an APTS age (APTS of Shackleton et al., 1995)
Oberli et al. (1990)	30	FCT zircon	28.41 ± 0.1 Ma	U-Pb: $^{206}\text{Pb}/^{238}\text{U}$ single grain
Lanphere et al. (1990)	17	FCT biotite-sandine	27.55 ± 0.12 Ma ^f (biotite)	$^{40}\text{Ar}-^{39}\text{Ar}$ age relative to MMhb-1 of 513.9 ± 2.3 Ma
Duffield and Dalrymple, 1990	18	(I) FCT-3 sanidine (II) Mn-72 sanidine	(I) 27.73 ± 0.20 (II) 27.57 ± 0.14	(I) Mean age of 6 experiments relative to TCR-KPM (=85G003) of 27.88 Ma which is intercalibrated to SB-3 of 162.9 Ma (II) Mean age of 7 experiments relative to TCR-KPM (=85G003) of 27.88 Ma which is intercalibrated to SB-3 of 162.9 Ma

Publication	Ref # figure	Sample information	Age ± 2σ (Ma)	Method
Carpéna and Mailhé, 1987	(I) 11	(I) Apatite from 72N8, FC3	(I) 26.8 ± 4.2 Ma (Poisson standard error)	(I) Mean age of 10 apatite fission tracks determinations
	(II) 10	(II) Zircon from 72N8, FC3, 84-2, 84-1	(II) 27.9 ± 2.2 Ma	(II) Mean age of 6 zircon fission track determinations
	(III) - (I) 15	(I) FC-3 sanidine-biotite	(III) 27.7 ± 1.9 Ma (I) 27.79 Ma	(III) Weighted mean age of fission tracks experiments of concordant plateau, total gas and total fusion ages, no uncertainty quoted)
Cebula et al, 1986	(II) 16		(II) 27.84 Ma ^a	(II) Same age as (I) relative to MMhb-1 520.4 ± 1.7 Ma (Samson and Alexander, 1987)
	(III) 8	(III) FC-3 zircon	(III) 27.79 ± 2.0 Ma	(III) Age based on 17 zircon fission tracks determinations
	(IV) 9	(IV) FC-3 apatite	(IV) 28.0 ± 2.9 Ma	(IV) Age based on 9 apatite fission tracks determinations
	(V) -		(V) 27.9 ± 1.6 Ma	(V) Weighted mean age of fission tracks ages
	(VI) 3	(VI) FC-3 biotite, sanidine, plagioclase, hornblende FCT sanidine-biotite	(VI) 27.9 ± 1.2 Ma	(VI) Mean age of 5 K/Ar experiments
	Kunk et al, 1985	14		27.79 Ma
(I) 3		(I) FCT biotite	(I) 27.80 ± 0.20 Ma	(I) ⁴⁰ Ar- ³⁹ Ar age relative to Bed4M-muscovite of 18.5 ± 0.2 Ma (plateau age)
Hurford and Hammerschmidt, 1985	(II) - (III) 2	(III) FCT biotite-sanidine-plagioclase-hornblende	(II) 27.46 ± 0.50 Ma (III) 27.42 ± 0.41 Ma	(II) Idem (total degassing age of (I)) (III) Weighted mean K-Ar age of 6 experiments
	(I) 5	(I) FCT (70L126, 72N8) zircon	(I) 28.4 ± 0.7 Ma	(I) Average fission tracks age with $\lambda_t \sim 7.0 \times 10^{-17}$ for the spontaneous-fission decay constant of ²³⁸ U
Näser et al, 1981	(II) 6 (III) 7	(II) FCT (70L126, 72N8) apatite (III) FCT (70L126, 72N8)	(II) 28.5 ± 0.7 Ma (III) 23.6 ± 1.0 Ma	(II) Average fission track age with $\lambda_t \sim 8.4 \times 10^{-17}$ (III) Average fission tracks age with $\lambda_t \sim 7.0 \times 10^{-17}$
	(I) - (II) - (III) 1	(I) FCT: biotite-sanidine-hornblende-plagioclase (II) La Garita Quartz latite: sanidine	(I) 27.2 ± 0.7 Ma (II) 27.8 ± 1.3 Ma (III) 27.3 ± 0.6 Ma	(I) Mean K/Ar age of 5 experiments (II) Mean K/Ar age of 2 experiments (III) Weighted mean of both ages

All errors are quoted at the 2σ level according to the publications, unless stated otherwise. Data are calculated with $\lambda_e + \lambda_{e'} = 0.581 \times 10^{-10} \text{ yr}^{-1}$, $\lambda_{e'} = 4.962 \times 10^{-10} \text{ yr}^{-1}$, $^{40}\text{K}/\text{K} = 1.167 \times 10^{-4}$ mol/mol (Steiger and Jäger, 1977).

^a) Preferred age includes systematic decay constant errors and uncertainty in Pb/U tracer calibration.

^b) Lanphere and Baadsgaard (2001) publish a combined K/Ar and total fusion ⁴⁰Ar/³⁹Ar age of 27.57 ± 0.36 Ma. Because a ⁴⁰Ar/³⁹Ar-age is dependent on the absolute age of a primary standard used in age calculations this combined age is separated in a K/Ar and total fusion ⁴⁰Ar/³⁹Ar age by calculating a weighted mean and error on basis of the data in the publication.

^c) Recalculated age with $\lambda = 5.428 \pm 0.068 \times 10^{-10}$ (Audi et al, 1997).

^d) According to Baksi et al, 1996 these data have been measured with a laser system at Queens University. Data are not shown in the publication.

^e) Recalculated age with $\lambda_e + \lambda_{e'} = 0.584 \times 10^{-10} \text{ yr}^{-1}$, $\lambda_{e'} = 4.72 \times 10^{-10} \text{ yr}^{-1}$, $^{40}\text{K}/\text{K} = 1.22 \times 10^{-4}$ mol/mol. Recalculation of the ages with the Steiger and Jäger, 1977 decay constants and isotopic abundances result in an age of 28.1 ± 0.7 Ma for the Fish Canyon Tuff.

^f) It is not clear if errors are quoted at the 1σ or 2σ level and/or what kind of error propagation has been applied.

Table 1.2 An overview of the published ages for Fish Canyon Tuff (FCT).

Overview of published ages for FCT with a short description of the methods used for age determinations. Error bars represent a 2σ error, unless stated otherwise. However, not all studies present a clear overview of their error propagation methods and only a few studies (e.g., Min et al., 2000) incorporate "true" errors in the decay constants. See the text for a more detailed discussion.

U/Pb ages by Oberli et al. (1990) and Schmitz and Bowring (2001) are older than $^{40}\text{Ar}/^{39}\text{Ar}$ ages for FCT, which might be due to prolonged residence times of crystallized zircon in the magma chamber. Nearly identical U/Pb zircon and titanite ages (Schmitz and Bowring, 2001) supported a model, which precluded long residence times in the magma chamber. However, the model of complex multi-stage history of the FCT does not require long magma chamber residence times (<50 kyr; Bachmann et al., 2002) and recent U/Pb ages from Oberli et al. (2002) spanned an interval of ~28.04 - 28.62 Ma interpreted as extended magma chamber residence which invalidates the use of FCT zircon ages as a constraint for $^{40}\text{Ar}/^{39}\text{Ar}$ calibration (Oberli et al., 2002)

Indirect U/Pb studies concerned the studies of Min et al. (2000) and Villeneuve et al. (2000). Both studies determined an U/Pb age of an independent sample and used this age in combination with the $^{40}\text{Ar}^*/^{39}\text{Ar}_K$ ratios of respectively feldspar and biotite of these independent samples to intercalibrate with FCT sanidine. Other methods encompass intercalibration to a historic eruption, like the Vesuvius in Renne et al. (1997) and Renne and Min (1998). Unfortunately samples less than 2000 years old can only be dated with a precision less than 5%, provided that samples show low atmospheric contamination, contain high amounts of K and sufficient material can be collected. Renne et al. (1994) and Hilgen et al. (1997) proposed intercalibration of astronomical and radio isotopic time. Renne et al. (1994) used the $^{40}\text{Ar}/^{39}\text{Ar}$ dates for geomagnetic polarity transitions in the interval 0.78 – 3.40 Ma and in combination with the APTS age for each polarity reversal of Shackleton et al. (1995) an age for FCT was derived. Hilgen et al. (1997) used a direct approach to infer an age for FCT by using the astronomical ages of volcanic tephtras intercalated in astronomically tuned stratigraphic sections in combination with the $^{40}\text{Ar}/^{39}\text{Ar}$ ratios of biotite and sanidine from these tephtras.

THE AGE OF TAYLOR CREEK RHYOLITE?

The published database of TCR ages is much less extensive than for FCT. Elston et al. (1973) published the first K-Ar ages of the TCR (table 1.3). Dalrymple and Duffield (1988) reported $^{40}\text{Ar}/^{39}\text{Ar}$ ages for 7 of the 20 eruptive units mapped by Duffield et al. (1987) relative to a K/Ar dated standard. Duffield and Dalrymple (1990) reported $^{40}\text{Ar}/^{39}\text{Ar}$ ages for 17 of the 20 eruptive units. The weighted mean age for those 17 eruptive units of TCR was 27.92 ± 0.04 Ma (with the extremes of 27.71 and 28.10 Ma) and they concluded that the TCR was emplaced in a period of no more than 100.000 year. However, Duffield and Du Bray (1990) claim that the total emplacement of the TCR ranged from period less than 0.42 Ma and possibly less than 0.13 Ma. However, from a neutron fluence monitor point of view it is important that the TCR is sampled from only one eruptive unit with a well-constrained 'absolute' age. The sample split 85G003 distributed for neutron fluence monitoring originated from the KPM unit, which is among the oldest units in terms of field-defined stratigraphy. Recently, a new separation of the TCR has become available (M. Pringle, M.

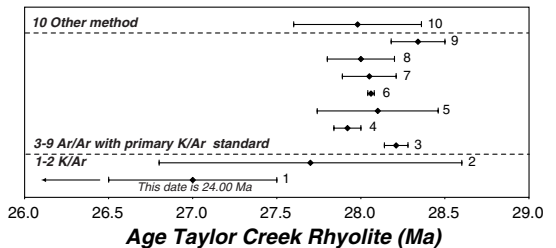


Figure 1.3 An overview of the published ages for Taylor Creek Rhyolite.

Error bars represent 2σ errors. See text for details. Numbers correspond to publications listed in table 1.3.

Publication	Ref # figure	Sample information	Age ± 2σ (Ma)	Method
Renne et al, 1998	9	TCR sanidine	28.34 ± 0.16 Ma ^a	⁴⁰ Ar- ³⁹ Ar age relative to GA1550 biotite 98.79 ± 0.96 Ma
Hilgen et al, 1997	10	85G003 sanidine	27.98 ± 0.38 Ma	⁴⁰ Ar- ³⁹ Ar age relative to tephros with an APTS age
Bakshi et al, 1996	(I) 8 (II) 7	(I) TCR sanidine (II) TCR sanidine	(I) 28.00 ± 0.20 Ma (27.98 ± 0.14 Ma) (II) 28.05 ± 0.16 Ma ^b	(I) Mean ⁴⁰ Ar- ³⁹ Ar age relative to SB-3 of 162.9Ma (weighted mean age between brackets) (II) Mean ⁴⁰ Ar- ³⁹ Ar age relative to GA1550 of 97.8Ma
Van den Boogaard, 1995	6	TCR sanidine	28.06 ± 0.02 Ma (MSWD = 1.2)	Weighted mean of 37 single crystal ⁴⁰ Ar/ ³⁹ Ar experiments relative to MMhb-1 of 520.4 ± 1.7 Ma
McIntosh et al, 1990	5	Mean of sanidine of samples 85G003 and 116	28.10 ± 0.36 Ma	Mean of two ⁴⁰ Ar- ³⁹ Ar ages relative to FCT-3 biotite of 27.83Ma (FCT age of Kunk et al, 1985 recalculated with MMhb-1 of 520.4 Ma)
Duffield and Dalrymple, 1990	(I) 4 (II) -	(I) Sanidine of 17 of the eruptive units of TCR (II) Tcr, equivalent of TCR located 40 km from TCR	(I) 27.92 ± 0.08 Ma (II) 27.92 ± 0.34 Ma	(I) Weighted mean ⁴⁰ Ar/ ³⁹ Ar age of 17 eruptive units relative to TCR-KPM (=85G003) of 27.88 Ma which is intercalibrated to SB-3 of 162.9 Ma, each unit age consists of 6-12 experiments (II) Mean ⁴⁰ Ar/ ³⁹ Ar age of 6 experiments relative to TCR-KPM (=85G003) of 27.88 Ma which is intercalibrated to SB-3 of 162.9 Ma
Dalrymple and Duffield, 1988	(I) 3 (II) -	(I) Sanidine of 85G001 – 85G005, 85G012 and 85G013 (II) idem	(I) 28.21 ± 0.07 Ma (II) 27.90 ± 0.06 Ma ^c	(I) ⁴⁰ Ar- ³⁹ Ar ages relative to SB-3 ^d (II) ⁴⁰ Ar/ ³⁹ Ar age relative to SB-3 ^d
Ratté et al, 1984	2	WL-2a-79 (sanidine)	27.7 ± 0.9 ^e Ma	K-Ar age
Elston et al, 1973	1	TCR sanidine	24.0 ± 0.5 ^f Ma (24.6 Ma)	K-Ar age (between brackets the recalculated age with Steiger and Jager decay constants and isotopic abundances)

All errors are quoted at the 2σ level according to the publications, unless stated otherwise. Data are calculated with $\lambda_e + \lambda_c = 0.581 \times 10^{-10} \text{ yr}^{-1}$, $\lambda_g = 4.962 \times 10^{-10} \text{ yr}^{-1}$, $^{40}\text{K}/\text{K} = 1.167 \times 10^{-4} \text{ mol/mol}$ (Steiger and Jäger, 1977).

^a Full external error is ± 0.28, including uncertainties in decay constants. ^b According to Baksi et al, 1996 these data have been measured with a laser system at Queens University. Data are not shown in this publication. ^c This age is mentioned in McIntosh et al, 1990 based on personal communication with Dalrymple (1989). ^d The used standard is not specified in this publication. Based on remarks of McIntosh et al, 1990 and Lanphere et al, 1990 it is supposed that the ages are calculated relative to SB-3 biotite. McIntosh et al, 1990, mention a reassessment of the age of the standard by Lanphere, but it is unclear what age has been used in the calculations. ^e Significance level error unknown. ^f Analytical error.

Table 1.3 An overview of the published ages for Taylor Creek Rhyolite (TCR).

Overview of published ages for TCR with a short description of the methods used for age determinations. Error bars represent a 2σ errors, unless stated otherwise. See the text for a more detailed discussion.

Lanphere, pers. comm.) sampled from the same eruptive unit, which will replace the use of 85G003. As was the case for the FCT, the revised age published by Renne et al. (1998) of 28.34 ± 0.32 Ma for TCR is currently widely used. This age is based on intercalibration relative to FCT, which in turn was intercalibrated to the K/Ar age of primary standard GA1550. Also Hilgen et al. (1997) calibrated the 85G003 split of TCR to an astronomical dated volcanic tephra as they did for FCT. In table 1.3 and figure 1.3 all the data for TCR are summarized and visualized.

THE ISSUE OF THE DECAY CONSTANT

Apart from the wide range of “absolute” ages for the standards FCT and TCR there exists also a range in the values of the decay constants of ^{40}K . Since Steiger and Jäger (1977) summarized the recommendations of the IUGS Subcommittee on Geochronology longstanding acceptance was reached on the value of the decay constants of ^{40}K . However, a number of recent publications (e.g., Renne et al., 1998; Steenbrink et al., 1999; Min et al., 2000) drew attention to the fact of possible uncertainties in the decay constants, which were not accounted for in the publication of Steiger and Jäger (1977). The ^{40}K decay constants, the related physical parameters and changes in these constants and parameters were discussed in detail by Min et al. (2000) and are briefly summarized here.

The ^{40}K decay constants are mainly based on counting of the number of disintegration products per unit time emitted from the radioactive material, which can be expressed as

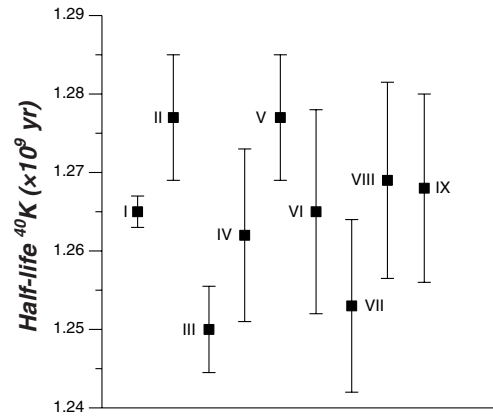
$$\lambda = A \frac{WS}{fN_0} = (A_{\beta^-} + A_e) \frac{WS}{fN_0} \tag{1.2}$$

where λ is the total decay constant of ^{40}K , A is the nuclear activity per second per gram of natural K, W is the atomic weight of K, f is the fraction of ^{40}K in natural K, N_0 is Avogadro’s number, S is the number of seconds in a mean solar year, A_e is the activity of the decay of ^{40}K to ^{40}Ar (activity of γ , β^+ and electron capture) and A_{β^-} is the β^- activity. The compilations of activity data discussed in Min et al. (2000) are all based on this method. As stated by Min et al. (2000) summarizing the experimental activity data is difficult because of unclear definition of the reported errors, lack of clarity in the contributions to the error estimation and in the applied statistical methods for many of the studies. Beckinsale and Gale (1969) and Endt and Van der Leun (1973) both used an error-weighted mean of the individual activity values from a subset of published determinations in their compilations which assumes implicitly that the errors of individual determinations are statistically equivalent (see discussion in Min et al., 2000). Further, the error assignment in the Beckinsale and Gale (1969) compilation differs from the Endt and Van der Leun (1973) compilation by the fact that Endt and Van der Leun (1973) multiply the error by $\sqrt{\text{MSWD}}$ when $\text{MSWD} > 1$. Adjustment to the more realistic error assignments of Endt and Van der Leun (1973), doubles the error in γ activity in the Beckinsale and Gale (1969) compilation (Min et al., 2000).

Table 1.4 summarizes the activity data, physical constants and related decay constants. The Steiger and Jäger (1977) study is the “consensus” in the geochronology community. This compilation was based on the data from Beckinsale and Gale (1969) and Garner et al. (1975) and is used in this thesis unless stated otherwise. Min et al. (2000) updated the activity data of Beckinsale and Gale (1969) with improved values

Figure 1.4 ^{40}K half-lives and associated errors based on different data compilations.

The “consensus” half-life of ^{40}K in the geochronology community (Steiger and Jäger, 1977) is significantly different from the “consensus” half-life in the nuclear physics community (Endt and Van der Leun, 1973). Reconsideration of physical parameters and error propagation methods results in a half-life for ^{40}K , which cannot be statistically distinguished. See text for further explanation. Roman numbers correspond to the column number in table 1.4. Errors are given at 1σ (68% confidence level).



for physical parameters and multiplied the uncertainties by $\sqrt{\text{MSWD}}$. This resulted in a slightly higher decay constant (or lower half-life) with higher uncertainties. This approach is also used in this thesis when discussing the full error estimates in $^{40}\text{Ar}/^{39}\text{Ar}$ ages. The Endt and Van der Leun (ENSDF, cut-off date 1 June 1997) and Audi et al. (1997, NUBASE) compilations do not include the Garner et al. (1975) value for ^{40}K abundance, although this value is much more accurate than the ^{40}K abundance of Nier (1950). Figure 1.4 visualizes the half-lives of ^{40}K based on the compilations in table 1.4. The main conclusion is that all values are not significantly different at the 1σ (68% significance) level ONLY when errors are estimated as realistic as possible. Unfortunately, the consensus value in geochronology of Steiger and Jäger (1977) shows unrealistic small errors and revision and improvement is strongly recommended (see e.g. Begemann et al., 2001).

PART II: APPLICATION OF THE $^{40}\text{Ar}/^{39}\text{Ar}$ DATING TECHNIQUE AT THE DUA.

IMPLEMENTATION OF THE $^{40}\text{Ar}/^{39}\text{Ar}$ TECHNIQUE AT THE DUA

Part of this section is based on the paper of Wijbrans et al. (1995). The description of instrumentation, measurement procedures and data reduction will be briefly summarized. Modifications of the procedures compared to Wijbrans et al. (1995) will be described in more detail.

SAMPLE PREPARATION

Volcanic tephra was collected in the field. Before sampling the surface layer of the outcrop was removed and care was taken that sampling equipment (e.g., hammers and knives) were clean. Samples were both dried at 50°C and crushed with a jaw crusher, or samples were mixed with demineralized water and stored during a minimum period 24 hours at 50°C . Then the samples were washed either by hand (using thoroughly cleaned sieves of 32, 63, 125, 250 and $500\ \mu\text{m}$) or by use of the desliming apparatus, which takes out the fine dust fraction. Samples are loaded in a ~ 60 cm long cylinder with a diameter of ~ 30 cm. At the bottom demineralized water (with a few drops of Calgon®) flows into the cylinder. The sample swirls to the top of the column and steadily settles down. Depending on the density and grain size the required

	I Beckinsale and Gale (1969)	II Endt. and Van der Leun (1973)	III Steiger and Jäger (1977)	IV Holden (1990)	V NUBASE (Audi et al, 1997) ^f	VI ENSDF (Cutoff date 1-Jun-1997)	VII Min et al (2000) updated B & G (1969)	VIII Min et al. (2000) updated E & L (1973)	IX Based on Holden (1990) ^g
A_{1p} ($\text{g}^{-1}\text{sec}^{-1}$)	28.27 ± 0.10 (89.52 ± 0.32 %)	27.89 ± 0.30 89.33 ± 0.22 %	28.27 ± 0.10 ^h	28.08 ± 0.23 ^h	89.28 ± 0.26 (27.67 ± 0.08) 10.72 ± 0.26	27.89 ± 0.30 89.14 ± 0.22 %	28.27 ± 0.10	27.89 ± 0.30	28.00 ± 0.26
A_{α} ($\text{g}^{-1}\text{sec}^{-1}$)	3.26 ± 0.04 (10.32 ± 0.13 %)	3.31 ± 0.06 10.67 ± 0.22 %	3.26 ± 0.04 ^h	3.28 ± 0.03 ^h	3.32 ± 0.241 (3.32 ± 0.08)	-	3.31 ± 0.08	3.31 ± 0.06	3.21 ± 0.02
A_{β^+} ($\times 10^{-4}$ $\text{g}^{-1}\text{sec}^{-1}$)	3.25 ± 0.74 (1.03 ± 0.23 $\times 10^{-3}$ %)	(3.21 ± 0.68) ^d 1.03 ± 0.22 $\times 10^{-3}$ %	3.25 ± 0.74 ^h	-	-	-	-	-	-
A_{β^-} ($\text{g}^{-1}\text{sec}^{-1}$)	0.050 ± 0.020 (0.16 ± 0.06 %)	-	0.050 ± 0.020 ^h	-	-	-	-	-	-
A_{tot} ($\text{g}^{-1}\text{sec}^{-1}$)	(31.58 ± 0.11)	31.20 ± 0.30	(31.58 ± 0.11) ^h	(31.37 ± 0.12)	(31.00 ± 0.11)	31.29 ± 0.34	-	-	1.17 ± 0.02
f ($\times 10^{-4}$)	1.18 (within ± 1%)	1.178 ± 0.008	1.167 ± 0.008 ^h	1.17 ± 0.02	1.17 ± 0.02 ^h	1.17 ± 0.02	1.17 ± 0.02	1.17 ± 0.02	39.0983 ± 0.00012 ^b
W	39.102 (on the ¹² C scale)	(39.102) ^e	39.0983 ± 0.00012 ^b	-	-	39.095	39.0983 ± 0.00012 ^b	39.0983 ± 0.00012 ^b	6.0221367 ± 0.0000072 ^c
N_0 ($\times 10^{23}$ atoms/mole)	6.02252 (on the ¹² C scale)	(6.02252) ^e	6.02252 ^h	-	-	-	6.0221367 ± 0.0000072 ^c	6.0221367 ± 0.0000072 ^c	3.155693
S ($\times 10^3$ sec/yr)	3.15569	(3.1556) ^e	3.15569 ^h	-	3.15569259747	-	3.155693	3.155693	4.884 ± 0.095
λ_{1p} ($\times 10^{-10}$ yr ⁻¹)	4.905 ± 0.018	(4.851 ± 0.062)	4.962 ± 0.038	4.917 ± 0.084	-	-	4.950 ± 0.086	4.903 ± 0.095	0.562 ± 0.010
λ_{α} ($\times 10^{-10}$ yr ⁻¹)	0.566 ± 0.0070	(0.576 ± 0.011)	0.581 ± 0.011	0.011	-	-	0.574 ± 0.017	0.562 ± 0.010	-
λ_{β^-} ($\times 10^{13}$ yr ⁻¹)	8.67 ± 3.48	-	-	-	-	-	-	-	-
λ_{β^+} ($\times 10^{15}$ yr ⁻¹)	-	(5.6 ± 1.1)	-	-	-	-	-	-	-
$\lambda = \lambda_{\beta^+} + \lambda_{\alpha} + \lambda_{\beta^-}$ ($\times 10^{-10}$ yr ⁻¹)	5.480 ± 0.020	(5.427 ± 0.073)	5.543 ± 0.047	5.491 ± 0.094	(5.428 ± 0.068)	5.479 ± 0.111	5.530 ± 0.097	5.463 ± 0.107	5.465 ± 0.106
$T_{1/2} = \ln 2 / \lambda$ ($\times 10^5$ yr)	1.265 ± 0.004	1.277 ± 0.016	1.250 ± 0.011	1.262 ± 0.022	1.277 ± 0.016	1.265 ± 0.026	1.253 ± 0.022	1.269 ± 0.025	1.268 ± 0.024

^{a)} Adapted from Beckinsale and Gale (1969).
^{b)} This value is calculated in Min et al (2000) using the activity data for β^- decay (27.89 ± 0.30 $\text{g}^{-1}\text{sec}^{-1}$, 89.33 ± 0.22 %) and β^+ decay (1.03 ± 0.22 $\times 10^{-3}$ %). Calculation of this value using the weighted mean of the two β^+/β^- ratios published in Endt and van der Leun (1973) in combination with the β^- activity of 27.89 ± 0.30 $\text{g}^{-1}\text{sec}^{-1}$ results in 3.20 ± 0.75 $\times 10^{-4}$ $\text{g}^{-1}\text{sec}^{-1}$.
^{c)} Values are not given in original publications, but using these values and the quoted activity data for the calculation for $T_{1/2}$ the result is 1.277 Ga equivalent to the original publication.
^{d)} NUBASE of Audi et al (1997) is the same version of the Evaluated Nuclear Structure Data File (ENSDF) of 1994 for ⁴⁰K constants. The value in Audi et al (1997) for $T_{1/2}$ is 1.277 ± 0.016 $\times 10^9$ as given in Endt (1990) and calculated in Endt and Van der Leun (1973).
^{e)} Holden (1990) only reports the ⁴⁰K half-life of the studies used in his compilation. Here the used the simple means and standard error of the means of γ and β^+ activities of the studies included in the compilation of Holden (1990) are given.
^{f)} This column represents the activities and decay constants calculated with the data included in the data compilation of Holden (1990), but with the physical constants, weighted mean of activities and error propagation as in Min et al (2000).

Table 1.4 Summary of activity data, physical constants and related decay constants for different compilations (partly adapted from Min et al., 2000).
 Parameters and physical constants required for the calculation of ⁴⁰K decay constant. Results for different data compilations are shown (see text for detailed discussion). See for references Min et al. (2000). Errors are given at 2 σ (95% confidence level). Errors in Steiger and Jäger (1977) constants are propagated based on uncertainties of Beckinsale and Gale (1969) and Garner et al. (1975).

time to settle down can be calculated according to Stokes law. In this way the fraction smaller than $32\ \mu\text{m}$ can easily be removed. Samples are dried at 50°C . Biotite is removed from the sample by either the use of a vibration or Faul table or a Frantz magnetic separator. After use of a vibration table biotite is purified using a Frantz magnetic separator. Biotite is further purified by heavy liquid separation with diiodomethane (at ρ is $3.05\ \text{g}/\text{cm}^3$) and the final step is hand picking.

Part of the samples is decalcified with $\sim 6\text{N}$ nitric acid after the removal of the biotite and/or other magnetic minerals. Then all samples were separated with heavy liquid (sodiumtungstate, lithiumtungstate, diiodomethane or bromoform) with a density of $2.55\ \text{g}/\text{cm}^3$. The sink of $2.55\ \text{g}/\text{cm}^3$ is separated with heavy liquid with a density of $2.58\ \text{g}/\text{cm}^3$. The fraction $2.55\text{-}2.58\ \text{g}/\text{cm}^3$ was either directly hand picked for sanidine or purified using the Frantz magnetic separator followed by hand picking. Picked sanidine separates were leached with 6N HNO_3 and $\sim 8\%$ HF during 5 minutes in an ultrasonic bath. Subsequently the samples were thoroughly rinsed with MilliQ water and dried. Depending on sample quality samples might be leached before the final heavy liquid step at $2.58\ \text{g}/\text{cm}^3$.

IRRADIATION

In all experiments in this study samples were wrapped in aluminum foil. Standards (FCT as well as TCR) were wrapped in copper foil. Samples and standards were loaded in a quartz vial with an ID $6\ \text{mm}$ and in the case of VU37 vial B a tube with an ID of $9\ \text{mm}$ was used. Between every 3 or 4 unknowns a standard was loaded. Different batches of samples were all irradiated for 7 hours in the OSU TRIGA reactor in the CLICIT facility. In the CLICIT facility the Cd-lined tube is placed into one of the core's inner grid positions, which is normally occupied by a fuel element. The energies of the neutrons are higher than $0.4\text{-}0.5\ \text{eV}$ and fluence rates are around $1\ \text{MWh}$. Temperatures inside the CLICIT reached at least 93°C and are likely somewhat higher (Hughes, 1989). VU41 and VU42 were irradiated in the extended TRIGA tube. Correction factors for the CLICIT facility were already discussed in the previous paragraph.

INSTRUMENTATION

The analytical system consists of an argon ion laser, beam optics, a low volume, ultra high vacuum (UHV) gas inlet system and a Mass Analyser Products Ltd. MAP 215-50 noble gas mass spectrometer. The laser is an $18\text{-}24\ \text{W}$ argon ion laser (actual maximum laser power is tube-dependent). Samples are melted with a visible light multiline ($454.5\text{--}514.5\ \text{nm}$) laser beam. To assure uniform heating with a defocused laser, the beam diameter can be trimmed with an adjustable iris aperture allowing a spot size of circa $5\ \text{mm}$.

The sample tray is loaded into the sample house with a Pyrex glass window. This sample house is attached to the inlet system with a $50\ \text{cm}$ flexible stainless steel tube and a right angle all-metal valve. Because the sample trays are changed regularly, the sample house can be pumped separately from the inlet system with the turbo pump, keeping the inlet system and getters under ultra high vacuum.

The inlet system consists of a central getter cross with two SAES Fe-V-Zr (ST172) alloy getter elements operated at about 250°C with an effective pumping speed of $30\ \text{l/s}$. A SAES AP10 appendage pump with a filament heated Zr-Al cartridge is included in the sample house segment right before the getter cross. The

system is pumped either with a 20 l/s Vacion triode ion pump, or with a Balzers TPU062 hybrid turbo/drag pump. This last pump is used as the main pump due to its better pumping speed for noble gases and the triode ion pump is used as back up. Routinely, vacuum levels of $3\text{--}6 \times 10^{-9}$ mbar are reached. Further, two gas pipettes (~ 1 ml each) operated with two pneumatic NUPRO (SSBG8 series fitted with Cu-sealing tips) valves are connected to the getter cross and are used to admit aliquots of air or ^{38}Ar enriched air-reference gas into the system both from a 10,000ml reservoir.

Clean argon gas is let into the mass spectrometer using a pneumatic NUPRO SS8BG valve fitted with a Cu tip. The total volume of the gas inlet system (including the sample house) is circa 100ml (with a volume ratio of 2:1 for the sample house segment versus the getter cross). The total volume of the mass spectrometer is circa 1500ml, thus a simple expansion of the gas into the mass spectrometer ensures the transfer of more than 90% of the gas into the mass spectrometer.

The mass spectrometer is a 90° sector instrument with a 17 cm radius magnet and extended magnet geometry. It is fitted with a Nier type electron bombardment source (operated at 72eV electron energy, 200 μA trap current and 3 kV acceleration voltage). The source is fitted with a coiled filament and has a sensitivity for argon $\sim 4.0 \times 10^4$ A/torr. The source housing is continuously pumped with a SAES NP50 getter pump with a Zr-Al alloy cartridge at room temperature. The variable collector slit is set at resolution 400. Behind the collector slit the beam is deflected 90° with a 50 mm radius electrostatic filter onto a Johnston MM1 secondary electron multiplier (SEM). The amplifier of the SEM collector uses a 10^7 , 10^8 or $10^9 \Omega$ resistor and these resistor settings can be changed using a set of sapphire insulated solenoid switches. The

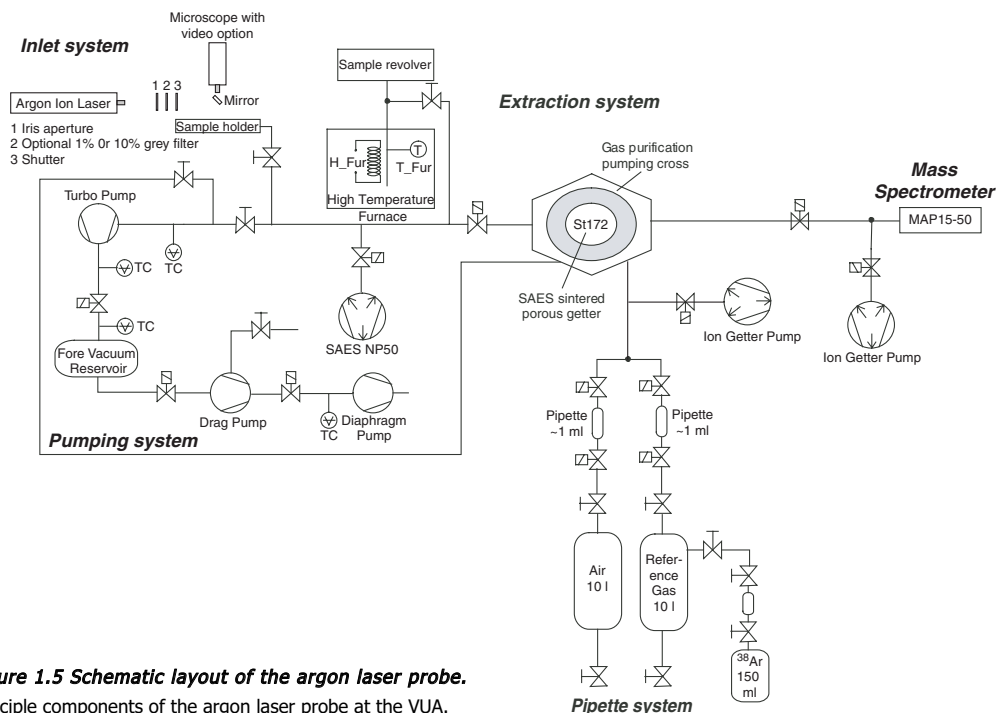


Figure 1.5 Schematic layout of the argon laser probe.
Principle components of the argon laser probe at the VUA.

amplifier of the Faraday cup collector uses a $10^{11} \Omega$ resistor, resulting in an effective gain factor of 500 for the SEM over the Faraday cup at the highest setting. This effective gain factor is checked periodically (~twice a year) to assess the performance of the SEM using the ^{40}Ar intensity of reference gas or air as reference. Because all the isotopes are measured on the SEM a precise gain calibration between the Faraday and the SEM is not required. Analyses are performed in a static mode of the mass spectrometer. A Hall probe controls peak jumping of the magnet. A schematic overview of the system is given in figure 1.5.

MEASUREMENT ROUTINES

After irradiation samples were unwrapped and loaded in a copper tray with 185 holes of 2 mm diameter each. This tray was placed in the sample holder of the argon extraction line. The copper tray is covered with a thoroughly cleaned 1 mm thick Pyrex cover glass to prevent jumping of crystals out of their holes when in contact with the laser-beam. Samples, sample holder and part of the extraction line are baked out for one night at $\sim 200^\circ\text{C}$.

Before measuring samples and standards sanidine are preheated with a defocused laser beam at $\sim 1.8\text{W}$ to remove contaminating volatiles. This gas is pumped away. During heat treatment samples do not start to glow. Tests indicate that these first gas fractions indeed contain only minor amounts of mainly non-radiogenic argon. Most of the biotite experiments involve stepwise heating experiments and thus preheating is unnecessary. For the rare biotite fusion experiments the samples are preheated with a defocused laser beam at $\sim 0.2\text{W}$. Incremental heating of the transparent sanidine crystals with an argon ion laser appeared to be difficult.

Samples are melted by exposure to a laser-beam focused to a diameter of ~ 3 mm during a few seconds or stepwise heated by a defocused laser-beam during 60 seconds, included in a total clean up time of 300 seconds in the UHV gas inlet system. Simple expansion of the gas from the inlet system to the mass spectrometer occurs during 90 seconds to allow for isotopic homogenization between the two reservoirs.

The mass spectrometer is operated with a modified version of the standard MAP software that allows data collection for argon using the SEM collector. Samples, standards, references gas or air aliquots are measured in 10 scans in peak jumping mode from m/e 40 to m/e 35.5 in half mass intervals. Baselines in each scan consist of typically 4-6 integration cycles of the Schlumberger Solartron 7060 DVM. ^{37}Ar and ^{38}Ar peaks consist of 8 integration cycles per scan (or 10-12 integration cycles for ^{38}Ar in reference gas), ^{40}Ar of 10-12 integration cycles per scan and ^{36}Ar and ^{39}Ar of 12-16 integration cycles per scan. During the 90 seconds equilibration time between the inlet system and gas spectrometer a peak centering routine is carried out on the ^{40}Ar peak. The exact positions of the other peaks relative to the ^{40}Ar peak are stored in the program and calibrated every 3-4 weeks using air argon centering both ^{40}Ar and ^{36}Ar in the magnetic field.

The average value of each integration cycle is stored in a raw data file together with the number of scans and the time elapsed since the inlet of the gas into the mass spectrometer. Recently, additional information like sample code, date, inlet time and the amplifier resistor of the SEM are also coded in the raw data file. Individual outliers in one integration cycle are not recognized and no standard deviation for an integration

cycle is recorded in the data file (only the simple mean is recorded). In most cases blanks are measured in 8 scans (this is time saving when running the system in the manual mode) and occasionally in 10 scans (in the automatic mode).

For samples of irradiation VU 32, VU37-I and VU41 the machine was run during 10-16 hours a day and during night the system was pumped. During the analyses of VU37-II the machine was run (manually) during 24 hours a day. Irradiation VU42 was run predominantly in the automatic mode aimed to run the system 24 hours a day. The peak-shape of the ^{40}Ar was checked regularly (about a few times per week). The peak-shape of the peaks of the other isotopes was checked infrequently (about once a year). However, when the ^{40}Ar peak-shape was flat and symmetric, the peak-shape of the other isotopes appeared to be flat and symmetric as well.

In principle, measurements start and end each day with a blank. Depending on the behavior of the system blanks were run between every 2, 3 or 4 unknowns. Air and/or reference gas measurements were performed regularly aiming to a minimum of 3 measured aliquots every 48 hours. A new reference gas was installed to improve the monitoring of the mass discrimination, which will be described later in this chapter. For irradiation VU32 first the J-curve was determined followed by the unknowns. For the other irradiations samples were measured alternating with the standards surrounding the samples in the irradiation vial.

An estimate for the system sensitivity was made on basis of the radiogenic $^{40}\text{Ar}^*$ content of biotite GA1550 (1.34×10^{-9} mol/g; McDougall and Roksandic, 1974). Biotite grains are weighted prior to loading into the vacuum sample house and analyzed. An initial system sensitivity was estimate of 1.8×10^{-17} mol/mV (Wijbrans et al., 1995). Currently the system sensitivity is estimated around 3.3×10^{-15} mol/mV, following a different approach to the SEM-gain setting (gain ~ 500 on $10^9 \Omega$ relative to Faraday collector run at $10^{11} \Omega$).

AGE CALCULATION AND ERROR PROPAGATION AT THE VUA

This paragraph discusses the calculation of a $^{40}\text{Ar}/^{39}\text{Ar}$ age and how to assign a realistic uncertainty to an age. The ArArCALC program, developed as in-house software by A.A.P. Koppers at the VUA from earlier Macintosh Quickbasic based software (Koppers, 2002), is used for reduction of the raw $^{40}\text{Ar}/^{39}\text{Ar}$ data. A summary of the main characteristics of this data reduction program is given here (partly adapted from Koppers, 2002). First, the determination of the $^{40}\text{Ar}^*/^{39}\text{Ar}_K$ (or F) ratio and error in this ratio for a single measurement is described. This is expanded to the development of a series of equations required for the calculation of the total variance of the F-ratio and the contribution of all individual parameters to the total variance of the F-ratio. These equations will be used to assess the major parameters contributing to analytical error and where possible to improve these parameters in future analyses. Then the calculation of a simple age and error in ArArCALC is described, followed by a more sophisticated age and error equation slightly modified from Min et al. (2000). Meanwhile, an independent numerical method for the age calculation and error propagation (Scaillet, 2000) is discussed.

Most algorithms used in the ArArCALC were already described in textbooks (Faure, 1986; McDougall and Harrison, 1999) or technical papers (Dalrymple et al. 1981; York, 1969; Karner and Renne, 1998; Renne et al., 1998; Min et al., 2000). Some equations are reproduced from their original publications to clarify the

explanation of the age calculation and error propagation as discussed here. Error propagation is based on linearized error expansion techniques where the variance contribution ($\sigma_{X_1}^2, \sigma_{X_2}^2, \dots, \sigma_{X_n}^2$) of each input parameter (X_1, X_2, \dots, X_n) is weighted by the squared partial derivative ($(\partial F/\partial X_1)^2, (\partial F/\partial X_2)^2, \dots, (\partial F/\partial X_n)^2$) of the age function $F(X_1, X_2, \dots, X_n)$ relative to this variable. The total variance of function F is then simply calculated by summing up all weighted variances for the individual parameters

$$\sigma_F^2 = \sum_{i=1}^n \left[\frac{\partial F}{\partial X_i} \right]^2 \sigma_{X_i}^2 \tag{1.3}$$

Numerical error propagation methods are an alternative option for error propagation (Roddick, 1987; Scaillet, 2000). Roddick (1987) used an extended version of this equation

$$\sigma_F^2 = \sum_{i=1}^n \left(\frac{\partial F}{\partial X_i} \right)^2 \sigma_{X_i}^2 + 2 \sum_i \sum_j \left(\frac{\partial F}{\partial X_i} \right) \left(\frac{\partial F}{\partial X_j} \right) \sigma_{ij} \tag{1.4}$$

with $i < j$ and σ_{ij} is the covariance between X_i, X_j variables (Hahn and Saphiro, 1969). If variables are all independent, the covariance is 0 and the second term is omitted (as is assumed in the analytical error propagation as described here). In the numerical error propagation as proposed by Roddick (1987) and further elaborated for ⁴⁰Ar/³⁹Ar dating by Scaillet (2000) this second term is not neglected.

One of the differences between analytical and numerical solutions is (apart from assuming no correlation between the variables in the analytical solution) that in analytical solutions all the partial derivatives have to be derived. Sequentially deviating each variable from its mean value by a small fractional amount and determining the corresponding change in a function can solve the numerical solutions. Both methods (analytical linear error expansion and numerical solutions) will be discussed in more detail.

DATA REDUCTION WITH ANALYTICAL SOLUTIONS

In ArArCALC data regression of the individual isotopes can be applied using exponential, parabolic, linear or averaging methods. In practice an exponential fit is generally chosen for the ⁴⁰Ar and ³⁹Ar isotopes in samples, standards, blanks and air measurements and for the ⁴⁰Ar and ³⁸Ar isotopes in the reference gas. A linear fit is often used for the other isotopes (³⁸Ar, ³⁷Ar, and ³⁶Ar for samples, standards, blanks and airs and ³⁶Ar for reference gas), because scatter is too high to justify a curve fit. The linear regression is performed by the standard Excel worksheet function LINEST using the "least squares" method. The exponential fit is based on $Y_i = aZ_i + b$ with $Z_i = e^{cX_i}$, where Y_i represents the intensity of the measurements (in volts), X_i represents the time of the measurements following the inlet of the sample to the mass spectrometer. The coefficients a, b and c are derived by changing the curvature of the line iteratively while concurrently solving the coefficients "a" and "b" with the LINEST function. When the Pearson's squared correlation coefficient R^2 reaches its maximum and the difference in R^2 for two consecutive iterations is smaller than the convergence level (0.01% convergence level is adequate), the best solution for the coefficients a, b and c is found (Koppers, 2002). The standard errors (SE) on the intercept value are calculated with equation 1.5 (Taylor, 1997):

$$SE = SE_{yx} \sqrt{\frac{\sum_{i=1}^n X_i^2}{n \sum_{i=1}^n X_i^2 - \left(\sum_{i=1}^n X_i\right)^2}} \quad (1.5)$$

where n is the number of data points and SE_{yx} is the standard error predicted on Y_i for each X_i using Excels worksheet function STEYX. Intercept values are corrected for blanks by simple subtraction of the blank intercept values of the intercept values of the unknowns. Error propagation is according to equation 1.3.

In ArArCALC blank corrected intercept values are corrected for mass fractionation (see Koppers, 2002 for formulas). The determination of the mass fractionation factors at the VUA will be discussed in detail in the next paragraph. After blank and mass fractionation corrections, intercept values must be corrected for nuclear interference reactions and for the radioactive decay of the ^{37}Ar and ^{39}Ar isotopes. Correction of nuclear interference reactions is described in McDougall and Harrison (1999) and the radioactive decay correction is according to the algorithm of Wijbrans and McDougall (1987). The uncertainties in the time elapsed between measurement and irradiation and duration of irradiation are assumed to be 0. The uncertainties in the ^{37}Ar and ^{39}Ar decay constants are propagated using formula 1.3 (or see Koppers, 2002).

The data reduction of one analysis to a $^{40}\text{Ar}^*/^{39}\text{Ar}_K$ ratio for this analyses requires the regressions and corrections described above. Combination of all parameters in one equation and linearized error propagation allows the assessment of the main parameters contributing to the analytical uncertainty in the F-ratio. Improvement in the parameters dominating the total uncertainty directly improves the analytical precision of the final ages. Efforts for more precise ages should therefore focus on the parameters with the highest contribution to the variance. The contribution of all parameters to the variance can in principle be also assessed by the numerical error analysis as described in Scaillet (2000). Comparison of both methods allows us to say something about the reliability of both error propagation methods. The F-ratio is calculated with (modified from McDougall and Harrison, 1999)

$$F = \frac{\frac{(40_u - 40_b)}{(39_u - 39_b) \times \left(\frac{C\lambda_{39} e^{\lambda_{39}B}}{1 - e^{-\lambda_{39}C}}\right) \times \frac{1}{D}} - A \times \frac{(36_u - 36_b) \times \left(\frac{4}{D} - 3\right)}{(39_u - 39_b) \times \left(\frac{C\lambda_{39} e^{\lambda_{39}B}}{1 - e^{-\lambda_{39}C}}\right) \times \frac{1}{D}} + A \times Z_{Ca} \times \frac{(37_u - 37_b) \times \left(\frac{C\lambda_{37} e^{\lambda_{37}B}}{1 - e^{-\lambda_{37}C}}\right) \times \left(\frac{3}{D} - 2\right)}{(39_u - 39_b) \times \left(\frac{C\lambda_{39} e^{\lambda_{39}B}}{1 - e^{-\lambda_{39}C}}\right) \times \frac{1}{D}}}{1 - Y_{Ca} \times \frac{(37_u - 37_b) \times \left(\frac{C\lambda_{37} e^{\lambda_{37}B}}{1 - e^{-\lambda_{37}C}}\right) \times \left(\frac{3}{D} - 2\right)}{(39_u - 39_b) \times \left(\frac{C\lambda_{39} e^{\lambda_{39}B}}{1 - e^{-\lambda_{39}C}}\right) \times \frac{1}{D}} - X_K} \quad (1.6)$$

where M_u is the measured mAr intensity in Volt for the isotopes $m = 40, 39, 37$ and 36 , M_b is the measured ^mAr blank intensity in volt for the isotopes $m = 40, 39, 37$ and 36 , A is the atmospheric $^{40}\text{Ar}/^{36}\text{Ar}$ ratio of 295.5, D is the mass discrimination factor, Y_{Ca} is the $(^{39}\text{Ar}/^{37}\text{Ar})_{Ca}$ correction factor, Z_{Ca} is the $(^{36}\text{Ar}/^{37}\text{Ar})_{Ca}$ correction factor, X_K is the $(^{40}\text{Ar}/^{39}\text{Ar})_{Ca}$ correction factor, C is the duration of the irradiation, B is the time elapsed between irradiation and measurement, λ_{39} is the decay constant of ^{39}Ar and λ_{37} is the decay constant of ^{37}Ar . The total variance can be calculated with equation 1.7:

$$\sigma_F^2 = \left(\frac{\partial F}{\partial P}\right)^2 \sigma_P^2 + \left(\frac{\partial F}{\partial R}\right)^2 \sigma_R^2 + \left(\frac{\partial F}{\partial V}\right)^2 \sigma_V^2 + \left(\frac{\partial F}{\partial T}\right)^2 \sigma_T^2 + \left(\frac{\partial F}{\partial Q}\right)^2 \sigma_Q^2 + \left(\frac{\partial F}{\partial S}\right)^2 \sigma_S^2 + \left(\frac{\partial F}{\partial W}\right)^2 \sigma_W^2 + \left(\frac{\partial F}{\partial U}\right)^2 \sigma_U^2 + \left(\frac{\partial F}{\partial A}\right)^2 \sigma_A^2 + \left(\frac{\partial F}{\partial D}\right)^2 \sigma_D^2 + \left(\frac{\partial F}{\partial Y_{Ca}}\right)^2 \sigma_{Y_{Ca}}^2 + \left(\frac{\partial F}{\partial Z_{Ca}}\right)^2 \sigma_{Z_{Ca}}^2 + \left(\frac{\partial F}{\partial X_K}\right)^2 \sigma_{X_K}^2 + \left(\frac{\partial F}{\partial \lambda_{37}}\right)^2 \sigma_{\lambda_{37}}^2 + \left(\frac{\partial F}{\partial \lambda_{39}}\right)^2 \sigma_{\lambda_{39}}^2 + \left(\frac{\partial F}{\partial B}\right)^2 \sigma_B^2 + \left(\frac{\partial F}{\partial C}\right)^2 \sigma_C^2 \quad (1.7)$$

It is assumed that σ_B and σ_C are 0 and the last two terms can thus be omitted from the total variance equations. The partial derivatives of the other parameters are given in appendix 1. These equations were used to assess the contribution of the different parameters to the variance for each single experiment.

To check the appropriateness of the proposed error assessment as in equation 1.7, the data as presented in table 1, 2, and 3 of Scaillet (2000) have been used to calculate the age of the sample and the variance contributions of the different parameters used to determine the F-ratio. The variance contributions of the parameters required for the age calculation (e.g., the ⁴⁰K decay constants and the age of the standard) are not assessed here. In table 1.5 the contribution of the parameters to the total variance is reproduced from Scaillet (2000). Because Scaillet (2000) assessed all parameters required for an age calculation the sum of the variances of the parameters contributing to F is not 100%. For that reason the data of Scaillet (2000) are normalized to 100% and then can be compared with the results of this study. As can be seen in table 1.5 and figure 1.6a-f the variance contributions of Scaillet (2000) and this study, i.e. the numerical and analytical solutions are indeed in close to very close agreement. This suggests the linearized error expansion technique indeed is justified for propagation of the analytical ⁴⁰Ar/³⁹Ar uncertainty.

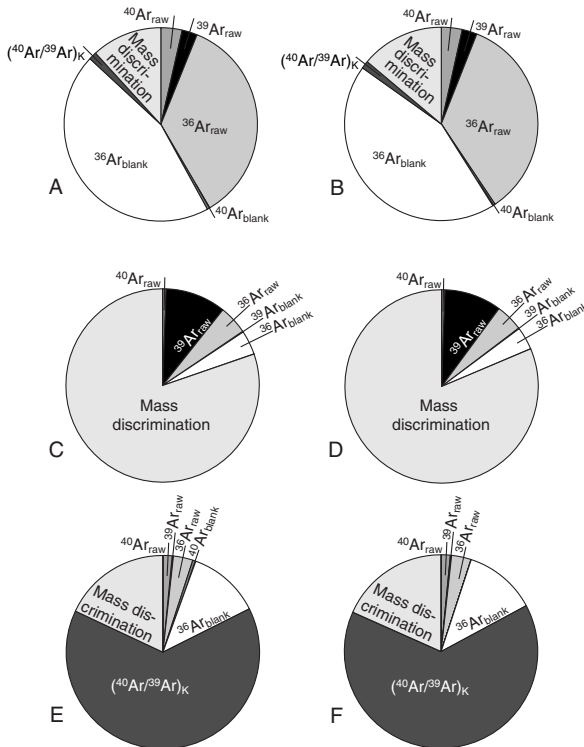


Figure 1.6a-f Contributions of different parameters to the analytical error, an example adapted from Scaillet (2000).

Visualization of data from table 1.5. The variance contributions of 14 parameters (i.e., ⁴⁰Ar_{raw}, ³⁹Ar_{raw}, ³⁷Ar_{raw}, ³⁶Ar_{raw}, ⁴⁰Ar_{blank}, ³⁹Ar_{blank}, ³⁷Ar_{blank}, ³⁶Ar_{blank}, (⁴⁰Ar/³⁹Ar)_K, (³⁹Ar/³⁷Ar)_{Ca}, (³⁶Ar/³⁷Ar)_{Ca}, λ₃₇, λ₃₉ and mass discrimination) responsible for the variance in the ⁴⁰Ar/³⁹Ar_K ratios are plotted for both error propagation methods. As can be seen from the figures the numerical approach of Scaillet (2000) and the analytical approach presented here are consistent. Figures 1.6a, c and e represent the numerical error approach of Scaillet (2000) for the analysis of respectively a 182 Ma old single grain spot fused metamorphic biotite, an intermediate heating step of a 1739 Ma old amphibole and a final fusion step for a 18.3 Ma old igneous grain of muscovite. Figures 1.6b, d and f represent the analytical error approach for the same samples. The parameters responsible for less than 0.1% of the variance are excluded in these figures.

Sample	% of total variance in table 1, Scaillet (2000)	% of total variance normalized to 100%, Scaillet, (2000)	% of total variance based on equation 1.7, this thesis	% of total variance as in table 2, Scaillet (2000)	% of total variance normalized to 100%, Scaillet (2000)	% of total variance based on equation 1.7, this thesis	% of total variance as in table 3, Scaillet (2000)	% of total variance normalized to 100%, Scaillet (2000)	% of total variance based on equation 1.7, this thesis
Single grain spot fused metamorphic biotite	182.197	182.264	1737.90	1739.08	1737.90	1737.90	18.316	18.316	18.293
Age	2.758	3.492	0.407	0.407	0.586	0.554	1.176	1.524	1.528
⁴⁰ Ar raw	1.974	2.500	7.028	7.028	10.124	9.561	0.158	0.205	0.204
³⁹ Ar raw	0.001	0.001	0.001	0.001	0.001	0.002	0.005	0.006	0.006
³⁷ Ar raw	27.488	34.611	3.347	3.347	4.821	4.556	2.519	3.265	3.272
³⁶ Ar raw	0.347	0.440	0.007	0.007	0.010	0.009	0.385	0.499	0.005
⁴⁰ Ar blank	0.001	0.001	0.089	0.089	0.128	0.121	<0.001	0.001	<0.001
³⁹ Ar blank	<0.001	<0.001	0.001	0.001	0.001	0.001	0.016	0.021	0.021
³⁷ Ar blank	34.789	43.805	2.790	2.790	4.019	3.800	9.315	12.075	12.102
³⁶ Ar blank	1.009	1.276	0.004	0.004	0.006	0.005	49.666	64.382	64.530
(⁴⁰ Ar/ ³⁹ Ar) _K	<0.001	<0.001	0.014	0.014	0.020	0.018	<0.001	0.001	<0.001
(³⁹ Ar/ ³⁷ Ar) _{Ca}	<0.001	<0.001	0.007	0.007	0.010	0.009	<0.001	0.001	<0.001
(³⁶ Ar/ ³⁷ Ar) _{Ca}	9.144	13.874	55.721	55.721	80.268	81.365	13.898	18.016	18.332
Mass discrimination	--	0	--	--	--	0	--	--	0
Atmospheric ⁴⁰ Ar/ ³⁶ Ar	<0.001	<0.001	<0.001	<0.001	<0.001	<0.001	<0.001	<0.001	<0.001
λ ₃₇	<0.001	<0.001	0.002	0.002	0.001	<0.001	<0.001	<0.001	<0.001
λ ₃₉									

Table 1.5 Comparison of numerical and analytical linearized error propagation for the error in the measured ⁴⁰Ar/³⁹Ar_K ratio.

Three examples of the contribution to the total variance of all parameters required to calculate a ⁴⁰Ar/³⁹Ar_K (= F) ratio. Presented data are from Scaillet (2000). The variances of Scaillet (2000) are based on numerical error expansion. The variances are first normalized to 100% (see text) and can then be compared with the variances calculated with the linearized error expansion method presented here. Both methods are in close to very close agreement.

WEIGHTED (PLATEAU/MEAN) AGE, ISOCHRON AND MSWD CALCULATIONS

Calculation of a ⁴⁰Ar/³⁹Ar age is often based on replicate experiments. Combination of replicate experiments with the same J value (or in other words the same F ratio for the standard) is based on the calculation of a weighted F ratio

$$F_w = \frac{\sum_{i=1}^n E_i F_i}{\sum_{i=1}^n E_i} \quad \text{with} \quad SE = \sqrt{1/\sum_{i=1}^n E_i} \tag{1.8}$$

(see e.g. Taylor, 1997) where F_w is the weighted ⁴⁰Ar*/³⁹Ar_K-ratio, the weighting factor is $E_i = 1/\sigma_i^2$ and SE the standard error. Also plateau ages for incremental heating experiments were combined this way. For the combination of samples with different J-values and calculated relative to the one or more different standards weighted mean intercalibration factors between samples and standards were used in the age equations. Intercalibration factors and uncertainties for individual experiments can be established with

$$R_{St1}^u = \frac{F_u}{F_{St1}} \quad \text{with} \quad \sigma_R = \sqrt{\frac{\sigma_{F_u}^2}{F_{St1}^2} + \frac{F_u^2 \times \sigma_{F_{St1}}^2}{F_{St1}^4}} \quad \text{or}$$

$$R_{St1}^u = \frac{F_u}{F_{St2}} \times \frac{F_{St2}}{F_{St1}} = \frac{F_u}{F_{St2}} \times R_{St2} \quad \text{with} \quad \sigma_R = \sqrt{\frac{\sigma_{F_u}^2}{F_{St2}^2 \times (R_{St1}^{St2})^2} + \frac{F_u^2 \times \sigma_{F_{St2}}^2}{F_{St2}^4 \times (R_{St1}^{St2})^2} + \frac{F_u^2 \times \sigma_{R_{St2}}^2}{F_{St2}^2 \times (R_{St1}^{St2})^4}} \tag{1.9}$$

where F_u is the F ratio of the sample, F_{St1} or F_{St2} are the F ratios of the standards. These intercalibration factors can be combined to a weighted intercalibration factor and error (equation 1.8).

The Mean Square Weighted Deviates (MSWD) is commonly used as a statistical test to assess the validity of the plateau / weighted mean / isochron age. The analytical errors account for the observed scatter, when the MSWD is 1. Additional scatter, which can not be explained by the analytical errors alone, is observed, when the MSWD is >1 and the analytical errors are overestimated when MSWD <1. In ArArCALC MSWD is calculated following the methodology of York (1969) and Roddick (1987) with 1 or 2 degrees of freedom for respectively plateau (or weighted mean) and isochron ages. Analytical errors are multiplied by $\sqrt{\text{MSWD}}$ when MSWD is >1 and the MSWD values are smaller than the F-test (for isochrons) or T-test (for plateau / weighted mean ages) statistics. If this is not true "error chrons" or "error plateaus" are reported in ArArCALC (Koppers, 2002).

Isochron calculations are performed using the least square fit of a straight line with correlated errors in X_i and Y_i (York, 1969). In this study normal and inverse isochron calculations are used to check if the assumption of an atmospheric ⁴⁰Ar/³⁶Ar ratio required for weighted mean age calculations is correct. Due to the fact that most analyses consist of multiple fusion experiments, the data of the different fusion analyses plot mostly clustered around a single point and do not result in an accurate isochron analysis. Further, normal and inverse isochrons show for most data the same results.

AGE CALCULATION

$^{40}\text{Ar}/^{39}\text{Ar}$ ages calculated in ArArCALC are based on a simple age equation (1.1). A simple error is calculated by partial differentiation of 1.1 to

$$\sigma_{t_u}^2 = \left[\frac{J}{C\lambda} \right]^2 \sigma_F^2 + \left[\frac{F}{C\lambda} \right]^2 \sigma_J^2 + \left[\frac{-\ln C}{\lambda^2} \right]^2 \sigma_\lambda^2 \quad (1.10)$$

where $C = 1 + J \times F$ and F is $^{40}\text{Ar}^*/^{39}\text{Ar}_K$. The first part of equation reflects the analytical error in the determination of the $^{40}\text{Ar}^*/^{39}\text{Ar}_K$ ratio in the sample as previously described. Comparison of replicate results from a single package should be compared ideally with the analytical uncertainty only, i.e. excluding the error in J as that error is equal for each sub-analysis (Foland, 1983) The first and second term of 1.10 represent the internal error. This combines the analytical error and the error in J . The complete error equation accounts for the so-called external error, which is a combination of the analytical error, the error in J and the error in the total decay constant.

However, in contrast to the ArArCalc software we prefer to separate the error in J into the analytical uncertainty of the standard and the uncertainty in standard age (which by definition includes the uncertainty in the decay constants and $^{40}\text{Ar}^*/^{40}\text{K}$ ratio required to calculate a K/Ar for the standard). Therefore equation 1.1 and 1.10 should be changed to

$$t_u = \frac{1}{\lambda} \ln \left(\frac{F_u}{F_{St1}} (e^{\lambda t_{St1}} - 1) + 1 \right) = \frac{1}{\lambda} \ln(X) \quad \text{with}$$

$$\sigma_{t_u}^2 = \left(\frac{e^{\lambda t_{St1}} - 1}{\lambda X F_{St1}} \right)^2 \sigma_{F_u}^2 + \left(\frac{-F_u (e^{\lambda t_{St1}} - 1)}{\lambda X F_{St1}^2} \right)^2 \sigma_{F_{St1}}^2 + \left(\frac{F_u e^{\lambda t_{St1}}}{X F_{St1}} \right)^2 \sigma_{t_{St1}}^2 + \left(\frac{-\ln X}{\lambda} + \frac{F_u t_{St1} e^{\lambda t_{St1}}}{\lambda X F_{St1}} \right)^2 \sigma_\lambda^2 \quad (1.11)$$

where the F_u ratios represent weighted mean ratios (1.9) for replicate experiments from a single irradiation package. This equation changes to

$$t = \frac{1}{\lambda} \ln \left(R_{St1}^u (e^{\lambda t_{St1}} - 1) + 1 \right) = \frac{1}{\lambda} \ln(X)$$

$$\sigma_{t_u}^2 = \left(\frac{e^{\lambda t_{St1}} - 1}{\lambda X} \right)^2 \sigma_{R_{St1}^u}^2 + \left(\frac{R_{St1}^u e^{\lambda t_{St1}}}{X} \right)^2 \sigma_{t_{St1}}^2 + \left(\frac{-\ln X}{\lambda} + \frac{R_{St1}^u t_{St1} e^{\lambda t_{St1}}}{\lambda X} \right)^2 \sigma_\lambda^2 \quad (1.12)$$

for replicate experiments from different irradiation positions. The purpose of this exercise was to be able to determine a combined analytical error of unknowns and standard for comparison of experiments using the same monitors. In contrast to equation 1.10, where only the analytical error of the unknown or the analytical error in combination with the uncertainty in J (thus by definition including the uncertainties in decay constants and $^{40}\text{Ar}^*/^{40}\text{K}$ of the primary standard), equation 1.11 (first two terms of variance equation) and 1.12 (first term of variance equation) report analytical uncertainties of standards and unknowns.

Equations 1.11 and 1.12 will be used throughout this thesis to calculate ages and uncertainties.

However, 1.11 and 1.12 are not completely correct with respect to the last to terms, because the uncertainty in the standard age includes by definition already decay constants. Therefore, if we report an uncertainty excluding decay constant errors, we use FCT or TCR ages of Renne et al. (1998) throughout this thesis with 1σ uncertainties of ± 0.16 Ma excluding decay constant uncertainties and omit the last term in 1.11/1.12. Thus, in actuality we only include the uncertainties in $^{40}\text{Ar}^*$ and ^{40}K in the primary standard (and analytical errors). Or when we assess the total 1.11/1.12 equations, we use the uncertainty of ± 0.28 Ma for the age of FC and TC including decay constant uncertainties, as reported in Renne et al. (1998). In summary, we will report uncertainties at four levels: the analytical error of the unknown (I), the analytical uncertainty of standard and unknown (II), the analytical uncertainty of standard and unknown and uncertainty in intercalibration of primary and secondary standards as well as ^{40}K and radiogenic ^{40}Ar contents in primary standards (III) and all the foregoing additionally including the decay constant errors (IV).

A slightly different, but fundamentally better approach was proposed in e.g. Renne et al. (1998) or Min et al. (2000). The age equation as published in Min et al. (2000) is given by

$$T_u = \frac{f N_0}{(A_e + A_\beta) WS} \ln \left[\left(\frac{A_e + A_\beta}{A_e} \right) \left(\frac{^{40}\text{Ar}_p^*}{K_p f} \right) \prod_{i=1}^n R_{i-1}^i + 1 \right] \quad \text{where} \quad R_{i-1}^i = \left[\left(\frac{^{40}\text{Ar}^*}{^{39}\text{Ar}_K} \right)_i \right] / \left[\left(\frac{^{40}\text{Ar}^*}{^{39}\text{Ar}_K} \right)_{i-1} \right]$$

$$\sigma_{T_u}^2 = \left(\frac{\partial T_u}{\partial f} \right)^2 \sigma_f^2 + \left(\frac{\partial T_u}{\partial A_e} \right)^2 \sigma_{A_e}^2 + \left(\frac{\partial T_u}{\partial A_\beta} \right)^2 \sigma_{A_\beta}^2 + \left(\frac{\partial T_u}{\partial K_p} \right)^2 \sigma_{K_p}^2 + \left(\frac{\partial T_u}{\partial ^{40}\text{Ar}_p^*} \right)^2 \sigma_{^{40}\text{Ar}_p^*}^2 + \sum_{i=1}^n \left(\frac{\partial T_u}{\partial R_{i-1}^i} \right)^2 \sigma_{R_{i-1}^i}^2 \quad (1.13)$$

In this equation f is the fraction ^{40}K in natural potassium ($1.167 \pm 0.004 \times 10^{-2}$, Garner et al., 1975), N_0 is Avogadro's number ($6.0221367 \pm 0.0000036 \times 10^{23}$, Cohen and Taylor, 1987), W is the atomic weight of potassium (39.0983 ± 0.00006 , Garner et al., 1975), S is the number of seconds in a mean solar year (31556930), A is the nuclear activity of potassium, where A_β is the β^- activity ($^{40}\text{K} \rightarrow ^{40}\text{Ca}$, 28.27 ± 0.05 dgs/g K, Beckinsale and Gale, 1969) and A_e is the γ activity ($^{40}\text{K} \rightarrow ^{40}\text{Ar}$, 3.31 ± 0.04 dsg / g K, Beckinsale and Gale, 1969, with uncertainty as proposed in Min et al., 2000), $^{40}\text{Ar}_p^*$ is the concentration radiogenic ^{40}Ar in the primary standard ($1.343 \pm 0.007 \times 10^{-9}$ mol/g, McDougall and Roksandic, 1974) and K_p is the potassium concentration in the primary standard (7.626 ± 0.016 wt%, Renne et al., 1998). A recent compilation of potassium data for GA1150 resulted in a potassium content of 7.646 ± 0.006 wt% (Spell and McDougall, 2003). Min et al. (2000) calculated the standard error in T_u based on linearized error propagation. The full derivation of the equation can be found in Min et al. (2000).

Koppers (2002) adds in an additional calculation tool in ArArCalc another two sources of variance to the uncertainty in T_u as proposed by Min et al. (2000): N_0 (Avogadro's number) and W (atomic weight of potassium). The uncertainty in the number of seconds in a mean solar year is by both authors neglected, because its effect is insignificant. Here, the equation of Min et al. (2000) is slightly modified for the application of the calculation of an age relative to the secondary standard TCR, which in turn is intercalibrated to FC and primary standard GA1550. Equation 1.14 differs from 1.13 by the fact that the potassium content of the primary standard is expressed in wt%. Calculation of an age relative to FCT only implies that the intercalibration factor between TC and FC can be omitted and F_{TC} will change in F_{FC} (see appendix 1 for full derivation of this equation).

$$\begin{aligned}
T_u &= \frac{fN_0}{(A_e + A_\beta)WS} \ln \left(\frac{A_e + A_\beta}{A_e} \times \frac{F_u}{F_{TC}} \times R_{FC}^{TC} \times R_{GA1550}^{FC} \times \frac{{}^{40}\text{Ar}_p^* \times W \times 100}{K_p f} + 1 \right) \\
\sigma_{T_u}^2 &= \left(\frac{\partial T_u}{\partial f} \right)^2 \sigma_f^2 + \left(\frac{\partial T_u}{\partial N_0} \right)^2 \sigma_{N_0}^2 + \left(\frac{\partial T_u}{\partial A_e} \right)^2 \sigma_{A_e}^2 + \left(\frac{\partial T_u}{\partial A_\beta} \right)^2 \sigma_{A_\beta}^2 + \left(\frac{\partial T_u}{\partial W} \right)^2 \sigma_W^2 + \left(\frac{\partial T_u}{\partial S} \right)^2 \sigma_S^2 + \left(\frac{\partial T_u}{\partial F_u} \right)^2 \sigma_{F_u}^2 + \\
&\quad \left(\frac{\partial T_u}{\partial F_{TC}} \right)^2 \sigma_{F_{TC}}^2 + \left(\frac{\partial T_u}{\partial R_{FC}^{TC}} \right)^2 \sigma_{R_{FC}^{TC}}^2 + \left(\frac{\partial T_u}{\partial R_{GA1550}^{FC}} \right)^2 \sigma_{R_{GA1550}^{FC}}^2 + \left(\frac{\partial T_u}{\partial {}^{40}\text{Ar}_p^*} \right)^2 \sigma_{{}^{40}\text{Ar}_p^*}^2 + \left(\frac{\partial T_u}{\partial K_p} \right)^2 \sigma_{K_p}^2
\end{aligned} \tag{1.14}$$

Most parameters are described in 1.13, $R_{TC/FC}$ is the intercalibration factor between TCR and FCT (1.0112 ± 0.0010 , Renne et al., 1998) and $R_{FC/GA1550}$ is the intercalibration factor between FC and the primary standard GA1550 biotite (0.2781 ± 0.0003 , Renne et al., 1998). Derivation of the partial derivatives is described in the appendix. The age and error equation and values for parameters mentioned here will be used throughout the thesis to estimate the most realistic ages and uncertainties.

Apart from systematic errors like the absolute age of the standards, the values of the decay constants etc. it is assumed that no other systematic errors occur. Thus, systematic errors in the output of for example the voltmeter or a systematic error in the performance of the secondary electron multiplier are not assessed in this kind of errors propagation. Besides, such sorts of systematic errors are partly accounted for by mass discrimination corrections.

NUMERICAL ERROR ANALYSIS

Calculations using the principles of error propagation to obtain a final error in a parameter (e.g., as done in Min et al., 2000; Koppers, 2002; this thesis) are often very tedious to derive, because part of the procedure involves determining partial derivatives for each measurement variable. Additional complications arise if correlations exist between the different variables required to calculate a parameter, which means that the second term in equation 1.4 cannot be ignored, as usually done in these kinds of error propagations. Further, any change in the formula to define a parameter requires a new error age equation (Roddick, 1987).

The difference between analytical and numerical solutions is (apart from assuming no correlation between the variables in the analytical solution) that in the analytical solutions all the partial derivatives have to be derived. Sequentially deviating each variable from its mean value by a small fractional amount and determining the corresponding change in function F can solve the numerical solutions. In practice a deviation of about 0.01% from the mean value of the variable is adequate to approximate first partial derivatives of a range of functions. If parameter F indeed is a linear function of the variables $X_1 \dots X_n$ this calculation of the first partial derivative is exact (Roddick, 1987).

However, the parameter T_u (age of an unknown) based on ${}^{40}\text{Ar}/{}^{39}\text{Ar}$ dating is not determined by a linear relationship with the different variables. In the numerical model proposed by Roddick (1987) tests are included to test for non-linearity effects. For situations where the linear approximation is inadequate Monte Carlo simulation may be a better approach to error evaluation (but are computationally wasteful when more than a few input variables are required). Unfortunately, analytical solutions of error propagation are

incapable of assessing these non-linearity effects. In addition, error propagation in both methods, numerical as well analytical, assumes that the mean values of variables and calculated parameters are derived from approximately from normally distributed populations.

Scaillet (2000) describes the application of numerical error analysis to $^{40}\text{Ar}/^{39}\text{Ar}$ dating. The main conclusions of his paper are that the analytical linearized error estimates (e.g., Min et al., 2000; Koppers et al., 2002) is found acceptably close to the exact numerical error estimate, despite strong non-linearity components in the related equation (in numerical error expansion non-linearity components are corrected). An advantage of Scaillet (2000) is the overview of the contribution of each variable to the total variance. This can also be deduced in analytical error propagation, but requires a complex effort to derive the total variance equation. We circumvented this by assessing the contribution of the parameters to the analytical uncertainty and the contribution of the analytical uncertainty and other parameters (f , N_0 , W , S , A_e , A_β , K_p , $^{40}\text{Ar}_p$) to the total uncertainty separately. The disadvantage of Scaillet (2000) is that he only describes the full error analysis of one single analysis, while most $^{40}\text{Ar}/^{39}\text{Ar}$ ages are based on combined analyses (e.g., plateau ages, multiple single fusions). In conclusion, if no mistakes are made in the derivation of the partial derivatives in analytical solutions they will give a reliable absolute error estimate.

INTERCALIBRATION WITH ASTRONOMICALLY DATED STANDARD?

As stated before a wide range of ages was published for the neutron fluence monitors FCT and TCR. Alternative options have been sought to establish the age of the standards with methods independent of the K/Ar system (e.g., Min et al., 2000; Renne et al., 1994; Hilgen et al., 1997). We will try to derive the age for FCT and TCR using the $^{40}\text{Ar}/^{39}\text{Ar}$ ratio of FCT or TCR sanidine in combination with the $^{40}\text{Ar}/^{39}\text{Ar}$ ratio of sanidine from an astronomically dated standard. The astronomical dated standard is a volcanic ash layer intercalated in an astrochronological tuned sedimentary section assuming that the time of eruption (or closure of the system for Ar diffusion) is equivalent to the time of deposition in the sediment. It is assumed that the error in the astronomical age is very small. When using an astronomically dated standard a new age and error equation will be derived

$$T_{St} = \frac{f N_0}{(A_e + A_\beta)WS} \ln \left(R_{ash}^{St} \times \left(e^{\frac{(A_e + A_\beta)WS}{N_0} t_{ash}} - 1 \right) + 1 \right)$$

$$\sigma_{T_{St}}^2 = \left(\frac{\partial T_{St}}{\partial f} \right)^2 \sigma_f^2 + \left(\frac{\partial T_{St}}{\partial N_0} \right)^2 \sigma_{N_0}^2 + \left(\frac{\partial T_{St}}{\partial A_e} \right)^2 \sigma_{A_e}^2 + \left(\frac{\partial T_{St}}{\partial A_\beta} \right)^2 \sigma_{A_\beta}^2 + \left(\frac{\partial T_{St}}{\partial W} \right)^2 \sigma_W^2 + \left(\frac{\partial T_{St}}{\partial S} \right)^2 \sigma_S^2 +$$

$$\left(\frac{\partial T_{St}}{\partial R} \right)^2 \sigma_R^2 + \left(\frac{\partial T_{St}}{\partial T_{ash}} \right)^2 \sigma_{T_{ash}}^2 \quad (1.15)$$

Parameters are defined as in equation 1.13. Derivation of the partial derivatives is given in the appendix. The implications of this intercalibration will be discussed in detail in later chapters. However, one implication is that uncertainties in decay constant errors do not contribute significantly to the proposed ages of FCT and TCR. Therefore, ages of FCT and TCR can be established were the uncertainties are dominated by analytical errors only circumventing the recent discussions about decay constant uncertainties.

In the discussion of results of various sedimentary sections in the following chapters we will present the results in terms of equivalent FC ages. We use this approach to circumvent any perhaps confusing discussion of local stratigraphy. These calculations are based on the here presented equations (eq. 1.15).

PART III: MONITORING OF PERFORMANCE OF THE ANALYTICAL SYSTEM

MONITORING OF MASS DISCRIMINATION WITH $^{40}\text{Ar}/^{38}\text{Ar}$ REFERENCE GAS

INSTALLATION OF A REFERENCE GAS PIPETTE

Mass spectrometers generally do not yield the absolute abundance ratios of the isotopes being analyzed. Deviations from the absolute values are mostly mass dependent and are included in the term mass discrimination. To correct for this mass discrimination in the mass spectrometer commonly the $^{40}\text{Ar}/^{36}\text{Ar}$ ratio of an aliquot of atmospheric argon is measured. The measured $^{40}\text{Ar}/^{36}\text{Ar}$ -value will then be compared to the atmospheric $^{40}\text{Ar}/^{36}\text{Ar}$ ratio of 295.5 (Nier, 1950). The measured $^{40}\text{Ar}/^{36}\text{Ar}$

ratio will slightly deviate from this value due to fractionation of the gas in the mass spectrometer. To correct for this mass discrimination effect the measured argon intensities are multiplied by the mass discrimination factor after subtraction of the blank intensities.

Based on equation 1.7 the contributions of different parameters to the (analytical) variance can be derived. Figure 1.7 shows these contributions for two arbitrary samples. It appeared that for most samples the analytical error is mainly dominated by uncertainties in the mass discrimination factor and the measured ^{36}Ar intensities for blanks and unknowns. Therefore, improvement in the precision of one or both of these parameters will immediately result in reduction of the analytical error. To reduce the contribution of the mass discrimination to the analytical uncertainty it was assumed that ratio of about ~ 2 (in the $^{40}\text{Ar}/^{38}\text{Ar}$ reference gas) can be measured more precisely than a ratio of ~ 300 (the atmospheric $^{40}\text{Ar}/^{36}\text{Ar}$ ratio). Mass fractionation factors based on atmospheric argon and factors based on the $^{40}\text{Ar}/^{38}\text{Ar}$ of the reference gas are theoretically equivalent:

$$0.75 + \frac{\left(^{40}\text{Ar}/^{36}\text{Ar}\right)_{\text{atm}}}{4 \times \left(^{40}\text{Ar}/^{36}\text{Ar}\right)_{\text{m}}} = 0.5 + \frac{\left(^{40}\text{Ar}/^{38}\text{Ar}\right)_{\text{o}}}{2 \times \left(^{40}\text{Ar}/^{38}\text{Ar}\right)_{\text{m}}} \quad (1.16)$$

where $\left(^{40}\text{Ar}/^{38}\text{Ar}\right)_{\text{m}}$ and $\left(^{40}\text{Ar}/^{36}\text{Ar}\right)_{\text{m}}$ are the measured $^{40}\text{Ar}/^{38}\text{Ar}$ and $^{40}\text{Ar}/^{36}\text{Ar}$ ratio of respectively the reference gas and air pipettes, $\left(^{40}\text{Ar}/^{36}\text{Ar}\right)_{\text{atm}}$ is the atmospheric $^{40}\text{Ar}/^{36}\text{Ar}$ ratio of 295.5 (Nier, 1950) and $\left(^{40}\text{Ar}/^{38}\text{Ar}\right)_{\text{o}}$ is the unfractionated $^{40}\text{Ar}/^{38}\text{Ar}$ ratio in the reference gas. To determine the unfractionated $^{40}\text{Ar}/^{38}\text{Ar}$ ratio in the reference gas this equation is rewritten to

$$\left(\frac{^{40}\text{Ar}}{^{38}\text{Ar}}\right)_{\text{o}} = 0.5 \times \left(\frac{^{40}\text{Ar}}{^{38}\text{Ar}}\right)_{\text{m}} + \frac{\left(\frac{^{40}\text{Ar}}{^{36}\text{Ar}}\right)_{\text{atm}} \left(\frac{^{40}\text{Ar}}{^{38}\text{Ar}}\right)_{\text{m}}}{2 \times \left(\frac{^{40}\text{Ar}}{^{36}\text{Ar}}\right)_{\text{m}}} \quad (1.17)$$

where $\left(^{40}\text{Ar}/^{36}\text{Ar}\right)_{\text{m}}$ is the measured $^{40}\text{Ar}/^{36}\text{Ar}$ ratio of the air pipettes OR of the reference gas pipettes.

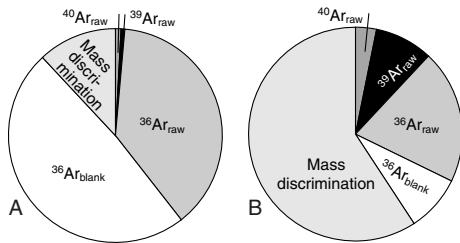


Figure 1.7a-b Contribution of mass fractionation to the analytical error, an arbitrary example.

Contribution of different parameters to the analytical error for two representative arbitrary standards FC (a) and 85G003 (b) measured during this study. All contributions <0.1% are omitted. Apart from the ^{36}Ar intensities for blanks and unknowns the analytical error can be dominated by the mass discrimination. Improvement of the precision of the mass discrimination will therefore directly be reflected in a reduction of the analytical error. Samples show generally the same overall picture.

One method (option I) to determine the unfractionated $^{40}\text{Ar}/^{38}\text{Ar}$ ratio of the reference gas is by alternating measurements of reference gas and air pipettes from the volume with atmospheric argon previously used for monitoring of the fractionation. The underlying assumption is that the $^{40}\text{Ar}/^{36}\text{Ar}$ ratio in the air volume was not fractionated over time and thus still has an original $^{40}\text{Ar}/^{36}\text{Ar}$ ratio of atmospheric argon. The second method (option II) involves calculation of the unfractionated $^{40}\text{Ar}/^{38}\text{Ar}$ ratio of the reference gas with the measured $^{40}\text{Ar}/^{36}\text{Ar}$ ratio of the reference gas. This assumes that the unfractionated $^{40}\text{Ar}/^{36}\text{Ar}$ ratio in the reference gas is atmospheric and no fractionation occurred in the reference gas volume.

A quick inspection of the data showed that the $^{40}\text{Ar}/^{36}\text{Ar}$ ratios measured from the air pipette are higher than the ratios of the reference gas pipette (287.7 ± 0.2 versus 284.7 ± 0.1). This difference might be explained by the fractionation of the atmospheric argon in the old reservoir over the years. The kinetic energy (E_k) of a gas is constant at a given T. As can be seen from equation 1.18 the velocity of ^{40}Ar is slightly smaller than the velocity of ^{36}Ar and therefore the lighter ^{36}Ar isotope will fractionate more easily.

$$E_k(^{40}\text{Ar}) = E_k(^{36}\text{Ar}) \rightarrow (1/2mv^2)_{^{40}\text{Ar}} = (1/2mv^2)_{^{36}\text{Ar}} \rightarrow \frac{v_{^{40}\text{Ar}}^2}{v_{^{36}\text{Ar}}^2} = \frac{m_{^{36}\text{Ar}}}{m_{^{40}\text{Ar}}} \rightarrow$$

$$\frac{v_{^{40}\text{Ar}}}{v_{^{36}\text{Ar}}} = \sqrt{36/40} = \sqrt{9/10} \approx 0.95 \rightarrow v_{^{40}\text{Ar}} = 0.95v_{^{36}\text{Ar}} \quad (1.18)$$

Preferential removal of ^{36}Ar over ^{40}Ar will result in a higher $^{40}\text{Ar}/^{36}\text{Ar}$ ratio, suggesting that some fractionation occurred in the atmospheric argon reservoir. Therefore option I cannot be used for the calibration of the newly installed reference gas reservoir.

In option II the $^{40}\text{Ar}/^{38}\text{Ar}$ and $^{40}\text{Ar}/^{36}\text{Ar}$ ratios are measured simultaneously. A change in the measured ratios due to a change in the fractionation process will therefore be reflected in both ratios. The reference gas data set will be split in several groups: One group contains all the reliable reference gas measurements of the period since installation of gas until the breakdown of the filament (June 6 – November 13, 2000). A second group contains all the reliable data since the installation of the new filament until the lab shut down due to renovation (December 13, 2000 – April 2, 2002). A third group contains all the reliable data collected since the renovation until the moment of writing this paper (August 1, 2001 – May 13, 2002) and the last group contains all the reliable reference gas data collected since installation of the pipette until writing (June 6, 2000 – May 13, 2002).

The ArArCALC software of Koppers (2002) has been used to calculate the intensities and their 1σ error of the individual isotopes (^{40}Ar , ^{38}Ar and ^{36}Ar) at the inlet time of the gas into the mass spectrometer for reference gas and blank analysis. Blanks were measured immediately before and after reference gas measurements. Errors were propagated using linearized error propagation as previously described. The weighted means of $(^{40}\text{Ar}/^{38}\text{Ar})_0$ for the different periods are not completely in agreement at the 1σ (68% confidence) level, at the 95% confidence level the initial ratios are not significantly different. Further, final mass discrimination factors calculated with the second part of 1.16 for an arbitrary, representative reference gas measurement based on the several $(^{40}\text{Ar}/^{38}\text{Ar})_0$ ratios of option II produce a statistically equal factor for all groups, when all sources of error are included in the calculations. Therefore, we suggest to use the overall value for the period June 6, 2000 – May 13, 2002 for the initial, unfractionated $^{40}\text{Ar}/^{38}\text{Ar}$ ratio in reference gas. This value is 1.94067 ± 0.00022 .

The principle aim of installing the reference gas pipette was to get a better control on the mass discrimination. In the reference gas the fractionation factor can be calculated with the $^{40}\text{Ar}/^{38}\text{Ar}$ as well with the $^{40}\text{Ar}/^{36}\text{Ar}$ ratio of the reference gas. It is clear that the error in the final fractionation factors is smaller for the $^{40}\text{Ar}/^{38}\text{Ar}$ than for the $^{40}\text{Ar}/^{36}\text{Ar}$ factors (figure 1.8). Most errors for individual experiments range from 0.0002 to 0.0010 for the $^{40}\text{Ar}/^{38}\text{Ar}$ factor and from 0.0006 to 0.0020 for the $^{40}\text{Ar}/^{36}\text{Ar}$ factor. Further, the resulting fractionation factors must ideally be equal for each individual measurement. A paired T-test was performed on the factors calculated with either the $^{40}\text{Ar}/^{38}\text{Ar}$ or the $^{40}\text{Ar}/^{36}\text{Ar}$ ratios of the reference gas (table 1.6). The test for the group I data was the only not significant test at a level of 95% implying that the mean of the fractionation factor based on the measured $^{40}\text{Ar}/^{38}\text{Ar}$ ratios is different from the mean of the fractionation factor based on the $^{40}\text{Ar}/^{36}\text{Ar}$ ratios. There are no clear indications of the reason for the different means of the $^{40}\text{Ar}/^{36}\text{Ar}$ and the $^{40}\text{Ar}/^{38}\text{Ar}$ fractionation factors for this group, but it might be explained by some erroneous "off-peak" measurements. To assess potential different behavior of the factor

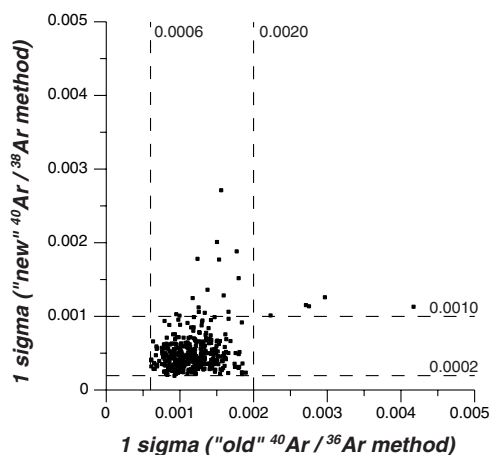


Figure 1.8 Errors in the mass discrimination factor: comparison of the "old" and "new" method.

1σ error for individual analyses based on the $^{40}\text{Ar}/^{36}\text{Ar}$ (X-axis) and the $^{40}\text{Ar}/^{38}\text{Ar}$ (Y-axis) ratio in reference gas.

based on the $^{40}\text{Ar}/^{38}\text{Ar}$ ratio versus the factor based on the $^{40}\text{Ar}/^{36}\text{Ar}$ ratio, the trends of the factors over time have been modeled with curvi-linear regression methods for both the $^{40}\text{Ar}/^{36}\text{Ar}$ and $^{40}\text{Ar}/^{38}\text{Ar}$ factors. The predicted values with associated errors are compared with the same values for the $^{40}\text{Ar}/^{38}\text{Ar}$ factors. In all cases the predicted factors are within error the same, though the errors in the $^{40}\text{Ar}/^{38}\text{Ar}$ predicted factors are smaller.

ASSIGNMENT OF MASS FRACTIONATION FACTORS TO EXPERIMENTS

Once the unfractionated $^{40}\text{Ar}/^{38}\text{Ar}$ ratio of the reference gas is determined, the fractionation factor and associated error for each individual reference gas experiment can be calculated. The first part of equation 1.17 is used to calculate the fractionation factor based on the measured $^{40}\text{Ar}/^{36}\text{Ar}$ ratio and the

	I	II	III	IV
Period	6 June – 13 November 2000	13 December 2000 – 2 April 2001	1 August 2001 – 13 May 2002	6 June 2000 – 13 May 2002
N	123	53	243	419
Weighted mean ($^{40}\text{Ar}/^{38}\text{Ar}$) _o	1.94152 ± 0.00040	1.94126 ± 0.00051	1.93992 ± 0.00032	1.94067 ± 0.00022
Example of mass discrimination factor of arbitrary analysis (00a0047a)	1.0053 ± 0.0004	1.0053 ± 0.0004	1.0049 ± 0.0004	1.0051 ± 0.0004
Paired T-test statistic	-2.37	-0.60	1.32	-0.20
Critical value (2-tailed, $\alpha =$ 0.05, Davis, 1977)	1.98	2.01	1.96	1.96

Table 1.6 Data for calculation of the original, unfractionated $^{40}\text{Ar}/^{38}\text{Ar}$ in reference gas.

Periods in which data are measured, weighted means of $[\text{Ar}/^{38}\text{Ar}]_o$ including all sources of uncertainty, an example of the final mass discrimination factor from an arbitrary analysis (in this case 00a0047a) and paired students T-test statistics are given.

second part of 1.17 is used to calculate the fractionation factor based on the measured $^{40}\text{Ar}/^{38}\text{Ar}$ ratio of the reference gas. The associated errors are based on linearized error propagation methods. Since all the individual fractionation factors for individual experiments now can be calculated, the next step is to decide how to determine the fractionation factor, which will be applied to the $^{40}\text{Ar}/^{39}\text{Ar}$ dating experiments. Different options are available. One method is to average the fractionation factors measured before and after the experiments and use the average fractionation value as correction factor for the isotope ratio of the experiments. The approach used in this study is a linear or curvi-linear regression through a series of data points over time. The model predicts a fractionation factor to experiments performed between these data points. In the appendix all the predicted fractionation factors for experiments relevant to this study are listed.

INTERCALIBRATION OF TCR AND FCT

As previously discussed a wide range of ages exist for the two standards used throughout this thesis (FCT and TCR). Although there is no consensus on the ages of standards, intercalibration factors between the two standards seem to be more constrained. Renne et al. (1998) report an intercalibration factor between TCR and FCT of 1.0112 ± 0.0010 ($\pm 1\sigma$) consistent with data of Dalrymple et al. (1993) and Baksi et al. (1996). In this study FCT and TCR sanidine were loaded as neutron fluence monitors in all irradiations. This gave us the opportunity to confirm the intercalibration proposed by Renne et al. (1998), but also allows us to check the system performance and reliability of the applied corrections (e.g., mass discrimination). Irradiation procedures in the study of Renne et al. (1998) differ from the VUA procedures. Both studies used the Oregon State TRIGA Reactor, CLICIT facility, for irradiation. However, we used a slightly different irradiation lay out (~ 80 mm long, 6 mm diameter vials at the VUA versus 190 mm diameter, ~ 3 mm thick discs at the Berkeley Geochronology Center BGC). Therefore, the statistical approaches to establish an intercalibration factor are not identical in both studies. Both studies determine the weighted mean F ($= ^{40}\text{Ar}^*/^{39}\text{Ar}_K$) ratio based on replicate experiments for each standard position on the disc / in the vial. Renne et al. (1998) used the simple mean and standard deviation of weighted mean F_{FC} -ratios of four wells

Sample	Identity	Vial height (mm)	$^{40}\text{Ar}^*/^{39}\text{Ar}^k$ ratio	c_F	MSWD	N
Irradiation VU32-C						
FCT	VU32 Cz	2.0	8.4818	0.0091	0.37	5
FCT	VU32 Cy	18.0	8.7505	0.0112	0.43	4
FCT	VU32 Cx	37.0	9.1902	0.0083	0.43	7
FCT	VU32 Cw	52.0	9.6374	0.0158	0.56	2
FCT	VU32 Cv	59.6	9.8962	0.0096	0.38	6
FCT	VU32 Ct	66.0	10.2062	0.0121	1.21	5
85G003	VU32 C1	1.0	8.5556	0.0129	0.43	6
85G003	VU32 C7	10.5	8.7118	0.0095	0.18	7
85G003	VU32 C13	18.5	8.8579	0.0087	0.58	9
85G003	VU32 C18	28.0	9.0398	0.0094	0.99	7
85G003	VU32 C23	38.5	9.3384	0.0095	0.56	8
85G003	VU32 C28	47.0	9.5824	0.0122	0.62	6
85G003	VU32 C33	53.0	9.8162	0.0124	1.31	6
85G003	VU32 C38	59.6	9.9940	0.0120	1.25	5
85G003	VU32 C43	65.0	10.2287	0.0105	0.28	6
Irradiation VU37-CI						
FCT	VU37 C2	2.0	8.4148	0.0131	0.29	5
FCT	VU37 C11 ^a	11.0	8.5830	0.0064	0.60	10
FCT	VU37 C20	20.0	8.7278	0.0070	1.11	5
FCT	VU37 C29	29.0	8.9088	0.0057	0.45	5
FCT	VU37 C38	38.0	9.1572	0.0083	0.32	4
FCT	VU37 C47	46.0	9.3956	0.0073	1.09	5
FCT	VU37 C56	55.5	9.7200	0.0082	0.16	5
FCT	VU37 C67	69.5	10.2899	0.0076	0.55	5
FCT	VU37 C79	80.5	10.7973	0.0084	1.04	4
85G003	VU37 C1	1.0	8.5350	0.0141	0.23	5
85G003	VU37 C6 ^a	7.0	8.6031	0.0075	1.43	11
85G003	VU37 C10 ^a	10.0	8.6658	0.0102	0.74	10
85G003	VU37 C15	15.0	8.6831	0.0139	0.79	5
85G003	VU37 C19	19.0	8.8172	0.0092	1.24	4
85G003	VU37 C24	24.0	8.8977	0.0081	0.43	5
85G003	VU37 C28	28.0	9.0072	0.0069	0.64	5
85G003	VU37 C33	33.0	9.0986	0.0071	0.54	8
85G003	VU37 C37	37.0	9.2005	0.0108	0.41	5
85G003	VU37 C42	41.0	9.3175	0.0084	0.68	5
85G003	VU37 C46	45.0	9.4775	0.0095	0.55	4
85G003	VU37 C51	50.5	9.6372	0.0065	0.99	4
85G003	VU37 C55	54.5	9.8090	0.0072	0.15	5
85G003	VU37 C61	63.0	10.1334	0.0082	0.72	6
Irradiation VU37-CI continued						
85G003	VU37 C66	69.0	10.3608	0.0100	0.20	5
85G003	VU37 C72	75.0	10.6141	0.0096	0.63	5
85G003	VU37 C78	80.0	10.8805	0.0101	0.87	5
Irradiation VU37-CII						
FCT	VU37 Cz	1.0	8.4097	0.0079	0.14	5
FCT	VU37 Cy	14.5	8.5389	0.0182	0.71	4
FCT	VU37 Cx	25.0	8.7116	0.0092	0.64	4
FCT	VU37 Cw	35.5	8.8926	0.0092	0.09	4
FCT	VU37 Cv	48.5	9.2770	0.0095	0.46	4
FCT	VU37 Cu	58.0	9.6270	0.0085	0.71	5
FCT	VU37 Cs	69.0	10.0673	0.0110	0.64	3
FCT	VU37 Ct	85.0	10.7561	0.0109	0.78	4
TCR2a	VU37 C79A	3.5	8.5186	0.0069	1.31	7
TCR2a	VU37 C83	8.5	8.5774	0.0083	0.70	4
TCR2a	VU37 C86A	13.0	8.6192	0.0235	0.53	5
TCR2a	VU37 C90	18.8	8.7041	0.0081	0.24	8
TCR2a	VU37 C94	24.0	8.7862	0.0106	0.05	5
TCR2a	VU37 C98	30.5	8.8782	0.0074	0.16	6
TCR2a	VU37 C102	34.5	9.0065	0.0080	0.18	5
TCR2a	VU37 C106	41.5	9.2143	0.0091	0.32	4
TCR2a	VU37 C110	47.5	9.3419	0.0125	1.21	3
TCR2a	VU37 C114	53.5	9.5297	0.0108	1.34	5
TCR2a	VU37 C118	57.0	9.6925	0.0108	0.48	4
TCR2a	VU37 C122	64.5	9.9582	0.0108	0.55	4
TCR2a	VU37 C126	68.0	10.1516	0.0107	0.12	4
TCR2a	VU37 C130	76.5	10.4937	0.0118	0.03	3
TCR2a	VU37 C134	81.0	10.7333	0.0129	0.43	3
85G003	VU37 C79B	2.0	8.4833	0.0184	0.44	5
85G003	VU37 C106A	43.0	9.2333	0.0115	0.06	3
85G003	VU37 C135	82.5	10.8052	0.0083	1.14	6
Irradiation VU37-B						
FC-2	VU37 B-2	1.0	8.3990	0.0057	0.58	5
FC-2	VU37 B19A	28.0	8.8471	0.0064	0.97	5
FC-2	VU37 B40A	58.5	9.7565	0.0084	1.33	5
FC-2	VU37 B63	87.5	11.0824	0.0076	0.35	5
FC-2	VU37 B3	7.5	8.4019	0.0229	0.04	2
FC-2	VU37 B6	10.0	8.4800	0.0087	0.73	3
FC-2	VU37 B10	15.5	8.5714	0.0136	0.20	2

Sample	Identity	Vial height (mm)	⁴⁰ Ar/ ³⁹ Ar ratio	σ _r	MSWD	N
Irradiation VU37-B continued						
FC-2	VU37 B13	19.5	8.6467	0.0103	0.23	2
FC-2	VU37 B17	24.5	8.7418	0.0084	0.00	2
FC-2	VU37 B19	27.0	8.7880	0.0123	0.92	3
FC-2	VU37 B27 ^a	38.5	9.1079	0.0114	0.74	3
FC-2	VU37 B29 ^a	41.5	9.1529	0.0117	0.44	2
FC-2	VU37 B30 ^a	43.0	9.1783	0.0236	0.27	2
FC-2	VU37 B37	53.5	9.5726	0.0107	0.14	2
FC-2	VU37 B38	55.0	9.6506	0.0108	0.93	3
FC-2	VU37 B39	56.5	9.6485	0.0115	0.00	2
FC-2	VU37 B45	65.0	9.9765	0.0201	0.35	2
FC-2	VU37 B47	67.5	10.0898	0.0153	0.23	3
FC-2	VU37 B57	82.0	10.8193	0.0141	0.39	3
TCR2a	VU37 B0	3.0	8.4813	0.0070	0.40	4
TCR2a	VU37 B4	8.5	8.5376	0.0071	0.30	4
TCR2a	VU37 B8	12.5	8.6382	0.0062	0.50	5
TCR2a	VU37 B12	18.0	8.7376	0.0065	0.41	5
TCR2a	VU37 B16	23.0	8.7840	0.0094	1.04	4
TCR2a	VU37 B20	29.0	8.9391	0.0098	0.52	4
TCR2a	VU37 B24	35.0	9.0808	0.0065	0.23	5
TCR2a	VU37 B28	40.0	9.2387	0.0070	0.19	5
TCR2a	VU37 B32	46.5	9.4376	0.0085	1.32	5
TCR2a	VU37 B36	52.0	9.6155	0.0070	0.85	5
TCR2a	VU37 B40	57.0	9.8123	0.0086	1.02	4
TCR2a	VU37 B44	64.0	10.0786	0.0082	0.77	5
TCR2a	VU37 B48	69.0	10.3365	0.0084	0.60	5
TCR2a	VU37 B51A	75.0	10.5455	0.0087	0.32	5
TCR2a	VU37 B55	79.0	10.7907	0.0088	1.16	5
TCR2a	VU37 B61 ^a	86.5	11.1560	0.0080	0.81	6
85G003	VU37 B-1	2.0	8.4809	0.0068	0.77	4
85G003	VU37 B31A	45.5	9.4174	0.0079	0.18	5
85G003	VU37 B62	87.0	11.1982	0.0114	0.71	5
Irradiation VU41-B						
FC-2	VU41 B2	2.3	8.2364	0.0101	0.13	6
FC-2	VU41 B6	9.3	8.2118	0.0096	1.28	7
FC-2	VU41 B10	15.3	8.2102	0.0110	0.09	7
FC-2	VU41 B14	21.8	8.2082	0.0087	0.14	10
FC-2	VU41 B18	29.8	8.2361	0.0125	0.37	7
FC-2	VU41 B23	37.5	8.2796	0.0128	0.18	6

Sample	Identity	Vial height (mm)	⁴⁰ Ar/ ³⁹ Ar ratio	σ _r	MSWD	N
Irradiation VU41-B continued						
FC-2	VU41 B27	44.3	8.3243	0.0100	0.39	8
FC-2	VU41 B31	50.3	8.4214	0.0075	1.10	12
FC-2	VU41 B35	56.0	8.4863	0.0069	0.93	15
FC-2	VU41 B39	61.3	8.5946	0.0088	0.39	8
FC-2	VU41 B43	66.5	8.6842	0.0084	0.96	9
FC-2	VU41 B47	72.0	8.7871	0.0074	0.21	9
TCR2a	VU41 B1	0.8	8.3284	0.0107	0.24	6
TCR2a	VU41 B22	36.5	8.3646	0.0112	0.57	6
TCR2a	VU41 B48	73.5	8.9133	0.0070	0.56	10
Irradiation VU42-A						
FC-2	VU42 A2	2	8.3777	0.0101	0.62	8
FC-2	VU42 A6	7	8.3496	0.0122	0.50	9
FC-2	VU42 A10	12	8.3615	0.0063	0.94	9
FC-2	VU42 A14	17.75	8.3658	0.0069	0.97	8
FC-2	VU42 A18	23	8.3697	0.0077	0.60	8
FC-2	VU42 A22	28.5	8.3705	0.0101	0.77	8
FC-2	VU42 A26	34	8.4142	0.0088	0.33	7
FC-2	VU42 A30	39.75	8.4416	0.0061	0.85	8
FC-2	VU42 A34	44.75	8.5030	0.0119	0.41	6
FC-2	VU42 A38	49.75	8.5591	0.0088	0.69	8
FC-2	VU42 A42	54.5	8.6511	0.0077	0.88	8
FC-2	VU42 A46	59.75	8.7359	0.0080	0.94	7
FC-2	VU42 A50	66.25	8.8605	0.0065	0.58	8
FC-2	VU42 A54	70.5	8.8960	0.0273	0.01	3
FC-2	VU42 A59	75.25	9.0093	0.0102	0.72	6
TCR2a	VU42 A1	0.75	8.4784	0.0059	0.94	7
TCR2a	VU42 A60	76.5	9.1396	0.0104	1.35	6

^a Standard measured before and after filament replacement.

Table 1.7: ⁴⁰Ar/³⁹Ar data for the FCT and TCR neutron fluence monitors.

Overview of all ⁴⁰Ar/³⁹Ar experiments performed on neutrons fluence monitors loaded in four irradiation batches containing six different irradiation vials. The standard, VU-identity, position of standard in the vial, the measured ⁴⁰Ar/³⁹Ar ratio and analytical uncertainty, the number of analyses and the MSWD values are summarized.

surrounding a fifth well loaded with TCR to estimate the F_{FC} ratio and σ_{FFC} for this fifth well. Then, an intercalibration factor was calculated. At the VUA curvi-linear regressions were applied to the weighted mean F-ratios of the standards with uncertainty prediction at the 68% confidence level to predict the standard F ratios for the intervening unknowns. Calculation of a simple mean of the nearest standards is not reliable for an 80 mm long vial, because the vertical gradient is too steep and (curvi-) linear interpolation is required. All weighted mean F ratios of the standards and standard errors of the mean are given in table 1.7 with the number of replicate analyses (n) and MSWD values. MSWD values were used to evaluate the sources of scatter in the data. When the MSWD value exceeds the critical value of $\sqrt{(1+2/(n-2))}$ for n data points the scatter in the data cannot be explained by the analytical error alone at the 95% probability level (Wendt and Carl, 1991). In those cases there must be another reason, e.g. some geological reason for the observed heterogeneity. However, only for VU37-C6 the MSWD value is slightly higher than the critical value. In ArArCalc standard errors of the mean are multiplied by \sqrt{MSWD} when the MSWD > 1 (Koppers, 2002).

Further, part of the data from VU32 is omitted from weighted mean calculations (see data- set <http://www.geo.vu.nl/users/kuik>). During outgassing of the system the glass window of the sample holder broke down and the copper tray loaded with standards completely oxidized. The standards were still measured, but show a tendency of lower radiogenic ^{40}Ar contents (<90%) and have been omitted from further interpretations. VU41 and VU42 were irradiated at a slightly different position in the Oregon State TRIGA reactor (extended TRIGA tube). This resulted in a range of F ratios varying about 7.5% over a vial length of ~80 mm for VU41 and VU42 with the lower 30 mm part of the vial showing a more or less constant neutron flux compared to a variation of ~22% over a 80 mm vial length in the other irradiations. Further, during the measurement of irradiation VU37 the filament of the ion source had to be replaced. A few standards of VU37-CI (C11, C6 and C10) and VU37-B (B27, B29, B30, B61) have been re-measured on the mass spectrometer after the new filament had been fitted. Apart from VU37-C6 the MSWD values suggests that the scatter can be explained by the analytical error alone and the filament replacement apparently did not influence the measured $^{40}\text{Ar}^*/^{39}\text{Ar}_k$ ratios. This implies that the system behavior apparently did not change due to the filament replacement and that the mass fractionation correction indeed accounted for the changed circumstances in the mass spectrometer.

The curvi-linear regressions applied to the weighted mean F ratios of the standards with the vial height as independent parameter resulted in a second or third order polynomial fit and an estimation of the F_{standard} for each height in the vial. For VU32 and VU37 two F-curves per vial were established (a curve for FCT and one for TCR), for VU41 and VU42 only F curves for FCT were established. Although the curves for the lower 30 mm in the vials of VU41 and VU42 seem to indicate more or less uniform neutron fluxes, it appeared that the weighted mean F values better could be modeled with a quadratic than linear fit (higher r^2). Errors were predicted at the 68% confidence level for each curve. The F-curves were transformed into J curves using the ages of 28.34 Ma for TCR and 28.02 Ma for FCT (Renne et al., 1998) ignoring the errors in the standard ages and decay constants. It appeared that in all cases the J curves based on TCR and FCT overlapped at

Table. 1.8: Intercalibration of TCR and FCT (next page).

Intercalibration data of TCR and FCT. The intercalibration procedure is explained in detail in the text. All data have been intercalibrated either to TCR with an age of 28.34 Ma or to FCT with an age of 28.02 Ma.

^{a)} Intercalibration between 85G003 and TCR2a.

Sample	Identity St ₂	vial in mm	F _{St2} ± σ _{St2}	F _{St1} ± σ _{St1}	R _{TC/FC} ± 1σ	Age ± 1σ (Ma)	N
Irradiation VU32-C							
FCT	Cz	2.0	8.4818 ± 0.0091	8.5735 ± 0.0301	1.0108 ± 0.0037	28.04 ± 0.10	5
FCT	Cy	18.0	8.7505 ± 0.0112	8.8409 ± 0.0261	1.0103 ± 0.0033	28.05 ± 0.09	4
FCT	Cx	37.0	9.1902 ± 0.0083	9.2925 ± 0.0266	1.0111 ± 0.0030	28.03 ± 0.08	7
FCT	Cw	52.0	9.6374 ± 0.0158	9.7518 ± 0.0257	1.0119 ± 0.0031	28.01 ± 0.09	2
FCT	Cv	59.6	9.8962 ± 0.0096	10.0191 ± 0.0268	1.0124 ± 0.0029	28.00 ± 0.08	6
FCT	Ct	66.0	10.2062 ± 0.0121	10.2623 ± 0.0302	1.0055 ± 0.0032	28.19 ± 0.09	5
Weighted mean						1.0104 ± 0.0013	28.05 ± 0.04
Irradiation VU37-CI							
FCT	VU37 C2	2.0	8.4148 ± 0.0131	8.5430 ± 0.0259	1.0152 ± 0.0035	27.92 ± 0.09	5
FCT	VU37 C11	11.0	8.5830 ± 0.0064	8.6600 ± 0.0234	1.0090 ± 0.0028	28.09 ± 0.08	10
FCT	VU37 C20	20.0	8.7278 ± 0.0070	8.8166 ± 0.0228	1.0102 ± 0.0027	28.06 ± 0.08	5
FCT	VU37 C29	29.0	8.9088 ± 0.0057	9.0130 ± 0.0229	1.0117 ± 0.0027	28.02 ± 0.07	5
FCT	VU37 C38	38.0	9.1572 ± 0.0083	9.2490 ± 0.0231	1.0100 ± 0.0027	28.06 ± 0.07	4
FCT	VU37 C47	46.0	9.3956 ± 0.0073	9.4921 ± 0.0231	1.0103 ± 0.0026	28.05 ± 0.07	5
FCT	VU37 C56	55.5	9.7200 ± 0.0082	9.8215 ± 0.0230	1.0104 ± 0.0025	28.05 ± 0.07	5
FCT	VU37 C67	69.5	10.2899 ± 0.0076	10.3876 ± 0.0236	1.0095 ± 0.0024	28.08 ± 0.07	5
FCT	VU37 C79	80.5	10.7973 ± 0.0084	10.8997 ± 0.0264	1.0095 ± 0.0026	28.08 ± 0.07	4
Weighted mean						1.0104 ± 0.0009	28.05 ± 0.02
Irradiation VU37 CII							
FCT	VU37 Cz	1.0	8.4097 ± 0.0079	8.5173 ± 0.0277	1.0128 ± 0.0034	27.98 ± 0.09	5
FCT	VU37 Cy	14.5	8.5389 ± 0.0182	8.6346 ± 0.0238	1.0112 ± 0.0035	28.03 ± 0.10	4
FCT	VU37 Cx	25.0	8.7116 ± 0.0092	8.7976 ± 0.0235	1.0099 ± 0.0029	28.07 ± 0.08	4
FCT	VU37 Cw	35.5	8.8926 ± 0.0092	9.0235 ± 0.0237	1.0147 ± 0.0029	27.93 ± 0.08	4
FCT	VU37 Cv	48.5	9.2770 ± 0.0095	9.3902 ± 0.0237	1.0122 ± 0.0028	28.00 ± 0.08	4
FCT	VU37 Cu	58.0	9.6270 ± 0.0085	9.7190 ± 0.0235	1.0096 ± 0.0026	28.07 ± 0.07	5
FCT	VU37 Ct	69.0	10.0673 ± 0.0110	10.1641 ± 0.0239	1.0096 ± 0.0026	28.07 ± 0.07	3
FCT	VU37 Cs	85.0	10.7561 ± 0.0109	10.9344 ± 0.0288	1.0166 ± 0.0029	27.88 ± 0.08	4
Weighted mean						1.0120 ± 0.0010	28.00 ± 0.03
85G003	VU37 C79B	2	8.4833 ± 0.0184	8.5224 ± 0.0272	1.0046 ± 0.0039	28.21 ± 0.11	5
85G003	VU37 C106A	43	9.2333 ± 0.0115	9.2233 ± 0.0238	0.9989 ± 0.0029	28.37 ± 0.08	3
85G003	VU37 C135	82.5	10.8052 ± 0.0083	10.8045 ± 0.0275	0.9999 ± 0.0027	28.34 ± 0.07	6
Weighted mean						1.0005 ± 0.0017	28.33 ± 0.05
Irradiation VU37-B							
FC-2	VU37 B-2	1.0	8.3930 ± 0.0057	8.4690 ± 0.0266	1.0091 ± 0.0032	28.09 ± 0.09	5
FC-2	VU37 B19A	28.0	8.8471 ± 0.0064	8.9158 ± 0.0229	1.0078 ± 0.0027	28.12 ± 0.07	5
FC-2	VU37 B40A	58.5	9.7565 ± 0.0084	9.8672 ± 0.0230	1.0113 ± 0.0025	28.02 ± 0.07	5
FC-2	VU37 B63	87.5	11.0824 ± 0.0076	11.2113 ± 0.0267	1.0116 ± 0.0025	28.02 ± 0.07	5
FC-2	VU37 B3	7.5	8.4019 ± 0.0229	8.5426 ± 0.0244	1.0167 ± 0.0040	27.88 ± 0.11	2
FC-2	VU37 B6	10.0	8.4800 ± 0.0087	8.5766 ± 0.0239	1.0114 ± 0.0030	28.02 ± 0.08	3
FC-2	VU37 B10	15.5	8.5714 ± 0.0136	8.6628 ± 0.0232	1.0107 ± 0.0031	28.04 ± 0.09	2
FC-2	VU37 B13	19.5	8.6467 ± 0.0103	8.7351 ± 0.0229	1.0102 ± 0.0029	28.06 ± 0.08	2
FC-2	VU37 B17	24.5	8.7418 ± 0.0084	8.8369 ± 0.0228	1.0109 ± 0.0028	28.04 ± 0.08	2
FC-2	VU37 B19	27.0	8.7880 ± 0.0123	8.8926 ± 0.0229	1.0119 ± 0.0030	28.01 ± 0.08	3
FC-2	VU37 B27	38.5	9.1079 ± 0.0114	9.1898 ± 0.0231	1.0090 ± 0.0028	28.09 ± 0.08	3
FC-2	VU37 B29	41.5	9.1529 ± 0.0117	9.2784 ± 0.0232	1.0137 ± 0.0028	27.96 ± 0.08	2
FC-2	VU37 B30	43.0	9.1783 ± 0.0236	9.3244 ± 0.0232	1.0159 ± 0.0036	27.90 ± 0.10	2
FC-2	VU37 B37	53.5	9.5726 ± 0.0107	9.6787 ± 0.0231	1.0111 ± 0.0027	28.03 ± 0.07	2
FC-2	VU37 B38	55.0	9.6506 ± 0.0108	9.7339 ± 0.0230	1.0086 ± 0.0026	28.10 ± 0.07	3
FC-2	VU37 B39	56.5	9.6485 ± 0.0115	9.7903 ± 0.0230	1.0147 ± 0.0027	27.93 ± 0.07	2
FC-2	VU37 B45	65.0	9.9765 ± 0.0201	10.1312 ± 0.0229	1.0155 ± 0.0031	27.91 ± 0.08	2
FC-2	VU37 B47	67.5	10.0898 ± 0.0158	10.2385 ± 0.0229	1.0147 ± 0.0028	27.93 ± 0.08	3
FC-2	VU37 B57	82.0	10.8193 ± 0.0141	10.9234 ± 0.0248	1.0096 ± 0.0026	28.07 ± 0.07	3
Weighted mean						1.0116 ± 0.0007	28.02 ± 0.02
85G003	VU37 B-1	2.0	8.4809 ± 0.0068	8.4789 ± 0.0262	0.9998 ± 0.0032	28.35 ± 0.09	4
85G003	VU37 B31A	45.5	9.4174 ± 0.0079	9.4037 ± 0.0232	0.9985 ± 0.0026	28.38 ± 0.07	5
85G003	VU37 B62	87.0	11.1982 ± 0.0114	11.1845 ± 0.0265	0.9988 ± 0.0026	28.37 ± 0.07	5
Weighted mean						0.9989 ± 0.0016	28.37 ± 0.04
Irradiation VU41-B							
TCR2a	VU41 B1	0.8	8.3282 ± 0.0107	8.2533 ± 0.0149	1.0091 ± 0.0022	28.27 ± 0.06	6
TCR2a	VU41 B22	36.5	8.3646 ± 0.0112	8.2726 ± 0.0124	1.0111 ± 0.0020	28.33 ± 0.06	6
TCR2a	VU41 B48	73.5	8.9132 ± 0.0070	8.8229 ± 0.0138	1.0102 ± 0.0018	28.30 ± 0.05	10
Weighted mean						1.0102 ± 0.0011	28.30 ± 0.03
Irradiation VU42-A							
TCR2a	VU42 A1	0.75	8.4784 ± 0.0059	8.3878 ± 0.0210	1.0108 ± 0.0026	28.32 ± 0.07	7
TCR2a	VU42 A60	76.5	9.1396 ± 0.0104	9.0478 ± 0.0222	1.0101 ± 0.0027	28.30 ± 0.08	6
Weighted mean						1.0105 ± 0.0019	28.31 ± 0.05

the 1σ level, supporting the intercalibration between TCR and FCT as proposed by Renne et al. (1998). Including the uncertainty in the standard ages only broadens the 1σ error band (error is 2 to 3 times higher) increasing the overlap even more.

The intercalibration can be confirmed by a slightly different approach. An intercalibration factor can be calculated according to 1.9 (see also Karner and Renne, 1998). In VU32 and VU37 TCR was loaded as the "main" standard, in VU41 and VU42 FCT was the "main" standard. Therefore, in VU32 and VU37 the interpolated F_{TC} ratios were used to determine $R_{TC/FC}$ at each position in the vial where FC was loaded. In VU41 and VU42 the interpolated F_{FC} ratios were used to determine $R_{TC/FC}$ at each position in the vial where TC was loaded. Table 1.8 showed the results of the intercalibration factor $R_{TC/FC}$ for all irradiations. Additionally, in VU37-CII and VU37-B the "old" and "new" split of TCR were intercalibrated against each other and should ideally result in an intercalibration factor of 1 (i.e., no difference in age). Further, the ages of the "minor" standards have been calculated relative to the "main" standards, i.e. relative to TCR of 28.34 Ma for VU32 and VU37 and relative to FCT of 28.02 Ma for VU41 and VU42. Age and error calculation were performed according to 1.12. The reported error in table 1.7 includes only the analytical uncertainty.

Renne et al. (1998) reported an intercalibration factor of 1.0112 ± 0.0010 . Comparison of our data (table 1.8) with this intercalibration factor shows that the weighted mean intercalibration factors of all irradiations are statistically not different from the value reported by Renne et al. (1998). A few data (VU32-Ct, VU37-Cs, B3, B30 and B45) show weighted mean intercalibration factors for individual heights in the vial that do differ at the 1σ level from the factor of Renne et al. (1998). However, most of these "outliers" have relatively large uncertainties and therefore, contribute to a less extent to the final weighted mean intercalibration factor. Cumulative probability distributions can be obtained by summing the probability distributions of a suite of data with normally distributed errors, which was done for all $R_{TC/FC}$ and $R_{TC/85G003}$. Both probability curves showed a more or less Gaussian distribution supporting that the weighted mean intercalibration factor indeed is the best estimate of the true value.

The confirmation of the intercalibration factor between FCT and TCR based on 4 different irradiations at the VUA over a period of 3 years has several implications. First, both laboratories seem to produce the same results (at least in a relative way), confirming that the interlaboratory error is very small indeed. Further, the establishment of the same intercalibration factor in several irradiations at the VUA implies that the long-term intralaboratory error is also small. Apparently, system performance is stable over the years and the applied mass discrimination correction seems to be reliable. Even replacement of the filament does not show systematic changes in the behavior of the system.

Additionally intercalibration factors, required for the replacement of the 85G003 split of Taylor Creek Rhyolite sanidine by a new split (TCR2a), are established. The amount of intercalibration data in irradiation VU37-CII and VU37-B is not extremely large ($n = 28$ over 6 vial positions), but the intercalibration factor does not differ from 1 at the 1σ level, which implies that they are equivalent in age. Lanphere (2000, personal communication) made the new split of TCR available as well sampled together with "our" TCR2a split. Successive mineral separation procedures were performed in different laboratories (VUA and USGS Menlo Park). Lanphere (2000, personal communication) intercalibrated the new split relative to 85G003 with an age of 27.92 Ma and his data resulted in a weighted mean age and standard error of the mean of 27.87

± 0.04 Ma for TCR2. Because the intercalibration factor between 85G003 and TCR2a in the Lanphere data is also 1 we decided to use the same age for both 85G003 and TCR2a (28.34 ± 0.16 Ma, Renne et al., 1998).

SUMMARY

This chapter described the theoretical background of and procedures in $^{40}\text{Ar}/^{39}\text{Ar}$ dating. One of the important aspects is how to obtain the highest accuracy and precision in a $^{40}\text{Ar}/^{39}\text{Ar}$ age and how to evaluate the assigned errors. As described in studies of e.g. Renne et al. (1998) or Min et al. (2000) apart from analytical errors the real uncertainties in decay constants and absolute ages of standards must be included in error propagation methods. Part of this chapter concentrated on published results of decay constants and ages of standards. Age calculations and error propagation methods evaluating errors related to analytical methods, decay constants and K/Ar dated primary standards were reproduced from Min et al. (2000) and Koppers (2002). A new set of error equations was established for the special case of $^{40}\text{Ar}/^{39}\text{Ar}$ dating with an astronomically dated standard. Further, a series of equations was derived to assess the contribution of the measured parameters to the error in the $^{40}\text{Ar}^*/^{39}\text{Ar}_k$ ratio of a sample or standard. One of the parameters contributing significantly to the total variance is the mass discrimination. Efforts to improve the assessment of this factor have also been described in this chapter. Results of the application of all the aspects described in this chapter will be presented in the next chapters.

CHAPTER 2

**ASTRONOMICAL DATING TECHNIQUE AND ITS
APPLICATION IN ACCURATELY DETERMINING THE
ABSOLUTE AGE OF NEOGENE VOLCANIC ASH LAYERS IN
THE MEDITERRANEAN.**

INTRODUCTION

Time is an indispensable tool in Earth Sciences for understanding all kinds of processes and for determining rates of change. Consequently geological time scales play a crucial role in reconstructing Earth's history. Before applying radiogenic isotope dating techniques to geological time scales, they were constructed on a relative scale. Since the beginning of the twentieth century along with the discovery of radioactivity and its potentials for dating of geological material, geological time scales have witnessed a dramatic increase in accuracy and resolution (e.g., Holmes, 1911). During the last decades an absolute dating method totally independent from radiogenic isotope dating has been developed based on perturbations in the Earth's orbit and rotation axis, and the influence they exert on insolation on Earth and hence climate. Paleoclimatic proxy records have been tuned to astronomical target curves (of eccentricity, precession, obliquity and/or insolation) providing absolute ages for both proxy cycles as well as paleomagnetic reversals, biohorizons and volcanic ash layers preserved in the stratigraphic record. Astronomical dating already underlies the Pliocene to Pleistocene part of the standard geological time scale and most likely will underlie the entire Neogene in the next version of the time scale to be published in 2004 (Lourens et al., 2004). As a consequence, the geological time scale is now based on two independent, but not intercalibrated dating techniques, i.e. radiogenic isotope (e.g., K/Ar, $^{40}\text{Ar}/^{39}\text{Ar}$, U/Pb) and astronomical dating. In this chapter we will briefly discuss the theory behind the astronomical dating method and the possible errors involved in determining the astronomical ages of volcanic ash layers of Neogene age in the Mediterranean region, because these volcanic ash layers are used for the intercalibration of the different methods.

BASIC PRINCIPLES OF ASTRONOMICAL DATING

More than a century ago, just before the invention of radiometric dating, Gilbert already realised that astronomically forced cyclicity in marine sedimentary archives could be used to estimate the duration of (parts of) the geological record (Gilbert, 1895). His estimates were in favour of a much older age for our planet than the 100 (or even 20) million years then calculated on the basis of a conductive cooling model of the Earth (e.g., Kelvin, 1897). Gilbert linked his sedimentary cycles to perturbations in the Earth's orbit and rotation axis, which are caused by gravitational interactions of our planet with the Sun, the Moon and the other planets of our solar system. These interactions give rise to cyclic changes in the eccentricity of the Earth's orbit, with main periods of 100,000 and 400,000 years, and in the tilt (obliquity) and precession of the Earth's axis with main periods of 41,000, and 21,000 years, respectively (Berger, 1977, figure 2.1). These perturbations in the Earth's orbit and rotation axis are climatically important because they affect the global, but especially the seasonal and latitudinal distribution of the incoming solar insolation (see Berger, 1988).

Orbitally forced climate oscillations are recorded in sedimentary archives through changes in sediment properties, fossil communities, chemical and stable isotopic characteristics. While earth scientists can read these archives to reconstruct palaeoclimate, astronomers have formulated models based on the mechanics of the solar-planetary system and the Earth-Moon system to compute the past variations in precession, obliquity and eccentricity of the Earth's orbit and rotation axis. These models for astronomical solutions of the Solar System, which comprise both a planetary and an Earth-Moon part necessary to compute eccentricity, obliquity and precession, are used to calculate the varying solar energy input at the top of the

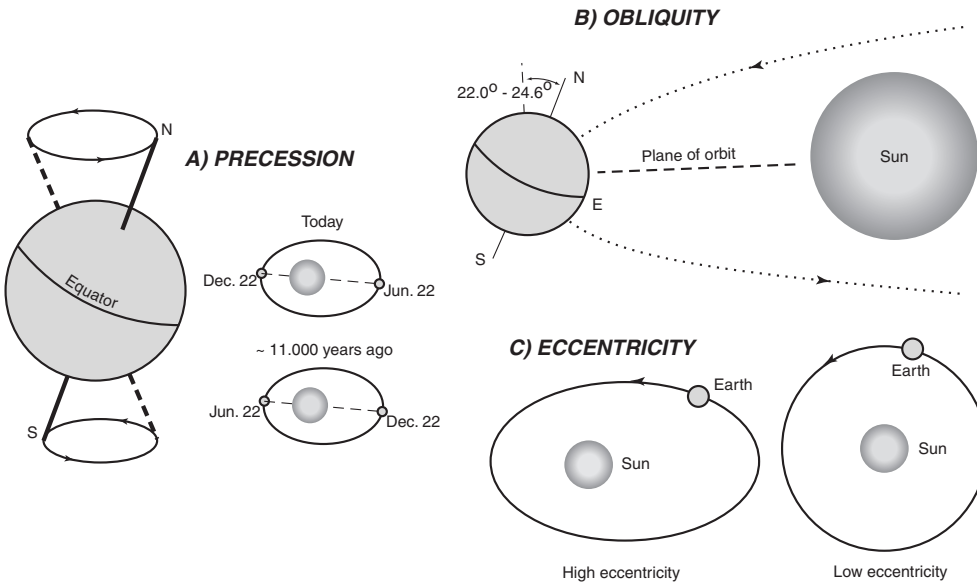


Figure 2.1a-c Orbital parameters.

Schematic overview of the orbital parameters precession (a), obliquity (b) and eccentricity (c).

atmosphere through time. These so-called astronomical target curves sustain an absolute time frame over a period from -20 Ma to $+10$ Ma (Laskar et al., 1993a). As a logical next step, sedimentary archives can be dated by matching patterns of palaeoclimate variability with patterns of varying solar insolation and are tied to the Recent through a direct match with astronomical target curves. Therefore, this astronomical tuning of the sedimentary record results in time scales based on (orbital) parameters that are totally independent from those underlying radio-isotopic dating.

ASTRONOMICAL TIME SCALES

The first serious attempt to link paleoclimate observations (of the ice ages) to orbitally induced variations in insolation was made by Köppen and Wegener (1924). They related the four separate glacial periods - Gunz, Mindel, Riss and Würm, distinguished by Penck and Brückner (1909) on the basis of river terraces in the northern Alps - to reduced (weak) summer insolation maxima in insolation curves computed by Milankovitch for high northern-latitudes. But acceptance of this astronomical theory of the ice ages first advocated in a different form by Adhémar (1841) and Croll (1866) had to await the recovery of continuous marine successions by piston coring techniques, major improvements in the dating of relatively young sediments (e.g. ^{14}C , U/Th, magnetostratigraphy) and the development of ice age proxies, in particular $\delta^{18}\text{O}$. The final breakthrough came from the thorough statistical analysis and astronomical tuning of late Pleistocene $\delta^{18}\text{O}$ records of marine piston cores, which reflect global ice volume (e.g. Hays et al., 1976; Imbrie et al., 1984). These efforts resulted in the standard and astronomically tuned SPECMAP time scale for global changes in the Milankovitch frequency band observed in the marine oxygen isotope record over the last 800,000 years. Following earlier attempts (Pisias and Moore, 1981; Ruddiman et al., 1989; Raymo et al., 1989), the

astronomical time scale was extended to the base of the Pliocene, using paleoclimatic records from Ocean Drilling Project (ODP) sites in the eastern equatorial Pacific and North Atlantic (Shackleton et al. 1990) and sedimentary cycle patterns in marine successions exposed on land in the Mediterranean (Hilgen, 1991a,b), tuned to the Ber90 solution (Berger and Loutre, 1991). Despite age discrepancies of up to 10% with conventional time scales, the astronomical time scale became the preferred time scale because its validity was soon confirmed by radiogenic isotope dating using the new $^{40}\text{Ar}/^{39}\text{Ar}$ laser fusion technique (Renne et al., 1993). Independent support of the APTS came from a study by Wilson (1993), who showed that the astrochronology resulted in a more consistent and steady history of seafloor spreading rates. The Plio-Pleistocene astronomical time scale is widely accepted as a standard (Cande and Kent, 1995; Berggren et al., 1995) and needs to undergo no or only minor revisions in the future (e.g. Lourens et al., 1996), thus avoiding the promulgation of new and fundamentally different time scales. It has been verified and slightly modified by adopting the La93 astronomical solution (Lourens et al., 1996).

In the Mediterranean, the tuning has been extended to 14 Ma using continental sequences in addition to the marine record (Abdul Aziz et al., 2003; Hilgen et al., 1995, 2000a, 2003). The astronomical time scale has been extended back into the Oligocene based on ODP Leg 154 sequences (Shackleton et al., 1999) and serious attempts are now undertaken to construct similar time scales for older parts of the Paleogene (Pälike et al., 2001). Also for this purpose, a reliable and accurate intercalibration of astronomical and radiogenic isotope dates is mandatory.

ASTRONOMICAL SOLUTIONS

In the Principia, Newton completely solved the problem of two attracting bodies, or better point masses, with the inverse square law of motion (Newton, 1687). A planet moving around the Sun describes an elliptical path and the orbital period depends only on the average distance from the Sun. In mathematical terms, he showed that the **"two-body problem"** was integrable. In other words it was possible to obtain a complete and exact analytical solution for this problem using relatively simple linear mathematical equations. Consequently, we can predict any future and past configuration of a two-body system with an arbitrary precision for all time. Newton had thus confirmed the empirically derived laws of Kepler and completely solved the two-body problem but stated that finding "an exact solution for three bodies exceeds, if I am not mistaken, the force of any human mind". Nevertheless many attempts were being made in the 18th as well in the 19th century to establish an analytical solution for the Solar System, starting from the newtonian concept of a Clockwork Universe and using simplified linearized equations (e.g. Laplace, 1799; Le Verrier, 1856). Poincaré showed however that it is impossible to find an exact solution for the three-body problem due to sensitivity to initial conditions as a consequence of what is nowadays termed the chaotic behavior of a complex non-linear system (Poincaré, 1890).

The first approximate analytical solution for the Solar System of Le Verrier was based on linearized equations and used by Milankovitch for his insolation computations. The analytical solution used to compute the long-term variations in the Earth's orbital elements was subsequently improved by including higher order terms connected with the disturbing masses of the planets and solve the equations up to a higher degree for the eccentricity and inclination of the planets. This development eventually resulted in the analytical solution of Laskar (1988) which includes terms of the second order for the planetary masses and

of the fifth degree for the planetary eccentricity and inclination (see Berger, 1988, for a review). In 1993, Laskar and others (1993b) added an improved solution for the Earth-Moon System to this orbital part of the solution to provide a full solution necessary for the computation of not only eccentricity but also obliquity and precession, and thus insolation.

At the same time the chaotic behavior of the Solar System was convincingly demonstrated because the perturbative time series showed evidence of divergence with Lyapunov times (a measure of the degree of chaos in a non-linear dynamical system) of 20 myr for the Outer Planetary System (Sussman and Wisdom, 1988) and of 5 myr for the Inner Planetary System (Laskar, 1989). The chaotic aspect of the Solar System limits the accuracy of any analytical solution over longer time intervals but this complication can be partly overcome by using a numerical instead of an analytical solution.

The first direct numerical integration of the entire Solar System over the last 3 myr was published by Quinn et al. (1991). From an astronomical point of view this solution is assumed to be very accurate with an error that is probably less than ~ 0.03 radians for the Earth's longitude and pole position at 3.0 Ma (Quinn et al., 1991). This numerical solution QTD90 is in excellent agreement with the La93 solution after introduction of the same tidal dissipation term (see Laskar et al., 1993a). This is also the case after an extended integration over 6 million years (Laskar et al., 1992), pointing to the accuracy of the La93 solution and its suitability for paleoclimate studies over the last 10-20 myr, the time span believed to be insensitive to exponential divergence of the solution as a consequence of the chaotic behavior of the Solar System. Moreover, the La93 solution for the first time offered the possibility to modify two parameters, the dynamical ellipticity of the Earth and the tidal dissipation by the Moon. Both these parameters affect the precession and obliquity frequencies and will be reduced for instance when entering an ice age (Laskar et al., 1993a). On longer time scales, dynamical ellipticity may also change as a consequence of secular changes in mantle convection (Forte and Mitrovica, 1997). La93_(1,1) denotes the La93 solution with present-day values (of 1) for dynamical ellipticity and tidal dissipation, respectively.

The chaotic nature of the Solar System will limit the accurate computation of the orbital and precession motion of the Earth over more than 35-50 myr (Laskar, 1999). The principal sources of uncertainty that limit the Earth's orbital calculations were reviewed by Laskar (1999). He showed that the largest source of error at present is uncertainty in the value of the oblateness (departure from spherical symmetry) of the Sun, limiting the validity of the solution to 26 myr. But even in case the value of this parameter is much more precisely determined as can be anticipated, other sources such as the effect of satellites and small bodies will still limit the validity of the solution to not more than 35-50 myr (Laskar, 1999). Laskar et al. (in preparation) recently completed a new solution, La2003, in an attempt to reach the currently possible limits of accuracy. This is the first completely numerical astronomical solution over a period of -100 to $+50$ Ma. The orbital model differs from La93, as it comprises now all 9 planets of the Solar System, including Pluto. The general relativity perturbation from the Sun is included and the Moon is treated as a separate object. The Earth-Moon system takes the most important coefficient (J_2) in the gravitational potential of the Earth and the Moon, and the tidal dissipation of the Earth Moon System, as well as the influence of the precession of the Earth axis on the Lunar orbit into account. The evolution of the Earth-Moon system and rotation of the Earth are treated in a comprehensive and coherent way, following the lines of Néron de Surgy and Laskar (1996) and Correia et al. (in press). The climate friction effect, due to the change of momentum of

inertia of the Earth arising from the change of ice load on the polar caps during ice ages has been estimated (Levrard and Laskar, submitted), but neglected as it was found to be too small and too uncertain to be taken into account.

THE MEDITERRANEAN

The Mediterranean region is extremely suitable for studies aimed at understanding astronomical climate forcing and building astronomical time scales. The Mediterranean basin is very sensitive to record astronomical forced climate change due to its semi-enclosed character and its latitudinal position at the crossing between the subtropical (semi)arid climates of Africa and the mid-latitude westerlies, while the influence of the tropical monsoonal system is felt via Nile river run-off. Another advantage of the Mediterranean region is that certain areas of the ancient seafloor underwent extremely rapid uplift during the last millions of years as a consequence of the active plate tectonic setting at the convergence between the African and European plates, resulting in the sub-aerial exposure of cyclically bedded deep-sea sequences on land.

Results of proxy studies reveal that the formation of Milankovitch-type of sedimentary cycles in Mediterranean deep marine sequences over the last 13.5 million years can be linked to a dominantly precession controlled oscillatory climate system. A recent climate modeling experiment of orbital extremes indicates that the African monsoon may be responsible (Tüenter et al., 2003), thereby confirming earlier ideas of Rossignol-Strick (1982; 1985), Kutzbach (1981) and Prell and Kutzbach (1987). In addition the outcome of this study validates the use of the classical 65°N latitude summer insolation curve as a target for tuning sedimentary cycles in the Mediterranean among others by demonstrating an obliquity control on the African monsoon mostly via heating of the Eurasian continent at latitudes higher than 30° (Tüenter et al., 2003). However, an additional and time-equivalent influence of the Atlantic mid-latitude climate system, the "westerlies", seems likely (Rossignol-Strick, 1987; Sierro et al., 2000) and may well explain the occurrence of sedimentary cycles in continental settings, such as the Ptolemais basin in Greece (Van Vugt et al., 1998, Steenbrink et al., 1999) and the Calatayud-Teruel basin in Spain (Abdul Aziz et al., 2000, 2003), and in the marine Gulf of Cadiz at the Atlantic site of Spain (Sierro et al., 2000).

One of the requirements for comparing the astronomically tuned time scales with independent radiogenic isotope methods is the occurrence of volcanic ash layers in astronomically tuned sedimentary sections. Apart from the suitability for the construction of astronomical time scales, the Mediterranean is also characterized by the common occurrence of volcanism during the Neogene due to the convergence of the African and European plates. Ash-layers have been found (and dated) in the astronomically tuned (deep) marine sequences on Crete, Greece, in the Sorbas and Nijar basins in SE Spain, in the Melilla basin in NE Morocco, at Monte Gibliscemi on Sicily, at Monte dei Corvi in NE Italy and in the continental sequence of the Ptolemais basin in northern Greece. Sedimentary cycles of all studied sections have been tuned to the La93_(1,1) solution and details of the tuning are described in Hilgen et al. (1995) for Crete, in Sierro et al. (2001) for the Sorbas and Nijar basin, in Hilgen et al. (2000a) for Monte Gibliscemi, in Hilgen et al. (2003) for Monte dei Corvi and in Van Vugt et al. (1998) and Steenbrink et al. (1999) for Ptolemais.

ERROR ESTIMATE FOR THE ASTRONOMICAL AGES OF THE ASH LAYERS

Errors in the astronomical ages of the ash layers used for the intercalibration of radiogenic isotope and astronomical dates in this thesis may result from uncertainties in the correctness of the tuning, and in the accuracy of the astronomical solution.

CORRECTNESS OF TUNING, PHASE-RELATIONS, SEDIMENTATION RATES AND TIME LAGS

The correctness of the tuning is of fundamental importance for building astronomical time scales with their unprecedented accuracy and resolution and mistakes are often made in this respect. A mistuning of one basic cycle typically results in an error of plus (or minus) 20 kyr in the case in which precession or 40 kyr in the case in which obliquity is used for tuning. Such an error may be restored in case the amplitude modulation of precession (by eccentricity) or obliquity is taken into account to validate the tuning of the basic cycles (pattern fitting between sedimentary cycles and target curves). The error might accumulate however when the tuning is based on counting the number of successive cycles. In the Mediterranean large-scale cycle patterns (e.g. the small and large-scale sapropel clusters in the marine domain) are used to establish a first-order tuning to eccentricity preceding the final tuning to precession and/or insolation, thus avoiding the possible accumulation of errors in the tuning. Tuning characteristics of the sedimentary sections studied in this thesis are described in detail in the next chapters.

An additional error may come from the uncertainty in the phase relations between the astronomical forced variations in climate proxy records used for tuning and the initial insolation forcing itself. Uncertainty in the phase relations, i.e. opposite phase relations with respect to the orbital parameters, can be excluded for the marine record, apart from a possible time lag of 1-3 kyr (see below); they have been convincingly established for the last 150.000 years (e.g. Hilgen, 1991a) and validated subsequently by the excellent fit with intricate details in the astronomical target curve (Lourens et al., 1996, 2001). As such opposite phase relations can be excluded for the marine record, but phase relations, in particular correlations to precession, are less straightforward for the continental succession of the Ptolemais basin in Greece in which several ash layers occur that are dated in this thesis. Uncertainties in the exact position of magnetic reversal boundaries do not allow us to determine phase relations based on a detailed comparison with the tuned marine record having a reliable magnetostratigraphy, while the intercalated ash layers have not been detected thus far in time equivalent and astronomically dated marine sections. Phase relations were ultimately based on interpretation of lithofacies in terms of lake level - lignites representing swamp deposits and marls open deeper lake conditions - in combination with the assumption that enhanced rainfall and higher lake levels will occur at times of precession minima / insolation maxima (Van Vugt et al., 1998 and references therein).

In addition to uncertainty in the sign of a phase relation, time lags may be present between the insolation forcing, and climate response and registration in the stratigraphic record. During the Pleistocene such time lags are found between insolation forcing and glacial response because it takes time to build up and melt an ice cap. These time lags depend among others on the time constant of a system and were assumed to be 5 kyr for precession and 8 kyr for obliquity in case of a time constant of 17 kyr; they were used in the construction of the SPECMAP time scale for the oxygen isotope record (Imbrie et al., 1984). But there is geological evidence that these time lags are too large (e.g. Lourens et al., 1996). The volcanic ashes

intercalated in the cyclic sequences used in this thesis study were deposited however at pre-Pleistocene times when glacial cyclicity was strongly reduced or even absent. But even in the Pleistocene, the time lag must have been smaller or even absent because the low-latitude monsoon climate system responsible for sapropel formation was at least partly decoupled from the high-latitude glacial regime.

Results of climate modelling using a simple energy balance model suggested that tropical climate response might lag insolation forcing by up to 3 kyr. It was this time lag that was thought to explain the 3 kyr offset in the ages of the last boreal summer insolation maximum (at 11.5 ka) and the midpoint of the youngest Holocene sapropel (at 8.5 ka). Initially this 3 kyr time lag was incorporated in constructing the astronomical time scale by making all sapropels 3 kyr younger than the correlative precession and/or insolation peak. More recently, a direct climate response is assumed in absence of a strong glacial cyclicity. The latter assumption is confirmed by the outcome of transient climate modelling experiments over 100,000 year thus covering several full precession and obliquity cycles. Registration of the climate signal in the sedimentary archives is ultimately assumed to be instantaneous (as is deposition of a volcanic ash layer after eruption), because Mediterranean circulation or continental lake levels will react almost directly to the signal.

Finally, astronomical ages of ash layers are calculated by means of linear interpolation between successive astronomically dated calibration points (e.g, sapropel midpoints) under the assumption of a constant sedimentation rate. This assumption is in essence not valid but it is difficult to get a good grip on changes in sedimentation rate within 1 cycle, which depends on the interpretation of the sedimentary cyclicity and flux calculations. It is estimated that such changes in sedimentation rate may result in an error of several 1000 yrs at maximum in the age of the ash layers.

These errors however do not take errors into account that are related to the accuracy of the astronomical solution. Because of the complexity of astronomical solutions error estimates for the astronomical solutions are difficult to obtain. To estimate a realistic error in the astronomical ages due to the accuracy of the astronomical solution we compared 1) the new La2003 solution (Laskar et al., in preparation) with the La93 solution, and 2) the La93 solution with different values for dynamical ellipticity and tidal dissipation. The La93 solution was shown to be in excellent agreement with the QTD90 solution, which had an error that was probably less than ~ 0.03 radians for the Earth's longitude and pole position at 3.0 Ma (Quinn et al., 1991), or less than a few 100 yrs.

ACCURACY OF THE ASTRONOMICAL SOLUTION: LA93 VERSUS LA2003

We subtracted the values for eccentricity, obliquity, precession and 65°N latitude summer insolation of the La93 solution from the La2003 solution and plotted these differences over the last 15 Ma to analyse and visually depict the consequences of these two solutions for astronomical time scale work. For this purpose we started from the solutions with present-day values for dynamical ellipticity and tidal dissipation. Figure 2.2a and b show the resulting curves for obliquity and precession. The obliquity curve is stretched in the La93_(1,1) solution relative to La2003_(1,1) which results in a shift of approximately a quarter cycle of back at 15 Ma and a difference in absolute age of ~ 11 kyr (figure 2.3a). Similarly the precession is stretched and shifted in La93_(1,1) resulting in a shift of approximately a quarter cycle back at 15 Ma and a difference in absolute age of ~ 6 kyr (figure 2.3b). Eccentricity in the La93 is not stretched compared to the La2003, but

shows approximately the same phase relation with slight differences in amplitude (figure 2.3c). The difference in summer insolation is also characterized by stretching of the La93 solution with occasionally differences in amplitude due to the effect of eccentricity in addition to the shifts in the position of the insolation peaks (figure 2.3d).

Assuming that these solutions are equally reliable this outcome results in an uncertainty in the astronomical age that is dependent of the astronomical frequency used for the tuning. It arrives at an ~ 11 kyr uncertainty if the climate proxy record used for tuning is dominantly obliquity controlled and calibrated to obliquity, and at a ~ 6 kyr uncertainty if the climate proxy record is dominantly precession controlled and tuned to precession. The corresponding errors may be expressed as ± 6 and ± 3 kyr (at 15 Ma), respectively. In the Mediterranean the error is rather ± 3 kyr since the sedimentary cycle patterns dominantly reflect the influence of precession. However, our assumption of equal reliability does not hold because the new solution is supposed to be more accurate due to improved initial conditions and the addition of extra parameters in the solution. The new solution is anticipated to be accurate over at least the last 20 myrs and most likely will only allow for an error of a few kyr at a maximum. However, it should be realized that this error does not take the error into account that may result from changes in the dynamical ellipticity and/or tidal dissipation.

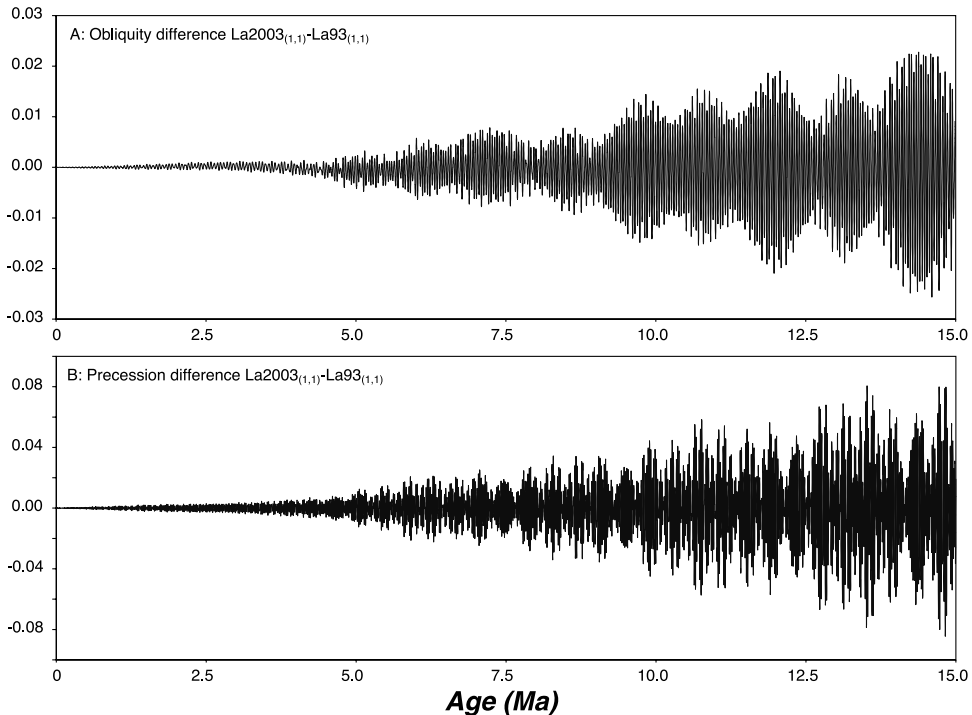
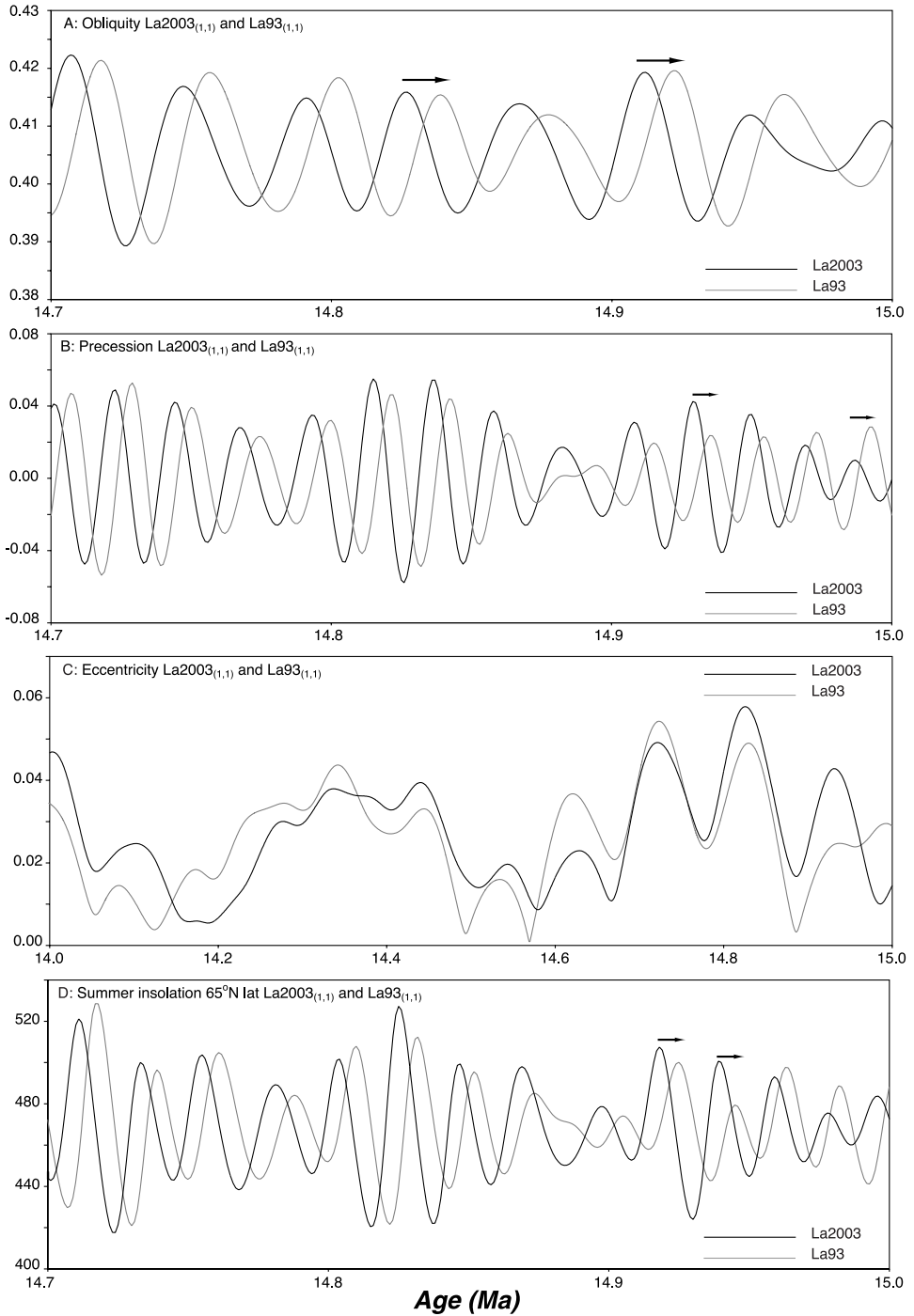


Figure 2.2a-b Difference between La2001_(1,1) and La93_(1,1) astronomical solutions. Difference between the La2001_(1,1) and La93_(1,1) astronomical solutions for obliquity (a) and precession (b) over the last 15 Ma.

CHAPTER 2



ACCURACY OF THE ASTRONOMICAL SOLUTION: $La93_{(1,1)}$ VERSUS $La93_{(1,0.5)}$

A test was carried out to estimate the error which results from changing the dynamical ellipticity and/or tidal dissipation. Lourens et al. (1996) suggested that the $La93_{(1,1)}$ solution is very accurate due to the excellent fit with all the intricate details of the sedimentary cycle patterns in the Mediterranean Plio-Pleistocene over the last 5.3 myr. However solutions with values close to the present-day values of dynamical ellipticity and tidal dissipation were not tested at that time but reveal a pattern in the 65°N latitude insolation target curve that is very similar to that of the $La93_{(1,1)}$ solution. Lourens et al. (2001) subsequently showed that an optimal fit between a high-resolution climate proxy record - the Ti/Al ratio reflecting African aridity and ranging from 2.4 to 2.9 Ma - and the insolation target curve is reached when the $La93_{(1,0.5)}$ solution is applied for tuning the paleoclimate record.

We can now estimate the possible error which may result from variations in these two parameters (dynamical ellipticity and tidal dissipation) by assuming that the most accurate solution will lie somewhere in between (1,1) and (1,0.5), or equivalently a decrease in dynamical ellipticity from 1 to 0.9997, while keeping tidal dissipation fixed at its present value. For this purpose we subtracted and plotted the values for obliquity, precession and 65°N latitude summer insolation of the $La93_{(1,1)}$ solution from the $La93_{(1,0.5)}$ solution for the last 15 myr to analyse and visually depict the consequences of a reduction of the tidal dissipation to half of its present-day value (figure 2.4a-c). Eccentricity is not influenced by dynamical ellipticity and tidal dissipation and will therefore not change. The obliquity difference follows an out-of-phase relationship around 10 Ma and again reaches almost zero values around 15 Ma (figure 2.4a). This can be explained by the fact the obliquity time series is relatively stretched in the $La93_{(1,0.5)}$ solution and contains one cycle less over the last 15 myr. This stretching of the obliquity time series is due to the reduced effect of the tidal dissipation parameter. Similarly the precession time series in $La93_{(1,0.5)}$ contains one cycle less over the last 15 myr (figure 2.4b). Since the sedimentary cycles in the Mediterranean are dominantly precession controlled the maximum uncertainty here is estimated to be in the order of 20 kyr at 15 Ma. It is anticipated that this uncertainty will eventually be eliminated by extending the approach of Lourens et al. (2001) to older time intervals, i.e. back to 15 Ma. Comparing the $La93_{(1,1)}$ with the $La93_{(1,0)}$ solution would result in an uncertainty that is twice as large (~40 kyr) but it is unlikely that such an error will be made because eccentricity, which modulates the precessional amplitude, remains unaffected by changes in dynamical ellipticity and tidal dissipation as it depends on the orbital part of the solution only.

CATEGORIES OF ASTRONOMICALLY DATED ASH LAYERS

Three different categories of astronomically dated ash layers can be distinguished. The first comprises ash layers that occur in cyclic marine sequences that have been tuned directly to astronomical target curves on the basis of characteristic cycle patterns. The tuning itself is assumed to be correct and the astronomical ages for the ash beds are considered the most reliable. This category includes the A1 ashbed from Crete, the Ancona and Respighi ashbeds in the Monte dei Corvi sections and the ash layers at Monte Gibliscemi.

Figure 2.3a-d Astronomical solutions of $La2001_{(1,1)}$ and $La93_{(1,1)}$ (previous page).

Astronomical solutions of $La2001_{(1,1)}$ and $La93_{(1,1)}$ for obliquity (a), precession (b) and the 65N latitude summer insolation (d) for the period 14.7 - 15.0 Ma and for eccentricity (c) for the period 14.0 - 15.0 Ma.

The second category includes ash layers found in cyclic marine sequences that have been astronomically dated by applying an astronomically dated integrated stratigraphic framework; this framework was constructed with the help of other sections that are more suitable for astronomical tuning. This category includes the ashbeds in the Sorbas basin in SE Spain and the important ash layers in the Melilla basin in Morocco. Consistency in the number of basic sedimentary cycles in between clear-cut planktonic foraminiferal bioevents known to be synchronous in the Mediterranean and the occurrence of characteristic sedimentary cycles indicate that these ages are reliable as well.

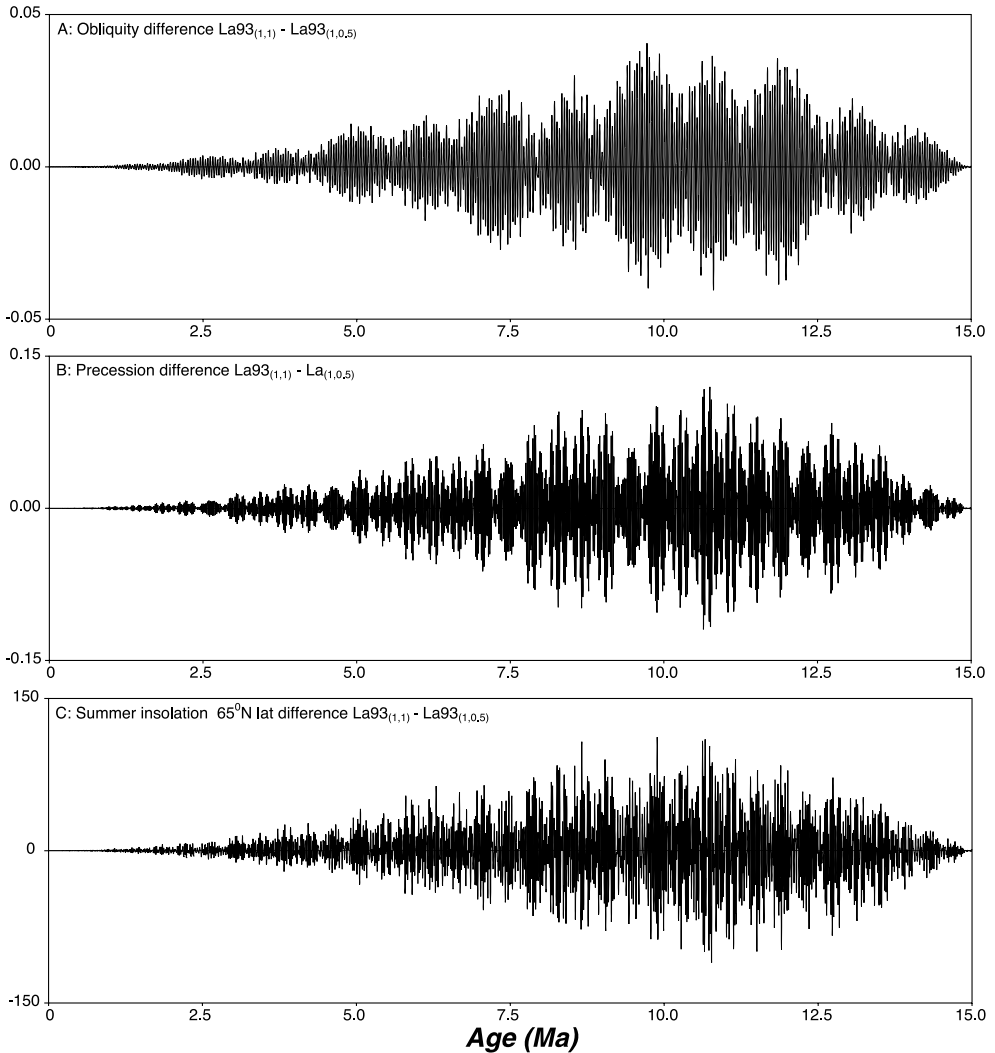


Figure 2.4a-c Difference between the $La93_{(1,1)}$ and $La93_{(1,0.5)}$ astronomical solutions. Difference between the $La93_{(1,1)}$ and $La93_{(1,0.5)}$ astronomical solutions for obliquity (a) and precession (b) and the $65^{\circ}N$ latitude summer insolation (c) over the last 15 Ma.

The third and last category includes ash layers intercalated in lacustrine sequences of the Ptolemais basin in Greece. The tuning started with applying astronomical age estimates of subchron reversal boundaries to the Ptolemais magnetostratigraphic record. The subsequent tuning to precession and insolation is not perfectly reliable because of minor differences in recognising the precession controlled basic cycles and a possible hiatus so that some uncertainties still exist. However in the critical ashbed containing intervals it seems difficult to change the tuning by more than one cycle in either direction. But since the tuning is not fully certain the astronomical ages for the basic cycles and hence ashbeds should be considered less reliable than the ages for the ashbeds in the other categories. Addition of an extra error of 20 kyr seems reasonable.

DISCUSSION AND CONCLUSIONS

The astronomical ages of ash layers used in this study are prone to several errors and uncertainties which result from 1) the accuracy of the applied astronomical solution, 2) the values of dynamical ellipticity and/or tidal dissipation incorporated in the solution, 3) the correctness of the tuning, 4) the magnitude of time lags between astronomical forcing, climate response and registration in the sedimentary archives and 5) the interpolation of sedimentation rate between calibration points. Although no exact uncertainty can be quantified for the astronomical age of the ash layers due to complexity of astronomical solutions and geological nature of (some of) the uncertainties, we conservatively estimate, that the combined uncertainties result in an (estimated) error estimate of ± 5 kyr at 5 Ma and of ± 10 -20 kyr at 15 Ma for ash layers in category 1. Hereby, we have to assume that the tuning of sedimentary cycles to the target curve is correct, but include uncertainties due to 1, 2, 4 and 5. For category 3 ash layers it is warranted to add 20 kyr to the error estimate (tuning might be diverge at maximum 1 cycle of correct tuning), whereas for second category ash layers the error will be close to that of category 1.

Summarizing errors in the astronomical ages over the last 10 myr suggests that they will be in the order of 0.1 %, assuming that the tuning itself is correct. The tuning is probably correct for the last 13 myr in view of the excellent fit between details in the Milankovitch cycle patterns in the Mediterranean (as confirmed in parallel sections) and the insolation target and if the assumed phase relations indeed are correct. For older time intervals the error will remain very small but the tuning of Ceara Rise (Shackleton et al., 2000) has to be independently confirmed.

CHAPTER 3

**$^{40}\text{Ar}/^{39}\text{Ar}$ AGES OF TEPHRAS INTERCALATED IN
ASTRONOMICAL TUNED NEOGENE SEDIMENTARY
SEQUENCES IN THE EASTERN MEDITERRANEAN.**

INTRODUCTION

$^{40}\text{Ar}/^{39}\text{Ar}$ dating is a versatile technique to determine the absolute age of a suite of K-bearing minerals while astronomical dating is based on the correlation or tuning of cyclic variations in the stratigraphic record to computed time series of orbital variations. The latter provides a completely independent method to determine the absolute age and duration of geological processes. The calibration of the standard geological time scale depends on two independent absolute dating techniques, namely astronomical tuning for the youngest Plio-Pleistocene part and radiogenic isotope dating (e.g., $^{40}\text{Ar}/^{39}\text{Ar}$ dating) for older parts of the time scale. A reliable intercalibration of these methods is urgently needed, also because the entire Neogene will rely on astronomical dating in the next version of the standard time scale (Lourens et al., 2004).

In a first attempt, Renne et al. (1994) compared $^{40}\text{Ar}/^{39}\text{Ar}$ ages of 7 geomagnetic polarity transitions over the last 3.4 Ma with astronomical ages assigned to the same polarity transitions, but in other sections. The disadvantage of this method is the required interpolation of the sedimentation rate between the stratigraphic positions of isotopic dated volcanic material to obtain the age of the reversal in the same section for 5 of the studied reversals.

Therefore, $^{40}\text{Ar}/^{39}\text{Ar}$ experiments were performed on volcanic tephra intercalated in astronomically tuned sedimentary sequences. In this way astronomical ages could directly be assigned to a tephra layer and both methods compared. Hilgen et al. (1997) reported the first $^{40}\text{Ar}/^{39}\text{Ar}$ ages of Miocene tephras from astronomically tuned marine sections on Crete and concluded that the $^{40}\text{Ar}/^{39}\text{Ar}$ ages were not significantly different from the astronomical ages. Subsequently, Steenbrink et al. (1999) published discrepancies between $^{40}\text{Ar}/^{39}\text{Ar}$ ages for a series of Pliocene tephra intercalated in the astronomically tuned sediments of the lacustrine Ptolemais basin with the $^{40}\text{Ar}/^{39}\text{Ar}$ ages being significantly younger by $\sim 3\%$. In an attempt to unravel the cause of the different outcome of these studies we decided to perform a new series of experiments. The data of these experiments on the ash layers in the lacustrine Ptolemais succession in NW Greece and in the slightly older marine succession on Crete are presented in this paper.

GEOLOGICAL SETTING

CRETE

The island of Crete represents an emerged part of the Hellenic Arc system (see figure 3.1 for location). The Alpine crystalline metamorphic basement rocks (or "pre-Neogene" rocks) of Crete are composed of highly heterogeneous tectonic nappes exposed in uplifted blocks and separated from the Neogene and Quaternary basins by normal faults. Thick series of basal Neogene clastics (mainly limestone breccias) unconformably overlie the metamorphic basement. The late middle Miocene on eastern Crete portrayed a continental borderland in the north and faulted E-W trending basins with fluvio-lacustrine sedimentation in the southern part of the island. The middle-late Miocene is marked by the breakup of the landmass and the basin bordering to the south related to extension caused by the onset of the rollback process of the Hellenic arc system (e.g., Meulenkamp et al., 1988). During the early Tortonian subsidence caused the deposition of a thick sequence of fluvatile, brackish and marine strata and during the middle to late Tortonian marine conditions became more open. Sedimentation changed from predominantly clastics (clay and marl) in the

Tortonian to carbonates during the transition period from Tortonian to Messinian. Coarse conglomeratic, non-marine and fluvio-lacustrine or lagoonal sediments were deposited during the late Messinian and evaporites occur as well in various parts of Crete. On central and eastern Crete, late Messinian and early Pliocene sediments are not present. In the early Pliocene marly limestones were deposited and at the end of the early Pliocene an overall regression resulted in the deposition of shallow marine sediments (Meulenkamp and Hilgen, 1986). During the Pleistocene Crete obtained its present shape. The ash layers studied here originate from Tortonian to Messinian deep marine sediments located on the eastern part of Crete and the island of Gavdos, immediately south of Crete.

Widespread volcanism in the Aegean has continued from the Oligocene to the present. Two main phases of volcanic activity can be recognized. From Oligocene to middle Miocene times the first phase developed in the North Aegean area and successively shifted southward resulting in a progressive enrichment in potassium (Fytikas et al., 1984). This phase of volcanism consisted mainly of calc-alkaline (andesites and dacites) and shoshonitic lavas and pyroclastics with minor occurrences of acidic (rhyolites) and basic (basaltic andesites) rocks. The second phase started in the Pliocene and is still building the active South Aegean volcanic arc. This phase mainly produced andesites with minor basalt and rhyolites, which chemical properties are characteristic for calc-alkaline series erupted on thin continental margins. Between these two phases volcanism of variable chemical composition occurred to a limited extent, essentially in zones of tensional strain along the borders of the Aegean microplate (Fytikas et al., 1984). The Cretan tephrae studied here are most likely the result of the volcanism in the period between the two main phases.

However, volcanic ash layers might originate from more distant volcanic centers than the ones described above. Walker (1971) described a relation between particle size and distance from the source and concluded that for the most powerful eruptions, particles greater than 50 μm are not typically found more than 1000 km from the source volcano. This implies that particles of about 300 μm are not likely to be found over more than several hundreds of kilometers from their source (see also Sparks et al., 1992). Clearly, wind directions play an additional role in the distribution of tephrae. Winds blew ash not only from the Aegean Arc, but also from the Campanian province of Italy into the deep basins of the eastern Mediterranean (Keller et al., 1978; Cramp et al., 1989). This might also have occurred in the late Miocene on for example Crete. However the grain size of the sanidine suggests that the Campanian province probably was too far away (~ 1000 km) to be the source of the Cretan ash layers.

PTOLEMAIS

The Florina-Vegora-Ptolemais basin is part of a 250 km long NNW-SSE trending graben system (see also figure 7.1). The 100 km long and 15-20 km wide basin is filled with Neogene to Quaternary sediments. The basin was formed in response to a late Miocene NE-SW extension. NW-SW extension during the Pleistocene resulted in the development of a sequence of sub-basins. The pre-Neogene rocks of the basin and surrounding area consist of Paleozoic metamorphic rocks (the crystalline basement), Mesozoic carbonate cover and ophiolites (Pavlidis and Mountrakis, 1987). The basin fill is divided into three lithostratigraphic units: the Lower Formation, Ptolemais Formation and Upper Formation. All units are of continental origin and mainly deposited under lacustrine conditions. The Lower formation unconformably overlies the basement and consists of Miocene to lowermost Pliocene sediments of conglomerates passing upwards into

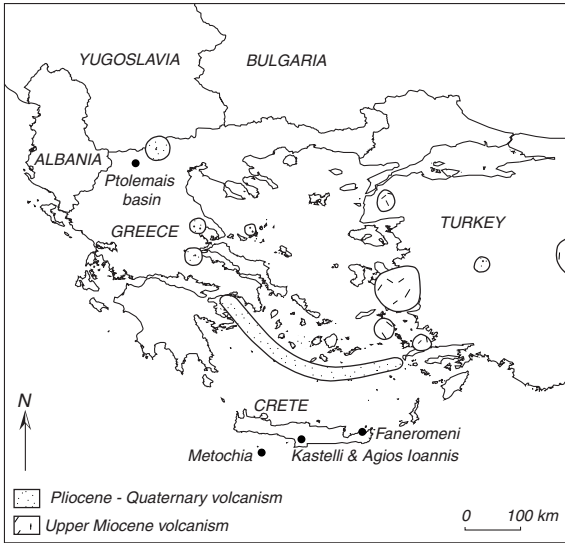


Figure 3.1: Neogene volcanism in the Aegean region.

Locations of the studied sections. The A1 ash is found on several locations on Crete. In this thesis only the A1 obtained in Faneromeni, Kastelli and Agios Ioannis is dated. The distribution of Neogene volcanism in this area is highlighted indicating possible sources of the studied volcanic ash layers (based on Fytikas et al., 1984).

"calc-alkaline" group (mainly low-K trachyte) (Kolios et al., 1980). K/Ar experiments on samples of the Voras volcanic rocks showed that the "shoshonitic" volcanism took place from 2.5 to 1.8 Ma and the "calc-alkaline" volcanism from 5.0 to 4.0 Ma (Kolios et al., 1980). Bellon et al. (1979) obtained four K/Ar ages between 4.0 to 2.65 Ma for samples from the area south of Aridea (north of Edessa). These samples showed the same geochemical and petrological characteristics as the "shoshonitic" series of the Voras Mountains, suggesting that the volcanism spanned the Pliocene. Chemical data revealed that the Voras complex represents several distinct magma types, all enriched in potassium. The Voras mountains volcanic complex is therefore a good candidate for the source of the Ptolemais tephras considering their location, age and phenocryst composition. However, no chemical and/or petrographic work is performed to confirm this, being outside the scope of this thesis.

ASTRONOMICAL TIME CONTROL FOR VOLCANIC ASH LAYERS

The astrochronological tuning for the volcanic ash layers on Crete is described in detail by Krijgsman et al. (1995) and Hilgen et al. (1995, 1997). The astronomical ages for the volcanic ash layers in the Ptolemais basin are based on Van Vugt et al. (1998) and Steenbrink et al. (1999). A summary of the astrochronological tuning is given here.

marl, sandy marl, sand, clay and lignite. The overlying Ptolemais Formation with a thickness of ~110 m has been subdivided in the Kyrio, Theodoxus and Notio members consisting of alternations of lignite and lacustrine marl. The Upper Formation unconformably overlies the Ptolemais Formation and consists of terrestrial and fluvio-terrestrial conglomerates, lateral fans and alluvial deposits of Pleistocene age (Pavlidis and Mountrakis, 1987). The volcanic ash layers studied here are intercalated in the lignite and marl beds of the Ptolemais Formation.

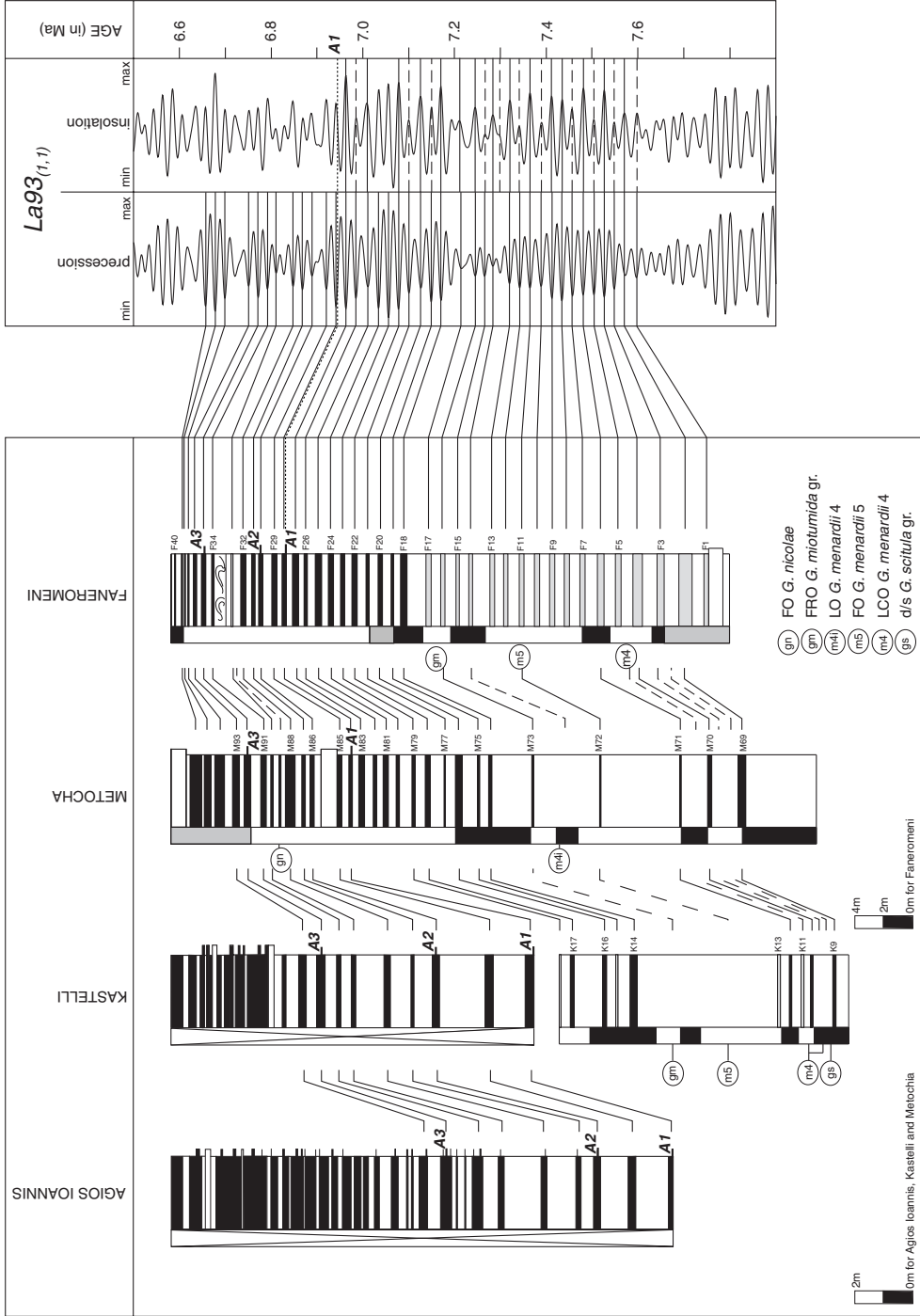
Pliocene volcanic rocks are found directly northeast of the Ptolemais basin in the Voras Mountains and near Aridea and Edessa. The volcanic rocks directly NE of Edessa predominantly consist of volcanic tuffs of latite-andesite, latite or trachyte composition, but their age is not determined directly (Marakis and Sideris, 1973). The Voras volcanic rocks consist predominantly of a "shoshonitic" group (mainly trachyte) and a

CRETE

The studied sections on Crete consist of cyclic alternations of whitish-colored, indurated, carbonate rich marls and grey carbonate poor marls (lower part Faneromeni section) or of homogeneous marls and sapropels; the latter are intercalated in or substitute the grey carbonate poor beds (Faneromeni upper part, Kastelli, Agios Ioannis and Metochia). The upper part of the Metochia section is characterized by cyclically bedded diatomites. Figure 3.2 shows the astronomical tuning to the 65°N hemisphere summer insolation curve (Laskar et al., 1993a), where each sapropel / grey marl is numbered as in Hilgen et al. (1995). Because the cycle patterns for these Miocene sections are similar to the patterns in the Mediterranean Pliocene (e.g., Hilgen et al., 1991a), the same phase relations were used for the tuning, i.e. individual sapropels correspond to precession minima, small scale sapropel clusters (consisting of 3 or 4 sapropels) correspond to 100 kyr eccentricity maxima and large scale sapropel clusters (containing 3 or 4 small scale clusters) correspond to 400 kyr eccentricity maxima. The youngest polarity reversal identified in the sections (C3An.2n (o)) with an age of 6.567 Ma according to the GPTS of Cande and Kent (1995) was used as a first order calibration point. For the astronomical tuning of the sections, large scale sapropel clusters were subsequently correlated to 400 kyr eccentricity maxima and small scale clusters to 100 kyr eccentricity maxima. The atypical large scale cluster (which includes the cycles K9-K13 and M69-M73 in figure 3.2) correspond well with the 400 kyr eccentricity maximum that lack the usual pronounced expression of the 100 kyr cycle (Hilgen et al., 1995). Therefore, alternative calibrations would need a shift in age of 400 kyr younger or older. Subsequent tuning of the individual sapropels to insolation maxima confirms the tuning because of the good to excellent fit between characteristic cycle patterns and patterns in the insolation curve. F18-F22 and M74-M78 show thick-thin-thick alternations that correspond to successive high-low-high amplitudes in insolation maxima. F23-F24 / M79-M80 have the same thickness or are slightly thinner than the preceding sapropel F22 / M78 as expected from the insolation curve, but F25 / M81 is thicker than expected. This small discrepancy in the tuning may disappear when an improved astronomical solution will become available. The tuning of Agios Ioannis and Kastelli is less straightforward, but was achieved by detailed cyclostratigraphic and biostratigraphic correlations to the other sections (Hilgen et al., 1997).

PTOLEMAIS

The Pliocene volcanic ash layers are intercalated in the lacustrine Ptolemais Formation, which consists of bipartite cycles of alternating gray or beige colored marls with lignite (marl-lignite couplets). The tuning of the sedimentary cycles in the Ptolemais basin to the 65°N hemisphere summer insolation curve with present day values for both dynamical ellipticity of the Earth and tidal dissipation (Laskar et al., 1993a) is described in detail by Van Vugt et al. (1998) and Steenbrink et al. (1999) (figure 3.3). Due to the lack of a clear expression of eccentricity, e.g. small and large scale clusters of precessionally forced cycles, the magnetostratigraphy of the Ptolemais composite was calibrated to the astronomical polarity time scale (APTS) of Lourens et al. (1996) for a first order age control. Ages of the corresponding reversals in the APTS served as a starting point for the tuning of the lignite-marl cycles as presented in figure 3.3. Further the phase relation between lignite or the marl and the insolation curve was not clear. Van Vugt et al. (1998) tried two possible options with lignites corresponding to insolation minima and to insolation maxima, where the first option appeared to be more consistent and resulted in less discrepancies in pattern fits between the geological record and the target curve.



The tuning started with the lignite/marl cycles from the Notio member (including the ash layers SL3L, SR3M, SR5L). Since cycle N1 contained the first lignite bed above the atypical Theodoxus member, this lignite was correlated to the first insolation minimum with a relative high amplitude following a series of low amplitude variations related to the 400 kyr eccentricity minimum around 4.4 Ma (figure 3.3). This tuning is supported by relatively thick lignites or dark clays in cycles N11, N12, N13, N16 and N21 which correspond to relatively high amplitude insolation minima (i-code cycles after Lourens et al., 1996; 399, 397, 395, 389 and 379 in figure 3.3) and by the thin clay/lignite layers in cycles N10, N14, N15, N17 and N19 which fit excellently with lower amplitude insolation minima. Other characteristics supporting the tuning are the relatively dark marl of N14 and thin marl of N18 which correspond to low amplitude insolation maxima, and the more than average thickness of the marl of cycle N5 which corresponds to an insolation maximum with a relatively long duration (Van Vugt et al., 1998). The only inconsistency is the thin dark layer (lignite phase of N10), which corresponds to a low-amplitude minimum with a long duration.

The tuning was continued with the lower 18 cycles of the Kyrio member (including the ash layers SL5L, SL7L and SL11L). Up to cycle K14 the cycles are fairly regularly developed apart from K1 and K2. This pattern fitted with the insolation pattern near the eccentricity minimum around 5.22 Ma and therefore cycles K1 and K 2 were correlated to i-cycle 499/498 and 497/496 and the overlying cycles to the insolation peaks of 495-472. The only significant inconsistency is the relatively thin and less pronounced lignite of cycle K9 that corresponds to the highest amplitude insolation minimum in this interval (Van Vugt et al., 1998).

Van Vugt et al. (1998) mentioned field evidence for a hiatus between cycle K18 and K19, where a shallow scouring surface pointed to erosion while the thin paleosol on the top the surface was interpreted as a period of non-deposition. Therefore, tuning of the cycles K19 to T6 is less straightforward and resulted in two options, one supporting a hiatus of three cycles and one without a hiatus. However, this uncertainty is assumed to affect the ages of the ash layers SLM2T and SLM3T only.

In summary, the tuning on Crete was straightforward, because climate changes related to the orbital parameters were recorded excellently in these marine sediments. Alternative correlations to the target curve showed less consistent patterns and therefore the astronomical calibration is assumed to be correct (Hilgen et al., 1995). Errors in the astronomical ages for the volcanic ash layers can therefore only be attributed to errors in the astronomical solution itself, uncertainty about the time lag between astronomically forced climate response and registration in the stratigraphic record and the assumption of a constant sedimentation rate between two astronomically calibrated points (i.e., sapropel midpoints). Therefore we assigned an uncertainty of 5 kyr to the astronomical ages of the Cretan tephra (see also chapter 2).

The uncertainties concerning the tuning of the Ptolemais composite section have been discussed already in Steenbrink et al. (1999). Because of the lack of a clear expression of larger eccentricity related cycles in

Figure 3.2: Astronomical tuning of studied sections on Crete (previous page).

Astronomical tuning of the Agios Ioannis, Kastelli, Metochia and Faneromeni sections to the 65°N summer insolation curve of Laskar et al. (1993a) with present day values for dynamical ellipticity and tidal dissipation (after Hilgen et al., 1995, 1997).

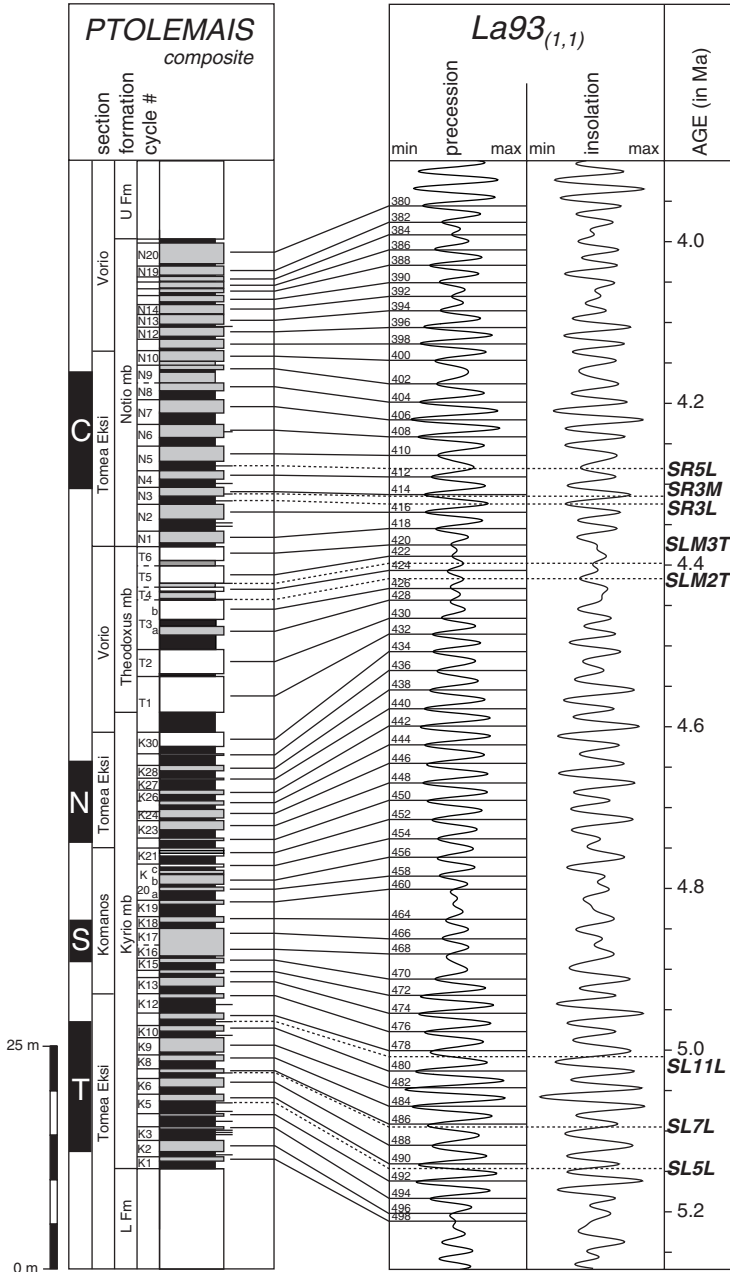


Figure 3.3: Astronomical tuning of the Ptolemais section.

Astronomical tuning of the Ptolemais section to the 65°N summer insolation curve of Laskar et al. (1993a) with present day values for dynamical ellipticity and tidal dissipation showing the “alternative” tuning of Van Vugt et al. (1998). The two different tuning options as described in Van Vugt et al. (1998) slightly change the astronomical ages of the volcanic ash layers SLM2T and SLM3T.

Ptolemais, the tuning in Ptolemais is dependent upon a correct magnetostratigraphy, although some of the detailed cycle patterns confirm the tuning of Van Vugt et al. (1998). The astronomical age for the volcanic ash layers would become older, if the magnetic signal in the Ptolemais section is affected by delayed acquisition (Steenbrink et al., 1999) and the discrepancy between $^{40}\text{Ar}/^{39}\text{Ar}$ and astronomical ages would increase. On the other hand, astronomical ages might be younger, if the effect of delayed acquisition has not been completely eliminated in the Rossello composite and if the magnetostratigraphy of the Ptolemais composite is not affected by delayed acquisition. However, this seems not likely, because in that case the pattern fit described above would no longer hold (Van Vugt et al., 1998). On basis of these uncertainties we assigned an uncertainty of ~ 25 kyr to the astronomical ages of the ash layers in Ptolemais (category 3 ash layer; see chapter 2).

MATERIALS AND METHODS

MATERIAL

On Crete and in the Ptolemais basin the volcanic ash levels were collected at several localities. Exact locations of the sampled sections are given in Hilgen et al. (1997) for the Cretan ashes and in Steenbrink et al. (1999) for the Ptolemais ashes. GPS coordinates are given in the appendix. Most of the ash layers contain the K-rich minerals biotite and sanidine. On Crete A3 and A1 showed mixed plagioclase / sanidine populations and A2 contained only plagioclase. In Ptolemais all the dated ash layers contained a plagioclase / sanidine population, but it was relatively easy to separate a pure sanidine fraction by heavy liquid separation and hand-picking. The biotite crystals in the Ptolemais ash layers have been partially altered to chlorite apart from the biotite of ash layer SR3M. The bulk samples were crushed (depending on their solidity), washed and sieved. The maximum grain size fraction of 400-500 μm or when not available smaller grain size fractions of 250-400 μm and/or 125-250 μm were used for standard magnetic and heavy liquid separations of micas and sanidine. Subsequently, all samples were handpicked and cleaned in an ultrasonic bath with distilled water and/or 6N HNO_3 and/or a 1:5 HF solution.

$^{40}\text{Ar}/^{39}\text{Ar}$ ANALYTICAL PROCEDURE

The samples were wrapped in Al-foil and loaded in a 6 mm internal diameter quartz vials. Two different standards consisting of Fish Canyon Tuff sanidine (FCT obtained from H. Baadsgaard for irradiation VU32, FC-2 obtained from P.R. Renne for all other irradiations) and Taylor Creek Rhyolite sanidine (85G003 for VU32 and VU37, TCR2a a new split obtained from M. Pringle for VU37 and VU41) were wrapped in Cu-foil and loaded at top and bottom positions in the vial and between each set of 3-5 samples. Samples were irradiated in several batches (VU32, VU37 and VU41) in the Oregon State University TRIGA reactor in the cadmium shielded CLICIT facility for 7 hours for all irradiations. After irradiation samples and standards were loaded in 2 mm diameter holes of a copper planchet and placed in an ultra-high vacuum extraction line. Samples and standards were stepwise heated or directly fused and gas was analyzed with a Mass Analyzer Products LTD 215-50 noble gas mass spectrometer (for details see chapter 2).

Multiple grain and in a very few cases single grains of sanidine of standards and samples were preheated using a defocused beam of a 24W Ar-ion laser with output set to 2W (samples did not glow and gas was

pumped away) to remove undesirable atmospheric argon. After this preheating step the samples and standards were analyzed by total fusion. Experiments were replicated 5-10 times for total fusion analyses. Multiple grain fractions of biotite samples were measured by stepwise heating or fusion (preheating step with 0.2W defocused laser beam). Most of the samples were included in several irradiations to check the reproducibility of the results. Beam intensities were measured in a peak-jumping mode over the 40-36 mass range on a secondary electron multiplier. For data collection the mass spectrometer is operated with a modified version of standard MAP software (i.e., adjustable integration cycles and valve control). System blanks were measured every 3 steps. The total system blanks were in the range of 5.0×10^{-14} moles for mass 40, 4.0×10^{-15} moles for mass 39, 2.6×10^{-15} moles for mass 38, 2.6×10^{-14} moles for mass 37 and 2.0×10^{-15} moles for mass 36. Mass discrimination (1.002-1.0100 per atomic mass unit) was monitored by frequent analysis of $^{40}\text{Ar}/^{38}\text{Ar}$ reference gas or $^{40}\text{Ar}/^{36}\text{Ar}$ air pipette aliquots (see chapter 1).

AGE CALCULATION

Regressions of the individual isotopes, blank corrections, corrections for nuclear interference reactions and mass discrimination corrections have been performed with the in-house developed ArArCalc (v2.20c) software (Koppers, 2002). The average blank value of blank analyses before and after measurement of an unknown is commonly applied as blank correction for all isotopes. When the contribution of different parameters to the variance ($= \sigma^2$) in the $^{40}\text{Ar}^*/^{39}\text{Ar}_K$ ratio of an individual analysis is assessed, it appeared that ^{36}Ar blank values are contributing significantly to the variance (figure 3.4). Therefore, ^{36}Ar blank corrections were studied in more detail and depending on their (daily) behavior occasionally a linear or polynomial fit of blank values over a certain (daily) period was applied for this isotope.

The analytical data are reported as weighted mean $^{40}\text{Ar}/^{39}\text{Ar}$ (or F) ratios and standard errors weighted with the inverse of the variance. The data of replicate experiments from one irradiation package are combined, although this not necessarily implies that all samples were analyzed within a single run. MSWD values >1 indicate heterogeneity in the sample or underestimation of analytical errors. Therefore, when MSWD values are >1 the analytical uncertainty in the $^{40}\text{Ar}/^{39}\text{Ar}$ ratio of the sample is multiplied by $\sqrt{\text{MSWD}}$. When combining data with different J-values (i.e., from different irradiation positions) the F-ratios of the unknowns are divided by the F-ratios of the standard (TCR in VU32, VU37 and older irradiations) and combined to a weighted mean intercalibration factor ($R_{\text{ash}/\text{TC}}$) with a standard error of the mean. For irradiation VU41 with FCT as main standard $R_{\text{ash}/\text{TC}} = R_{\text{ash}/\text{FC}} \times R_{\text{FC}/\text{TC}}$ is used to establish the weighted mean intercalibration factor where the intercalibration factor $R_{\text{FC}/\text{TC}}$ is 0.9889 ± 0.0010 of Renne et al. (1998; confirmed in chapter 1). This approach is slightly different from that used in the ArArCalc software where in the procedure of combining experiments with different J values (i.e., from different positions and/or irradiations) all data are normalized to the first J value in the data file introducing an extra normalization error (Koppers, 2002), which we prefer to avoid.

Ages and uncertainties have been calculated according to age equations 1.11 / 1.12 (chapter 1) using the consensus decay constants of Steiger and Jäger (1977) and an absolute age of 28.34 ± 0.16 Ma (or ± 0.28 Ma when decay constant errors are included) for TCR (Renne et al., 1998). Uncertainties are reported at four levels (see discussion in chapter 1, page 48). The first level includes the analytical uncertainty in the sample (table 3.1, I), the second adds the analytical

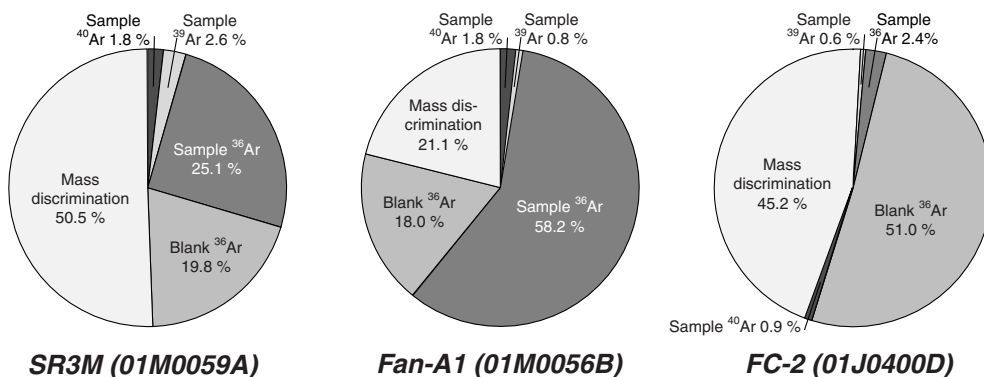


Figure 3.4: Contribution of analytical parameters to variance in $^{40}\text{Ar}^*/^{39}\text{Ar}_k$ ratio.

Contribution of analytical parameters to the variance for arbitrary, representative analyses (one sample of Ptolemais, one of Crete and one standard analysis). Details of derivation of the equations are given in chapter 1.

uncertainty in the standard (table 3.1, II), the third also includes the uncertainty in the absolute age of the standard (table 3.1, III) and the fourth level adds the uncertainty in the decay constants as reported in Steiger and Jäger (1977; σ_λ is $0.01 \times 10^{-10} \text{ yr}^{-1}$) (table 3.1, IV). All errors are quoted at the 1σ significance level.

Further, age and most realistic error estimates are made following an improved procedure based on Min et al. (2000) (see discussion chapter 1, equation 1.14, page 48). Intercalibration factors between FCT, TCR and GA1550 as well as K content of the primary standard GA1550 were used from Renne et al. (1998), the radiogenic ^{40}Ar content of primary standard GA1550 is taken from McDougall and Roksandic (1974). Avogadro's number is obtained from Cohen and Taylor (1987), the atomic weight of K and the atomic abundance from Garner et al. (1975) and the activities from Beckinsale and Gale (1969), where the uncertainty in the A_e activity is doubled based on the discussion in Min et al. (2000). The background dataset (intensities of all isotopes for individual experiments) is given in the appendix.

RESULTS

In table 3.1 the analytical data are given for all experiments (extended data tables are given in the appendix). When the "full error" estimation σ was applied (last column in table 3.1), it appeared that for all analyses the variance ($= \sigma^2$) is dominated by the uncertainty in the activity of the ^{40}K decay to ^{40}Ar ($\sim 70\%$) and the uncertainty in the radiogenic ^{40}Ar content in the primary standard ($\sim 15\%$). Figures 3.5 and 3.6 show $^{40}\text{Ar}/^{39}\text{Ar}$ age probability distributions, where the vertical dashed line represents the astronomical age for each volcanic ash layer and figure 3.5 shows incremental heating spectra for the biotite analyses. The $^{40}\text{Ar}/^{39}\text{Ar}$ data of the different ash layers will be discussed in more detail. Normal and inverse isochrons are shown in the online appendix for all data.

Identity	F_{unknown}	σ_{unknown}	N	MSWD	K/Ca	F_{TC}	σ_{TC}	Apparent $^{40}\text{Ar}/^{39}\text{Ar}$ age and error (Ma)										
								Age	I	II	III	IV	Equation 1.14					
SR5L																	4.280	
VU37 C53	1.4289	0.0012	5	0.31	49.9	9.7127	0.0230	4.197	0.004	0.011	0.026	0.044					4.196 ± 0.057	
SR3M																		4.318
VU32 C21	1.3734	0.0022	5	1.50	54.9	9.1945	0.0267	4.261	0.007	0.014	0.028	0.045					4.260 ± 0.059	
VU32 C22	1.3784	0.0018	5	1.00	33.7	9.2428	0.0268	4.255	0.006	0.014	0.028	0.045					4.253 ± 0.059	
VU37 C27	1.3325	0.0022	3	0.09	37.1	8.9654	0.0224	4.240	0.007	0.013	0.027	0.045					4.239 ± 0.058	
VU37 C30	1.3460	0.0016	3	0.14	27.7	9.0370	0.0226	4.249	0.005	0.012	0.027	0.045					4.248 ± 0.058	
VU37 C31	1.3414	0.0020	3	0.32	28.5	9.0629	0.0227	4.223	0.006	0.012	0.027	0.044					4.221 ± 0.058	
VU37 C32	1.3509	0.0015	3	0.48	40.2	9.0889	0.0227	4.241	0.005	0.012	0.027	0.044					4.239 ± 0.058	
VU37 C34	1.3593	0.0021	3	0.25	42.7	9.1414	0.0229	4.242	0.007	0.012	0.027	0.045					4.241 ± 0.058	
VU37 C44	1.3961	0.0018	3	0.31	34.7	9.3964	0.0216	4.239	0.005	0.011	0.027	0.044					4.238 ± 0.058	
VU37 C45	1.4036	0.0018	3	0.94	35.3	9.4300	0.0226	4.247	0.006	0.012	0.027	0.044					4.245 ± 0.058	
VU37 C16	1.3076	0.0034	2 (3)	0.01	55.7	8.7426	0.0227	4.267	0.011	0.016	0.029	0.046					4.266 ± 0.059	
VU37 C17	1.3064	0.0017	4 (1)	0.32	52.7	8.7620	0.0228	4.254	0.006	0.012	0.027	0.045					4.252 ± 0.058	
SR3L																		4.324
VU32 C24	1.4058	0.0040	5	4.40	50.0	9.3828	0.0264	4.275	0.012	0.017	0.030	0.046					4.273 ± 0.060	
VU32 C29	1.4440	0.0033	5	2.96	22.0	9.6204	0.0258	4.282	0.010	0.015	0.029	0.046					4.281 ± 0.059	
VU37 C13	1.2845	0.0022	5	0.55	69.1	8.6914	0.0232	4.216	0.007	0.013	0.027	0.045					4.215 ± 0.058	
VU37 C14	1.2897	0.0023	5	0.07	60.7	8.7078	0.0231	4.226	0.007	0.013	0.028	0.045					4.224 ± 0.058	
VU37 C26	1.3258	0.0015	5 (1)	0.03	11.9	8.9431	0.0228	4.229	0.005	0.012	0.027	0.044					4.227 ± 0.058	
SLM3T																		4.387
VU32 C25	1.4078	0.0025	4 (1)	0.21	41.6	9.4300	0.0264	4.259	0.008	0.014	0.028	0.045					4.258 ± 0.059	
VU37 C18	1.3240	0.0013	5	0.88	55.3	8.7814	0.0228	4.302	0.004	0.012	0.027	0.045					4.300 ± 0.059	
VU37 C22	1.3387	0.0018	5	0.15	64.3	8.8600	0.0230	4.311	0.006	0.013	0.028	0.045					4.309 ± 0.059	
VU37 C35	1.3843	0.0023	3	0.70	35.4	9.1679	0.0229	4.308	0.007	0.013	0.028	0.045					4.306 ± 0.059	
VU37 C36	1.3824	0.0021	2 (1)	0.01	70.6	9.1998	0.0230	4.287	0.007	0.013	0.027	0.045					4.286 ± 0.059	
VU37 C3 ^{a,b}	1.3097	0.0029	5 (2)	0.46	12.3	8.5656	0.0249	4.362	0.010	0.016	0.029	0.047					4.361 ± 0.061	
VU32 C3 ^b	1.3210	0.0058	4 (1)	1.29	15.7	8.6095	0.0181	4.377	0.019	0.021	0.033	0.049					4.376 ± 0.062	
SLM2T																		4.408
VU32 C17	1.3693	0.0015	5	0.97	50.1	9.0249	0.0266	4.329	0.005	0.014	0.028	0.046					4.327 ± 0.060	
VU32 C16	1.3639	0.0022	3 (1)	1.21	43.1	8.9790	0.0265	4.334	0.007	0.015	0.029	0.046					4.332 ± 0.060	
VU37 C49	1.4401	0.0018	3	0.21	45.9	9.5745	0.0230	4.291	0.005	0.012	0.027	0.045					4.290 ± 0.059	
VU37 C52	1.4571	0.0022	2 (1)	1.25	35.6	9.6774	0.0230	4.296	0.006	0.012	0.027	0.045					4.294 ± 0.059	
VU37 C57	1.4892	0.0018	5	0.10	33.3	9.8776	0.0230	4.301	0.005	0.011	0.027	0.045					4.300 ± 0.059	
SL11L																		5.015
VU37 C12	1.5129	0.0024	6 (1)	0.58	36.4	8.6756	0.0234	4.974	0.008	0.016	0.032	0.053					4.973 ± 0.069	
SL7L																		5.099
VU37 C9 ^c	1.4963	0.0040	4 (3)	0.66	6.0	8.6283	0.0190	4.947	0.013	0.019	0.034	0.053					4.945 ± 0.069	
VU37 C9 ^c	1.5215	0.0065	3 (4)	2.85	4.9	8.6283	0.0190	5.030	0.021	0.025	0.038	0.057					5.028 ± 0.072	

Identity	F _{unknown}	σ _{unknown}	N	MSWD	K/Ca	F _{TC}	σ _{TC}	Apparent ⁴⁰ Ar/ ³⁹ Ar age and error (Ma)															
								Age	I	II	III	IV	Equation 1.14										
SLSL																							
VU37 C7 ^c	1.5637	0.0050	4 (1)	1.55	4.0	8.6095	0.0189	5.181	0.017	0.022	0.037	0.057	5.146	5.179 ± 0.073									
VU37 C8 ^c	1.5399	0.0027	5	0.26	12.7	8.6189	0.0190	5.096	0.009	0.014	0.032	0.053		5.094 ± 0.070									
Crete A3																							
VU37 C93 Fan	2.1197	0.0026	3 (2)	0.10	42.5	8.7523	0.0236	6.905	0.009	0.020	0.044	0.073	6.771	6.902 ± 0.095									
VU37-C92 Al	2.1373	0.0025	9	2.46	5.3	8.7282	0.0236	6.981	0.008	0.020	0.045	0.073		6.979 ± 0.096									
VU37 C86 Kast ^c	2.0772	0.1255	1 (2)	-	0.3	8.6048	0.0241	6.882	0.415	0.415	0.417	0.421		6.880 ± 0.426									
VU41 B20 Met ^c	2.0099	0.2693	(2)	11.25	0.1	8.4372	0.0125	6.792	0.908	0.908	0.909	0.911		6.789 ± 0.913									
Crete A2																							
VU37 C84 Fan ^c	1.9217	0.0523	4	0.67	<0.1	8.5862	0.0249	6.382	0.173	0.174	0.178	0.186	6.887	6.379 ± 0.194									
VU37 C85 Fan ^c	2.1550	0.0384	3	0.91	<0.1	8.5955	0.0249	7.147	0.127	0.129	0.135	0.148		7.145 ± 0.161									
Crete A1																							
VU32-C19 Fan	2.1923	0.0026	10	0.27	43.3	9.1046	0.0264	6.865	0.008	0.021	0.045	0.073	6.941	6.862 ± 0.095									
VU32-C20 Fan	2.2127	0.0030	5	0.96	49.9	9.1467	0.0265	6.897	0.009	0.022	0.045	0.073		6.894 ± 0.096									
VU37-C39 Fan	2.2398	0.0031	3	0.03	30.5	9.2644	0.0232	6.893	0.009	0.020	0.044	0.072		6.890 ± 0.095									
VU37-C40 Fan	2.2447	0.0041	3	0.27	22.6	9.3080	0.0233	6.875	0.012	0.021	0.044	0.073		6.873 ± 0.095									
VU37-C41 Fan	2.2552	0.0073	1 (2)	-	25.0	9.3189	0.0233	6.899	0.022	0.028	0.048	0.075		6.897 ± 0.097									
VU37-C43 Fan	2.2662	0.0035	3	0.28	26.4	9.3686	0.0234	6.896	0.011	0.020	0.044	0.073		6.894 ± 0.095									
VU37-C97 Fan	2.1456	0.0018	8 (2)	1.33	26.4	8.8749	0.0240	6.892	0.006	0.019	0.044	0.072		6.890 ± 0.095									
VU41 B5 Fan	2.0158	0.0035	7	0.31	50.2	8.3087	0.0132	6.917	0.012	0.016	0.042	0.072		6.914 ± 0.095									
VU37-C89 Kast	2.0978	0.0014	12 (2)	1.05	46.6	8.6756	0.0234	6.894	0.005	0.019	0.044	0.072		6.891 ± 0.095									
VU37-C91 Kast	2.0999	0.0035	3 (2)	0.42	31.5	8.7042	0.0235	6.887	0.011	0.022	0.045	0.073		6.876 ± 0.095									
VU37-C96 Kast	2.1368	0.0021	6	0.45	43.2	8.8452	0.0239	6.887	0.007	0.020	0.044	0.072		6.885 ± 0.095									
VU37-C87 Al	2.0921	0.0019	9 (1)	0.41	51.4	8.6471	0.0233	6.898	0.006	0.020	0.044	0.072		6.895 ± 0.095									
VU37-C88 Al	2.0977	0.0018	11 (2)	1.60	39.8	8.6613	0.0234	6.905	0.006	0.020	0.044	0.072		6.902 ± 0.095									
VU37 C95 Al	2.1434	0.0026	5	0.94	29.2	8.8255	0.0238	6.924	0.008	0.020	0.044	0.073		6.921 ± 0.096									
VU41 B19 Met	2.0189	0.0032	9 (1)	0.50	53.2	8.3349	0.0124	6.905	0.011	0.015	0.042	0.071		6.903 ± 0.094									
VU32 C2 ^b	2.1005	0.0062	5	0.89	35.6	8.5908	0.0292	6.970	0.020	0.031	0.050	0.077		6.968 ± 0.098									
VU32 C2 ^{a, b}	2.6429	0.1283	10	940	9.0	8.5908	0.0292	8.766	0.424	0.426	0.428	0.435		8.763 ± 0.441									
VU41 B40 Fan ^{a, b}	2.1274	0.0055	8 (4)	0.48	22.2	8.7015	0.0121	6.970	0.018	0.020	0.044	0.073		6.967 ± 0.096									

^{a)} Incremental heating experiment ^{b)} Experiment on biotite ^{c)} Experiment on a sandline / plagioclase mixture or plagioclase

Table 3.1: ⁴⁰Ar/³⁹Ar data of Ptolemais and Cretean tephra with different error propagation methods.

⁴⁰Ar/³⁹Ar data obtained for the Ptolemais and Cretean tephtras. Astronomical ages for these tephtras are also given. All ages are reported relative to TCR of 28.34 Ma and the Steiger and Jäger (1977) consensus decay constants are used (5.543 ± 0.01 × 10⁻¹⁰ yr⁻¹). 1σ errors are reported including the analytical uncertainty in the sample (I), the analytical uncertainty in sample and standard (II), adding the uncertainty of ⁴⁰Ar/³⁹Ar of primary standard age (III) and adding the decay constant uncertainty as well (IV). Further, the age and uncertainty were calculated using equation 1.14 (see text for discussion). Astronomical ages for these tephtras are given in **bold italic**.

CRETE A2 AND A3

From the K/Ca ratios of the A2 and A3 ash layers on Crete (table 3.1), it appeared that we were not able to separate pure sanidine mineral separates for these ash layers. Petrographically, the A2 ash contains only plagioclase, resulting in very low ^{40}Ar intensities, little higher than the blank values and low amounts of radiogenic ^{40}Ar (37-87%), such that no reliable isochrons can be defined and the MSWD values are >1 , indicating heterogeneity. Therefore, the data obtained from ash layer A2 are discarded and not further discussed.

The K/Ca ratios of the A3 mineral separates are high (VU37-C93), intermediate (VU37-C92) or low (VU37-C86, VU41-B20) suggesting either a pure sanidine split, a mixed sanidine/plagioclase population or a plagioclase separate (table 3.1). For VU37-C92 MSWD values are >1 and isochron intercepts differ from 295.5 (inverse isochron 254.6 ± 12.0). For VU37-C93 2 of 5 measurements had to be excluded as outliers to produce an acceptable MSWD. VU37-C86 and VU41-B20 (both plagioclase) show huge uncertainties due to low amounts of K and therefore very low ^{40}Ar intensities, slightly higher than the blanks. Further, $^{40}\text{Ar}^*$ contents are low (34-60%) and isochrons show deviations from the atmospheric $^{40}\text{Ar}/^{36}\text{Ar}$ ratio of 295.5. Therefore, also the data obtained for A3 are from disputable quality and omitted from further interpretation.

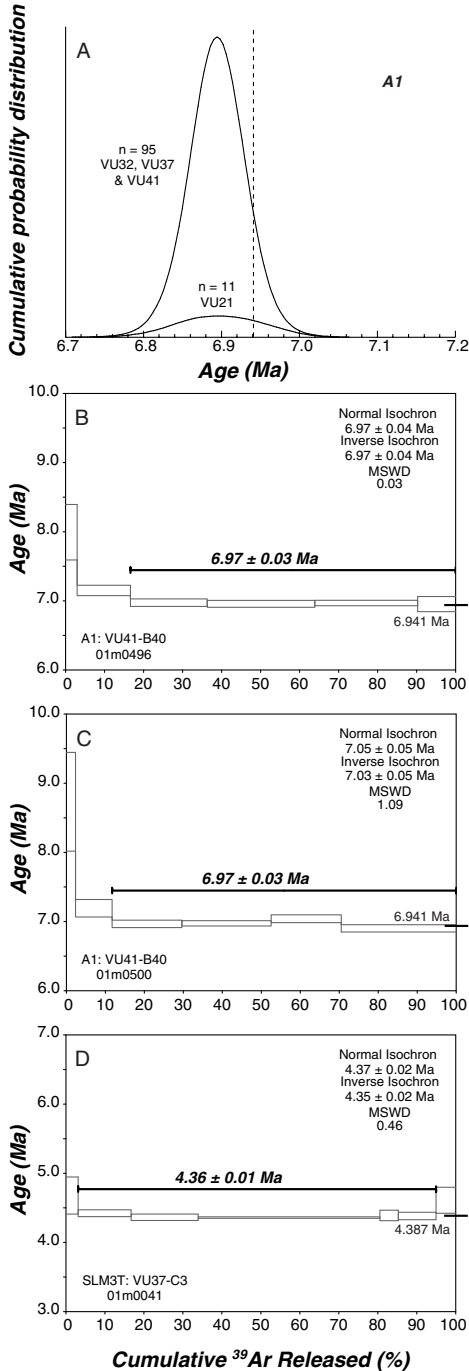


Figure 3.5a-d: Cumulative probability distribution of $^{40}\text{Ar}/^{39}\text{Ar}$ ages for A1 and incremental heating spectra of biotite.

Cumulative age probability distribution of $^{40}\text{Ar}/^{39}\text{Ar}$ sanidine ages of the A1 ash layer (a). The area under the curve is proportional to the number of analyses. The vertical dashed line represents the astronomical age of 6.941 Ma. Three incremental heating spectra of biotite from the A1 (b, c) and SLM3T (d) ash layers are shown. Weighted mean spectrum and isochron ages are also shown including their 1σ analytical error. Horizontal bars on the right represent astronomical ages of ash layer.

CRETE A1 SANIDINE

On Crete, the ash layer A1 is the most prominent of the three and was identified in several sections in different parts of Crete. This ash layer has been dated several times based on 6 different irradiations of sample splits obtained during several field campaigns and from various locations and using different mineral separations and mineral treatment techniques (HF-leaching, no leaching). Hilgen et al. (1997) already published part of the A1 data. The new experimental data on sanidine of irradiation packages from VU32, VU37 and VU41 are listed in table 3.1. MSWD values are near or smaller than 1. When all intercalibration factors $R_{A1/TC}$ for individual experiments are combined to a weighted mean R the MSWD value is 0.53 (with $n = 95$). Further, isochron intercepts deviate in some cases from an atmospheric $^{40}\text{Ar}/^{36}\text{Ar}$ intercept of 295.5 at the 68% confidence level (VU32-C20, VU37-C97, VU37-C88, VU37-C95 and VU41-B40). However, this deviation disappears for all samples at the 95% confidence level. Isochron intercepts of the combined A1 data ($n = 95$, table 3.3.) also deviate at the 68% confidence level (289.2 ± 1.8 normal isochron, 292.5 ± 1.8 inverse isochron). At the 95% confidence level intercepts are not significantly different from 295.5. Both isochrons are dominated by 2 analyses due to their low ^{36}Ar intensity compared to the other analyses. Omission of these two data from the isochrons results in intercepts equal to 295.5 at the 1σ level. We accepted a weighted mean $^{40}\text{Ar}/^{39}\text{Ar}$ age for the A1 sanidine based on 95 individual analyses from several locations on Crete in several irradiation batches of 6.893 ± 0.093 Ma (full external error).

CRETE A1 BIOTITE

In VU32 incremental heating and total fusion experiments and in VU41 incremental heating experiments have been performed on biotite of Faneromeni A1. We were not able to deduce a reliable incremental heating spectrum in VU32, but we were able to reproduce two incremental heating spectra in VU41. The combined age of two incremental heating spectra is 6.967 ± 0.096 Ma (table 3.1). The first steps were omitted from the plateau according to criteria for a reliable plateau as defined by Fleck et al. (1977) as 3 contiguous steps containing 60% of gas. Isochron intercepts did not differ from the atmospheric ratio at 95% confidence level (figure 3.5). The biotite age is older than the sanidine ages, which might be due to a recoil effect on slightly altered biotite (e.g., Huneke and Smith, 1976). However, recoil is accompanied by clearly increased $^{36}\text{Ar}_{\text{atm}}$ and resultant low percentage of $^{40}\text{Ar}^*$, which is not observed in our data (72-96% $^{40}\text{Ar}^*$ for the steps included in the plateau). Excess argon is also not observed, because isochron intercepts are atmospheric at the 2σ level.

PTOLEMAIS

Steenbrink et al. (1999) already showed that sanidine from the Ptolemais tephtras displayed straightforward incremental heating spectra where only the first and last steps were occasionally omitted because of the large uncertainties (but those steps were never statistically different from the mean age of the incremental heating spectrum). Therefore, we only performed total fusion experiments after a pre-heating step to increase the number of analyses and to decrease the amount of material required for analysis. Further, the seven isotopically dated ash layers in Ptolemais will be considered in two groups: the older ashes SL5L, SL7L and SL11L, and the younger ashes SLM2T, SLM3T, SR3L, SR3M and SR5L, because they are intercalated in different parts of the succession separated by a possible hiatus.

THE OLDER ASH LAYERS IN PTOLEMAIS

Table 3.1 shows the analytical details and ages for the three ash layers. Measurements on the oldest ash layer in Ptolemais (SL5L) appeared to be on sanidine/plagioclase mixtures with radiogenic ^{40}Ar contents between 86-97%. VU37-C7 is slightly heterogeneous (MSWD 1.55), has the lowest K/Ca and its isochron intercept is >295.5 , indicative for excess argon. VU37-C8 has a lower MSWD and is therefore a better age estimate for SL5L. Measurements on SL7L yield K/Ca ratios characteristic for a sanidine/plagioclase mixture. Combination of the 7 analyses of SL7L results in a MSWD of 4.8, indicating potential heterogeneity in the sample. A probability curve indeed shows a non-normal distribution, which can be divided in roughly two populations with about half of the data belonging to one group and the other half to the other (figure 3.6). Therefore, it is difficult to estimate the crystallization age of sanidine for SL7L. Ash layer SL11L yields K/Ca ratios indicative for sanidine and shows 1 outlier, which can easily be recognized and removed. We accepted the weighted mean ages of irradiation VU37 as best age estimates for the older

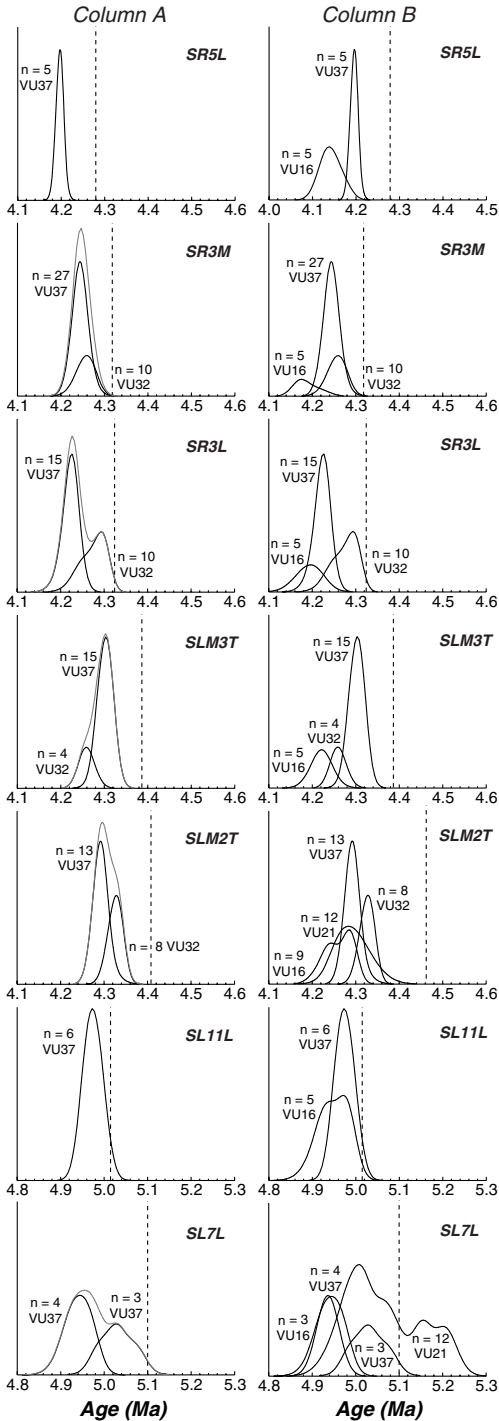
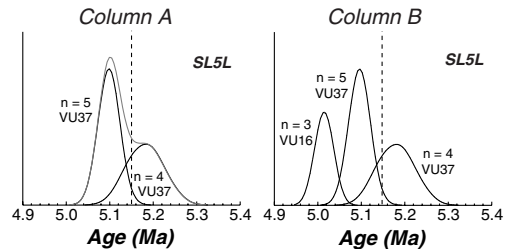


Figure 3.6: Cumulative probability distributions of ages of Ptolemais ash layers.

Cumulative probability distributions for $^{40}\text{Ar}/^{39}\text{Ar}$ sanidine ages of Ptolemais ash layers. Extreme outliers are excluded and distributions are separated on basis of the irradiation batch to which the data belong (column A). The X-axis spans in all cases a time interval of 0.5 Ma. Cumulative probability distributions to which the Steenbrink et al. (1999) data have been added in column B. The scale on the Y-axis is equal for each individual ash layer but is different between ash layers, because the area under the curve is proportional to the number of analyses.



Ptolemais ash layers (respectively 4.973 ± 0.069 Ma for SL11L and 5.094 ± 0.071 Ma for SL5L).

THE YOUNGER ASH LAYERS IN PTOLEMAIS

Pure sanidine separates have been analyzed (most K/Ca >30) for the five ash layers higher in the stratigraphic succession (table 3.1). SLM2T and SR3M both show a few outliers, which can easily be removed. After culling SR3M shows a normal probability distribution in contrast to SLM2T, SLM3T and SR3L. Dividing the data in two groups after their irradiation results in more or less two normal distributions (figure 3.6). This is not due to analyses of different sample splits, because part of the VU37 data originates from (not irradiated) material separated for VU32 and from newly sampled and separated ash layers. It is also unlikely that changes in irradiation circumstances or system performance cause this bimodality, because ash layer A1 shows a good reproducibility and normal distributions over several irradiations (VU32, VU37, VU41). Additionally, the reproducibility of intercalibration data of TCR and FCT over irradiations VU32, VU37, VU41 and VU42 (chapter 1) indicate also that the analytical system has been stable over a period several years. Therefore it is not straightforward to estimate the best age estimate for the Ptolemais tephras. Moreover, several of the data show isochron intercepts deviating from the atmospheric $^{40}\text{Ar}/^{36}\text{Ar}$ ratio of 295.5 at the 1σ level, although this difference disappears at the 2σ level. Experiments on SR3L (VU32 C29: 243 ± 14) and SLM3T (VU32-C5: 168 ± 52) significantly deviate from the atmospheric ratio of 295.5. For these ash layers the VU37 data are considered as more reliable. "Accepted" ages for the younger Ptolemais ash layers are respectively 4.196 ± 0.057 Ma, 4.242 ± 0.057 Ma, 4.223 ± 0.057 Ma, 4.301 ± 0.058 and 4.290 ± 0.058 Ma for respectively SR5L, SR3M, SR3L, SLM3T and SLM2T.

PTOLEMAIS BIOTITE

$^{40}\text{Ar}/^{39}\text{Ar}$ experiments on biotite have been performed for ash layer SLM3T. The data of VU32-C3 are fusion experiments resulting in an age of 4.376 ± 0.062 Ma (with a pre-heating step, which is not analyzed, to remove undesirable atmospheric argon), VU37-C3 is a stepwise heating experiment resulting in a reliable plateau (4.361 ± 0.061 Ma). Biotite ages tend to be older than the ages on sanidine, which might be due to a recoil effect on slightly altered biotite (e.g., Huneke and Smith, 1976), although recoil is accompanied by clearly increased $^{36}\text{Ar}_{\text{atm}}$ and resultant low percentage of $^{40}\text{Ar}^*$, which is not observed in our data (77-97% $^{40}\text{Ar}^*$ for the steps included in the plateau). Excess argon is also not observed, because isochron intercepts are all atmospheric at the 2σ level.

DISCUSSION

PREVIOUS $^{40}\text{Ar}/^{39}\text{Ar}$ STUDIES ON ASHES FROM CRETE AND PTOLEMAIS

All ash layers, which have been dated in this chapter, have been studied before. Hilgen et al. (1997) studied the A1, A2 and A3 ash layers on Crete, Steenbrink (1997; unpublished results) also dated the A1 ash layer and Steenbrink et al. (1999) performed $^{40}\text{Ar}/^{39}\text{Ar}$ experiments on the Ptolemais ash layers. In fact, the main reason to extend the $^{40}\text{Ar}/^{39}\text{Ar}$ -astronomical intercalibration studies was the remarkable discrepancy found by Steenbrink et al. (1999) between $^{40}\text{Ar}/^{39}\text{Ar}$ and astronomical ages.

All previous experiments were performed in the same laboratory, with the same laser extraction system and mass spectrometer (MAP215-50). However, the data originate from different sample collections and mineral separations. All samples were analyzed in the Oregon Triga Reactor CLICIT facility with irradiation times varying between 1 and 12h and 85G003 was used as "main" neutron fluence monitor. Measurement protocols differed slightly from procedures used here (e.g., blanks were measured every 5 to 10 unknowns, mass fractionation was monitored less frequently with air pipettes of atmospheric argon). The original data, i.e. the original $^{40}\text{Ar}^*/^{39}\text{Ar}_K$ ratios of samples and standards and their analytical errors, have been used to recalculate the ages according to the same procedures as in this study. Table 3.2 lists the published and recalculated ages of the previous studies.

We only need to consider the analytical error (II) to compare our data with the $^{40}\text{Ar}/^{39}\text{Ar}$ data of Hilgen et al. (1997) and the $^{40}\text{Ar}/^{39}\text{Ar}$ data presented here, because potential systematic errors in decay constants and standard ages have the same effect on all data. The data of Hilgen et al. (1997) are not very consistent, but are overall older than the data presented here. The biotite ages are total fusion ages and the assumption of a flat undisturbed age spectrum has not been tested. New biotite analyses were either too heterogeneous to define a reliable incremental heating plateau or reliable plateaus could only be obtained with omission of several steps from the plateau, indicating that the assumption of a flat undisturbed age spectrum by Hilgen et al. (1997) is not met. Apart from biotite plagioclase has been measured and for A1 also a sanidine split. As for the new data it appeared that all analyses on plagioclase produced large analytical errors due to the low ^{40}Ar yields. One sanidine age (VU7-E6) shows a heterogeneous population and VU7-E2 yields an isochron intercept >295.5 (~ 323), which is indicative for excess argon. Therefore, the $^{40}\text{Ar}/^{39}\text{Ar}$ data (and conclusions) of Hilgen et al. (1997) must be treated with caution and are further not included in the discussion.

The $^{40}\text{Ar}/^{39}\text{Ar}$ data of Ptolemais as published in Steenbrink et al. (1999) seem very reliable. MSWD values are low, K/Ca ratios are high, radiogenic ^{40}Ar yields are high and stepwise heating plateaus of sanidine are excellent. Due to the high radiogenic argon yields isochron analysis is precluded (clustering of data around x-axis in inverse isochrons, huge error bars in normal isochrons), but slight deviations from the atmospheric ratio for the non-radiogenic argon component will hardly influence the age. Cumulative probability distributions for the VU16 and VU21 data of Steenbrink et al. (1999; recalculated relative to TCR of 28.34 Ma) are plotted in figure 3.6 (column B) together with our VU32 and VU37 data. The VU16 data show younger age peaks and therefore add another population to the probability distributions. Additionally, the VU16 distributions for SL11L and SLM2T do not display normal distributions. The VU21 data show a multi-modal distribution for SL7L, which is also shown in our dataset. The VU21 distribution of SLM2T is equal to the distribution of VU37. For A1 the distribution of the VU21 data of Steenbrink (1997; unpublished results; table 3.2; figure 3,5) is also in agreement with the data presented here. One explanation for the deviation of the VU16 data might be a systematic error in the behavior of the analytical system. From VU37 onwards the behavior of the system is monitored more systematically by frequent analyses of mass fractionation, assessment of flat peak shapes and better magnet calibrations. Therefore we regard, the VU37 data as the best age estimates, although problems due to sample heterogeneity cannot be completely excluded.

Identity	Published age (Ma)	F _{unknown}	σ _{Funknown}	N	MSWD	K/Ca	F _{TC}	σ _{TC}	Apparent ⁴⁰ Ar/ ³⁹ Ar age and error (Ma)																	
									Age	I	II	III	IV	Equation 1.14												
SR5L																										
VU16 D6	4.083 ± 0.023	4.4687	0.0089	5	1.32	37.5	30.76	0.092	4.145	0.008	0.015	0.028	0.044											4.280		
VU16 D6 ^a	4.036 ± 0.036	4.4174	0.0178	7 (2)	0.42	41.0	30.76	0.092	4.097	0.016	0.021	0.031	0.046												4.143 ± 0.058	
SR3M																										
VU16 D4	4.122 ± 0.026	4.4673	0.0108	5	2.35	35.5	30.46	0.091	4.184	0.010	0.016	0.029	0.045												4.318	
VU16 D4 ^a	4.162 ± 0.029	4.5107	0.0129	8 (2)	0.66	45.0	30.46	0.091	4.225	0.012	0.018	0.030	0.046												4.183 ± 0.058	
SR3L																										
VU16 D5	4.132 ± 0.026	4.5050	0.0111	5 (1)	0.63	45.0	30.64	0.091	4.195	0.010	0.016	0.029	0.045												4.324	
VU16 D5 ^a	4.137 ± 0.035	4.5106	0.0171	7 (1)	0.44	48.1	30.64	0.091	4.200	0.016	0.020	0.031	0.047												4.193 ± 0.059	
SLM3T																										
VU16 D3	4.158 ± 0.024	4.4896	0.0096	5	0.02	51.8	30.34	0.091	4.221	0.009	0.016	0.029	0.045												4.387	
VU16 D3 ^a	4.207 ± 0.034	4.5423	0.0161	7 (1)	0.45	97.9	30.34	0.091	4.271	0.015	0.020	0.031	0.048												4.220 ± 0.059	
VU21 A10 ^{a,b}	4.323 ± 0.042	1.3508	0.0060	7 (2)	0.93	21.8	8.781	0.026	4.388	0.019	0.023	0.034	0.050												4.269 ± 0.061	
SLM2T																										
VU16 D2	4.178 ± 0.023	4.4849	0.0084	5	2.02	53.3	30.16	0.090	4.242	0.008	0.015	0.028	0.045												4.408	
VU16 D2 ^a	4.191 ± 0.030	4.4982	0.0136	12 (2)	0.41	70.6	30.16	0.090	4.254	0.013	0.018	0.030	0.047												4.240 ± 0.059	
VU16 D14	4.222 ± 0.023	4.8237	0.0050	4 (1)	0.42	50.1	32.09	0.096	4.288	0.004	0.014	0.028	0.045												4.253 ± 0.060	
VU16 D14 ^a	4.224 ± 0.019	4.8002	0.0140	10 (2)	0.78	62.1	32.09	0.096	4.268	0.012	0.018	0.030	0.047												4.287 ± 0.059	
VU21 A13	4.204 ± 0.030	1.3372	0.0025	12	1.19	50.9	8.902	0.026	4.286	0.008	0.015	0.029	0.046												4.266 ± 0.060	
SL11L																										
VU16 D10	4.888 ± 0.031	5.4266	0.0131	5	2.39	49.5	31.19	0.093	4.962	0.012	0.019	0.034	0.054												5.015	
VU16 D10 ^a	4.843 ± 0.035	5.3762	0.0164	8 (1)	0.54	39.0	31.19	0.093	4.916	0.015	0.021	0.035	0.054												4.961 ± 0.069	
SL7L																										
VU16 D9	4.862 ± 0.029	5.3763	0.0119	3 (2)	0.33	38.1	31.06	0.093	4.936	0.011	0.018	0.034	0.053												5.099	
VU16 D9 ^a	4.888 ± 0.034	5.4051	0.0155	8 (1)	0.59	35.2	31.06	0.093	4.963	0.014	0.021	0.035	0.054												4.934 ± 0.069	
VU21 A5	5.002 ± 0.051	1.5365	0.0072	12	16.38	36.1	8.631	0.025	5.078	0.024	0.028	0.040	0.059												4.961 ± 0.070	
SL5L																										
VU16 D7	4.841 ± 0.025	5.3106	0.0086	3 (2)	0.59	40.6	30.82	0.092	4.915	0.008	0.017	0.033	0.052												5.076 ± 0.074	
VU16 D7 ^a	4.885 ± 0.033	5.3588	0.0147	10 (1)	0.73	20.6	30.82	0.092	4.959	0.014	0.020	0.035	0.054												4.913 ± 0.068	
																										4.957 ± 0.070

Table 3.2: Recalculated ⁴⁰Ar/³⁹Ar data of Ptolemais and Cretan tephra of previously published data (continued on next page).

Identity	Published age (Ma)	F _{unknown}	O _{Funknown}	N	MSWD	K/Ca	F _{TC}	O _{FTC}	Apparent ⁴⁰ Ar/ ³⁹ Ar age and error (Ma)					
									Age	I	II	III	IV	Equation 1.14
Crete A3														
VU7 E9 Kast ^c	6.749 ± 0.044	14.5834	0.2097	5	0.17	0.1	60.68	0.091	6.851	0.098	0.099	0.106	0.121	6.771
VU7 E4 Al ^c	6.776 ± 0.066	14.4175	0.2821	4	0.02	0.1	59.75	0.089	6.78	0.134	0.135	0.140	0.152	6.849 ± 0.135
VU7 E10 Kast ^b	6.668 ± 0.010	14.4812	0.0414	5	0.53	40.6	60.99	0.091	6.769	0.019	0.022	0.044	0.072	6.876 ± 0.164
VU7 E5 Al ^b	6.747 ± 0.014	14.3991	0.0608	4 (1)	0.24	97.6	59.94	0.089	6.849	0.029	0.031	0.050	0.076	6.766 ± 0.094
VU10 A26 Met ^c	Unpublished	15.0269	1.0406	3	0.52	3.8	60.71	0.091	7.056	0.488	0.488	0.489	0.493	6.846 ± 0.097
VU10 A14 Met ^b	6.632 ± 0.021	14.2078	0.0620	5	1.94	1071	60.17	0.090	6.732	0.029	0.031	0.049	0.075	7.054 ± 0.497
Crete A2														
VU7 E12 Kast ^c	Unpublished	15.6593	1.0071	2	0.01	<0.1	61.69	0.092	7.236	0.464	0.465	0.466	0.470	6.730 ± 0.096
Crete A1														
VU7 E2 Fan	6.936 ± 0.006	14.6696	0.0188	5	0.28	24.1	59.39	0.089	7.041	0.009	0.014	0.042	0.072	6.941
VU7 E6 Kast	6.844 ± 0.008	14.6633	0.0304	4 (1)	1.22	19.8	60.17	0.090	6.947	0.014	0.018	0.043	0.072	7.233 ± 0.475
VU7 E3 Fan ^b	6.934 ± 0.016	14.6645	0.0710	5	0.23	57.4	59.39	0.089	7.039	0.034	0.036	0.054	0.080	6.945 ± 0.095
VU7 E8 Kast ^b	5.691 ± 0.055	12.2605	0.2919	4 (2)	0.35	62.7	60.52	0.090	5.777	0.137	0.138	0.141	0.149	7.036 ± 0.101
VU10 A23 Al ^c	6.923 ± 0.013	14.9322	0.0518	3 (2)	2.20	12.9	60.56	0.090	7.028	0.024	0.027	0.048	0.076	5.775 ± 0.158
VU10 A24 Kouf ^c	7.164 ± 0.032	15.4639	0.1215	4 (1)	2.60	4.4	60.61	0.090	7.272	0.057	0.058	0.071	0.094	7.026 ± 0.098
VU10 A12 Al ^b	6.893 ± 0.013	14.7518	0.0281	5	1.25	1073	60.10	0.090	6.997	0.013	0.017	0.043	0.073	7.270 ± 0.114
VU10 A13 Kouf ^b	6.813 ± 0.012	14.5869	0.0257	4 (1)	0.95	704	60.12	0.090	6.917	0.012	0.016	0.042	0.072	6.995 ± 0.096
VU21 A4 Fan	Unpublished	2.0813	0.0036	11	2.67	55.9	8.597	0.025	6.901	0.012	0.024	0.046	0.074	6.914 ± 0.095

^{a)} Incremental heating experiment ^{b)} Experiment on biotite ^{c)} Experiment on a sanidine / plagioclase mixture or plagioclase
 ash layers is given in bold italics. Met = Metochia section, Fan = Faneromeni section, Al = Agios Ioannis section, Kast = Kastali section, Kouf = Koufonisi section.
 The astronomical age of the volcanic

Table 3.2: Recalculated ⁴⁰Ar/³⁹Ar data of Ptolemais and Cretan tephras of previously published data .

Previously published ⁴⁰Ar/³⁹Ar data (Hilgen et al., 1997; Steenbrink et al., 1999) obtained for the Ptolemais and Cretan tephras. Astronomical ages for these tephras are given in **bold italic**. Ages are recalculated relative to TCR of 28.34 Ma and the Steiger and Jäger (1977) consensus decay constants are used (5.543 ± 0.01 × 10⁻¹⁰ yr⁻¹). Errors are reported including the analytical uncertainty in the sample (I), the analytical uncertainty in sample and standard (analytical error in J is assumed to be 0.15% for VU7/VU10 and 0.3% for VU16/VU21 (II), adding the uncertainty in ⁴⁰Ar/⁴⁰K of the primary standard (III) and adding the decay constant uncertainty as well (IV). Ages and uncertainties according to equation 1.14 are given in the last column (see text for discussion). All errors are reported at the 1σ level.

SYSTEMATIC DIFFERENCES BETWEEN $^{40}\text{Ar}/^{39}\text{Ar}$ AND ASTRONOMICAL AGES?

Hilgen et al. (1997) concluded in their study that $^{40}\text{Ar}/^{39}\text{Ar}$ ages were in good agreement with the astronomical ages. In contrast, Steenbrink et al. (1999) noticed a systematic discrepancy of ~3%, with $^{40}\text{Ar}/^{39}\text{Ar}$ ages being younger. To solve this inconsistency all volcanic ash layers are re-dated. Figure 3.6 clearly shows that all $^{40}\text{Ar}/^{39}\text{Ar}$ ages are systematically younger, in spite of the occasional lack of clarity about the “real” ages due to multi-modal distributions. However, figure 3.6 incorporates only the analytical uncertainties of sample and standard. To be able to compare two independent methods, all uncertainties in both methods must be assessed. $^{40}\text{Ar}/^{39}\text{Ar}$ studies commonly report analytical errors only, which is correct when the purpose of a study is to provide relative ages. Here, we try to determine absolute $^{40}\text{Ar}/^{39}\text{Ar}$ ages and hence error estimates must include all uncertainties related to ages of standard and decay constants (e.g., Min et al., 2000). Table 3.3 lists the “accepted” $^{40}\text{Ar}/^{39}\text{Ar}$ age estimates including a full error estimate according to a slightly modified procedure as proposed in Min et al. (2000).

CRETE

Although figure 3.5 shows that $^{40}\text{Ar}/^{39}\text{Ar}$ age for A1 is younger than the astronomical age, the $^{40}\text{Ar}/^{39}\text{Ar}$ age is not statistically different from the astronomical age, when the so-called full error propagation is applied. This is caused by a proper incorporation of the uncertainties in the activities of the ^{40}K , K and Ar contents in the primary standard and other physical parameters in the error equation. The overall error is not dominated by analytical uncertainties, but as stated before by the activity of the decay of ^{40}K to ^{40}Ar and the amount of radiogenic ^{40}Ar in the primary standard GA1550. Improvement in the accuracy of the $^{40}\text{Ar}/^{39}\text{Ar}$ ages should therefore be focused on improvements in the accuracy of these two parameters or on a method to avoid or reduce the influence of the two parameters on the final age.

THE LOWER ASHES IN PTOLEMAIS

Although the lower $^{40}\text{Ar}/^{39}\text{Ar}$ Ptolemais ashes need to be considered with some caution, i.e. SL7L is heterogeneous, and one of the two age populations in SL5L is characterized by excess argon, the remaining $^{40}\text{Ar}/^{39}\text{Ar}$ ages are also younger than their astronomical counter parts (figure 3.6). Full error propagation cancels the statistical significance of this discrepancy (like for the A1 data).

THE UPPER ASHES IN PTOLEMAIS

The situation for the upper Ptolemais ashes is different. Even when full error propagation is applied, the ash layers SLM2T, SLM3T, SR3L, SR3M and SR5L are still significantly younger than the astronomical ages at the 1σ level. Apart from the uncertainties in $^{40}\text{Ar}/^{39}\text{Ar}$ dating, which have been accounted for in the error equations, some other possible sources of error might exist. Uncertainties in $^{40}\text{Ar}/^{39}\text{Ar}$ ages can originate from e.g. contamination during sampling or mineral separation (in this case with younger crystals), loss of radiogenic ^{40}Ar , systematic biases during mass spectrometry or combination of these factors. These kinds of systematic errors are difficult to account for. In theory, single crystal analyses might detect possible contamination effects. Unfortunately, most samples have grain sizes that are too small (<500 μm) to allow reliable single crystal analyses, but this will be done in chapter 5 with ash layers in the Melilla Basin.

N	MSWD	R	σ_R	Astr. age (Ma)	$\sigma_{\text{astr. age}}$	Apparent $^{40}\text{Ar}/^{39}\text{Ar}$ age (Ma)		Apparent astr. calibrated age (Ma)		Astr. calibrated FCT age combined data ($\pm 1\text{sd}$)			
						Age	Analytical & total uncertainties	TCR	$\sigma_{\text{age TCR}}$		FCT	$\sigma_{\text{age FCT}}$	
SR5L	5	0.31	6.7971	0.0171	0.025	4.196	0.011	0.057	28.89	0.18	28.58	0.18	
SR3M	27	0.54	6.7232	0.0046	0.025	4.242	0.003	0.057	28.83	0.17	28.52	0.17	
SR3L	15	0.22	6.7543	0.0076	0.025	4.223	0.005	0.057	29.01	0.17	28.69	0.17	
SLM3T	15	0.42	6.6313	0.0065	0.025	4.301	0.004	0.058	28.89	0.17	28.58	0.17	
SLM2T	13	0.29	6.6474	0.0066	0.025	4.290	0.004	0.058	29.10	0.17	28.78	0.17	
SL11L	6	0.58	5.7344	0.0180	0.025	4.973	0.016	0.069	28.57	0.17	28.26	0.17	
SL7L	(3)	(2.85)	(5.6708)	(0.0285)	0.025	(5.028)	(0.025)	(0.072)	(28.73)	(0.20)	(28.41)	(0.20)	
SL5L	5	0.26	5.5972	0.0186	0.025	5.094	0.017	0.071	28.62	0.17	28.30	0.17	
A1	95	0.53	4.1346	0.0017	0.005	6.893	0.003	0.093	28.53	0.02	28.21	0.04	
						U/Pb age (Ma)							
						1097.6 \pm 2.65							
						Historical age							
						1919 \pm 0 yr							
Pallisade Rhyolite						1.8903 $\times 10^{-2}$	0.0042 $\times 10^{-2}$					28.32	0.14
Vesuvius 79 AD						623.1	5.0					28.06	0.23

Table 3.3: Best $^{40}\text{Ar}/^{39}\text{Ar}$ age and error estimates for Ptolemais and Cretan tephras used for intercalibration with TCR (and FCT).

The “accepted” ages for the individual ash layers. Intercalibration factors between the standard (TC) and ash layer are given. This intercalibration factor is used to calculate the $^{40}\text{Ar}/^{39}\text{Ar}$ age including the analytical and full errors according to equation 1.14 (analytical error is calculated by only including the terms in the variance equation of 1.14 related to the analytical error. i.e. F_u , F_{TC}). Further, these intercalibration factors were used to calculate the age of TCR relative to an astronomically dated standard assuming an uncertainty of 25 kyr in the astronomical age in Ptolemais and of 5 kyr on Crete (equation 1.15). Using the intercalibration factor of Renne et al. (1998; confirmed in chapter 1) for TC and FC the age for FC is calculated relative to an astronomically calibrated standard as well.

On the other hand, an error in the astronomical tuning might also explain the observed difference. The accuracy of the astronomical tuning ultimately depends on 1) the correctness of the tuning, 2) the accuracy of the astronomical solutions, 3) uncertainties in the assumption of constant sedimentation rates between two astronomically tuned points to derive an astronomical age for a layer between such points and 4) uncertainties in the lag (or lead) between astronomical forcing and sedimentary expression. Points 2-4 are discussed in detail in chapter 2 and we estimated a combined uncertainty of about 5 kyr in the 5 to 7 Ma age range. Errors in the correctness of the tuning are more difficult to express. The tuning in Ptolemais was not so straightforward, because of the lack of a clear cyclic expression of eccentricity (e.g., small and large scale clusters of precession related cycles) and depends on the magnetostatigraphy and its calibration to the APTS. Even though the magnetostratigraphy and its calibration to the APTS seem reliable and a possible delayed acquisition of the magnetic signal in Ptolemais would only increase the discrepancy between $^{40}\text{Ar}/^{39}\text{Ar}$ and astronomical ages (Steenbrink et al., 1999), we decided to add an extra 20 kyr uncertainty to the astronomical ages of the Ptolemais ash layers. This 20 kyr expresses an uncertainty of one cycle in the tuning of the precession related lignite-marls cycles. This brings the total uncertainty on 25 kyr for the Ptolemais ash layers. However, this still leaves the SLM2T, SLM3T, SR3L and SR5L $^{40}\text{Ar}/^{39}\text{Ar}$ ages to be significantly younger.

INTERCALIBRATION BETWEEN $^{40}\text{Ar}/^{39}\text{Ar}$ AND ASTRONOMICAL DATING?

Sources of systematic error in $^{40}\text{Ar}/^{39}\text{Ar}$ dating are the absolute ages of standards and the exact values of the decay constants. Recent publications focussing on the "true" age of the standards (e.g., Lanphere and Baadsgaard, 2001; Renne et al., 1998; Schmitz and Bowring, 2001) show a range of 27.5-28.5 Ma for the age of the Fish Canyon Tuff. Other publications (e.g., Min et al., 2000; Begemann et al., 2001) call for improvements in decay constant values. Most of the FCT ages are based on intercalibration to a primary K/Ar dated standard. Min et al. (2000) and this study already showed that when a secondary standard FCT or TCR intercalibrated to a primary K/Ar dated standard (GA1550) is used, the final error is dominated by the uncertainty in the decay of ^{40}K to ^{40}Ar (>70%) and the uncertainty in the amount of radiogenic ^{40}Ar in the primary standard (~15%). To reduce the influence of the activity of the ^{40}K decay branch to ^{40}Ar on the final error and to elucidate the knowledge of the absolute amount of radiogenic ^{40}Ar in a primary dating standard, the absolute age of a dating standard can be determined by other means (e.g., U/Pb, although this method has its own disadvantages, as will be shown in chapter 7).

Therefore, Min et al. (2000) used the $^{40}\text{Ar}^*/^{39}\text{Ar}_K$ ratios of feldspars from a 1.1 Ga rhyolite and from the 79 AD eruption of the Vesuvius in combination with a Pb/Pb age of the 1.1 Ga rhyolite and the historical age of the eruption of the Vesuvius to determine the age of FCT as a function of the total decay constant. The age of FCT calibrated to the 1.1 Ga rhyolite is strongly dependent on the value of the decay constant in contrast to the age of FCT calibrated to the 79 AD eruption (see figure 9 in Min et al., 2000). Unfortunately, the analytical precision of this 79 AD eruption is not extremely high due to low amounts of radiogenic ^{40}Ar in such young samples.

A slightly different approach can be performed with the data presented here. The astronomical age can be used as the "true" age of a volcanic ash layer and the minerals it contains. Table 3.3 reports the ages for TCR and FCT derived on basis of the astronomical ages of the tephra and their $^{40}\text{Ar}^*/^{39}\text{Ar}_K$ ratios including a

total error propagation, according to equation 1.15 and activities of Beckinsale and Gale (1969) with the uncertainty for A_e based on Min et al. (2000; table 1.4, VII), atomic weight and abundances of Garner et al. (1975) and N_o of Cohen and Taylor (1987). Figure 3.7 visualizes the results from table 3.3, including the data for the Vesuvius eruption and Palisade rhyolite from Min et al. (2000). The main advantage of intercalibrating $^{40}\text{Ar}/^{39}\text{Ar}$ dating to astronomically dated standards instead of using FCT or TCR intercalibrated to primary standard GA1550 is that activity data and other physical parameters hardly contribute to the total variance anymore. The reported uncertainty for the age of FCT is now dominated by the analytical errors in the unknowns and standards.

The FCT sanidine age relative to A1 (28.21 ± 0.04 Ma) shows the most precise age estimate for FCT based on intercalibration with astronomically dated, historical or U/Pb dated volcanic material (figure 3.7 and table 3.3). This is due to a large, consistent $^{40}\text{Ar}/^{39}\text{Ar}$ dataset in combination with an excellent astronomical age control (category 1 ash, chapter 2). The data of Min et al. (2000) on the Palisade Rhyolite and the Vesuvius eruption support the FCT age based on A1, but uncertainties are higher. The uncertainty in the FCT age relative to U/Pb of the Palisade Rhyolite is dominated by the uncertainties in the decay constant and in U/Pb age, the uncertainty in FCT age relative to the 79 AD Vesuvius eruption is dominated by the analytical uncertainty, because the exponential nature of radioactive decay results in low amounts of $^{40}\text{Ar}^*$ in material of the 79 AD Vesuvius eruption.

The lower Ptolemais ashes are consistent with the FCT age relative to A1, although uncertainties are higher partly due to the higher uncertainty (± 25 kyr) assigned to the astronomical ages for ash layers in Ptolemais. The combined lower Ptolemais ashes yield an age of 28.28 ± 0.21 Ma for FCT (weighted mean of FCT ages with weighted standard deviation relative to individual $^{40}\text{Ar}/^{39}\text{Ar}$ data of ash layers). The upper Ptolemais ashes produce an older age for FCT and combination of the 5 upper Ptolemais volcanic ash layers result in an age of 28.59 ± 0.20 Ma. Although the $^{40}\text{Ar}/^{39}\text{Ar}$ ages might be subject to sources of error as discussed in the previous paragraph, an error in the astronomical tuning cannot be excluded for Ptolemais. The lower and upper Ptolemais ash layers are separated by a stratigraphic interval that might contain a

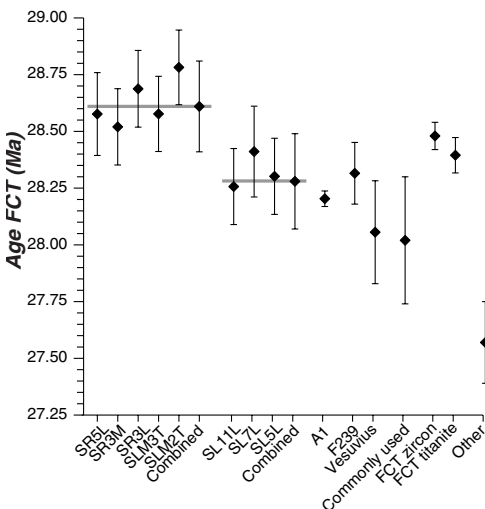


Figure 3.7: Age of Fish Canyon Tuff relative to independently dated standards with full error estimate.

Astronomically calibrated FCT ages calculated according to equation 1.14 (see chapter 1). The Ptolemais ash layers can be divided in the younger and older ones, where "combined" represents the weighted average age of respectively the younger and older ash layers. For comparison the data of Min et al. (2000) for the Vesuvius and F239 Palisade Rhyolite, the commonly used FCT sanidine age of Renne et al. (1998), the zircon and titanite ages of Schmitz and Bowring (2001) and a deviating value ("other") of Lanphere and Baadsgaard (2001) are included. The FCT sanidine age relative to A1 shows the smallest error.

hiatus. Consequently, a possible error in the tuning might not be identical for the lower and upper parts of the Ptolemais Formation in which the two clusters of ash layers occur. But this error will most likely be the same for ash layers in either of the two clusters because they are intercalated in parts of the Ptolemais Formation in which the undisturbed succession of successive individual precession related cycles is evident. We are inclined to assume that the agreement between A1, Palisade rhyolite, 79 AD Vesuvius and the older Ptolemais ashes points to an erroneous tuning for the younger Ptolemais ashes. However, the FCT age of 28.59 ± 0.20 Ma relative to upper Ptolemais ashes is consistent with the U/Pb zircon concordia age (28.48 ± 0.06 Ma) for FCT zircon (Schmitz and Bowring, 2001). Clearly, more research is required to support one of both options for the age of FCT relative to astronomically dated ash layers.

CONCLUSIONS

$^{40}\text{Ar}/^{39}\text{Ar}$ sanidine ages of volcanic ash layers indeed tend to be younger than astronomical ages. However, when a more realistic error propagation method is used the discrepancy statistically disappears for most ash layers. Unfortunately, errors in $^{40}\text{Ar}/^{39}\text{Ar}$ ages increase from ~ 0.3 to 1.3% when this improved full error propagation method is used. This increase can be mostly attributed to uncertainties in the absolute age of standards and parameters related to the decay constants.

To circumvent these problems we intercalibrated two commonly used standards (TCR / FCT) with the $^{40}\text{Ar}^*/^{39}\text{Ar}_K$ ratios of the astronomically dated ash layers. It appeared that the uncertainty in the newly derived ages for TCR / FCT was dominated by analytical errors only for A1 and analytical errors and uncertainties in the astronomical ages for Ptolemais. The new ages for TCR / FCT are respectively 28.53 ± 0.02 / 28.21 ± 0.04 Ma based on A1 and supported by the lower Ptolemais ash layers and data as published in Min et al. (2000). We showed however that intercalibration of FCT with the upper Ptolemais ashes results in an age equivalent to the U/Pb age of FCT zircon. Clearly, more research is required to solve this inconsistency.

One research line will focus on extension of the intercalibration approach to other well-constrained astronomically tuned marine sections in the western Mediterranean with intercalated volcanic ash layers. When the implicit assumptions in this intercalibration approach are true (e.g., time since closure of the mineral for argon diffusion (= moment of eruption) and deposition in the sediments must be negligible, no xenocrystic contamination must occur, no argon loss from samples, correct astronomical tuning), we expect to see the same systematic differences between both methods, and intercalibration must result in the same age for FCT. The very coarse grained tephra layers in the Melilla Basin, Morocco, will even allow for single crystal dating, providing the opportunity to detect potential contamination (chapter 5). In chapter 6 our research will be extended to the middle Miocene and we will check if our intercalibration between the $^{40}\text{Ar}/^{39}\text{Ar}$ isotopic system and the astronomical time scale still holds. Apart from intercalibration of $^{40}\text{Ar}/^{39}\text{Ar}$ and the astronomical methods, as described here, we will also expand our research towards intercalibration of these two systems with the U/Pb system (chapter 7), where we focus on the U/Pb systematics of one of the upper ashes of Ptolemais.

CHAPTER 4

**MESSINIAN ASTROCHRONOLOGY OF THE MELILLA BASIN:
STEPWISE RESTRICTION OF THE MEDITERRANEAN -
ATLANTIC CONNECTION THROUGH MOROCCO.**

INTRODUCTION

During the late Miocene, the Mediterranean was connected to the Atlantic Ocean through at least two marine gateways: the Betic and Rifian Corridors (e.g., Benson et al., 1991). The evolution of these corridors is of major importance to our understanding of the late Neogene isolation of the Mediterranean Sea, which resulted in the Messinian Salinity Crisis. The recently developed Astronomical Time Scale (ATS) for the Messinian of the Mediterranean Realm (Hilgen et al., 1995; Krijgsman et al., 1999a) can now be used for detailed analysis of the paleogeographic evolution of these Neogene gateways.

The Melilla Basin in northeastern Morocco forms the easternmost part of the Rifian Corridor (figure 4.1). The sedimentary succession of this basin consists of an upper Miocene carbonate platform, grading laterally into basinal marine clays, marls and laminites, which display repetitive lithological alternations (Choubert et al., 1966; Gaudant et al., 1994; Saint Martin & Cornée, 1996). The intercalation of volcano-clastic levels provides a correlation tool between the basinal sequences and the carbonate-platform (Cunningham et al., 1994, 1997; Roger et al., 2000). Isotopic dating of these volcanic ashes has provided a scenario for three stages of the pre-evaporitic Messinian basin-evolution (Münch et al., 2001; Roger et al., 2000); 1) the onset of a prograding bioclastic carbonate unit, coeval with the onset of diatomaceous marl deposition, 2) a transition to warm-water conditions, evidenced by the start of warm-water diatomites and prograding *Porites* coral-reefs, and 3) the termination of the prograding carbonate complex.

Our current study focuses on the astronomical tuning of the cyclically developed marls of the Melilla Basin. This paper presents a detailed integrated bio-, magneto- and cyclostratigraphy of the basinal sedimentary sequence, which enables a direct bed-to-bed correlation to the late Miocene framework of the Mediterranean (Hilgen et al., 1995; Sierro et al., 2001; Krijgsman et al., 2001, 2002) and open ocean records (Hodell et al., 2001). Additionally, astronomical ages are derived for the intercalated volcanic ashes, which allow a direct comparison with recently determined isotopic ($^{40}\text{Ar}/^{39}\text{Ar}$) ages obtained from the carbonate platform (Cunningham et al., 1994, 1997; Münch et al., 2001; Roger et al., 2000).

GEOLOGICAL SETTING

The Melilla Basin is located along the northeastern coast of Morocco and is named after the Spanish enclave located on the peninsula of Cap de Trois Fourches (figure 4.2). The basin extends from the peninsula towards Algeria in the east and the Rif Mountains near Tamsaman in the west (Guillemin and Houzay, 1982), and is bordered to the south by the remnants of the folded structures of the metamorphic Rif foreland.

The basin formed after the main orogenic movements of the Rif during the middle Miocene (Choubert et al., 1966; Guillemin and Houzay, 1982). An early extensional phase commenced during the Serravallian, and resulted in the deposition of a molassic "clastic wedge" accompanied by rhyolitic volcanism (El Bakkali et al., 1998). This phase was followed by a N-S directed compression, which resulted in uplift of the Paleozoic metamorphic core complex of the Melilla peninsula. A transgressive conglomerate of an assumed late Tortonian age (Choubert et al., 1966; Guillemin and Houzay, 1982) indicates the final Miocene, basin-

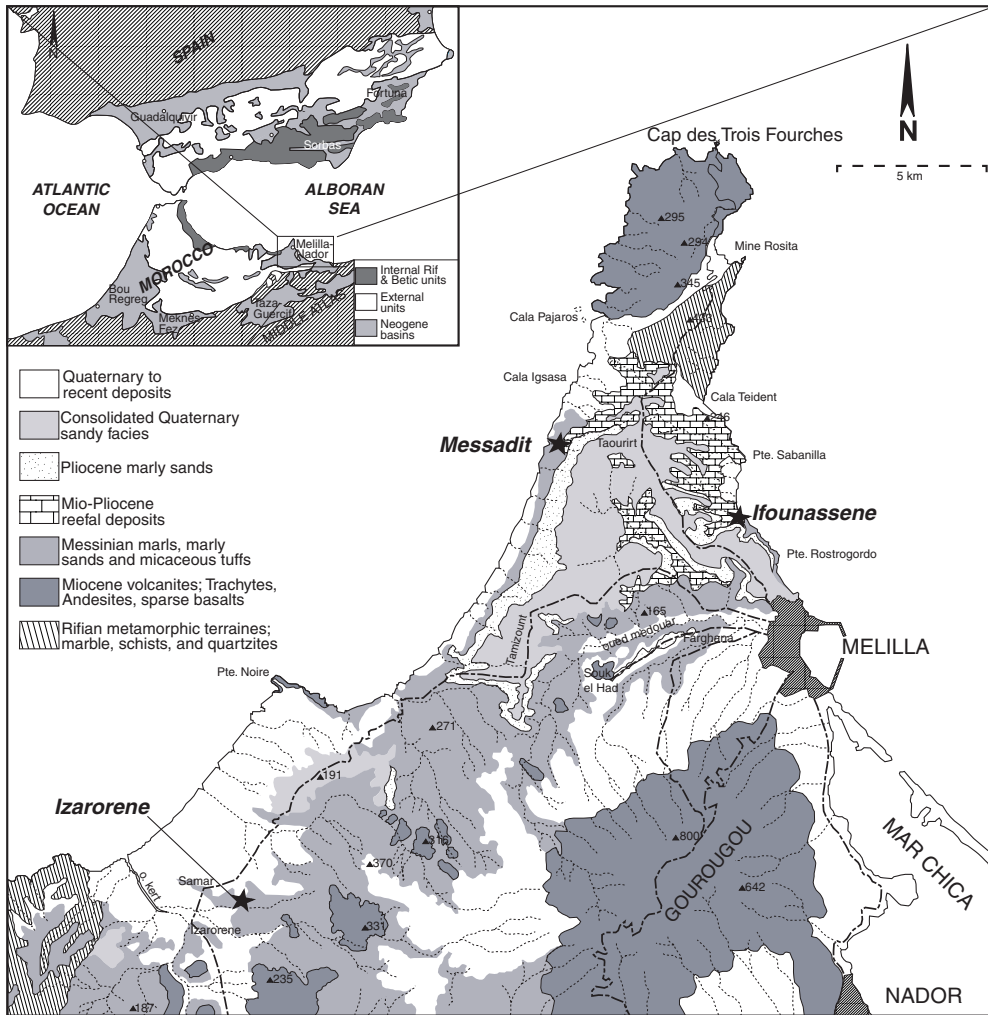
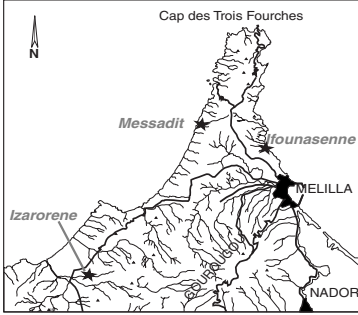


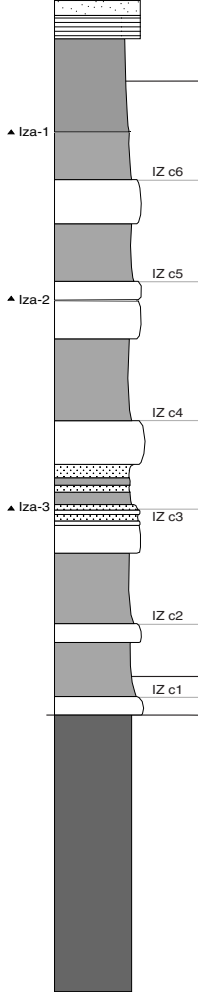
Figure 4.1 Geographic location of the sampled sections in the Melilla Basin, North-east Morocco.

The main geologic units included in the figure are based on the work of Choubert et al. (1966).

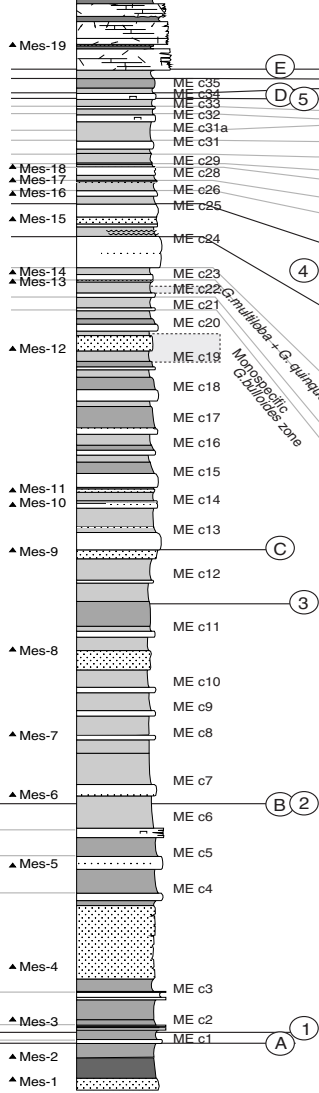
forming extension, which provided the accommodation space for basal marl deposition and the formation of a marginal carbonate platform. This phase ended with a lagoonal to lacustrine regressive sequence (Arias et al., 1976; Barbiéri et al., 1976; Saint Martin et al., 1991). Frequent coeval volcanism of the acidic Trois Fourches and alkaline Gourougou volcanoes resulted in the deposition of numerous ashes within these sediments and the development of seismites (El Bakkali et al., 1998). Deposition of a transgressive sandy facies, supposedly of Pliocene age (Choubert et al., 1966; Guillemin and Houzay, 1982) and unconformably overlying the open marine sequence is followed by a final compressional phase, uplifting the basin to its present altitude above sea level.



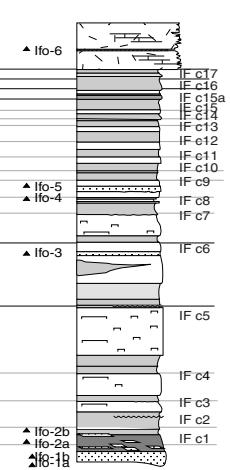
Izarorene



Messâdit



Ifouassene



LEGEND

Lithology

	Diatomite/Laminite
	Dark blue clay
	Blue clayey marls
	Grey to brown silty marls
	Tephras
	Halimeda-algae packstone
	Pycnodonte levels

Stratigraphic level (m)

The Neogene sediments are best exposed on the Melilla peninsula. South of the Cap de Trois Fourches, a well-developed carbonate complex is formed, laterally grading into a basal, silty to clayey marl sequence, including laminites and diatomites (Münch et al., 2001; Saint Martin and Cornée, 1996). The end of the basal marl deposition is marked by a final diatomite bloom, which is generally associated to upwelling (Roger et al., 2000; Saint Martin et al., 1991), followed by deposition of a *Halimeda*-algae packstone. This *Halimeda*-unit, indicating the final stage of the prograding bioclastic carbonate unit (Cunningham et al., 1994), can be traced towards the carbonate complex. The latter is overlain by a topography draping marine-to-continental transitional sequence composed of grainstones, reefs and stromatolites, referred to as the Terminal Carbonate Complex (TCC of Cunningham et al., 1994).

Previous works mainly concerned the carbonate platform, which displays a reef-geometry characteristic for the Alboran Basin (Cornée et al., 1996; Saint Martin and Rouchy, 1986; Saint Martin and Cornée, 1996). The timing of reef development is based on paleomagnetic analysis and isotopic ($^{40}\text{Ar}/^{39}\text{Ar}$) dating of intercalated ashes within the carbonate complex and transition zone (Cunningham et al., 1994, 1997; Roger et al., 2000). These studies have resulted in the first age-constraints of three major bio-sedimentary phases within the Melilla Basin (Münch et al., 2001; Roger et al. 2000). The onset of diatomite formation of boreal affinity and the coeval development of a prograding bioclastic carbonate started around 6.73 ± 0.02 Ma, while a change from boreal to warm floral assemblages, marking the onset of the carbonate reef-complex, is dated at 6.46 ± 0.01 Ma. The progradation of the carbonate reef-complex, displayed by *Porites*-reef build-ups and the production of *Halimeda*-algae beds, ended prior to 6.0 ± 0.1 Ma. This final phase of open marine deposition was precluded by the end of diatomite deposition, dated at 6.29 ± 0.02 Ma (Roger et al., 2000; Münch et al., 2001).

SECTIONS AND LITHOSTRATIGRAPHY

This chapter concentrates on three Neogene marl sections in the Melilla Basin: namely, the Izarorene section located west of the Gourougou volcanic complex, and the Messâdit and Ifounassene sections exposed along the west and east coast of the Cap de Trois Fourches peninsula (figure 4.1). The sections are characterized by well developed bipartite, and in part tripartite, sedimentary cycles, which consist of sub-horizontally bedded, laminated diatomaceous marls alternating with homogeneous (sandy) marls. The nature of the sedimentary cycles closely resembles those observed in other astronomically calibrated upper Miocene Mediterranean sequences.

Figure 4.2 Lithostratigraphic columns of the sampled sections in the Melilla Basin (previous page).

The biostratigraphic marker-events registered within the sections are: 1) FCO *G. nicolae* at 6.828 Ma, 2) LO *G. nicolae* at 6.722 Ma, 3) FCO *G. obesa* at 6.613 Ma, 4) sinistral/dextral coiling change of the *N. acostaensis* at 6.360-6.340 Ma (Krijgsman et al., 1999a; Sierro et al., 2001), and 5) 1st sinistral influx of the *N. acostaensis* at 6.129 Ma. Numbers A-E denote the bio-sedimentary events recorded within the Melilla Basin: A) Onset of sedimentary cyclicity and diatomite deposition, B) lithology transition, C) onset of pronounced diatomite blooms associated with tropical-water conditions, D) final diatomite deposition, and E) onset of *Halimeda*-algae units covering the basal sequences. On the right-hand side of the stratigraphic columns, the sedimentary-cycle numbers are included. The numbering on the left-hand side indicates the sampled volcanic and volcano-clastic levels.

THE IZARORENE SECTION (IZ)

Approximately 5 km west of the Gourougou volcano, several marl-cliffs with a height of 80 m outcrop over a Quaternary plain near the Kert river, forming the sections of Samar (SA-1 section of Cunningham et al., 1997) and Izarorene (figure 4.1; Arias et al., 1976). The lower part of the Izarorene section is composed of 50 m thick dark blue, poorly stratified, homogeneous clayey marl overlying a two-meter-thick, white cinerite (figure 4.2; 7^{bis-ter} of Arias et al., 1976; IR-1.0 of Cunningham et al., 1997). The distinct upward transition from the homogeneous clays to a pronounced, six-fold bipartite marl-diatomite alternation marks the onset of sedimentary cyclicity of the top part of the section (figure 4.2, Event A). These six cycles are numbered upward in stratigraphical order (IZc1 to IZc6) and consist of 1-3 m thick, finely laminated diatomites, and 3-6 m thick homogeneous marls, which grade from brownish gray to bluish marine deposits, and include a variety of macro-fauna, e.g. abundant echinoids and crabs. Within the homogeneous marls of IZc3 several tephra layers are present, corresponding to the 11^{bis-14^{ter}} ashes of Arias et al. (1976). In addition, two thin volcano-clastic layers are located at the base of IZc5 and within the marl IZc6, respectively. Unconformably overlying the cyclic succession is a reddish clay covered by a sandstone.

THE MESSÂDIT SECTION (ME)

The Messâdit section is located along the western coast of the peninsula, in the hillside opposite the village of Messâdit (figure 4.1; Gaudant et al., 1994; Rachid et al., 1997; Saint Martin and Cornée, 1996). It consists of a 70 m thick, well-exposed, blue-to-brownish diatomaceous marl sequence, rich in ostracods and bivalves. Several volcanic tuffs and ashes are intercalated, corresponding to recently dated tephtras (Münch et al., 2001; Roger et al., 2000). The Neogene sequence comprises a total of 35 well defined, mostly bipartite sedimentary cycles capped by a *Halimeda*-algae packstone. These cycles are numbered successively with increasing stratigraphic level, hereafter referred to as MEc1 to MEc35 (figure 4.2).

The base of the section is formed by a volcanic tuff. An angular unconformity separates this ash from the underlying glauconitic sand unit, described as a "Basal Messinian glauconitic conglomerate above the Tortonian substratum" (e.g., Gaudant et al., 1994; Rachid et al., 1997). The tuff is directly overlain by blue clayey marl, followed by twelve bipartite cycles composed of indurated cherty laminites and homogeneous sediments (MEc1-MEc12). The basal cycles have an average thickness of 200 cm, except for MEc7 (380 cm) and MEc11 (370 cm). The first cycle (MEc1) marks the onset of sedimentary cyclicity in the section (Event A). Additionally, a conspicuous change in color from bluish to brownish-gray marls is observed in MEc6 (Event B in figure 4.2).

The base of MEc13 marks the next distinct change in lithology from cherty laminites to well-developed white diatomites (Event C in figure 4.2). Numerous sponge spicules, bivalve fragments, bryozoans, planktonic and benthic foraminifera and abundant fish remains are found from this level upwards. Additionally, MEc15 to MEc20 display a change to tripartite cyclicity, in which the diatomites grade upward into reddish-brown laminated marls, followed by grayish homogeneous silty marls containing numerous oysters. From MEc21 upward, bipartite sedimentary cyclicity of distinct diatomites and homogeneous brown marls is continued. The laminite of MEc21 is thin (22 cm) compared to other laminites (30-50 cm). MEc24 contains an extreme thick diatomite bed (213 cm), above which two levels rich in *Neopycnodonte* oysters are recorded. This

oyster-rich level can be traced along the entire outcropping cliff.

The sedimentary cyclicity is less regularly developed from MEC29 upward, due to an increase in siliciclastic influx. Nevertheless, a variety of bipartite lithological alternations is observed. Both MEC29 and MEC33 are composed of thin, pronounced diatomites and brown, homogeneous silty marls. MEC32 and MEC34 consist of thick, cherty diatomites, while MEC30 contains a vaguely laminated diatomaceous marl. Within MEC31, a bipartite alternation of a gray indurated marl and a soft brown marl is taken as a possible extra bipartite interval (MEC31a). The uppermost interval of the section (above laminite MEC34) consists of an alternation of silty marl, gray indurated marl and soft brownish marl, most likely representing the last bipartite couples (MEC35) prior to the deposition of the capping *Halimeda*-algae packstone.

A total of 19 tephras intercalated in the cyclic marls have been sampled for isotopic dating (figure 4.2). The stratigraphic position of the tephras forms an additional correlation tool and especially allows the Messâdit section to be correlated to the Ifounassene section (table 4.2; Münch et al., 2001; Roger et al., 2000).

THE IFOUNASSENE SECTION (IF)

The Ifounassene section is formed by a steep-sided coastal cliff incised by two narrow river valleys just north of the border with the Spanish enclave of Melilla and corresponds to the basal part of the Rostrogordo section (Cunningham et al., 1994; Gaudant et al., 1994; Rachid et al., 1997; Saint Martin and Rouchy, 1986). The section is composed of a cyclic marl sequence with a stratigraphic thickness of 30 m. It is capped by a pronounced *Halimeda*-algae packstone, which can be traced land-inwards towards the prograding reef complex (Cunningham et al., 1994). A total of 17 bipartite sedimentary cycles are recorded, consisting of an alternation of laminated lithologies and homogeneous, partly silty marls, which have been numbered in a stratigraphic order from base to top (named as IFc1-IFc17, figure 4.2). The laminated lithologies grade from clayey laminites to well-developed (cherty) diatomites, containing abundant bryozoan and bivalve fragments as well as shallow benthic foraminifera. By contrast, planktonic foraminifera are more dominant in the homogeneous sandy marls, where bryozoans are usually less abundant.

The base of the section is formed by a volcanic tuff (Ifo-01/02), which covers gray, homogeneous marls with load-structures. This tuff is overlain by two laminated, dark-brown clays, which grade upward into homogeneous clay (IFc1-IFc2). The interval above the basal clay is characterized by a diatomaceous sequence, comprising nine cycles of which the individual cycle-thickness varies significantly (range: 170-230 cm). An extreme thick diatomite (230 cm) characterizes IFc5, above which two distinct *Neopycnodonte* levels occur within a homogeneous marl, as in Me24. Within the homogeneous interval of IFc7, mixing with volcano-clastic detritus occurs. A thin diatomaceous cycle (27 cm), including a concentrated ash layer (Ifo-4 ash) is present above this level. Cycles IFc12 to IFc15 consist of a bipartite cyclicity of laminated, partly diatomaceous marls alternating with silty homogeneous marls, which are in general burrowed and contain abundant mollusks, sponge spicules and a variety of shallow marine macro-fauna (fish, echinoids). The uppermost part of the section is composed of an alternation of homogeneous, fine-grained yellow sands, two laminated thin cherts (IFc15a and IFc17) and a diatomaceous, laminated marl (IFc16). These layers are covered by the *Halimeda* algae packstone, which contains thin silt-intercalations as well as a thin, well-developed volcanic ash (V3 of Cunningham et al., 1994).

BIOSTRATIGRAPHY

The planktonic foraminiferal biostratigraphy of the Melilla Basin is based on the stratigraphic distribution of selected marker species, which occur synchronously over the Mediterranean basin and have been astronomically dated (Krijgsman et al., 1999a; Sierro et al., 2001). Five marker-events have been identified in the Melilla Basin (figures 4.2 and 4.4, table 4.1).

The basal sediments of the Izarorene and Messâdit sections contain forms of the *Globorotalia miotumida* group, indicating that both sections were deposited above the first common occurrence of the group of *G. miotumida*, astronomically dated at 7.24 Ma (Hilgen et al., 1995; Sierro et al., 2001). This event can be used as a reliable marker of the Tortonian-Messinian boundary since it closely coincides with its global boundary stratotype recently defined in Morocco at 7.251 Ma (Hilgen et al., 2000b, 2000c).

In the lowermost part of Messâdit and Izarorene, the first occurrence (FO) of the *Globorotalia nicolae* was observed below the second cherty indurated level, while its last common occurrence (LCO) is located above the sixth diatomite in Izarorene and right below diatomite MEC7 in Messâdit. The FO of *G. nicolae* was first identified and astronomically dated (6.829 Ma) in the Faneromeni and Metochia sections in Greece (Hilgen et al., 1995; Krijgsman et al., 1995). Both the FO and the LCO of the species were also recognized in the Abad composite section in SE Spain that has been proposed as the reference section for the late Messinian part of the APTS (Sierro et al., 2001). They were astronomically dated at 6.828 and 6.713 Ma, respectively.

Intermediate specimens between *Globigerina obesa* and *Globigerinella siphonifera* are relatively rare in Izarorene and the lower part of the Messâdit section, but a prominent incursion of these forms was identified in the brownish marls above indurated layer MEC11. The FCO of these forms are also observed in the Abad composite section and other Mediterranean sections (6.613 Ma; Sierro et al., 2001, 2003).

A prominent sinistral-to-dextral coiling change of *Neogloboquadrina acostaensis* is located slightly above the extremely thick diatomites in the Messâdit and Ifounassene sections (MEC24/IFc5). A similar change has been recorded in the pre-evaporite marls of many Mediterranean sections and in the North Atlantic, slightly predating the onset of the latest Miocene glaciation (Hodell et al., 1989, 1994, 2001; Krijgsman et al., 1999a, 2002; Hilgen and Krijgsman, 1999; Sierro et al., 2001). It is therefore astronomically dated at 6.360 Ma. Above this event, the Neogloboquadrinids are dominantly dextral coiled, but a prominent influx of

Event	Bio-Sedimentary Events	APTS age (Ma)
A	Onset (Cyclic) Diatomite Deposition	6.850
1	FO <i>G. nicolae</i>	6.850
2	LCO <i>G. nicolae</i>	6.713
B and 3	FaO <i>G. obesa</i>	6.613
C	Onset Tropical Diatomite blooms	6.580
-	Monospecific <i>G. bulloides</i>	6.455-6.475
-	<i>G. quinquiloba</i> and <i>G. multiloba</i>	6.41-6.39
4	Sinistral/Dextral coiling change <i>G. acostaensis</i>	6.360-6.340
5	Sinistral influx <i>G. acostaensis</i>	6.126
D	Final Diatomite Bloom	6.11
E	Base of <i>Halimeda</i> -bed	6.07

Table 4.1 Biostratigraphic marker-events recorded within the Melilla basin.

The astronomical ages correspond to APTS ages of Krijgsman et al. (1999a) and Sierro et al. (2001).

sinistral forms was identified within the homogeneous marls of cycle MEc33 and IFc15. This bio-event was correlated with the first of two influxes of sinistral Neogloboquadrinids occurring in Spain, Italy and Greece below the onset of the evaporite deposition (Hilgen et al., 1999; Krijgsman et al., 1999a; Sierro et al., 2001) and dated at 6.126 Ma. The uppermost levels of Messâdit and Ifounassene are almost devoid of planktonic foraminifera, preventing the recognition of other younger foraminiferal events in this part of the sections.

Additionally, the common to abundant occurrence of *Turborotalita quinqueloba* and *Turborotalita multiloba* in cycle MEc22, and the abundant, almost monospecific, occurrence of *Globigerina bulloides* in cycles MEc18 and MEc19 in Messâdit, can be used as secondary bio-events (table 4.1). Similar events have been observed in the Abad composite section in SE Spain from 6.47 to 6.43 Ma (Sierro et al., 2001, 2003).

MAGNETOSTRATIGRAPHY

Oriented samples have been taken from each section for paleomagnetic analysis at a resolution of at least 5 drilled levels per sedimentary cycle, using an electrical field-drill and magnetic compass. To avoid overprinting by weathering, samples (2.5 cm diameter each) were taken from material as fresh as possible. A total of 222 sample-levels were drilled: 30 at Izarorene, 141 at Messâdit and 51 at Ifounassene. Paleomagnetic analysis in the laboratory included stepwise (per 30°C) thermal demagnetization and measurement of NRM decay was performed on a 2G DC SQUID cryogenic magnetometer. Tectonic correction was not necessary because of sub-horizontal bedding of the sections.

The bulk of the samples typically display a weak magnetic signal (<1 mA/m). Generally, a two-component magnetization is observed, consisting mostly of a sub-recent normal overprint (80°C-210°C) and a characteristic remanent magnetization (ChRM). This ChRM could be isolated after moderate thermal demagnetization (240°C-390°C). Stepwise demagnetization was continued until complete removal of the high-temperature component or until the NRM became inconsistent or scattered.

Several demagnetization diagrams are given in figure 4.3, showing examples of samples with either a clear polarity (figures 4.3a,b), a valid but extremely weak signal (figure 4.3c), or a clustering at temperatures ranging from 200°C - 480°C (figure 4.3d). Other samples show poorly or unreliably determined components, as the NRM's bypass the origin, after which a clustering is observed (figures 4.3e), or consist only of scattering (figure 4.3f). The latter types of samples do not yield any reliable results regarding polarity. Therefore, the polarity zones as shown in figure 4.4, are based on the first group of data.

The magnetostratigraphic results of Izarorene display a reversed polarity interval for the lower part of the section, whereas no reliable results are available for the top of the section. The basal 15 m of Messâdit do not display a clear polarity, whereas a N-R-N polarity is apparent for the main part of the section. Between MEc5 and MEc19, the section shows an overall normal polarity, followed by a reversed interval between MEc20 and MEc27, changing into a normal polarity from MEc27 upwards. The basal 10 m of the Ifounassene section have not been sampled for magnetostratigraphy. From IFc6 to IFc10 the section is reversed, whereas from IFc11 upward the section displays normal polarity. We can conclude that the paleomagnetic signal of the Melilla Basin displays a weak but straightforward R-N-R-N reversal pattern, although no certainty can be given on the precise location of each reversal.

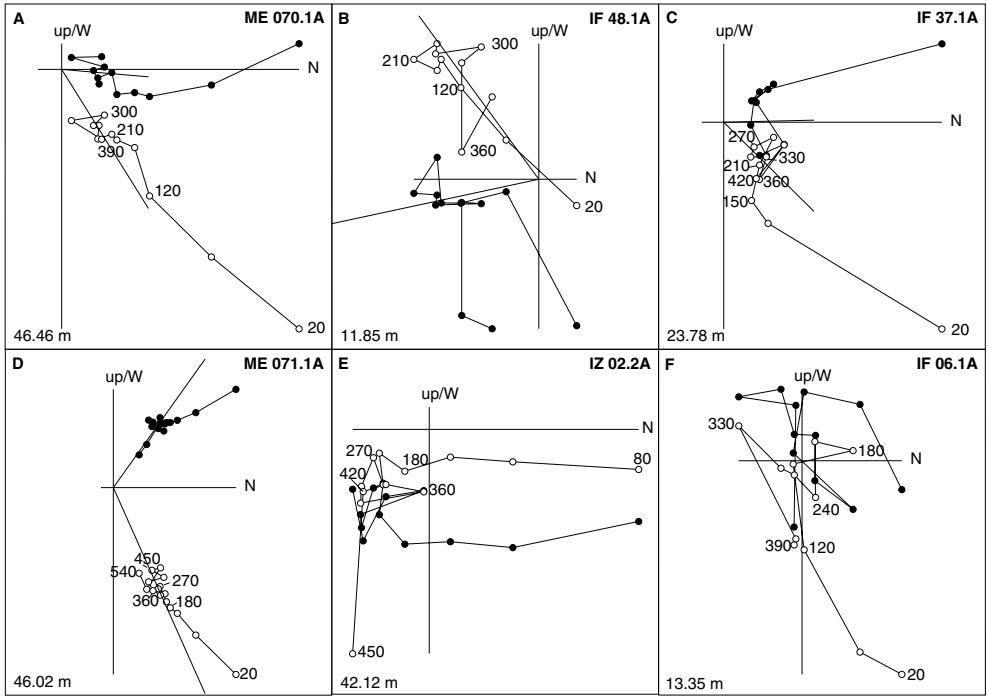


Figure 4.3 Stepwise thermal demagnetization (Zijderveld) diagrams of selected samples from the Izarorene, Messâdit, and Ifounassene sections.

Closed (open) symbols denote the projection of the ChRM vector end-points on the horizontal (vertical) plane. The included values represent temperature in °C; stratigraphic levels are included in the lower left corners.

INTEGRATED STRATIGRAPHIC FRAMEWORK

The astronomical tuning of the Neogene marl sequence of the Melilla Basin is primarily based on the recognition of planktonic foraminiferal events. A large number of late Neogene bio-events are synchronous over the Mediterranean Basin, as demonstrated by detailed biostratigraphic studies on astronomically calibrated Mediterranean sections (Hilgen et al., 1995; Hilgen and Krijgsman, 1999; Siero et al., 2001). Five of these have been identified in the Melilla Basin. The stratigraphic order of these events, supplemented by the ATS ages, is (figures 4.2 and 4.4; Krijgsman et al., 1999a):

- 1) *G. nicolae* FO at 6.828 Ma;
- 2) *G. nicolae* LCO at 6.713 Ma;
- 3) *G. obesa* FAO at 6.613 Ma;
- 4) Sinistral-to-dextral coiling change of *N. acostaensis* at 6.360-6.340 Ma;
- 5) First sinistral influx of *N. acostaensis* at 6.126 Ma.

The accurate age-control of these planktonic foraminiferal events allows direct correlation of the bipartite sedimentary cycles to the summer insolation target-curve of Laskar (La93_(1,1); Laskar et al., 1993a; figure

4.4). The phase-relation of the sedimentary cyclicity with respect to the target-curve is primarily based on the lithostratigraphic position of the tuned bio-events, supplemented by variations in planktonic foraminiferal assemblage and abundance per lithology. Overall, the homogeneous intervals contain a high planktonic foraminiferal content and minor amounts of bryozoan and bivalve fragments within the homogeneous intervals, while a reduction in planktonic foraminifera and large amounts of mainly bryozoans are observed within the laminated lithologies. This alternation resembles a similar pattern in the Upper Abad member of the Sorbas Basin (Sierra et al., 2001, 2003), in which a strong periodic reduction in the abundance of planktonic foraminifera occurs near the transition from homogeneous marls to sapropels. Moreover, the presence of warm-oligotrophic foraminifera within the upper part of the homogeneous marls of several cycles in the Melilla Basin corresponds to a similar pattern within the sapropels of the Upper Abad. Based on these repetitive patterns, we suggest a bed-to-bed correlation of the upper part of the homogeneous marls in Melilla to the sapropels in Sorbas. Since sapropels are undoubtedly linked to precession minima and insolation maxima, we therefore assume that the homogeneous levels in Melilla correlate to the summer insolation maxima.

The stratigraphic position of the biomarker events from the FO of *G. nicolae* (6.828 Ma) to the *N. acostaensis* coiling change (6.360-6.340 Ma), and the number of cycles between these marker events within the Melilla Basin, is similar to astronomically calibrated Mediterranean sections. Moreover, characteristic patterns in the target-curve are mirrored by the more-than-average cycle thickness of MEC11 and MEC24/IFc5: the extra thick marl of MEC11 corresponds to a precession cycle with a prolonged period of 29 kyr, correlating to the cycle UA4 in Sorbas, and the thick diatomite of MEC24/IFc5 corresponds to a double minimum peak at 6.360-6.340 Ma (figure 4.4; Krijgsman et al., 1999a; Sierra et al., 2001). The resulting astronomical tuning of the sections indicates that no cycles are missing in this interval of the sedimentary record, and moreover confirms the precession-induced origin of the sedimentary cycles of the Melilla Basin (figure 4.4). The tuning has resulted in astronomical ages for the bio-sedimentary events of the Melilla Basin: 6.85 Ma for the onset of diatomaceous cyclicity (Event A), 6.73 Ma for the marl-lithology and faunal transition (Event B), and 6.58 Ma for the start of pure diatomite deposition in the basin (Event C).

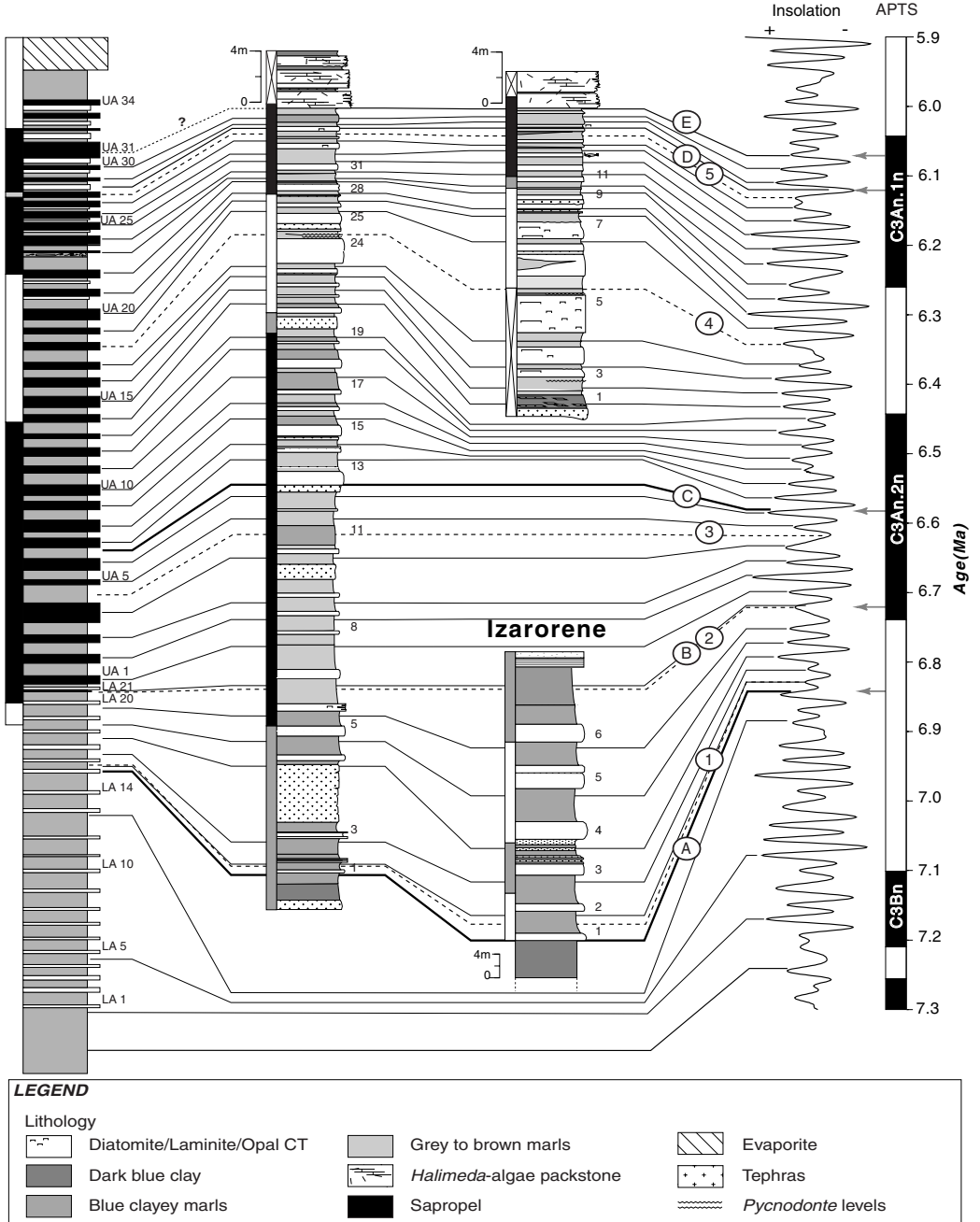
Tuning of the interval above the *N. acostaensis* coiling change is less straightforward due to an increased terrigenous influx and enhanced volcanic activity. In particular, the lithology alternations at Messâdit are, in part, poorly developed. At Ifounassene, however, a total of ten sedimentary repetitions are present between the *N. acostaensis* coiling change datum and the first sinistral influx level of the *N. acostaensis* (6.126 Ma), which is in perfect agreement with ten sedimentary cycles in the Sorbas basin and the ten insolation minimum peaks in the ATS (figure 4.4). We therefore change to the Ifounassene section for the upward continuation of the astronomical calibration, making use of the *Pycnodonte* level located above the coiling change level in both sections. As a result, the youngest diatomite bed in the basin (2 m below the *Halimeda*-algae packstone) has an astronomical age of 6.11 Ma (Event D in MEC34/IFc16). Because another two sedimentary cycles are present above this youngest diatomite both at Ifounassene and Messâdit, the onset of the *Halimeda*-packstone has an astronomical age of 6.07 Ma (Event E). The tuning of the individual sedimentary cycles of the Melilla basin to the ATS also provides astronomical ages for the intercalated ashes. These are given in table 4.2, in which they are compared with the isotopic $^{40}\text{Ar}/^{39}\text{Ar}$ ages of recent studies (Cunningham et al., 1994, 1997; Roger et al., 2000).

Sorbas Basin
Spain

Messâdit

Ifounassene

Summer 65°N
La93_(1,1)



Even though part of the paleomagnetic signal of the sampled marls is unreliable, the magnetostratigraphic results are in good agreement with the presented biostratigraphy (figure 4.4). Our results are consistent with the findings of Cunningham et al. (1994, 1997), and show that the normal polarity intervals correspond to the chrons C3An.1n and C3An.2n (Cande and Kent, 1995). Several minor discrepancies, however, do occur between the APTS and the cyclostratigraphic position of the reversals in the Melilla Basin. The C3An.2n(y) reversal is recorded in the homogeneous marl of MEc19, which is one cycle below its ATS position. This shift can be attributed to a delayed acquisition of the magnetic signal, which is a commonly observed phenomenon in cyclically bedded sequences of the Mediterranean Neogene (Van Hoof and Langereis, 1992). Again, a similar discrepancy is observed for C3An.1n(o) in Messâdit (MEc27), whereas the recording of this reversal in Ifounassene is at least two sedimentary cycles higher in the stratigraphic sequence with respect to Messâdit (figure 4.4).

DISCUSSION

COMPARISON TO PREVIOUS WORK ON THE MELILLA BASIN

Previous geochronological studies in the Melilla Basin mainly concerned isotope geochronology and were focused on the petrology and volcanology of the domes and lava flows of the Gourougou and Trois Fourches volcanic complexes (e.g. El Bakkali et al., 1998; Cunningham et al., 1994, 1997; Hernandez and Bellon, 1985; Roger et al., 2000). Münch et al. (2001) and Cornée et al. (2002) focus on the geochronology and development of the carbonate platform and its basinal equivalents using $^{40}\text{Ar}/^{39}\text{Ar}$ ages of volcanic horizons. Several of the volcanic horizons described in these two studies are located in the astronomically tuned sections of this study. Astronomical ages can therefore be assigned to $^{40}\text{Ar}/^{39}\text{Ar}$ dated volcanic tephras and the results of two independent dating methods can be compared (table 4.2). The $^{40}\text{Ar}/^{39}\text{Ar}$ ages of Cunningham et al. (1994, 1997), have been recalculated with the Fish Canyon Tuff standard (FCT) of 28.02 Ma (Renne et al., 1998) to allow a reliable comparison of different studies.

Cunningham et al. (1997) have dated the basal cinerite in the Izarorene section at 6.90 ± 0.02 Ma (table 4.2). This isotopic age is in good agreement with our findings, because the first astronomically dated sedimentary cycle (IZc1), dated at 6.85 Ma, is located 40 m above this ash layer (IR-1 ash in table 4.2; Cunningham et al., 1997). The tephras between sedimentary cycles IZc3 and IZc4, corresponding to the 11^{bis}-14^{ter} ashes of Arias et al. (1976), have an astronomical age of 6.79 Ma, which falls within the 2σ -error

Figure 4.4 High-resolution astrochronological tuning of the basinal sections of the Melilla Basin (previous page).

The tuning is based on the biostratigraphic position of astronomically calibrated marker events (events 1-5), in comparison to the sedimentary cyclicity (lithostratigraphic columns). The magnetostratigraphic columns (included on the left side of each lithostratigraphic column) enable further comparison to the APTS curve at the right. Black (white) intervals represent normal (reversed) polarity, the polarity in the gray intervals is uncertain. The composite section of the Sorbas basin in southern Spain is included for comparison to other astrochronologically-tuned sequences in the Mediterranean basin. Based on a repetitive pattern of abundant planktonic foraminifera within the homogeneous marl intervals and numerous bryozoa fragments, echinoids, fish fragments etc. and only sparse planktonic foraminifera within the laminated intervals, astronomical tuning of the sedimentary cyclicity is based on the relationship that the top of the homogeneous levels corresponds to insolation maxima. This is equivalent to a similar pattern in Sorbas.

This study		Previous studies	
Izarorene	APTS age (Ma)	Arias et al. (1976)	Cunningham et al. (1997)
Iza-3	6.72	-	-
Iza-2	6.76	-	-
Iza-1	6.79	11 ^{bis} -14 ^{ter} 5.6 ± 0.3 (K/Ar biotite) 5.9 ± 0.3 (K/Ar biotite) 7.1 ± 0.4 (K/Ar biotite) 6.7 ± 0.6 (FT glass) 6.6 ± 1.0 (FT glass)	-
Basal Cinerite	<6.85	7 ^{bis-ter} 6.8 ± 0.3 (K/Ar glass) 6.0 ± 0.3 (K/Ar glass) 6.4 ± 0.6 (FT glass) 6.3 ± 0.6 (FT glass) 6.8 ± 1.16 (FT glass)	IR-1.0: 6.90 ± 0.02
Messâdit	APTS age (Ma)	Cunningham et al. (1997)	Roger et al. (2000)
-	-	V3: 6.0 ± 0.1	-
Mes-19	6.05 ± 0.02	-	-
Mes-18	6.27	-	-
Mes-17	6.29	-	Located
Mes-16	6.31	-	-
Mes-15	6.33	-	-
Mes-14	6.38	-	-
Mes-13	6.39	-	-
Mes-12	6.45	-	-
Mes-11	6.54	-	Located
Mes-10	6.56	-	-
Mes-9	6.58	-	Me-16: 6.46 ± 0.03
Mes-8	6.63	-	Me-13: 6.54 ± 0.04
Mes-7	6.68	-	-
Mes-6	6.72	-	-
Mes-5	6.76	-	-
Mes-4	6.79	V2: 6.72 ± 0.02 V2: 6.76 ± 0.02	Me-5: 6.73 ± 0.02
Mes-3	-	-	-
Mes-2	-	-	-
Mes-1	<6.83	V1: 7.05 ± 0.14	Located
Ifounassene	APTS age (Ma)	Cunningham et al. (1997)	Roger et al. (2000)
-	-	V3: 6.0 ± 0.1	-
Ifo-6	6.05 ± 0.02	-	-
-	-	-	If-4: 6.29 ± 0.02
Ifo-5	6.26	-	-
Ifo-4	6.28	-	-
Ifo-3	6.32	-	-
Ifo-2	6.46	-	-
Ifo-1	6.46	-	-

Table 4.2 Compiled correlation table of the astronomical and isotopic ($^{40}\text{Ar}/^{39}\text{Ar}$) ages of the volcanic ashes, embedded in the Messinian marl and carbonate sequences of the Melilla Basin.

The ashes are ordered by their stratigraphic position. The astronomical ages are obtained by a bed-to-bed correlation of the marl-sections to the APTS (Krijgsman et al., 1999a; Sierro et al., 2001). The isotopic ages of Arias et al. (1976) and Cunningham et al. (1997) have been recalculated relative to FCT of 28.02 Ma (Renne et al., 1998). The located ashes of Roger et al. (2000), represent ashes which are mentioned in the article of Roger et al. (2000) without $^{40}\text{Ar}/^{39}\text{Ar}$ dates. For the $^{40}\text{Ar}/^{39}\text{Ar}$ ages of Roger et al. (2000), the 1σ analytical error is displayed.

of the isotopic ages of ~ 6.7 Ma (FT age). Nevertheless, we prefer not to take into account the less precise K/Ar derived isotopic ages of the latter study in the comparison of astronomical and isotopic ages.

Roger et al. (2000) studied six volcanic horizons interbedded in the Messâdit section from which three have been used for $^{40}\text{Ar}/^{39}\text{Ar}$ dating. The most straightforward correlation of these volcanic horizons to the ash layers found in our study is given in table 4.2. Based on their stratigraphic position within the Messâdit section, the following correlation can be given. The three most pronounced volcanic ashes in Messâdit are the thick basal ash (Mes-4), and the Mes-8 and Mes-9 ashes in the central part of the section. These ashes correspond respectively to the Me-5, Me-13 and Me-16 ashes of Roger et al. (2000).

Cunningham et al. (1994, 1997) sampled and dated two volcanic tuffs (V1 and V2 in their Irhzer Ifzatenne section) in the bioclastic platform north of Ifounassene. These two ashes are likely the equivalents of the lowermost ashes of our study (Mes-1 and Mes-4). Similar to our Mes-1 ash, V1 is located directly above glauconitic ramp deposits at the base of the marl sequence, while V2 is located 10 m above V1 within the lowermost marls at a comparable position as our Mes-4. V2 therefore has a younger isotopic age of ~ 6.74 Ma with respect to the inferred ATS age of 6.79 Ma (table 4.2), whereas V1 is clearly older than the onset of sedimentary cyclicity within the basin. Comparison of the isotopic and astronomical ages of these ashes indicates that the $^{40}\text{Ar}/^{39}\text{Ar}$ ages in Messâdit are systematically younger than the astronomical counterparts (table 4.2).

$^{40}\text{Ar}/^{39}\text{Ar}$ ages are also available for several volcanic layers in the Ifounassene section (Cunningham et al., 1997; Münch et al., 2001; Roger et al., 2000). Although stratigraphic distances in the Rostrogrado section of Münch et al. (2001) do not fully agree with ours, their three volcano-clastic horizons most likely correspond with our Ifo-3, Ifo-4 and Ifo-5 ashes (figure 4.2). Roger et al. (2000) have only dated one volcanic tuff (If-4) below the *Halimeda*-index bed, but the stratigraphic position of this ash is uncertain. Based on the correlation of their work to that of Münch et al. (2001), the If-4 ash of Roger et al. (2000) might be the lateral equivalent of our Ifo-5 ash (table 4.2). This is mainly supported by the ash-thickness, which implies, however, that the $^{40}\text{Ar}/^{39}\text{Ar}$ age of this volcanic tuff is slightly older than its stratigraphic position would suggest (table 4.2).

Additionally, Cunningham et al. (1997) sampled ash V3 above the *Halimeda*-index bed. Because the base of this *Halimeda*-bed forms the top of the astronomically tuned part of our section, V3 must be younger than the ATS age of 6.05 Ma (figure 4.4), which is in agreement with the isotopic age (6.0 ± 0.1 Ma in table 4.2; Cunningham et al., 1997).

In summary, the $^{40}\text{Ar}/^{39}\text{Ar}$ ages of three tephras in Messâdit are systematically younger than the astronomical ages of these layers, while at Ifounassene the correlation is not certain. As previously mentioned, all $^{40}\text{Ar}/^{39}\text{Ar}$ ages have been calculated with the currently common-used age of 28.02 Ma for the Fish Canyon Tuff sanidine mineral dating standard of Renne et al. (1998). A recent discussion about the precision and accuracy of the absolute ages of neutron fluence monitors and decay constants used in $^{40}\text{Ar}/^{39}\text{Ar}$ geochronology (Begemann et al., 2001) calls for new assessment of these parameters. A shift towards slightly older absolute ages for the Fish Canyon Tuff, based on U/Pb dating on zircon and titanite (Schmitz and Bowring, 2001) will result in older absolute $^{40}\text{Ar}/^{39}\text{Ar}$ ages reducing the age differences

between the isotopic and astronomical ages in Messâdit. Roger et al. (2000) assign $^{40}\text{Ar}/^{39}\text{Ar}$ ages to three main pre-evaporitic biosedimentary events within the Melilla Basin, for which we have now derived the astronomical ages (Events A, C and E). The differences between the astronomical and isotopic ages of these events resulted in part from the differences in dating method, as described above. An additional error stems from the lack of a stratigraphic correction in the study of Roger et al. (2000), who simply assign the $^{40}\text{Ar}/^{39}\text{Ar}$ age of the tephra nearest to a biostratigraphic event to this event, without correcting for the time between the event and the deposition of the tephra.

COMPARISON TO THE PRE-EVAPORITIC MESSINIAN

The integrated stratigraphic framework of this study provides high-resolution dating of the open marine marls of the Melilla Basin. Comparison of these results to both Rifian and Mediterranean basins emphasizes the role of the Melilla Basin in the evolution of the Rifian Corridor. Although no details can yet be given on the onset of marine sedimentation within the Melilla Basin itself, the occurrence of Messinian homogeneous marine clays overlying "Tortonian" glauconitic sands, implies a rapid transgression prior to 6.85 Ma at which moment open marine, cyclic sedimentation started (Event A). Several authors argue an early Messinian age for the basal blue, homogeneous clayey marls, in which case these deposits are coeval with the "late Tortonian-early Messinian Blue Marls" in the Taza-Guercif, Saïss and Chelif basins in the Rifian Corridor (Barbiéri and Ori, 2000; Bernini et al., 1992; Gelati et al., 2000; Krijgsman et al., 1999a; Mansour and Saint Martin, 1999). The late Tortonian deepening of these central Rifian basins is attributed to an advancing thrust front in the central part of the Rif (Sani et al., 2000), corresponding to the late Miocene compression within the Alboran Basin (e.g., Comas et al., 1992; Sani et al., 2000). Rapid uplift of these basins resulted after 7.17 Ma in the obstruction of Atlantic water inflow and therefore the onset of closure of the Rifian Corridor (Krijgsman et al., 1999b). This early Messinian restriction of marine water-exchange through the Rifian Corridor is thought to have caused a so-called siphoning of cold Atlantic waters into the western Mediterranean (e.g., Benson et al., 1991; Cunningham and Collins, 2002). This might explain the cold-water signature within the first open marine deposits in the Melilla Basin (figure 4.5; Barbiéri et al., 1976; Benmoussa et al., 1987).

At 6.85 Ma (Event A), cyclic sedimentation was triggered within the deeper parts of the Melilla Basin, while in the nearshore zone surrounding the Trois Fourches and Gourougou volcanoes, carbonate ramp-deposition was replaced by a prograding bioclastic platform (unit 2 of Saint Martin and Cornée, 1996; Roger et al., 2000). Saint Martin and Cornée (1996) attribute this depositional change to a transgressive to highstand relative sea-level fluctuation, coincident with an increased influx of boreal prone-waters (Rachid et al., 1997). Our astronomical tuning allows the testing of this hypothesis by a high-resolution correlation to the climate $\delta^{18}\text{O}$ record of the world oceans (figure 4.5; Hodell et al., 1994, 2001). It then appears that the onset of cyclicity within the Melilla Basin does not correspond to a significant decrease in $\delta^{18}\text{O}$ of the world ocean (figure 4.5; Hodell et al., 2001). Since no coeval, evident depositional changes have been recorded for other Mediterranean basins at 6.85 Ma, a climate-induced sea-level rise can therefore not be considered as the triggering mechanism for Event A (figures 4.4 and 4.5). Moreover, the possibility of enhanced influx of boreal-prone waters through the Rifian Corridor is not supported by the shallow marine facies in the Taza-Guercif basin (figure 4.5; Gomez et

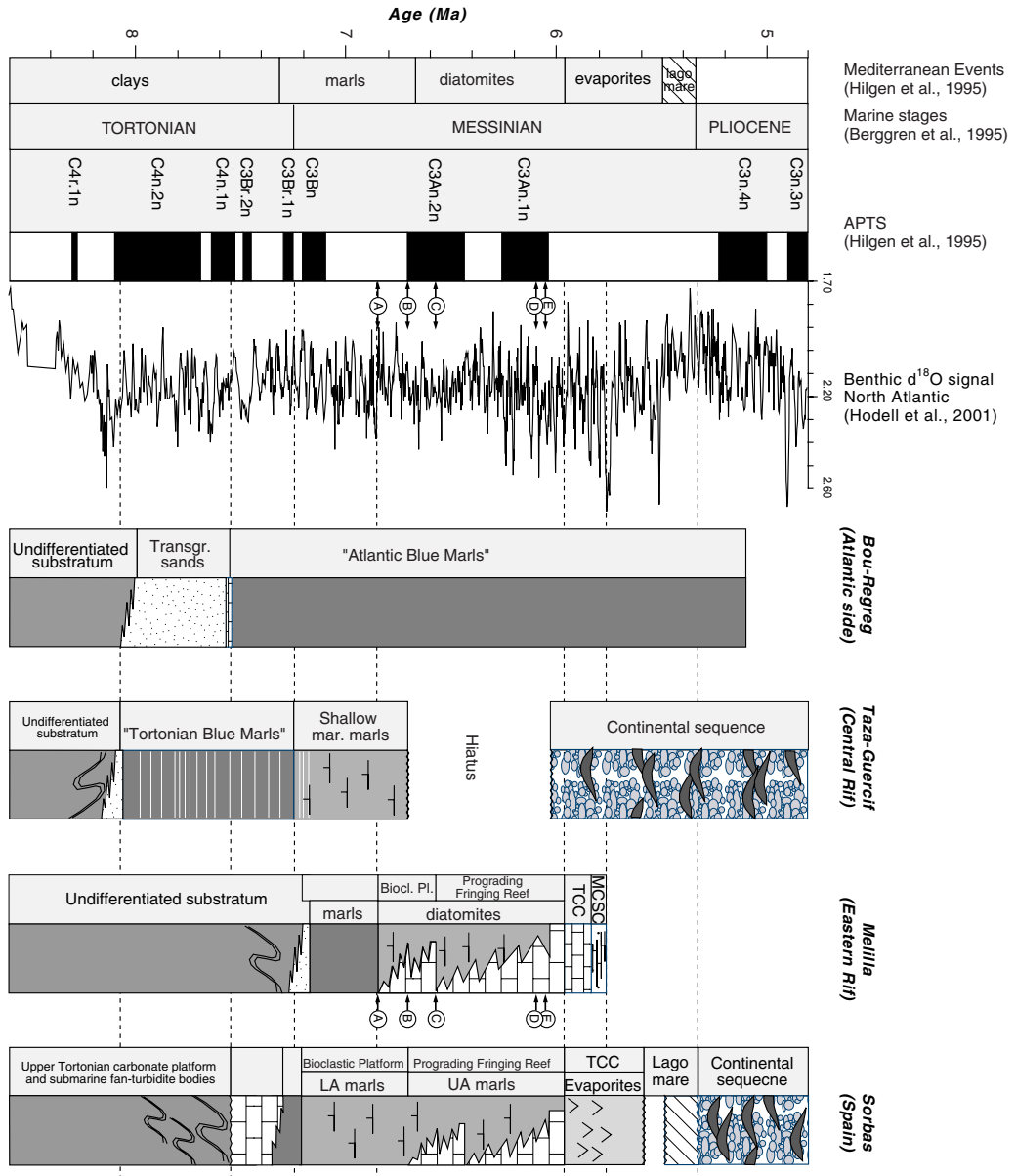


Figure 4.5 Regional correlation between major basin components of the Rifian Corridor for the late Miocene. Time-calibration is based on the astronomical tuning of various sections in each of the basins, including the Melilla Basin. MCSCTCC and TCC stand for the brackish to continental Mixed Carbonate Siliciclastic Complex and Terminal Carbonate Complex, respectively.

al., 2000; Krijgsman et al., 1999b). Tectonic activity within the Rif is therefore the most likely triggering mechanism for the change in depositional environment within the Melilla Basin at 6.85 Ma.

The distinct lithology transition of Event B above the *G. nicolae* Zone (6.72 Ma; figures 4.2 and 4.4) is recorded both within the Izarorene and Messâdit sections. Event B marks the prominent coeval change in the benthic foraminiferal assemblages that flourish in restricted waters. This suggests a sudden restriction of bottom water circulation at 6.72 Ma, which resulted in lower rates of oxygen turnover in the Melilla Basin. Final marine deposition upon the western plain of the Melilla basin is halted directly above Event B (e.g., Izarorene section), which coincides with the base of the unconformity marking the nearshore-continental transition in the Taza-Guercif basin (Krijgsman et al., 1999b).

Coeval to Event B is the lower-to-upper-Abad transition in the Sorbas Basin in Spain (figures 4.4 and 4.5), which is generally attributed to an increase in tectonic activity in the internal Betics (figure 4.5; Martín and Braga, 1994; Sierra et al., 2001, 2003). A coeval increase in tectonic activity is present within the Rif.

The transition from indurated cherty layers to white, mm-laminated diatomites in Messâdit is indicated as Event C (MEc13; 6.58 Ma) and corresponds to the change from boreal-prone to tropical diatom assemblages within the marginal facies (Cunningham and Collins, 2002; Saint Martin and Rouchy, 1986; Saint Martin and Cornée, 1996). Roger et al. (2000) correlate this transition to the onset of prograding *Porites*-fringing reefs of the carbonate platform (unit 3 of Saint Martin and Cornée, 1996; Cunningham et al., 1994). This is supported by the presence of abundant influx of bryozoan-fragments starting at the base of diatomite of MEc13 (Event C). Although several authors attribute this (bio-)facies transition to an increased nutrient supply caused by enhanced upwelling (Pestrea et al., 1999; Saint Martin and Cornée, 1996; Rachid et al., 1997; Roger et al., 2000), we infer that increased upwelling rates are not supported by either observations from the central Rifian basins, or by the fact that temperate water-conditions were replaced by (sub-) tropical conditions (Gaudant et al., 1994). Cunningham and Collins (2002), on the other hand, have suggested that this transition marks the end of an early Messinian siphoning of Atlantic waters through the Rifian Corridor. This would explain both the transition in benthic taxa in the marginal facies as well as the transition from temperate-type limestone facies (molechfor) to (sub-) tropical limestone facies (chlorozoan) on the carbonate platform (Cunningham and Collins, 2002).

The youngest diatomites recorded in the basin have an astronomical age of 6.11 Ma (Event D). This latest diatomite bloom (Roger et al., 2000) marks the end of a continuous period of 730 kyr of cyclic diatomite deposition, the last 460 kyr of which are represented by pronounced diatomites (MEc13 to MEc34/IFc15a). The stratigraphic interval between this last diatomite bloom and the base of the *Halimeda*-packstone contains one or two precession-induced lithology cycles. Hence, we propose an astronomical age of at most 6.07 Ma for the base of the *Halimeda*-packstone and therefore for the final open marine deposition within the Melilla Basin

(Event E). Since Münch et al. (2001) and Roger et al. (2000) indicate that the *Halimeda*-packstones forms the basinal equivalent of the *Porites*-reefs in the Melilla Basin, we can now confirm their conclusion that the progradation of the *Porites* reefs ended prior to 6.0 Ma. Comparison of our work to the extensive work done on the carbonate platform of the Melilla Basin (Roger et al., 2000) implies that the aggrading *Porites* reefs (Fringing Reef unit of Cunningham et al., 1994, 1997) developed prior to the onset of Mediterranean evaporites (110 kyr before its start at 5.96 Ma; Krijgsman et al., 1999a, 2001, 2002). In addition, the onset of the Terminal Carbonate Complex (TCC -*sensu* Esteban, 1979) draping the carbonate platform can be considered coeval to the onset of the Lower Evaporites within the Mediterranean (Cunningham et al., 1994, 1997; Krijgsman et al., 2001; Fortuin and Krijgsman, 2003).

Additionally, the final open marine deposition within the Melilla Basin, as indicated by Event E, and the following final *Porites* reef progradation is roughly coeval with the emergence of the Taza-Guercif Basin (Krijgsman et al., 1999b). Altogether, these results imply a closure of the Rifian Corridor prior to 6.0 Ma, which is also suggested by the earliest African-European mammal-migration, which is dated roughly at 6.1 Ma (Benammi et al., 1996; Garcés et al., 1998).

CONCLUSIONS

Based on a detailed study of the Messinian marine marl sequence of the Melilla Basin, we can present a high-resolution time frame for this basin, with main emphasis on the importance of timing with respect to the evolution of the Rifian Corridor. Five bio-sedimentary marker events, representing time horizons for the Messinian evolution of the Mediterranean Realm, have been recorded within the studied basinal marl sequence. These marker events confirm a bed-to-bed correlation between the studied sections, which is based on the recognition of a cyclic pattern in lithology. We achieved a direct correlation of our sections to astronomically tuned sequences within the Mediterranean Sea and the insolation curve of Laskar (La93_(1,1); Laskar et al., 1993a), showing a precession-dependence of the sedimentary cyclicity in the Melilla Basin.

The resulting astronomical time frame significantly refines the timing for three basin-evolution events presented in previous articles by the French (Saint Martin and co-workers), and exemplifies the importance of the Melilla Basin with respect to the evolution of the Rifian Corridor. The new astrochronology for the marl sequences of the Melilla Basin allows an accurate dating of the stepwise restriction of the Mediterranean-Atlantic connection through Morocco, including the following events:

- 1) The onset of marine sedimentation within the Melilla Basin coincides with a tectonically induced shallowing of the Taza-Guercif Basin, and possibly with the onset of siphoning of Atlantic intermediate water through the narrowing Rifian Corridor. This phase appears moreover to be coeval to the deepening of several Betic Corridor basins (e.g., Sorbas and Nijar).
- 2) The initiation of cyclic deposition (Event A) in the Melilla Basin started at 6.85 Ma. This events marks a restriction in paleo-circulation within the basin, and was reflected by the onset of the progradation of a bioclastic platform along shore.

3) The bio-lithofacies transition of Event B at 6.72 Ma, coincides with main events within the Mediterranean, including the lower-upper Abad transition in Sorbas, and is coeval with the erosion-controlled closure or even emergence of the Taza-Guercif area.

4) Event C marks at 6.58 Ma the onset of white diatomite deposition reflecting a change in diatom species from boreal-to-tropical species and is coincident with the onset of prograding *Porites* reefs along the platform. We believe therefore that this event most likely reflects a decrease in upwelling rates and thus diminishing input of cold Atlantic waters (end of siphoning of Benson et al., 1991).

5) Closure of the open marine realm of the Melilla Basin was indicated by the final diatomite bloom (Event D at 6.11 Ma), followed by the production of *Halimeda*-algal beds, covering the cyclic marl sequence, starting at 6.07 Ma (Event E).

In summary, we conclude that the onset of open marine deposition within the Melilla Basin was initiated by tectonic activity of the Rif. The refined timing clearly shows that input of Atlantic waters through the Rifian Corridor was restricted after 6.85 Ma, and reduced to a minimum at 6.58 Ma. Moreover, the end of open marine deposition prior to 6.0 Ma supports the theories of a terminal carbonate complex (TCC) as the marginal equivalent of the evaporites of the Messinian Salinity Crisis. The high-resolution timing of the Melilla Basin indicates that the importance of diatomite sequences of the 'Tripoli'-type within Mediterranean basins reflects a superposition of local basin-configurations upon changes in the Mediterranean-wide paleo-circulation. Finally, the comparison of the isotopic ages for the bio-sedimentary basin-events (Cunningham et al., 1997; Münch et al., 2001; Roger et al., 2000) to our new astronomically calibrated ages indicates that the isotopic ages are dominantly younger.

CHAPTER 5

**$^{40}\text{Ar}/^{39}\text{Ar}$ DATING OF TEPHRA LAYERS INTERCALATED IN
ASTRONOMICALLY TUNED MARINE, UPPER MIOCENE
SEDIMENTARY SEQUENCES IN THE WESTERN
MEDITERRANEAN.**

INTRODUCTION

Steenbrink et al. (1999) confirmed the astronomical theory of climate change for the Pliocene by $^{40}\text{Ar}/^{39}\text{Ar}$ dating of volcanic ash layers distributed at several stratigraphic positions in the astronomically tuned sections in Ptolemais, resulting in an average period of 21.7 kyr for a cycle, equivalent to the expected duration of the cycles based on astronomical theory. $^{40}\text{Ar}/^{39}\text{Ar}$ data of the volcanic deposits in the Melilla Basin will be used to confirm the astronomical theory of climate change for the late Miocene for the first time with a method (i.e., $^{40}\text{Ar}/^{39}\text{Ar}$) completely independent from astronomical theory.

Once confirmed, the $^{40}\text{Ar}/^{39}\text{Ar}$ ages will be used for comparison with astronomical ages of the ash layers. In chapter 3 a discrepancy between isotopic $^{40}\text{Ar}/^{39}\text{Ar}$ and astronomical ages for the eastern Mediterranean was presented, where $^{40}\text{Ar}/^{39}\text{Ar}$ ages tended to be systematically younger than the astronomical counterparts. In chapter 4 an astronomical time frame was established for late Miocene sediments in the Melilla Basin, Morocco. This basin is located near the source area of two volcanic complexes active during the late Miocene, resulting in a large number of very coarse grained volcanic deposits intercalated in the astronomically tuned sections. Therefore, the existence (or non-existence) of systematic differences between the $^{40}\text{Ar}/^{39}\text{Ar}$ and astronomical tuning methods could be further explored in great detail, while the large crystal size (>1 mm) in some of the Melilla volcanic deposits enabled us to perform single crystal $^{40}\text{Ar}/^{39}\text{Ar}$ dating, allowing the detection of contaminating (xenocrystic) grains. To supplement the data for the western Mediterranean a few volcanic ash layers intercalated in the astronomically tuned Sorbas and Nijar Basins (Sierra et al., 2001) have been dated as well, although the crystal sizes were much smaller (125-250 μm) and biotite was the main suitable K-rich mineral.

GEOLOGICAL BACKGROUND

The Betic-Rif Cordilleras of southern Spain and northern Morocco constitute the westernmost extension of the Mediterranean Alpine orogenic belt, which formed in response to the convergence between the European and African plates during the Cenozoic. During the early to middle Miocene this convergence caused thrusting and westward migration of the Internal zones over the External zones (Figure 5.1a). Ongoing convergence between Africa and Iberia caused deformation along NE-SW and NW-SE strike slip faults and the formation of intramontane basins in SE Spain (Sanz de Galdeano and Vera, 1992). The Sorbas and Nijar Basins are two of those basins. The oldest Neogene sediments are conglomerates of Serravallian age, which are overlain by turbiditic sandstones. A major unconformity separates the turbiditic sandstones from overlapping shallow marine calcarenites (Azagador member) of latest Tortonian age (~7 Ma). The Azagador member changes upward into marls, clays and diatomites of early Messinian age (the Abad member). The Abad marls are deposited in the relatively deep parts (200-300 m, Troelstra et al., 1980) of the basins and they change laterally and vertically into platform carbonates and reefs. The Abad marls can be divided in two distinct units: the Lower and the Upper Abad marls. The Lower Abad unit consists of an alternation of indurated homogenous whitish marls and soft homogeneous grey marls rich in foraminifera. The Upper Abad is characterized by the intercalation of sapropels and indurated diatom-rich layers (Sierra et al., 2001). The Abad marls in the central part of the basin are overlain by massive gypsum deposits (Yesares member), which is correlated to the Lower Evaporites of the Central Mediterranean (Krijgsman et al., 1999a).

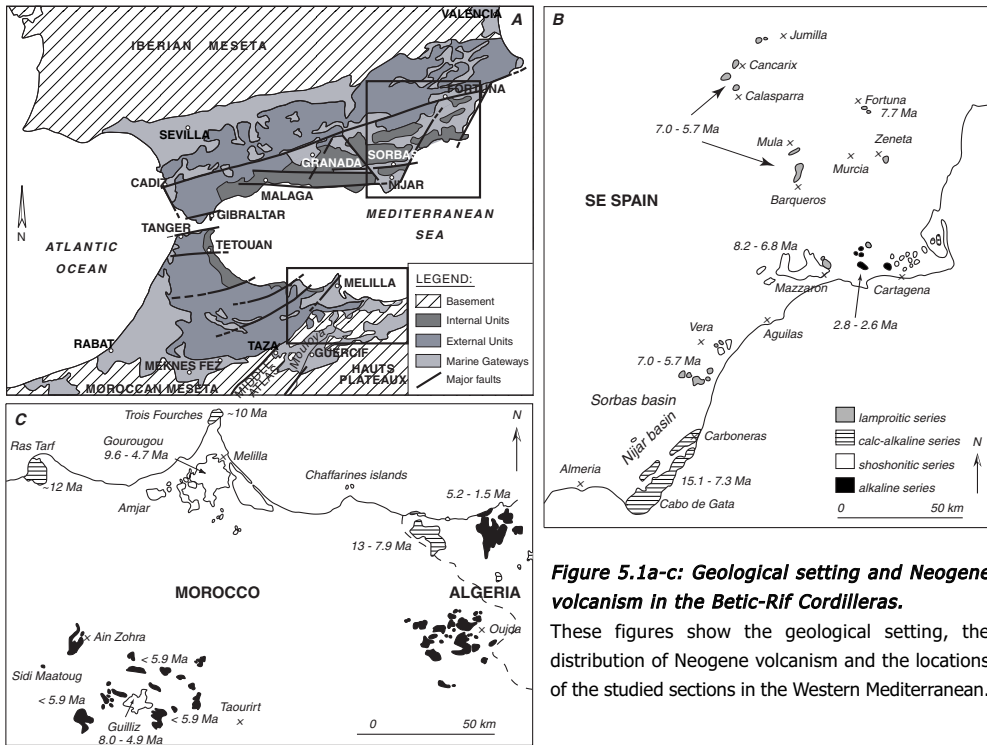


Figure 5.1a-c: Geological setting and Neogene volcanism in the Betic-Rif Cordilleras.

These figures show the geological setting, the distribution of Neogene volcanism and the locations of the studied sections in the Western Mediterranean.

The extension, forming the Melilla-Nador Basin, started in the Serravallian (~14 - 10 Ma) and resulted in the deposition of a folded, molassic clastic wedge (Guillemin and Houzay, 1982), followed by uplift of the Paleozoic metamorphic core due to NS-directed compression. Messinian extension provided accommodation space for marl deposition in the basin and the development of a carbonate platform. The onset of marine sedimentation in the Melilla Basin is coeval to the deepening of the central Betic Corridor basins like Sorbas and Nijar (Van Assen et al., in press, chapter 4). This marine sedimentation phase ended with a lagoonal to lacustrine regressive sequence (Saint Martin et al., 1991). Sedimentary cyclicity in the Melilla Basin starts with bipartite cycles composed of indurated cherty laminites and homogeneous sediments with a change in color from gray to brownish marls coeval to the change in color from the Lower to Upper (more brownish) Abad in the Sorbas and Nijar Basins. Therefore, a change in the bio-lithofacies characteristics in the Melilla Basin is coeval to the division in the Lower and Upper Abad (Van Assen et al., in press, chapter 4). Volcanic horizons suitable for $^{40}\text{Ar}/^{39}\text{Ar}$ dating are intercalated in both the cyclic sediments of the Sorbas, Nijar and Melilla Basins.

NEOGENE VOLCANISM IN THE WESTERN MEDITERRANEAN

Calc-alkaline, potassic and basaltic volcanism is scattered across the Alboran Sea and Betic-Rif systems (e.g., Hernandez and Bellon, 1985). The Neogene magmatic activity developed in the eastern Betics seems to be closely related to the major strike slip faults. In the Guercif Basin magmatic activity seems also be related to the faults along the border of the basin. The earliest Neogene igneous activity was a basaltic dyke

swarm around 22 Ma located in the central and western internal zones of the Betics (Torres-Roldán et al., 1986). Furthermore, the oldest volcanic rocks are mainly calc-alkaline and are restricted to the Cabo de Gata-Carboneras area in Spain (figure 5.1b). In the eastern Rif calc-alkaline series are more widespread (figure 5.1c). Dates obtained for this calc-alkaline volcanic suite range from 15-7 Ma in southern Spain, whereas the Rif-Tell (northern Africa) calc-alkaline mountains range from 13-8 Ma in age (e.g., Bellon et al., 1981; Hernandez and Bellon, 1985). In the Alboran Sea the Alboran Island is a calc-alkaline volcanic edifice with volcanism at 18-7 Ma (Aparico et al., 1991). A second suite of dominantly potassic-ultrapotassic rocks with a wide variety of compositions (shoshonitic to lamproitic) erupted in Spain between 8 and 5 Ma and in North Africa between 9 and 4 Ma. The lamproitic volcanic rocks are widely scattered in southern Spain, but do not occur in northern Africa. The youngest volcanic rocks are alkaline basalts with an age of Pliocene to Quaternary in southern Spain, in North Africa the youngest volcanic rocks are Messinian to Quaternary alkaline basalts.

Considering the ages of the different Neogene volcanic complexes in the western Mediterranean (figure 5.1b and c), and the relation between tephra thickness and distance from the source (Watkins et al., 1978), the volcanic tephras in the Messadit basin most probably originate from the Gourougou volcano located immediately south of the basin. The Trois Fourches complex, at ~10 Ma immediately north of the basin is too old to be the source of the tephras studied here. The Guillez complex, approximately 100 km south of the Melilla Basin, is Messinian, but might be too far from the basin to account for the sometimes meters thick coarse grained (>1 mm) tephras.

The origin of the thin tephras intercalated in the Abad marls of the Sorbas and Nijar Basins in southern Spain is less clear. They might be related to the local lamproitic volcanism in southeast Spain. However, Bellon et al. (1983) described the existence of some thin vitreous tuffs in several Messinian Basins (e.g., in the Sorbas Basin) and noticed that the mineralogy was completely different from the lamproitic volcanism. Therefore, the thin tephras intercalated in the basin probably have another (andesitic / dacitic) source. They might for example originate from the Gourougou volcanic complex as well which is located ~250 km to the southwest. Chemical analyses could confirm this hypothesis, but this is beyond the scope of this study. It must, however be remarked that tephra Mes-4 in the Messadit section, which is by far the thickest tephra in this section, and the volcanic horizon a.1.2 from the Sorbas and Nijar Basins occur in exactly the same cycle suggesting that they originate from the same volcanic event.

ASTROCHRONOLOGICAL TIME CONTROL IN SORBAS, NIJAR AND MELILLA BASINS

In this study astronomical ages for the volcanic tephra layers intercalated in the sedimentary basins are indispensable. Therefore, the astrochronological timeframe of the relevant sections is summarized here with a focus on potential uncertainties in astronomical ages (see also chapter 2). The detailed astrochronological timeframe is described in detail in Sierra et al. (2001) and Krijgsman et al. (2001) for the Sorbas and Nijar Basins and in Van Assen et al. (in press) for the Melilla Basin. The astronomical ages assigned to the volcanic tephras are given in table 5.1 in combination with the $^{40}\text{Ar}/^{39}\text{Ar}$ data.

THE ABAD MARLS

The cyclostratigraphic relations in the Abad marls (Sorbas and Nijar Basin) are discussed in detail by Sierro et al. (2001). The Lower Abad consists of bipartite cycles of indurated homogeneous whitish marls and softer grey homogeneous marls. From cycle LA17 upwards a sapropelitic layer appears in the middle part of the homogeneous marls between two consecutive indurated layers. The Upper Abad is characterized by the intercalation of sapropels and indurated diatom rich layers in the homogeneous marls. The transition between the Lower and Upper Abad marls is complicated by a hiatus near the margins or by sediment instability (several slumps) in the basin depocenter (Sierro et al., 2001). A second slump is located in the Upper Abad marls. However, the combination of several subsections, the presence of tephra interval a.1.3, the occurrence of the top acme of the *G. scitula* dextral group and the only continuous transition in the Gafares section resulted in a reliable and continuous composite. The occurrence of the tephra and several biostratigraphic events in the several subsections were useful to confirm the cyclostratigraphic relations.

The Lower Abad marls could unambiguously be correlated to astronomically dated sections in Italy and on Gavdos and Crete (Sierro et al., 2001; Hilgen et al., 1995; Krijgsman et al., 1997). Therefore all sedimentary cycles, bio-events and ash-layers of the Lower Abad can be directly related to the 65°N summer insolation curve of the La93 astronomical solution (Laskar et al., 1993a) with present day values for tidal dissipation and dynamical ellipticity. Although no sapropels occur in the cycles of the Lower Abad, the middle to upper part of the homogeneous marls are rich in warm oligotrophic planktonic foraminiferal faunas, which are also present in sapropels of the Upper Abad and other Neogene marine successions in the Mediterranean (Sierro et al., 1999). Sapropels in the Mediterranean Neogene are all linked to precession minima. Therefore, the middle to upper part of the homogeneous marls is tuned to precession minima and summer insolation maxima. The first sapropels in the Abad marls are without exception recorded in the middle to upper part of the homogeneous marls confirming this phase relation. The tuning of the lowermost 19 cycles seems straightforward. The homogeneous marl below the first indurated bed is characterized by a maximum in oligotrophic foraminifera and correlates well with the first prominent sapropel in other Messinian sections. Therefore this layer is correlated to the first high amplitude peak in insolation following an interval of low-amplitude fluctuations that corresponds to the interval at the base of the Abad marls where no distinct cyclicity occurs (Sierro et al., 2001). Upward tuning of each middle to upper part of the homogeneous marl levels shows also other characteristics supporting the proposed tuning, like an extra thick marl in cycle LA12 corresponding to a longer precession cycle, the alternately thin-thick-thin marls of LA13, LA14 and LA15 corresponding to lower-higher-lower amplitude in the insolation maxima and the relatively thin marls of LA15 and LA16 corresponding to minimum amplitudes in the insolation minima. Therefore, an error in the astronomical ages of the tephra a.1.1 (just below the indurated bed of LA1) and a.1.2 (in the homogeneous marl of LA17) due to incorrect tuning or "missing" cycles seems unlikely. This is supported by the occurrence of several bio-events in the same cycles in sections throughout the Mediterranean, also indicating the synchronicity of these events (Sierro et al., 2001).

The correlation of the Upper Abad marls to the insolation curve also produces a series of characteristic patterns observed in the sediments and the target curve. The extra-ordinary thick homogeneous marl (UA4) does fit with a precession cycle having a prolonged 29 kyr period. The thick homogeneous marl of UA17 represents a double cycle where the upper sapropel corresponding to a very low amplitude insolation

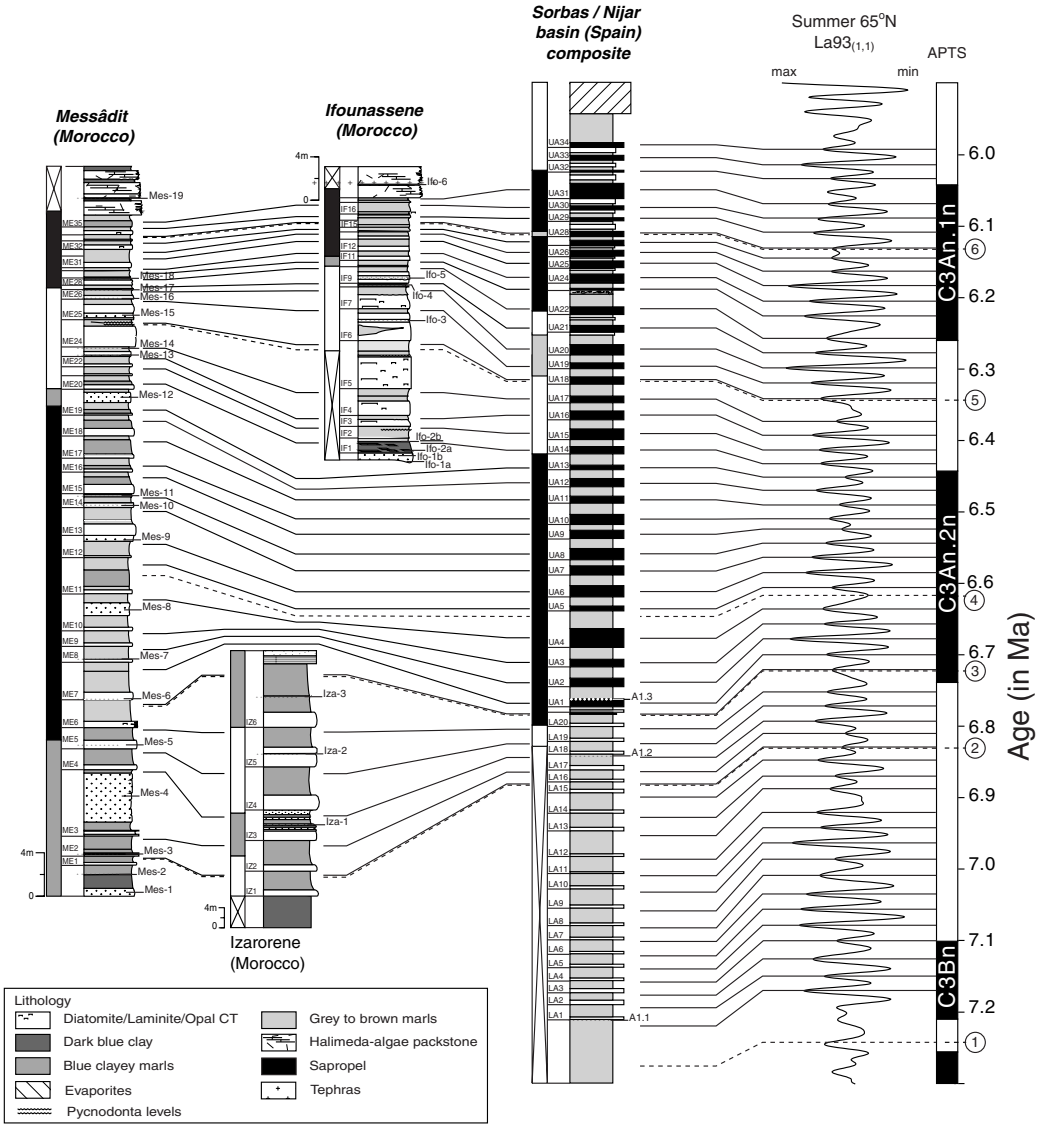


Figure 5.2 Stratigraphic column of the Abad member in the Sorbas and Nijar basin and the Messinian marls in the Melilla-Nador basin and its correlation to the APTS.

This figure shows the tuning of the sedimentary sections to the astronomical solutions of La93 (Laskar et al., 1993a). The locations of ash layers are indicated. For details the reader is referred to Sierra et al. (2001) or Van Assen et al. (in press). The main biostratigraphic marker-events registered within the studied sections correspond to 1) *G. miotumida* gr. FRO at 7.242 Ma (T/M boundary), 2) *G. nicolae* FCO at 6.828 Ma, 3) *G. nicolae* LO at 6.722 Ma in the Moroccan sections (chapter 4) and at 6.713 in Sorbas, 4) *G. obesa* FCO at 6.613 Ma, 5) *N. acostaensis* sinistral/dextral coiling change at 6.360 - 6.340 Ma (Krijgsman et al., 1999a; Sierra et al., 2001) and 6) *N. acostaensis* first sinistral influx at 6.129 Ma in Morocco and 6.126 Ma in Sorbas.

maximum indeed lacks expression. Cycle UA31 is also interpreted as a double cycle in which the upper sapropel lacks expression. Further, the sapropel of cycle UA13 is extremely thin and devoid of warm oligotrophic fauna, but also cycles UA11 and UA9 are thinner than adjacent sapropels. These alternating thin-thick-thin-thick patterns are reflected in the insolation curve by lower-higher-lower-higher insolation maxima due to the combined effect of the eccentricity modulation of precession and precession-obliquity interference. The sapropel thickness of UA4-UA8 also agrees with the pattern of the insolation curve apart from the expected reduction in amplitude in the insolation curve for cycle UA7, which is not observed. The thickness of the diatomites in cycles UA26-UA33 correspond perfectly with the pattern of the insolation minima of the target curve where the thicker and more prominent diatomites correspond to the higher amplitude insolation minima.

THE MELILLA MARLS

Van Assen et al. (in press) discuss the cyclostratigraphic relations in the Neogene marls in the Melilla Basin in detail. The Melilla marls are characterized by mainly bipartite cycles of homogeneous marls and laminated cherty layers or diatomites. The upper part of the section shows more sandy influxes. The astronomical tuning of the Melilla marls is primarily based on five biostratigraphic marker-events, which occur simultaneously in the Mediterranean Neogene (Krijgsman et al., 1995; Sierro et al., 2001) and have been identified in the Melilla Basin (Van Assen et al., in press). The astronomical ages of these bio-events are used as calibration points to tune all sedimentary cycles, volcanic ash layers and other events to the summer insolation target curve of $\text{La93}_{(1.1)}$. The phase relation of the sedimentary cycles with respect to the target curve is based on the occurrence of high planktonic foraminifera contents within the homogeneous intervals resembling the pattern as discussed above for the Abad marls (Sierro et al., 2001). Therefore, the homogeneous marls in the Melilla Basin are correlated to a precession minimum or insolation maximum. Additionally, the number of sedimentary cycles between the different bio-events is equivalent to other astronomically calibrated Mediterranean sections. Characteristic patterns are also recognized in the Melilla marls, like for examples the extra thick marl of Mec11 corresponds to UA4 of the Abad marls caused by an extra long (29 kyr) precession cycle. The extra thick cycles of MEc24 and IFc5 corresponding to the extra thick marls of cycle UA17 in the Abad marls are linked to a double minimum peak. The tuning of the upper part of the Melilla marls above the sinistral to dextral coiling change of *N. acostaensis* is less straightforward due to increased terrigenous influx. However, the number of 10 sedimentary alternations between the two recorded bio-events (figure 5.2) are in agreement with the ten cycles formed in other astronomically tuned Mediterranean sections between these bio-events.

In chapter 2 we made a division in so-called category 1, 2 and 3 ash layers, where second category ash layers were found in cyclic marine sequences that have been astronomically dated by applying an astronomically dated integrated stratigraphic framework, which was constructed with the help of other sections that are more suitable for astronomical tuning. Consistency in the number of basic sedimentary cycles in between clear-cut planktonic foraminiferal bio-events known to be synchronous in the Mediterranean and the occurrence of characteristic sedimentary cycles indicate the reliability of the tuning. Above we discussed this category 2 tuning for the Sorbas, Nijar and Melilla Basins. Apart from the "correctness" of the tuning uncertainties in astronomical ages of volcanic ash layers might be due to 1) uncertainties in the applied astronomical solutions including the values for tidal dissipation and dynamical

ellipticity, 2) uncertainties in the assumption of a constant sedimentation rate between two astronomically tuned points to derive an astronomical ages for a layer intercalated between two such points and 3) uncertainties in the lag between the orbital forcing and sedimentary expression. Overall, the uncertainty in the astronomical ages for the volcanic ash layers in Melilla and Sorbas/Nijar is estimated at ± 5 kyr provided that the tuning is correct.

MATERIAL AND METHODS

In the Sorbas and Nijar Basin the three volcanic levels (a.1.1, a.1.2 and a.1.3) were collected at several sites. Exact geographic locations of the sampled sections are given in figure 1 of Sierro et al., (2001). In the Melilla Basin the volcanic tephra were sampled in the Messadit, Ifounassene and Izarorene sections as is described in Van Assen et al. (in press) and chapter 4. The bulk samples were crushed (depending on their solidity), washed and sieved. For the Melilla samples the 500-1000 μm fractions were used for standard magnetic and heavy liquid separations for micas or sanidine. For the Sorbas and Nijar samples smaller size fractions had to be used, but size fractions smaller than 125 μm were removed. Subsequently, all samples were handpicked. The samples were wrapped in Al-foil and loaded in a 5 mm ID quartz vial. Fish Canyon Tuff (FC-2) sanidine and Taylor Creek Rhyolite (85G003) were wrapped in Cu-foil and loaded at the top and bottom positions and between each set of 3-5 samples. Samples were irradiated in several irradiation batches (VU37, VU41 and VU42 for Melilla and VU32 and VU41 for Sorbas) for 7 hours in the Oregon State University TRIGA reactor in the cadmium shielded CLICIT facility for VU32 and VU37 and in the extended tube CLICIT facility for VU41 and VU42. After irradiation samples and standards were loaded in 2 mm diameter holes of a copper planchet and placed in an ultra-high vacuum extraction line. Samples and standards were stepwise heated or directly fused and gas was analyzed with a Mass Analyzer Products LTD 215-50 noble gas mass spectrometer (for details see chapter 1).

Multiple grain fractions of biotite samples have been measured by stepwise heating and in a few cases by fusion with a 24W continuous wave argon-ion laser. Multiple grain or single grain sanidine fractions of standards and samples have been preheated using a defocused laser beam with an output of 2W (samples did not glow and gas was pumped away) to remove undesirable atmospheric argon adsorbed to the crystal surface. After the preheating step the samples and standards were analyzed by total fusion. Experiments were replicated 5 to 10 times for the fusion experiments; most stepwise heating experiments have been performed in duplicate. Beam intensities were measured in a peak-jumping mode over the mass range 40-36 on a secondary electron multiplier. For data collection the mass spectrometer is operated with a modified version of standard MAP software (i.e., valve control, laser control, variable integration times for different isotopes). System blanks were measured every 3 steps. The total system blanks were in the range of 5.0×10^{-14} moles for mass 40, 4.0×10^{-15} moles for mass 39, 2.6×10^{-15} moles for mass 38, 2.6×10^{-14} moles for mass 37 and 2.0×10^{-15} moles for mass 36. Mass discrimination (1.002-1.0100 per atomic mass unit) was monitored by frequent analysis of $^{40}\text{Ar}/^{38}\text{Ar}$ reference gas or $^{40}\text{Ar}/^{36}\text{Ar}$ air pipette aliquots (chapter 1). The irradiation parameter J for each unknown was determined by interpolation using a 2nd order weighted polynomial fitting between the individually measured standards (chapter 1).

Data reduction is performed using the in-house developed ArArCalc(v2.20c) software (Koppers, 2002). Blanks corrections are performed by subtracting the mean blank values of blank analyses before and after

measurement of the unknown. Mass discrimination and interfering nuclear isotope corrections are described in chapter 1. Weighted mean $^{40}\text{Ar}/^{39}\text{Ar}$ - (or F-) ratios and standard errors of the mean are given for combined experiments from the same irradiation package. Weighted mean intercalibration factors (λ) and standard errors of the mean are calculated when experiments on the same ash layer, but from different irradiation packages are combined. Ages have been calculated with standard age equations (equations 1.11 and 1.12) relative to TCR of 28.34 Ma or FCT of 28.02 Ma (Renne et al., 1998) and with the decay constants and decay constant errors of Steiger and Jäger (1977). Errors are reported at the 1σ level and include respectively the analytical error in the unknown (I), the analytical error in the unknown and standard (II), the analytical errors and the uncertainties in $^{40}\text{Ar}^*/^{40}\text{K}$ of the primary standard and intercalibration between primary and secondary standards (III) and the error including decay constant uncertainties as well (IV). MSWD values are used to assess homogeneity of the data. For comparison ages are also calculated with a slightly modified version of the full external error calculation as in Min et al. (2000). These ages and uncertainties are calculated according to equation 1.14 with physical parameters and activity data as reported in table 1.4, column VII. This last approach should present the most realistic age and error estimate (see also chapter 1 and 3).

RESULTS

Table 5.1 shows all the $^{40}\text{Ar}/^{39}\text{Ar}$ data obtained for volcanic ash layers in the Sorbas and Nijar Basins. Table 5.2 shows the data for the ash layers in the Melilla Basin. Figure 5.3 visualizes the $^{40}\text{Ar}/^{39}\text{Ar}$ age estimates for the Sorbas / Nijar ash layers, while in figure 5.5 cumulative age probability distributions are shown for the Melilla volcanic deposits.

SORBAS / NIJAR

All incremental heating experiments performed on biotite show reliable plateaus (figure 5.4) according to the criteria of e.g. Foland et al. (1986). The first steps and occasionally the last step are omitted from most plateaus. Omitted steps show lower amounts of radiogenic ^{40}Ar than the steps included in the plateaus. Although the fusion experiments on biotite produce MSWD's <1 , we do not consider these experiments in the integrated ages, because the stepwise heating experiments showed the necessity of the removal of some steps. $^{40}\text{Ar}/^{36}\text{Ar}$ isochron intercepts are indistinguishable from 295.5 at the 1σ level, but due to clustering around the axis, uncertainties are sometimes large. The only exceptions are two experiments on ash layer a.1.3 (VU32-C9 (fusion), VU32-C12), which show $^{40}\text{Ar}/^{36}\text{Ar}$ intercepts of respectively 307 ± 16 and 310 ± 10 , indicative of some excess argon. However, at a 95% confidence level they do not differ from the atmospheric ratio of 295.5. Further, we tried to separate pure sanidine from the same ash layers, but obtained and analyzed both sanidine/plagioclase mixtures (K/Ca 1-5) and sanidine separates (K/Ca >20) which appeared to be very heterogeneous and apart from VU41-B8 and VU41-B13 no reliable isochrons could be defined. The heterogeneity observed in the feldspar indicates that we might be dealing with a reworked tuff, although biotite minerals from the same ash layer are reproducible. All analytical data on feldspar are reported in table 5.1 and the "best" feldspar data (i.e., MSWD <1) also shown in figure 5.3.

For the biotite experiments all steps included in the different plateaus are combined to one integrated age. When all plateau steps are combined a.1.3 is 6.707 ± 0.010 (0.091) Ma, a.1.2 is 6.771 ± 0.009 (0.092) Ma

Identity and # corresponding to figure 5.3	Section	F _{unknown}	σ _f	N	MSWD	⁴⁰ Ar [*] %	³⁹ Ar _K %	K/Ca	F _{sk}	σ _{Fsk}	Apparent ⁴⁰ Ar/ ³⁹ Ar age and error (Ma)					
											Age	I	II	III	IV	Equation 1.14
Cycle UA1 = a.1.3																
1 VU32-C9 (fusion)	Gafares II	2.0583	0.0057	5	0.58	81.0	-	-	8.7426	0.0262	6.712	0.019	0.027	0.047	0.073	6.692
2 VU32-C8 (fusion)	Gafares I	2.0463	0.0089	5	0.12	64.8	-	-	8.7234	0.0262	6.688	0.029	0.035	0.052	0.076	6.686 ± 0.097
3 VU32-C12	Gafares III	2.0620	0.0043	6	0.73	83.7	79.1	-	8.8156	0.0264	6.669	0.014	0.024	0.045	0.072	6.667 ± 0.093
4 VU32-C10	Perales	2.0517	0.0075	6	0.19	61.2	88.7	-	8.7668	0.0263	6.673	0.024	0.031	0.049	0.074	6.670 ± 0.095
5 VU41 B28	Gafares I	1.9972	0.0079	4	0.18	77.2	82.1	-	8.3615	0.0125	6.732	0.027	0.029	0.048	0.074	6.732 ± 0.095
6 VU41 B28	Gafares I	2.0109	0.0072	3	0.16	69.3	75.7	-	8.3615	0.0125	6.778	0.024	0.026	0.047	0.074	6.778 ± 0.095
7 VU41 B26	Gafares III	2.0116	0.0195	3	0.72	77.6	24.0	-	8.3259	0.0125	6.810	0.066	0.067	0.077	0.096	6.810 ± 0.113
8 VU41 B26	Gafares III	1.9860	0.0085	4	0.34	76.2	51.2	-	8.3259	0.0125	6.723	0.029	0.030	0.049	0.075	6.723 ± 0.095
Cycle LA17 = a.1.2																
10 VU32-C4 (fusion)	Gafares	2.0721	0.0037	5	0.82	79.8	-	-	8.6236	0.0285	6.850	0.012	0.026	0.047	0.074	6.848 ± 0.096
11 VU32-C4	Gafares	2.0451	0.0041	7	0.09	80.2	99.1	-	8.6236	0.0285	6.761	0.014	0.026	0.046	0.073	6.759 ± 0.095
12 VU32-C6 (fusion)	Los Molinos	2.0460	0.0056	7	0.27	75.8	-	-	8.6708	0.0269	6.728	0.018	0.028	0.047	0.073	6.725 ± 0.095
13 VU32-C6	Los Molinos	2.0593	0.0060	5	0.25	80.8	98.8	-	8.6708	0.0269	6.771	0.020	0.029	0.048	0.074	6.769 ± 0.096
14 VU41 B45	Perales A	2.0937	0.0140	4	0.39	83.3	81.3	-	8.7153	0.0131	6.771	0.045	0.046	0.060	0.083	6.771 ± 0.102
15 VU41 B45	Perales A	2.0884	0.0087	4	0.61	85.6	71.2	-	8.7153	0.0139	6.754	0.028	0.030	0.049	0.075	6.754 ± 0.096
16 VU41 B44	Gafares	2.0910	0.0078	5	0.05	87.9	93.7	-	8.6960	0.0130	6.777	0.025	0.027	0.047	0.074	6.777 ± 0.095
17 VU41 B44	Gafares	2.0981	0.0095	5	0.10	86.7	92.2	-	8.6960	0.0130	6.800	0.031	0.032	0.051	0.077	6.800 ± 0.097
18 VU41 B32	Los Molinos	2.0252	0.0150	4	0.30	81.8	83.5	-	8.4336	0.0127	6.768	0.050	0.051	0.064	0.086	6.768 ± 0.104
19 VU41 B32	Los Molinos	2.0382	0.0205	3	0.01	87.1	42.4	-	8.4336	0.0127	6.812	0.068	0.069	0.079	0.098	6.811 ± 0.115
20 VU41 B32	Los Molinos	2.0334	0.0105	4	0.07	69.0	95.4	-	8.4336	0.0127	6.796	0.035	0.036	0.053	0.078	6.795 ± 0.098
21 VU41 B11 feldspar	Los Molinos	1.9522	0.0041	5	0.41	99.0	-	3.0	8.1994	0.0123	6.711	0.014	0.017	0.042	0.071	6.711 ± 0.092
VU41 B12 feldspar	Perales A	2.3117	0.0689	4	141	97.1	-	2.2	8.1994	0.0123	7.944	0.236	0.237	0.241	0.250	7.944 ± 0.259
22 VU41 B13 feldspar	Gafares	1.9617	0.0042	5	0.37	95.1	-	4.5	8.1994	0.0123	6.743	0.014	0.018	0.043	0.071	6.743 ± 0.092
23 VU32-C26 feldspar	Gafares	2.2568	0.0026	6	0.29	94.4	-	22.3	9.4808	0.0265	6.787	0.080	0.021	0.044	0.072	6.784 ± 0.094
Cycle LA1 = a.1.1																
25 VU32-C5 (fusion)	Los Molinos SS	2.1637	0.0071	5	0.54	76.3	-	-	8.6471	0.0277	7.133	0.023	0.033	0.052	0.079	7.131 ± 0.102
26 VU32-C5	Los Molinos SS	2.1803	0.0068	4	0.25	84.0	79.0	-	8.6471	0.0277	7.188	0.022	0.032	0.052	0.079	7.185 ± 0.102
27 VU41 B29	Los Molinos	2.1451	0.0094	5	0.26	81.4	90.0	-	8.3794	0.0126	7.215	0.031	0.033	0.053	0.081	7.214 ± 0.103
28 VU41 B29	Los Molinos	2.1741	0.0112	4	0.20	83.2	91.6	-	8.3794	0.0126	7.312	0.038	0.039	0.057	0.084	7.312 ± 0.106
29 VU41 B29	Los Molinos	2.1608	0.0060	4	0.34	83.0	84.7	-	8.3794	0.0126	7.267	0.020	0.023	0.048	0.078	7.267 ± 0.100
30 VU41 B30	Los Molinos SS	2.1644	0.0143	4	0.02	86.7	67.7	-	8.3929	0.0126	7.268	0.048	0.049	0.064	0.089	7.267 ± 0.109
31 VU41 B30	Los Molinos SS	2.1753	0.0191	3	0.66	84.2	82.8	-	8.3929	0.0126	7.304	0.064	0.065	0.077	0.099	7.304 ± 0.118
32 VU41 B30	Los Molinos SS	2.1619	0.0047	4	0.04	86.3	76.0	-	8.3929	0.0126	7.259	0.016	0.019	0.046	0.077	7.259 ± 0.100
33 VU41 B46	Los Molinos SS	2.2554	0.0054	5	0.56	78.8	90.0	-	8.7494	0.0131	7.265	0.017	0.021	0.046	0.077	7.264 ± 0.100
34 VU41 B46	Los Molinos SS	2.2470	0.0055	4	0.19	87.0	86.0	-	8.7494	0.0131	7.238	0.018	0.021	0.047	0.077	7.237 ± 0.100
VU41 B7 feldspar	Los Molinos	2.2360	0.0169	12	68	93.2	-	19.9	8.2080	0.0123	7.676	0.058	0.059	0.074	0.098	7.676 ± 0.118
35 VU41 B8 feldspar	Los Molinos SS	2.0709	0.0046	5	0.09	91.0	-	-	8.2037	0.0123	7.114	0.016	0.019	0.045	0.075	7.114 ± 0.097
VU41 B9 feldspar	Los Molinos SS	2.1481	0.0373	8	154	92.6	-	2.7	8.2037	0.0123	7.379	0.128	0.129	0.135	0.149	7.379 ± 0.162
VU32 C30 feldspar	Los Molinos SS	2.6887	0.0552	6	116	85.3	-	1.6	9.6542	0.0261	7.938	0.163	0.164	0.170	0.183	7.935 ± 0.195

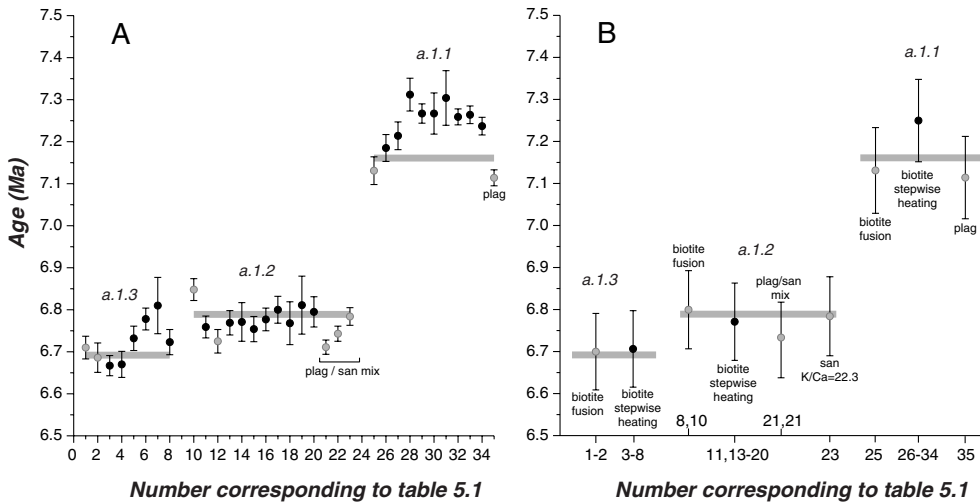


Figure 5.3: ⁴⁰Ar/³⁹Ar ages of volcanic ash layers in the Sorbas and Nijar Basins.

The ⁴⁰Ar/³⁹Ar ages of the experiments performed on the Sorbas / Nijar volcanic layers are compared with the astronomical ages (gray horizontal bars). Error bars represent analytical errors in samples and standards only (a) and a full error propagation including uncertainties in absolute age of standards and activities according to equation 1.14 (b). The thickness of the bar depicting the astronomical age represents the uncertainty in the astronomical age. The gray (black) markers represent combined fusion experiments (incremental heating experiments). Experiments on plagioclase / sanidine are indicated in the figure. The numbers on the X-axis correspond to the data reported in table 5.1.

and a.1.1 is 7.251 ± 0.008 (0.098) Ma. Uncertainties represent the analytical errors, between brackets full error estimates are given. Combined plateau ages are calculated by first establishing a weighted mean F_{ash}/F_{TC} ratio of all steps included in a plateau, which is then inserted in equation 1.14. Combined plateau ages of a.1.1 and a.1.2 show almost normal probability distributions, MSWD values lower than 1 and isochron intercepts indiscernible from the atmospheric ratio of 295.5 (296.2 ± 3.9 for A.1.1, 294.9 ± 3.4 for A.1.2 for both normal and inverse isochrons). Ash layer a.1.3 has a slightly higher MSWD value (1.04), an isochron intercept very slightly deviating from the atmospheric ratio at the 1σ level (298.3 ± 2.4) and an almost normal probability distribution. The inverse isochron age for a.1.3 is 6.679 ± 0.027 (or 0.094 full error) Ma.

Table 5.1: ⁴⁰Ar/³⁹Ar data of Sorbas/Nijar tephra with different error propagation methods (previous page).

Analytical data of Sorbas / Nijar ash layers. F ratios with standard error of the mean, number of analyses with between brackets number of experiments excluded from dataset, radiogenic ⁴⁰Ar* contents, ³⁹Ar content included in plateau (for biotite), analytical errors, ages calculated with standard age equations (equation 1.11/1.12) and "updated" ages with full error estimates (equation 1.14) are reported. Reported errors represent analytical error of unknown (I), of unknown and standard (II), analytical errors and uncertainties in ⁴⁰Ar*/⁴⁰K of primary standard and intercalibration factor(s) between primary and secondary standard(s) (III), and the foregoing errors with decay constant uncertainties (IV). All experiments are stepwise heating experiments on biotite, unless stated otherwise. For experiments on sanidine and/or plagioclase (mixtures) K/Ca ratios are mentioned. All experiments on feldspar are multigrain fusion experiments. N represents the number of steps included in the plateau (or number of replicate fusion experiments). Ages of VU32 experiments are calculated relative to TCR of 28.34 Ma and ages of VU42 experiments are calculated relative to FCT of 28.02 Ma (Renne et al., 1998).

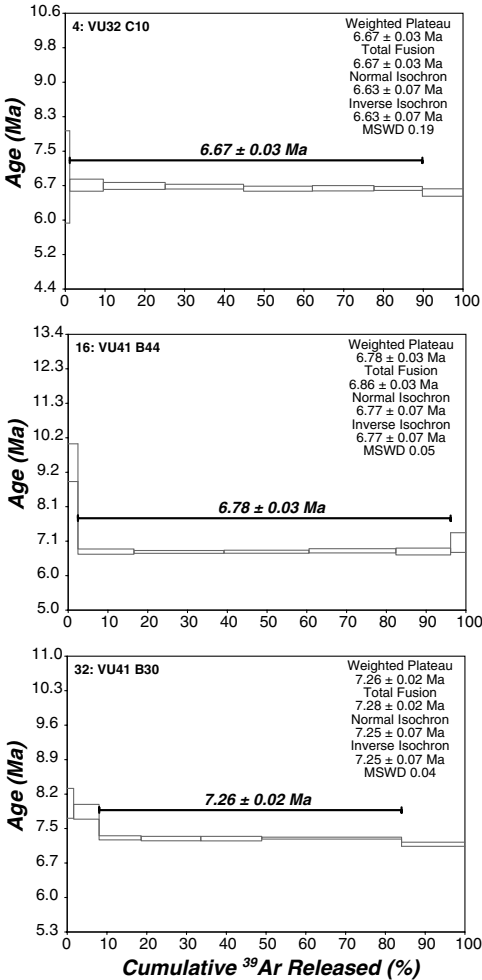


Figure 5.4 Examples of plateau ages for the Sorbas/Nijar Basins.

Plateaus are shown of three representative biotite samples of the three volcanic layers in the Sorbas/Nijar Basin. All plateaus fulfill the criteria as proposed by e.g. Foland et al. (1986).

Further, ash layer a.1.3 (cycle UA1) comprises 6 thin ash layers spread over a range of 15 cm, where 3 ash layers are coarser grained with Gafares I representing the lower coarser grained ash and Gafares III the upper coarser grained ash. In the same cycle in Perales only a double ash was found. Although sampling, mineral separation and ⁴⁰Ar/³⁹Ar dating has been performed on the individual ash layers, the “accepted” ⁴⁰Ar/³⁹Ar age for the a.1.3 is based on the combination of experiments, because with a cycle thickness of ~1.5 m only an uncertainty of 2 kyr will be introduced.

The feldspar experiments are also combined to assess the behavior of the isochrons and to check the possible occurrence of excess argon. Isochrons for a.1.1 indeed show intercepts significantly higher than the atmospheric ratio (normal 396 ± 48; inverse 470 ± 60), but uncertainties and MSWD values (68 and 71) are high. Isochron ages are respectively 7.16 ± 0.14 Ma (normal) and 7.17 ± 0.15 Ma (inverse) for a.1.1. For a.1.2 the combination of experiments VU41-B11, VU-B13 and VU32-C26 produces reliable isochrons with intercepts of 334 ± 10 and 324 ± 10, MSWD’s of 1.10 and 0.91 and ages of 6.72 ± 0.02 Ma and 6.73 ± 0.02

Ma for respectively normal and inverse isochrons. When VU41-B12 is included, isochrons are completely disturbed.

MELILLA

Most experiments on the volcanic layers in the Melilla Basin concern single crystal sanidine fusions, but single crystal stepwise heating experiments have been performed in a few cases. Stepwise heating on feldspar was not successful, because the major amount of gas was released in one or two steps due to unsuitability of the -argon ion continuous wave- laser for stepwise heating of transparent minerals. Analyses with a ⁴⁰Ar yield lower than 1 Volt (at 10⁹ Ω with a relative gain of ~500) or with very low K/Ca ratios were omitted from further interpretation and not included in table 5.2. For Ifo-6 the results of three stepwise heating experiments on biotite from the same package are reported. MSWD values have been used to assess the heterogeneity of the samples. Almost all MSWD values (with a few exceptions) are lower than 1,

Identity	F _{unknown}	σ _F	N	MSWD	⁴⁰ Ar [*] %	³⁹ Ar/ _K %	K/Ca	F _{sk}	σ _{est}	Apparent ⁴⁰ Ar/ ³⁹ Ar age and error (Ma)												
										Age	I	II	III	IV	Equation 1.14							
Ifo-5																						
VU42-A21	1.8456	0.0013	8 (2)	0.79	98.7	-	25.7	8.3749	0.0176	6.212	0.004	0.014	0.038	0.065							6.270	
VU37-B22	1.9708	0.0034	1	-	94.8	-	23.2	9.0267	0.0226	6.222	0.011	0.019	0.040	0.066								6.212 ± 0.085
VU37-B21	1.9619	0.0028	1	-	94.4	-	19.7	8.9909	0.0234	6.222	0.009	0.018	0.040	0.066								6.223 ± 0.086
VU37-B19	1.9433	0.0015	3	0.55	96.7	-	22.4	8.8949	0.0231	6.230	0.005	0.017	0.039	0.065								6.220 ± 0.086
VU37-B18	1.9367	0.0023	1	-	94.8	-	21.7	8.8600	0.0230	6.233	0.007	0.018	0.040	0.065								6.227 ± 0.086
Ifo-4																						6.231 ± 0.086
VU42-A20	1.8611	0.0014	8 (2)	1.02	98.8	-	23.9	8.3704	0.0176	6.268	0.005	0.014	0.039	0.066								6.261
VU37-B14	1.9230	0.0022	2 (1)	0.07	98.3	-	25.2	8.7620	0.0228	6.258	0.007	0.018	0.040	0.066								6.267 ± 0.085
VU37-B15	1.9223	0.0020	2	0.04	99.0	-	20.4	8.7620	0.0228	6.256	0.007	0.018	0.040	0.066								6.256 ± 0.086
VU37-B17	1.9322	0.0021	2	0.67	98.1	-	20.7	8.8353	0.0230	6.236	0.007	0.017	0.040	0.065								6.253 ± 0.086
Ifo-3																						6.234 ± 0.086
VU42-A19	1.8627	0.0024	8 (2)	0.35	98.1	-	21.5	8.3615	0.0176	6.280	0.008	0.015	0.039	0.066								6.333
VU37-B13	1.9250	0.0016	3	0.62	95.8	-	16.2	8.7330	0.0227	6.285	0.005	0.017	0.040	0.066								6.280 ± 0.086
VU37-B11	1.9094	0.0020	2	0.77	97.7	-	19.1	8.6898	0.0235	6.265	0.006	0.018	0.040	0.066								6.283 ± 0.086
VU37-B10	1.9001	0.0020	2 (1)	0.19	96.7	-	19.7	8.6613	0.0234	6.255	0.006	0.018	0.040	0.066								6.263 ± 0.086
Ifo-2																						6.253 ± 0.086
VU42-A16	1.8997	0.0013	9 (1)	1.05	99.6	-	22.4	8.3526	0.0184	6.411	0.004	0.015	0.040	0.067								6.432
Ifo-1																						6.411 ± 0.087
VU42-A17	1.9005	0.0034	8 (2)	0.16	97.2	-	22.8	8.3570	0.0175	6.411	0.011	0.018	0.041	0.068								6.443
Mes-18																						6.410 ± 0.088
VU42-A15	1.8451	0.0017	7 (3)	0.33	99.4	-	23.1	8.3526	0.0184	6.227	0.006	0.015	0.039	0.065								6.260
Mes-17																						6.227 ± 0.085
VU42-A13	1.8499	0.0027	10	0.35	96.7	-	25.5	8.3481	0.0184	6.247	0.009	0.016	0.039	0.066								6.298
VU37-B23 (th)	1.9729	0.0065	2	0.19	95.1	96.8	29.1	9.0629	0.0227	6.207	0.020	0.026	0.044	0.068								6.246 ± 0.086
VU37-B25	1.9887	0.0063	2	0.11	95.5	-	21.3	9.1203	0.0228	6.218	0.020	0.025	0.043	0.068								6.205 ± 0.087
VU37-B25 (th)	1.9966	0.0064	2	0.01	97.1	100	27.9	9.1203	0.0228	6.242	0.020	0.025	0.044	0.068								6.215 ± 0.087
Mes-16																						6.240 ± 0.088
VU42-A12	1.8550	0.0028	10	0.43	97.3	-	23.7	8.3481	0.0184	6.264	0.009	0.017	0.040	0.066								6.313
Mes-15																						6.263 ± 0.086
VU42-A11	1.8558	0.0037	8	0.09	95.6	-	22.2	8.3481	0.0184	6.267	0.012	0.018	0.040	0.067								6.337
																						6.266 ± 0.086

Table 5.2: ⁴⁰Ar/³⁹Ar data of Melilla tephra with different error propagation methods. (continued on next pages)

Identity	F _{unknown}	σ _F	N	MSWD	⁴⁰ Ar ⁺ %	³⁹ Ar/ ^K %	K/Ca	F _{st}	σ _{Fst}	Apparent ⁴⁰ Ar/ ³⁹ Ar age and error (Ma)										
										Age	I	II	III	IV	Equation 1.14					
Mes-14																				
VU42-A9	1.8678	0.0030	8 (2)	0.64	95.2	-	20.9	8.3526	0.0184	6.304	0.010	0.017	0.040	0.067	6.379	6.304 ± 0.086				
VU37-B37	2.1524	0.0057	1 (1)	-	99.7	-	52.9	9.6778	0.0232	6.342	0.017	0.023	0.042	0.068	6.339 ± 0.088					
VU37-B38	2.1575	0.0026	3	1.70	98.4	-	13.4	9.7313	0.0234	6.322	0.007	0.017	0.040	0.066	6.319 ± 0.087					
VU37-B39	2.1734	0.0035	2	2.47	99.5	-	10.2	9.7915	0.0235	6.329	0.010	0.018	0.040	0.067	6.327 ± 0.087					
Mes-12																				
VU42-A8	1.9035	0.0030	9 (1)	0.25	95.8	-	23.1	8.3526	0.0184	6.424	0.010	0.017	0.041	0.068	6.450	6.424 ± 0.088				
VU37 B30	2.0918	0.0029	2 (1)	0.32	97.1	-	22.3	9.3244	0.0233	6.396	0.009	0.018	0.041	0.067	6.394 ± 0.088					
VU37 B29	2.0895	0.0039	1 (1)	-	97.3	-	19.0	9.2807	0.0232	6.420	0.012	0.020	0.042	0.068	6.417 ± 0.089					
VU37 B27	2.0628	0.0016	3	1.30	98.4	-	24.3	9.1891	0.0230	6.401	0.005	0.017	0.040	0.067	6.398 ± 0.088					
Mes-11																				
VU37-Cl17	2.1978	0.0022	5	0.71	97.8	-	1.2	9.6483	0.0232	6.421	0.006	0.017	0.040	0.068	6.421 ± 0.088					
Mes-10																				
VU42-A7	1.9295	0.0043	6 (3)	0.63	95.0	-	20.3	8.3570	0.0192	6.508	0.015	0.021	0.043	0.070	6.552	6.508 ± 0.090				
Mes-9																				
VU42-A5	1.9297	0.0032	9 (1)	0.30	97.1	-	28.5	8.3660	0.0192	6.502	0.011	0.018	0.042	0.069	6.582	6.501 ± 0.089				
VU37-B3 (fh)	1.9582	0.0044	3 (1)	0.15	98.4	97.1	28.2	8.5445	0.0248	6.534	0.015	0.024	0.044	0.070	6.532 ± 0.091					
VU37-B3 (fh)	1.9571	0.0070	1 (1)	-	99.6	80.7	27.5	8.5445	0.0248	6.531	0.023	0.030	0.048	0.072	6.528 ± 0.093					
VU37-B3 (fh)	1.9613	0.0056	2	0.04	94.9	99.9	27.7	8.5445	0.0248	6.545	0.019	0.027	0.046	0.071	6.542 ± 0.092					
VU37-B1	1.9476	0.0026	1	-	99.5	-	24.7	8.5077	0.0255	6.527	0.009	0.021	0.043	0.069	6.525 ± 0.091					
VU37-B2	1.9544	0.0018	3	0.21	99.3	-	22.8	8.5215	0.0247	6.539	0.006	0.020	0.042	0.069	6.537 ± 0.090					
VU37-B5	1.9653	0.0042	1	-	98.9	-	25.0	8.5630	0.0240	6.544	0.014	0.023	0.044	0.070	6.542 ± 0.091					
Mes-8																				
VU42-A4	1.9542	0.0032	10	0.19	96.7	-	21.5	8.3704	0.0201	6.581	0.011	0.019	0.042	0.070	6.638	6.581 ± 0.091				
VU37-B56	2.5400	0.0096	(2)	0.41	98.0	-	53.8	10.8444	0.0249	6.678	0.025	0.030	0.048	0.074	6.676 ± 0.095					
VU37-B54	2.5240	0.0124	(2)	1.41	98.8	-	95.8	10.7269	0.0236	6.708	0.033	0.036	0.052	0.077	6.706 ± 0.097					
VU37-B53	2.4897	0.0067	(1)	-	96.0	-	40.5	10.6979	0.0235	6.635	0.018	0.023	0.044	0.071	6.633 ± 0.092					
Mes-6																				
VU37 B45	2.3772	0.0109	2	0.34	98.3	-	11.2	10.1298	0.0233	6.691	0.031	0.034	0.051	0.076	6.688 ± 0.096					
VU37 B46	2.3430	0.0287	(1)	-	95.6	-	20.9	10.1754	0.0234	6.565	0.080	0.082	0.090	0.105	6.563 ± 0.120					
VU37 B47	2.4041	0.0081	2 (1)	0.67	94.8	-	19.2	10.2412	0.0225	6.693	0.023	0.027	0.047	0.073	6.691 ± 0.094					

Identity	F _{unknown}	σ _F	N	MSWD	⁴⁰ Ar [*] %	³⁹ Ar _K %	K/Ca	F _{st}	σ _{rst}	Apparent ⁴⁰ Ar/ ³⁹ Ar age and error (Ma)			Equation 1.14		
										Age	I	II		III	IV
Mes-4															
VU42-A3	2.0031	0.0039	10	0.68	98.0	-	25.6	8.3749	0.0209	6.742	0.013	0.021	0.044	0.072	6.792 6.741 ± 0.093
VU41 B4	1.9647	0.0025	9 (1)	0.43	99.0	-	25.7	8.2339	0.0140	6.725	0.008	0.014	0.041	0.070	6.725 ± 0.092
VU37 B56	2.6048	0.0119	(1)	-	99.1	-	14.8	10.8444	0.0249	6.848	0.031	0.035	0.052	0.077	6.845 ± 0.099
VU37 B57	2.5802	0.0051	2 (1)	0.30	99.7	-	26.0	10.9268	0.0251	6.732	0.013	0.020	0.043	0.071	6.730 ± 0.093
Mes-1															
VU37 B5	2.0709	0.0022	2	2.97	99.4	-	35.1	8.5630	0.0240	6.895	0.007	0.021	0.044	0.073	>6.86 6.892 ± 0.095
VU37 B6	2.0733	0.0015	3	0.36	99.5	-	39.5	8.5769	0.0240	6.892	0.005	0.020	0.044	0.072	6.889 ± 0.095
VU37 B7	2.0766	0.0020	2	0.00	98.9	-	46.7	8.6002	0.0232	6.884	0.007	0.020	0.044	0.072	6.881 ± 0.095
VU37 B9	2.0938	0.0032	1	-	99.7	-	43.4	8.6377	0.0233	6.911	0.011	0.021	0.045	0.073	6.908 ± 0.096
Iza-1															
VU37 B43	2.3690	0.0025	2	0.07	99.1	-	24.3	10.0463	0.0231	6.723	0.007	0.017	0.042	0.070	6.792 6.721 ± 0.092
VU37 B42	2.3591	0.0026	2	1.53	98.5	-	22.4	9.9892	0.0230	6.733	0.007	0.017	0.042	0.070	6.731 ± 0.092
VU37 B41	2.3445	0.0024	2 (1)	0.07	97.6	-	19.2	9.9266	0.0228	6.734	0.007	0.017	0.042	0.070	6.731 ± 0.092
VU37 C115	2.3083	0.0067	(4)	0.03	94.0	-	24.2	9.9266	0.0239	6.630	0.019	0.025	0.045	0.071	6.627 ± 0.093
Mes-17															
VU37 C121 (Ih)	2.1407	0.0061	6 (5)	0.34	94.9	89.4	-	9.8956	0.0237	6.169	0.018	0.023	0.042	0.066	6.298 6.167 ± 0.086
Ifo-6															
VU42-A23 (Ih)	1.7830	0.0081	4 (4)	0.41	78.3	80.7	-	8.3839	0.0176	5.996	0.027	0.030	0.046	0.068	<6.07 5.995 ± 0.086
VU42-A23 (Ih)	1.7892	0.0077	6 (3)	1.19	69.3	98.0	-	8.3839	0.0176	6.016	0.026	0.029	0.045	0.068	6.016 ± 0.086
VU42-A23 (Ih)	1.7996	0.0060	6 (3)	0.32	79.8	98.4	-	8.3839	0.0176	6.051	0.020	0.024	0.042	0.066	6.051 ± 0.085

Table 5.2: ⁴⁰Ar/³⁹Ar data of Melilla tephra with different error propagation methods.

Analytical data of Melilla ash layers. F ratios with standard error of the mean, number of analyses with between brackets number of experiments excluded from dataset, radiogenic ⁴⁰Ar^{*} contents, ³⁹Ar_K content, included in plateau (for biotite), K/Ca ratios, analytical errors, ages calculated with standard age equations (equation 1.11) and "updated" ages with full error estimates (equation 1.14) are reported (see discussion in chapter 1). Reported errors represent analytical error of unknown (I), of unknown and standard (II), analytical errors and uncertainties in ⁴⁰Ar/³⁹Ar of primary standard and intercalibration factor(s) between primary and secondary standard(s) (III), and the foregoing errors with decay constant uncertainties (IV). Ages are calculated with Steiger and Jäger (1977) decay constants. Ages and errors according to equation 1.14 are calculated with parameters as in table 1.4, column VII. (1977) Most experiments are single crystal fusion experiments on sanidine, a few are incremental heating experiments on single crystals of sanidine. The experiments of ash layer Ifo-6 and mineral split VU37-C121 of Mes-17 are incremental heating experiments on biotite. VU37 experiments are calculated relative to TCR of 28.34 Ma and VU41 and VU42 experiments are calculated relative to FCT of 28.02 Ma (Renne et al., 1998). The stratigraphic sections are indicated by If = Ifounassene, Me = Messadit, Iz = Izarorene. (Ih) = incremental heating experiment.

indicating that the analytical uncertainty is overestimated. Cumulative probability distributions were used to visualize the presence of contaminating crystals. On basis of inspection of the probability distributions some analyses were removed from further interpretation (figure 5.5).

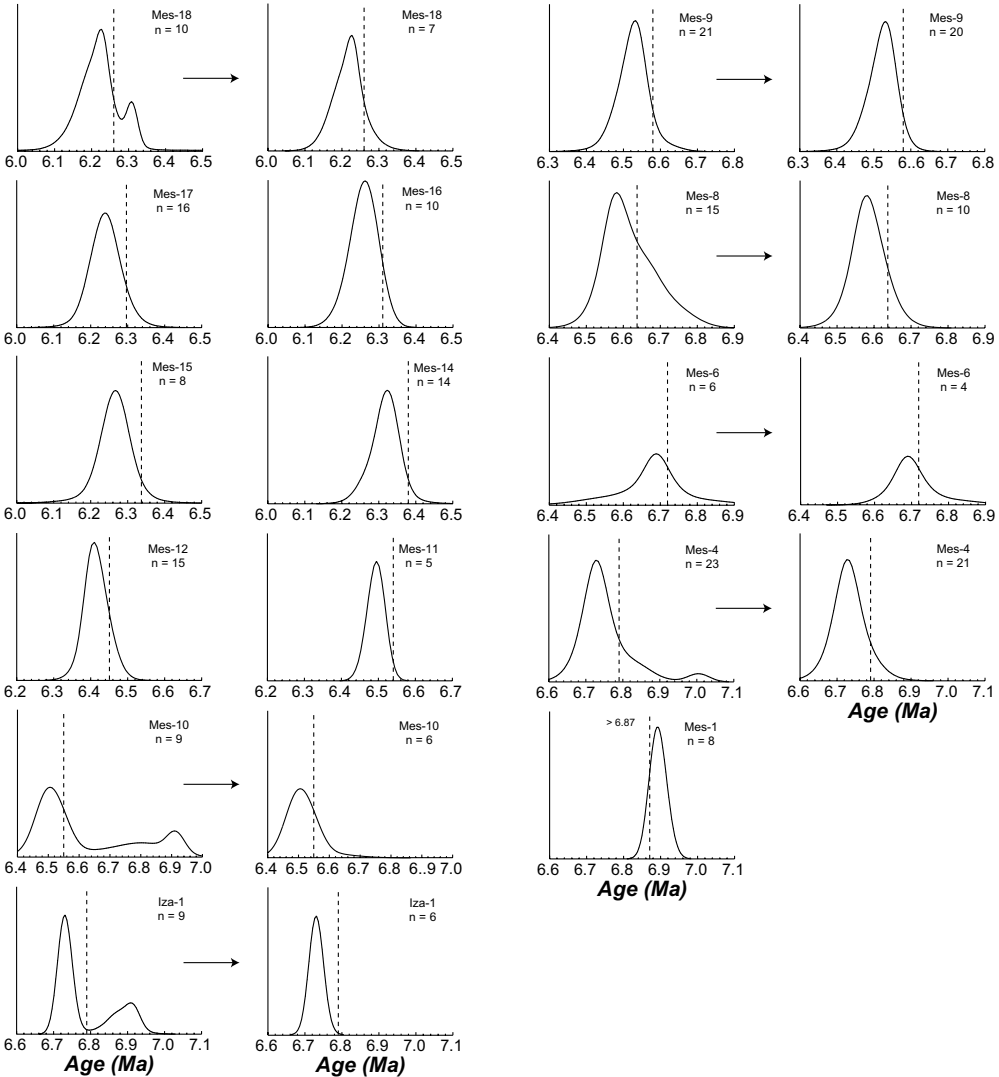


Figure 5.5. Examples of probability distributions for Melilla volcanic deposits. Probability distributions are shown for the Melilla tephras. In addition, the effect of removal of “outliers” on the age distributions is shown as well. The area under the curve is proportional to the number of experiments. Therefore, the Y-axis does not display the same scale in all figures. The Y-axes of Ifo-5, Ifo-4, Ifo-3, Mes-9 and Mes-4 is stretched 2.5 times, of Mes-17, Mes-14, Mes-12 2 times and of Ifo-1, Mes-1 and Iza-1 1.5 times relative to the Y-axes of the other figures.

The isochron intercepts of some ash layers (Mes-18, Mes-14 and Mes-11) deviate very slightly from the atmospheric ⁴⁰Ar/³⁶Ar ratio at the 1σ level. However, isochron ages differ <10 kyr from the weighted mean ages and at the 95% significance level the ⁴⁰Ar/³⁶Ar is indiscernible from 295.5 for the three ash layers. Further, the crystals analyzed from ash layer Mes-11 appeared to be plagioclase/sanidine mixtures with K/Ca <1.2. Combination of the VU37 data of Mes-8 with those obtained in VU42 resulted in a non-normal probability distribution for this tephra. Omitting the VU37 data is supported by the significant deviation (134 ± 51) from the atmospheric ⁴⁰Ar/³⁶Ar ratio. For the other volcanic ash layers, it appeared that outliers are consistently older than the main age population indicating xenocrystic contamination. Only for Mes-6 the outlying age appeared to be younger than the main population, but this analysis showed a significantly lower amount of radiogenic ⁴⁰Ar. Table 5.3 reports the combined weighted mean "tephra / standard" intercalibration factors (R) by weighting all individual R's with the inverse variance for each ash layer.

DISCUSSION

PREVIOUS RADIO-ISOTOPIC STUDIES IN THE MELILLA BASIN

Early chronological studies in the Melilla Basin focused on the petrology and volcanology of the domes and lava flows of the Trois Fourches and Gourougou volcanic complexes (Choubert et al., 1968; Hernandez and Bellon, 1985). More recent studies (Cunningham et al., 1994, 1997; Roger et al., 2000; Münch et al., 2001; Cornée et al., 2002) focused on the geochronology and development of the carbonate platform and its basinal equivalents. Several of the published ⁴⁰Ar/³⁹Ar ages are obtained for tephras intercalated in the astrochronologically tuned sections of Van Assen et al. (in press) and can be compared with the ⁴⁰Ar/³⁹Ar ages obtained here. In table 5.4 we summarize the relevant ⁴⁰Ar/³⁹Ar data from the original publications. The data of Cunningham et al. (1997) have been recalculated relative to FCT of 28.02 Ma. MWSD values have been estimated from data reported in the original publications. The ⁴⁰Ar/³⁹Ar ages for Me-13 and Me-5 of Roger et al. (2000) and Ta-2 of Cornée et al. (2002), show MSWD values <1. Ta-2 shows a narrow, symmetrical probability distribution. Therefore, the results for Ta-2 (Cornée et al., 2002) are considered as a good ⁴⁰Ar/³⁹Ar age estimate, where the reported uncertainty will increase when a full error estimate according to the modified method of Min et al. (2000) is given. The ⁴⁰Ar/³⁹Ar age estimates for Me-13 and

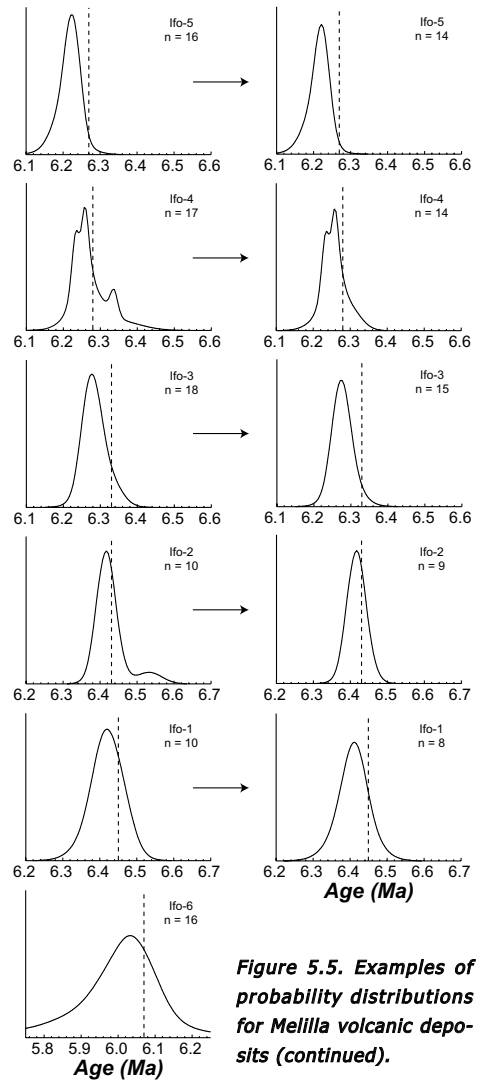


Figure 5.5. Examples of probability distributions for Melilla volcanic deposits (continued).

Ash layer	Cycle	Mineral	N	MSWD	R	σ_R	Astronomical age (Ma)	σ_{best}	$^{40}\text{Ar}/^{39}\text{Ar}$ age (Ma) $\pm 1\sigma$	Apparent FCT age (Ma) $\pm 1\sigma$
a.1.3	UA1	Biotite	26	1.04	4.2028	0.0064	6.692	0.005	6.71 \pm 0.01 (0.09)	27.96 \pm 0.05
a.1.2	LA17	Biotite	41	0.21	4.1629	0.0058	6.789	0.005	6.77 \pm 0.01 (0.09)	28.10 \pm 0.04
a.1.1	LA1	Biotite	37	0.57	3.8867	0.0044	7.161	0.005	7.25 \pm 0.01 (0.10)	27.68 \pm 0.04
a.1.2	LA17	San/plag mix	16	1.34	4.1728	0.0047	6.789	0.005	6.75 \pm 0.01 (0.09)	28.16 \pm 0.04
a.1.1	LA1	San/plag mix	5	0.08	3.9614	0.0093	7.161	0.005	7.11 \pm 0.02 (0.10)	28.20 \pm 0.07
Ifo-5	Ifo-9	Sanidine	14 (2)	0.18	4.5400	0.0057	6.270	0.005	6.21 \pm 0.01 (0.08)	28.29 \pm 0.04
Ifo-4	Ifo-8	Sanidine	14 (3)	0.44	4.4980	0.0059	6.281	0.005	6.27 \pm 0.01 (0.08)	28.08 \pm 0.04
Ifo-3	Ifo-6	Sanidine	15 (3)	0.14	4.4886	0.0067	6.333	0.005	6.28 \pm 0.01 (0.08)	28.25 \pm 0.05
Ifo-2	Ifo-1	Sanidine	9 (1)	0.32	4.3945	0.0051	6.432	0.005	6.41 \pm 0.01 (0.09)	28.10 \pm 0.04
Ifo-1	Ifo-1	Sanidine	8 (-)	0.13	4.3973	0.0087	6.443	0.005	6.41 \pm 0.01 (0.09)	28.16 \pm 0.06
Mes-18	Me-28	Sanidine	7 (3)	0.22	4.5307	0.0080	6.260	0.005	6.22 \pm 0.01 (0.08)	28.19 \pm 0.05
Mes-17	Top Me-26	Sanidine	16 (-)	0.40	4.5191	0.0060	6.298	0.005	6.24 \pm 0.01 (0.08)	28.29 \pm 0.04
Mes-16	Base Me-26	Sanidine	10 (-)	0.35	4.5011	0.0076	6.313	0.005	6.26 \pm 0.01 (0.08)	28.24 \pm 0.05
Mes-15	Me-25	Sanidine	8 (-)	0.08	4.4984	0.0097	6.337	0.005	6.27 \pm 0.01 (0.08)	28.33 \pm 0.06
Mes-14	Top Me-23	Sanidine	14 (3)	0.68	4.4616	0.0050	6.379	0.005	6.32 \pm 0.01 (0.08)	28.29 \pm 0.04
Mes-12	Me-19	Sanidine	15 (3)	0.38	4.3974	0.0046	6.450	0.005	6.41 \pm 0.01 (0.09)	28.19 \pm 0.04
Mes-11	Top Me-14	Plagioclase	5 (-)	0.31	4.3419	0.0068	6.542	0.005	6.49 \pm 0.01 (0.09)	28.23 \pm 0.05
Mes-10	Base Me-14	Sanidine	6 (3)	0.52	4.3310	0.0107	6.552	0.005	6.51 \pm 0.02 (0.09)	28.21 \pm 0.07
Mes-9	Me-12	Sanidine	20 (3)	0.42	4.3201	0.0045	6.582	0.005	6.52 \pm 0.01 (0.09)	28.26 \pm 0.04
Mes-8	Me-10	Sanidine	10 (5)	0.15	4.2826	0.0081	6.638	0.005	6.58 \pm 0.01 (0.09)	28.26 \pm 0.06
Mes-6	Me-8	Sanidine	4 (2)	0.32	4.2127	0.0132	6.718	0.005	6.69 \pm 0.02 (0.09)	28.13 \pm 0.09
Mes-4	Me-3	Sanidine	21 (3)	0.45	4.1880	0.0045	6.792	0.005	6.73 \pm 0.01 (0.09)	28.28 \pm 0.04
Iza-1	Iz-3	Sanidine	6 (5)	0.17	4.1891	0.0050	6.792	0.005	6.73 \pm 0.01 (0.09)	28.28 \pm 0.04
Ifo-6	>Ifo-17	Biotite	16	0.73	4.6779	0.0112	<6.07	0.025	6.03 \pm 0.01 (0.08)	28.22 \pm 0.07
Mes-1	<Me-1	Sanidine	8 (-)	0.25	4.0901	0.0047	>6.86	0.04	6.89 \pm 0.01 (0.09)	27.91 \pm 0.04
Mes-17	Top Me-26	Biotite	6	0.07	4.5689	0.0398	6.298	0.005	6.17 \pm 0.05 (0.10)	28.60 \pm 0.25

Table 5.3: Best $^{40}\text{Ar}/^{39}\text{Ar}$ age estimates for Sorbas/Nijar and Mellilla tephras and intercalibration with FCT.

In this table data presented in table 5.1 and 5.2 are combined to a single age estimate for each ash layer. In addition, the cycle in which the ash layer occurs, the number of analyses included and MSWD values are mentioned. The intercalibration factors R between ash layers and the FCT standard have been calculated and estimates for the astronomical calibrated ages for FCT are given. The R's of the VU37 data were calculated relative to TCR and have been recalculated relative to FCT with the intercalibration factor of 1.0112 ± 0.0010 between TCR and FCT (Renne et al., 1998). The analytical standard errors of the mean are reported for the $^{40}\text{Ar}/^{39}\text{Ar}$ ages of the ash layers with - between brackets - the full error estimate (eq. 1.14). 1σ errors according to equation 1.15 are reported for the astronomical calibrated FCT ages.

Me-5 of Roger et al. (2000) seem reliable, although probability distributions are asymmetrical (different populations can not clearly be distinguished). Me-16 and If-4 of Roger et al. (2000) have MSWD values >1 , indicating that either the assigned errors are too small to explain the observed scatter, or that the samples are heterogeneous. Both, Me-16 and If-4 show a bimodal probability distribution (not shown). MSWD values for the data published by Cunningham et al. (1997, table 5.4) are all >1 . Additionally, none of ash layers shows a perfect normal probability distribution. Especially V1 and V2 display a multi modal distribution, V3 shows a small age component around 6.3 Ma, while the dominant age is around 6.0 Ma and IR-1.0 is not completely symmetrical but represent the best approach to a normal distribution of the Cunningham et al. (1997) data. Nevertheless, the $^{40}\text{Ar}/^{39}\text{Ar}$ data of Cunningham et al. (1997), Roger et al. (2000) and Cornée et al. (2002) do not contradict the astronomical ages where the age constraints cannot be specified in more detail than older or younger than a certain astronomical age, because the volcanic layers are intercalated in the sedimentary section at a position either below the first tuned or above the last tuned cycle (V1, IR-1.0, V3, Ta-2). The $^{40}\text{Ar}/^{39}\text{Ar}$ ages of V2, Me-5, Me-13 and Me-16 (Cunningham, 1997; Roger et al., 2000) are systematically younger than the astronomical ages, If-4 (Roger et al., 2000) is older. Further, most of the $^{40}\text{Ar}/^{39}\text{Ar}$ ages of Cunningham et al. (1997), Roger et al. (2000) and Cornée et al. (2002) can not be distinguished at the 1σ level (analytical uncertainties only) from the data reported here (table 5.4). Only the bimodal (with peaks at 6.38 and 6.55 Ma) Me-16 of Roger et al. (2000) deviates from the $^{40}\text{Ar}/^{39}\text{Ar}$ age reported here. The $^{40}\text{Ar}/^{39}\text{Ar}$ data in three different laboratories (New Mexico Geochronology Research Center, Nice and the VUA) confirm the reproducibility of the $^{40}\text{Ar}/^{39}\text{Ar}$ ages.

Previous chronological studies in SE Spain mainly focussed on the lamproitic volcanism and on the Cabo de Gata volcanic complex. The thin volcanic horizons intercalated in sediments described by Bellon et al. (1983) are dated as Messinian based on the biostratigraphic constraints in the basin. No previous radio-isotopic studies on the volcanic ash layers studied here are known.

SEDIMENTARY CYCLES IN THE MELILLA BASIN PRECESSION CONTROLLED?

Apart from the discussion about the accuracy of $^{40}\text{Ar}/^{39}\text{Ar}$ ages in an absolute way, $^{40}\text{Ar}/^{39}\text{Ar}$ ages provide a relative time frame, where only the analytical uncertainty has to be accounted for. When plotting the $^{40}\text{Ar}/^{39}\text{Ar}$ data of the ash layers versus the cycle number in which they occur, an average period of 20.8 kyr is derived for a cycle based on simple linear regression. In this way it is confirmed by a completely independent method that the observed cyclicity is indeed precession controlled. This was already established independently for Pliocene cyclic continental successions (Steenbrink et al., 1999), but is now also confirmed for late Miocene marine successions.

DISCREPANCY BETWEEN $^{40}\text{Ar}/^{39}\text{Ar}$ AND ASTRONOMICAL AGES?

Figure 5.3 shows the $^{40}\text{Ar}/^{39}\text{Ar}$ data compared to the astronomical ages for incremental heating and combined fusion experiments of ash layers from the Sorbas/Nijar Basin (table 5.1). The error bars in the figure represent the combined analytical uncertainty of standards and samples (figure 5.3a). Most geochronological studies report analytical errors only. This is correct, when ages are only regarded as relative ages or when comparing ages to check on reproducibility. When radio-isotopic data are compared with astronomical ages, i.e. completely independent methods, the full realistic error estimate must be

Ash layer	$^{40}\text{Ar}/^{39}\text{Ar}$ age, published (Ma)	N	MSWD	Astronomical ages (Ma)	$^{40}\text{Ar}/^{39}\text{Ar}$ age, this study (Ma)
Cunningham et al, 1997					
V3	5.99 ± 0.10	12	3.20	<6.05 ± 0.02	6.03 ± 0.01
V2	6.72 ± 0.02	7	1.39	6.79	6.73 ± 0.01
V2	6.76 ± 0.02	8	2.42		
V1	7.05 ± 0.14	10	8.48		
V1	7.05 ± 0.14	7	3.29	>6.83	6.89 ± 0.01
IR-1.0	6.90 ± 0.02	10	1.94	>6.86	-
Roger et al, 2000					
Me-16	6.46 ± 0.03	10	1.45	6.58	6.53 ± 0.01
Me-13	6.54 ± 0.04	10	0.35	6.63	6.58 ± 0.01
Me-5	6.73 ± 0.02	1 + 1 + 1	0.87	6.79	6.73 ± 0.01
If-4	6.29 ± 0.02	3 + 4 + 3	1.52	6.29	-
Cornée et al, 2002					
Ta-2	6.87 ± 0.02	4 + 4 + 3	0.66	>6.83	6.89 ± 0.01

Table 5.4: Previously published geochronological data for the Melilla basin.

The "accepted" $^{40}\text{Ar}/^{39}\text{Ar}$ ages of previous publications on the Melilla basin are reported relative to FCT is 28.02 Ma. Errors are quoted at the 1σ level and represent analytical standard errors of the means.

reported to consider a $^{40}\text{Ar}/^{39}\text{Ar}$ age as an absolute age. Therefore, also other uncertainties i.e. in absolute ages of standards, decay constants must be accounted for. Using a slightly modified error propagation method based on Min et al. (2000), the uncertainties in $^{40}\text{Ar}/^{39}\text{Ar}$ ages increase (figure 5.3b) and almost all data are indistinguishable from their astronomical counterparts. However, the general picture is that the plateau ages of biotite are consistently older than the astronomical age for ash layer a.1.1. For ash layer a.1.2. the biotite plateau and astronomical ages are the same and for ash layer a.1.3. data are more scattered. When all plateau steps are combined a.1.3 is 6.707 ± 0.010 (0.091) Ma, a.1.2 is 6.771 ± 0.009 (0.092) Ma and a.1.1 is 7.251 ± 0.008 (0.098) Ma. Uncertainties are analytical errors, between brackets full error estimates were given. Combined plateau ages of a.1.1 and a.1.2 show almost normal probability distributions, MSWD values lower than 1 and isochron intercepts indistinguishable from the atmospheric ratio of 295.5 (296.2 ± 3.9 for A.1.1, 294.9 ± 3.4 for A.1.2). Ash layer a.1.3 has a slightly higher MSWD value (1.04), an isochron intercept that very slightly deviates from the atmospheric ratio at the 1σ level (298.3 ± 2.4) and an almost normal probability distribution. The inverse isochron age for a.1.3 is 6.679 ± 0.027 (or 0.094 full error) Ma. Overall, it can be concluded that the $^{40}\text{Ar}/^{39}\text{Ar}$ biotite data of Sorbas do not show a systematic deviation towards younger ages relative to the astronomical ages (i.e., 6.71 ± 0.09 Ma versus 6.69 Ma for a.1.3, 6.77 ± 0.09 Ma versus 6.77 Ma for a.1.2 and 7.25 ± 0.10 Ma versus 7.16 Ma for a.1.1). Due to the lack of high quality data on sanidine, we can not tell if there exist a difference between sanidine and biotite $^{40}\text{Ar}/^{39}\text{Ar}$ ages, although biotite ages in Ptolemais and Faneromeni (chapter 3) appeared to be significantly older than the sanidine ages. The data reported on the sanidine / plagioclase mixtures for Sorbas / Nijar do show a tendency to be younger than the biotite (and astronomical) ages as well. This might for example be due to recoil effects in biotite (e.g., Huneke and Smith, 1976).

In Melilla predominantly single crystals of sanidine have been dated. This enabled us to unequivocally detect xenocrystic contamination. Figure 5.5 directly shows the influence of removal of contaminating data

on the age distributions. Therefore, the accepted $^{40}\text{Ar}/^{39}\text{Ar}$ ages for all tephras are normal distributions with MSWD <1 substantially lower than 1 (see table 5.3), indicating that samples are homogeneous and analytical errors are not underestimated. A full error assessment has also been applied to the Melilla data increasing the (analytical) uncertainty about ~4 times. Looking at the analytical error only, all reliable $^{40}\text{Ar}/^{39}\text{Ar}$ ages are systematically younger than their astronomical counterparts (even the biotite of Mes-6). With a full error assessment this discrepancy is not significant anymore. It must be remarked that the variance of such a full error assessment is dominated for >75% by the uncertainty in the activity of the decay of ^{40}K to ^{40}Ar and for ~14% by the uncertainty in the amount of radiogenic ^{40}Ar in the primary standard for all analyses. To obtain more accurate $^{40}\text{Ar}/^{39}\text{Ar}$ ages effort must be directed to decreasing the uncertainties in the values of these parameters (e.g., Begemann et al., 2001). Overall, it can be concluded $^{40}\text{Ar}/^{39}\text{Ar}$ ages on sanidine indeed tend to be systematically younger than the astronomical counterparts in the eastern (chapter 3) as well as in the western part (this chapter) of the Mediterranean, although with a full error assessment this discrepancy might disappear partly. Biotite ages show a less consistent picture.

IMPLICATIONS FOR AN ASTRONOMICALLY CALIBRATED $^{40}\text{Ar}/^{39}\text{Ar}$ STANDARD?

As stated before the uncertainties in the activity of the decay of ^{40}K to ^{40}Ar and in the amount of radiogenic ^{40}Ar in the primary standard dominate the total variance of $^{40}\text{Ar}/^{39}\text{Ar}$ ages. One way to diminish the influence of these two parameters is to use a primary standard, which is dated by completely independent methods. Here we will use the astronomically dated ash layers as "primary" standard to establish an age for FCT. In that case the amount of radiogenic ^{40}Ar in the primary standard does not occur in the age equation and the activity of the decay of ^{40}K to ^{40}Ar occurs only once (instead of twice) (Chapter 1). Table 5.3 shows the obtained ages for FCT based on the ash layers in the western Mediterranean. The FCT ages intercalibrated to biotite ages show a different pattern than sanidine ages, but are not consistent. The FCT ages obtained on the Sorbas/Nijar sanidine/plagioclase mixtures seem to support the data obtained for Melilla, but unfortunately, these data were not of the same excellent quality. The Melilla ash layers produce a consistent age for FCT with only one ash layer (Ifo-4) significantly different at the 1σ level. This ash layer appeared to be the only multi-modal ash layer in Melilla (figure 5.5) with no indications for the "true" age, but with the youngest peak of 6.235 Ma producing an age of 28.22 Ma for FCT. Total variance is now dominated by the analytical uncertainties (~70-90%) and the uncertainty in the astronomical age of the volcanic ash layer (~10-30%). As shown in chapter 3 uncertainties in decay constants (or related parameters) hardly influence the data in this time interval and therefore the discussion about the "true" values for decay constants (e.g., Begemann et al., 2001) can be circumvented. The weighted mean age for FCT intercalibrated to all reliable sanidine data of Melilla (excluding Ifo-4 and plagioclase Mes-11) is 28.24 ± 0.01 Ma (standard error of the mean, with a 10 kyr uncertainty in the astronomical age). The probability distribution is normal and the MSWD is 0.51. This age for FCT is in agreement with the age of 28.21 ± 0.03 Ma for the A1 ash on Crete, but is different from the age of 28.02 Ma of Renne et al. (1998) and 28.476 ± 0.064 Ma zircon concordia age of Schmitz and Bowring (2001). However, Renne et al. (1998) report an uncertainty of 0.28 Ma, when all sources of error are included and therefore, the Renne et al. (1998) age is not significantly different than ours, but ours is more accurate. The U/Pb age of Schmitz and Bowring (2001) might be affected by residence time in the magma chamber, producing an older age than the age of eruption.

CONCLUSIONS

Sanidine $^{40}\text{Ar}/^{39}\text{Ar}$ ages are indeed systematically younger than astronomical ages for volcanic ash layer from which the sanidine originates. This is most probably due to the uncertainties in decay constants and the absolute age of the standards. Intercalibrating the $^{40}\text{Ar}/^{39}\text{Ar}$ data of FCT and 16 ash layers in Melilla results in an age of 28.24 ± 0.01 Ma for FCT equivalent to 28.21 ± 0.03 Ma based on the A1 ash layer on Crete. The intercalibration with the Ptolemais data (chapter 3) is not consistent with these data. Xenocrystic contamination observed (and accounted for) in Melilla could not be assessed in Ptolemais and Crete. However, possible occurrence of xenocrystic contamination in Ptolemais does not fully explain the observed difference, because $^{40}\text{Ar}/^{39}\text{Ar}$ ages are too young and xenocrystic contamination tends to result in older $^{40}\text{Ar}/^{39}\text{Ar}$ ages. This may imply possible uncertainties in the tuning in Ptolemais unrecognized so far. Additionally, to confirm an age of 28.24 Ma for FCT relative to an astronomically dated standard, we will extend our research to deep marine astronomically dated sections of middle Miocene age (category 1 ash layers).

CHAPTER 6

SYSTEMATIC DISCREPANCIES BETWEEN $^{40}\text{Ar}/^{39}\text{Ar}$ AND ASTRONOMICAL DATING IN THE MIDDLE MIOCENE?

INTRODUCTION

In chapters 3 and 5 a systematic discrepancy between $^{40}\text{Ar}/^{39}\text{Ar}$ and astronomical ages of ash layers in the late Miocene and Pliocene of the Mediterranean was found with $^{40}\text{Ar}/^{39}\text{Ar}$ ages being younger by $\sim 1\%$. This might be due to uncertainties in the age of standards used in argon geochronology or to uncertainties in decay constants. As discussed in chapters 3 and 5 intercalibrating argon standards with astronomically dated ash layers can reduce the influence of uncertainties in decay constants. This resulted in an age estimate of 28.24 ± 0.01 Ma for the commonly used standard FCT sanidine (chapter 5). Although the quality of the $^{40}\text{Ar}/^{39}\text{Ar}$ and astronomical ages underlying this intercalibration is excellent, we would like to confirm the proposed standard age by extending our study to the middle Miocene. Unfortunately, the occurrence of sanidine containing volcanic ash layers intercalated in sections with an accurate astronomical time control is not so widespread. In this chapter $^{40}\text{Ar}/^{39}\text{Ar}$ ages of several middle Miocene volcanic levels intercalated in the Gibliscemi section on Sicily and the Monte dei Corvi section in northern Italy will be discussed.

GEOLOGICAL SETTING

The Gibliscemi section is located around Monte Gibliscemi near Mazzarino on Sicily, east of road S110 from Gela to Mazzarino (figure 6.1). The sedimentary sequence was deposited in the Caltanissetta Basin, which was part of the Apenninic-Maghrebian foredeep (Hilgen et al., 2000a). This foredeep developed externally to the evolving orogeny. The African foreland is presented by the nearby Ragusa platform of southeastern Sicily (Hilgen et al., 2000a). The Gibliscemi section overlies the intensely deformed multi-colored clays of the "Argille Scagliose". It consists of deep marine cyclically bedded sediments, followed by the Tripoli Formation (diatomites) and the section is covered by the Gessoso-Solfifera Formation (Calcarea di Base limestones), which is the sedimentary expression of the Messinian Salinity Crisis in Gibliscemi. Deformation in the Gibliscemi section is extensional only and resulted in low angle shear planes in the lower part of the section which tectonically reduce the stratigraphy. The sedimentary cyclicity mainly consists of whitish-colored homogeneous marl and dark, grey colored marl (or marly clay). In the top and bottom part of the Gibliscemi section brownish, often laminated, beds (sapropels) replace these darker colored marls. Cycles are not strictly bipartite, but might also be quadripartite due to intercalation of a greyish beige marl within the white homogeneous marl. Four distinct fine-grained ash layers were found in the lower part of the section around the Serravallian-Tortonian boundary (Hilgen et al., 2000a).

The Monte dei Corvi section is exposed in the coastal cliffs of the Conero Riviera south of Ancona in northern Italy (figure 6.1, Hilgen et al., 2003). This area was the last to be involved in the orogenic deformation due to the developing Alpine-Apennine orogenic system. Therefore the system remained pelagic until the Pliocene and included the Aquitanian to Langhian Bisciaro Formation, the Langhian to Tortonian Schlier Formation, and the Messinian Euxinic Shale and Gessoso Solfifera Formations of the northern Apennines (Montanari et al., 1997). The section consists of cyclic alternating marls, marly limestones and organic-rich beds (sapropels). A basic small-scale cycle is a couplet of an indurated whitish marly limestone and a softer grey to greenish-grey marl, where sapropels are occasionally intercalated in the limestones (Hilgen et al., 2003). Volcanic intervals have been found in the Serravallian (Respighi level), around the Serravallian-Tortonian boundary (Ancona level) and in the Rossini level around the Tortonian-

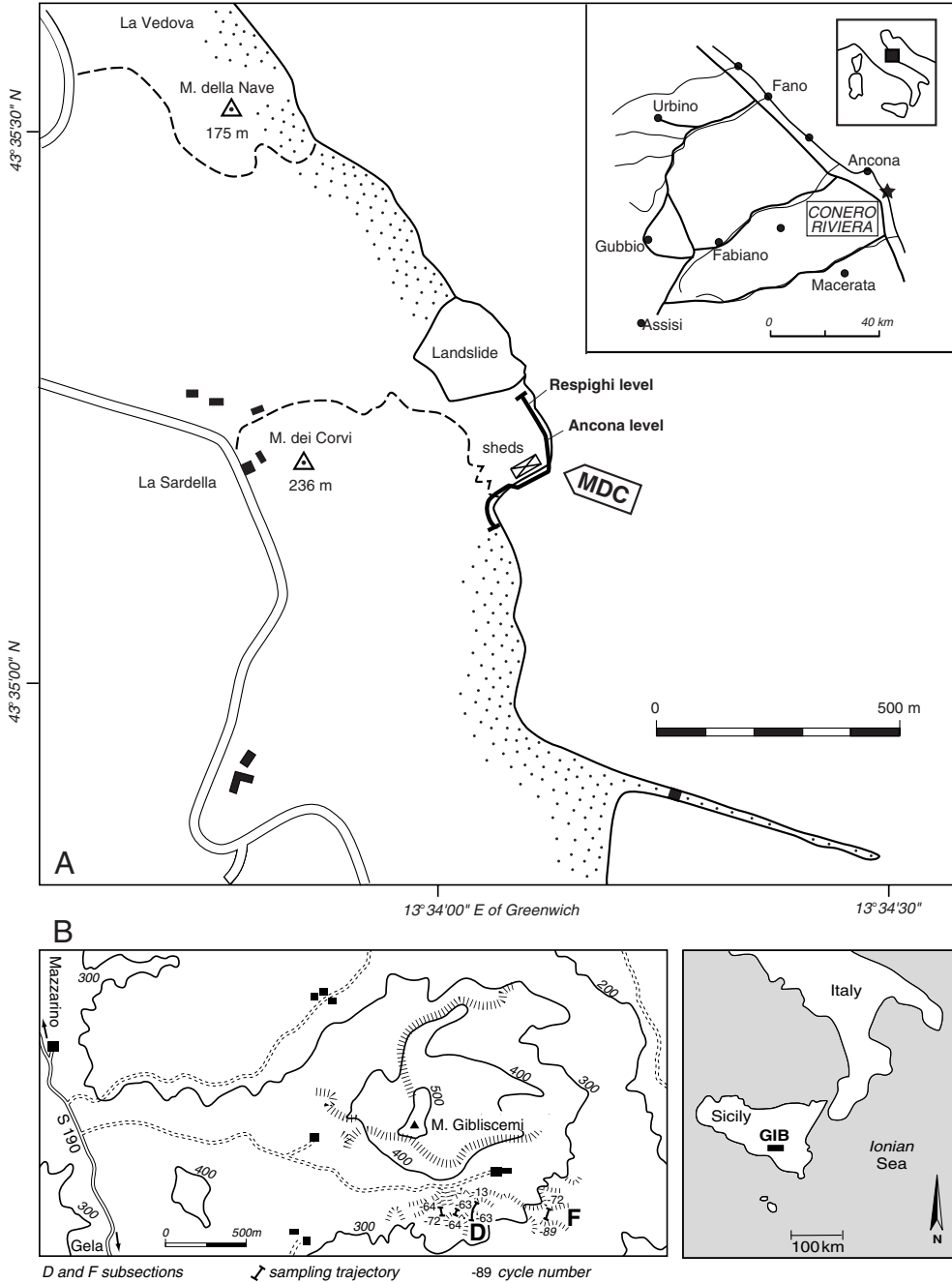


Figure 6.1: Geographic locations of studied sections.

Locations of the studied sections are shown. The exact locations are described in Hilgen et al. (2000a, 2003).

Messinian boundary, which includes several volcanic events. The chemical composition of biotites from the Respighi level is more or less similar to the biotites found in the underlying Biscario Formation. The Ancona biotite is more similar to biotite of the late Eocene-Oligocene Scaglia Cinerea formation (Montanari et al., 1997 and references therein), suggesting the western Sardinian volcanic province as source for the Respighi level, or at least that the source was different from that of the Ancona level (Montanari et al., 1994).

ASTRONOMICAL TIME FRAME

As discussed before, the accuracy of astronomical ages of volcanic ash layers intercalated in these sedimentary sequences ultimately depends on 1) the correctness of the tuning, 2) the accuracy of the astronomical solution and its associated values for tidal dissipation and dynamical ellipticity, 3) the correctness of the assumption of constant sedimentation rates between two astronomical tie points (e.g., sapropel midpoints) and 4) uncertainties about the lag time between astronomically forced climate response and registration in the sediments. Assumptions 2-4 were already discussed in chapter 2 and for the time interval 11-13 Ma an uncertainty of 10 kyr is assumed for astronomical ages of volcanic layers. Thus, assuming a correct tuning, an error of 10 kyr will be used in intercalibration calculations. The tuning procedures and the "correctness" of the tuning for both the Gibliscemi and Monte dei Corvi sections are summarized here from Hilgen et al. (2000a, 2003).

The astronomical tuning of the Gibliscemi section started with the construction of an integrated framework for the Mediterranean upper Miocene sequences (Krijgsman et al., 1995). The magnetostratigraphic calibration of in part the Metochia section to the GPTS of CK95 in combination with the calcareous planktonic biostratigraphy provided the first order time control. Unfortunately, no magnetostratigraphy was available for the lower part of the Gibliscemi section, but tuning of the upper part of the section (subsections A/B) could be extended downwards to older levels. Ages for polarity reversals in the section obtained from the GPTS (Cande and Kent, 1995) provided a first order time control. Then a first order tuning was proposed by correlating large-scale sapropel clusters to 400 kyr eccentricity maxima followed by correlation of the small-scale sapropel clusters to 100 kyr eccentricity maxima. Phase relations between sapropels and orbital times series as established for the late Miocene and Plio-Pleistocene (Hilgen et al., 1991a, 1995; Lourens et al., 1996) were adopted for the middle Miocene based on a study of 9.5 Ma old sapropels (Schenau et al., 1999). The tuning was completed by tuning of the individual sapropels to precession minima and corresponding insolation maxima of the $La90_{(1,1)}$ 65°N hemisphere insolation curve. This resulted in a good fit between characteristic patterns in the astronomical and sedimentary records. Figure 6.2 shows the lower part of the tuning of the Gibliscemi section displaying only the subsections D and F. Hilgen et al. (2003) slightly modified the tuning of cycles -84 to -79 by shifting one cycle up compared to Hilgen et al. (2000a). This only effects the age of GiF-2. However, comparison of the sedimentary cycle pattern with the insolation pattern of $La90_{(1,1)}$ does not fully support the newly proposed tuning. Therefore, an extra "tuning" uncertainty of 20 kyr is added for the astronomical age of GiF-2.

Biostratigraphic correlations between Gibliscemi and Monte dei Corvi are straightforward and biostratigraphic events were used as starting point to correlate the sedimentary cycle patterns of both sections. The detailed correlations between Gibliscemi and Monte dei Corvi in combination with an average periodicity of ~20 kyr for the sedimentary cycles based on $^{40}\text{Ar}/^{39}\text{Ar}$ ages of the Respighi and Ancona levels (Montanari et

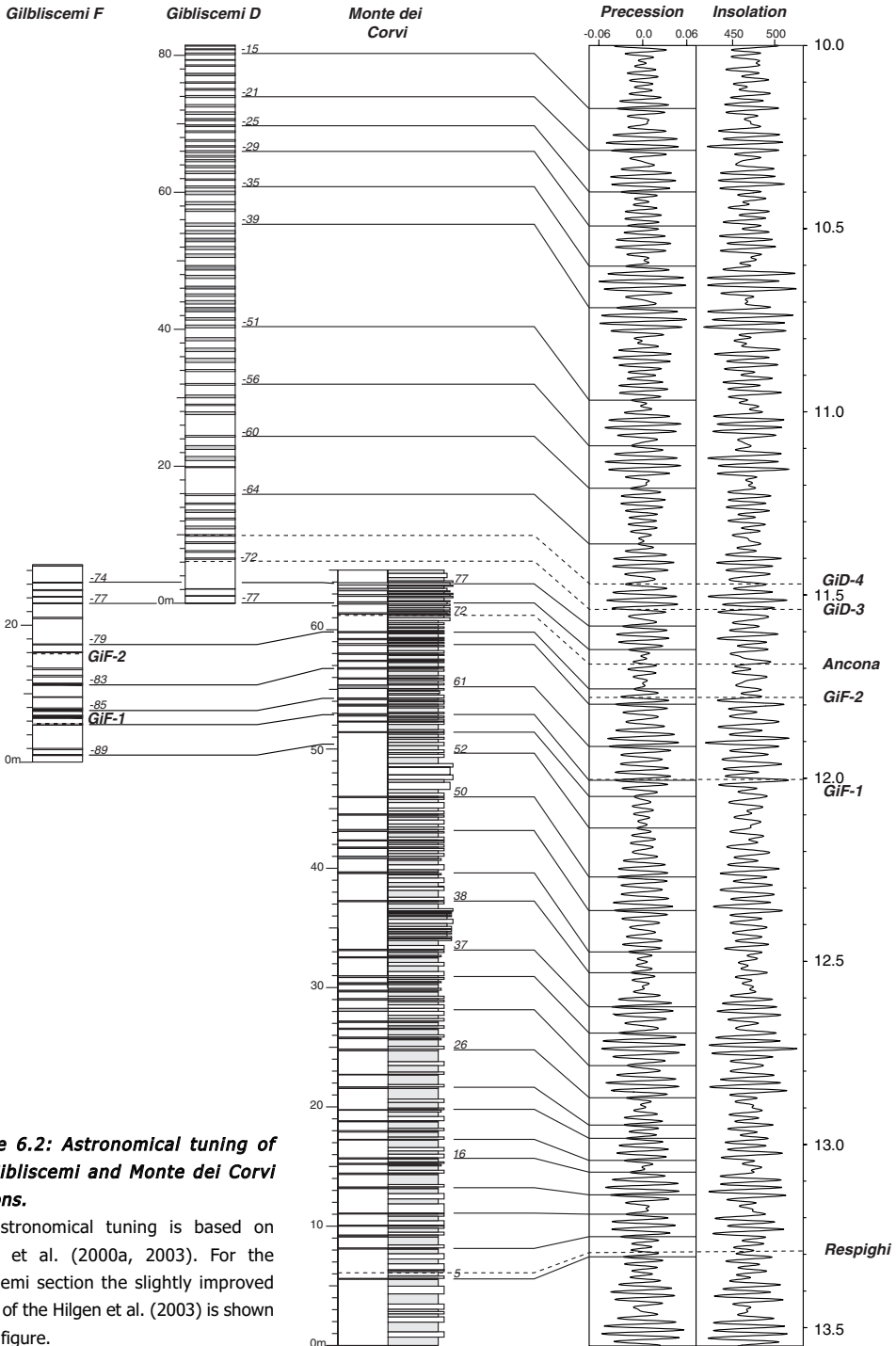


Figure 6.2: Astronomical tuning of the Gibilscemi and Monte dei Corvi sections.

The astronomical tuning is based on Hilgen et al. (2000a, 2003). For the Gibilscemi section the slightly improved tuning of the Hilgen et al. (2003) is shown in this figure.

al., 1997) confirmed the astronomical origin of the sedimentary cycles in Monte dei Corvi. The phase relations between the cycles and the individual astronomical parameters are based on the detailed correlations to the Gibliscemi section and the fact that the phase relation for sapropels in the latter section is known. The astronomical tuning in Monte dei Corvi started by tuning the large- and small-scale sapropel clusters to respectively 400 kyr and 100 kyr eccentricity maxima followed by calibrating the individual cycles to precession and insolation. The tuning intervals of interest for this study are cycles 52-86 containing the Ancona level and cycles 4-37 with the Respighi level. The tuning of the basic cycles 52-86 is straightforward, although no perfect match is found with insolation. This is most likely due to the fact that precession/obliquity interference is not reliably solved for this time interval (e.g., due to uncertainties in the value for tidal dissipation term or uncertainties in the orbital solution itself). Cycles 4-37 can be tuned to precession unambiguously, because there is only one option to tune sapropels of the small-scale clusters to precession (Hilgen et al., 2003).

METHODS

In the Monte dei Corvi two volcanic levels (Ancona and Respighi) were collected along the beach section. In the Monte Gibliscemi section four volcanic layers have been identified and sampled (GiF-1, GiF-2, GiD-3, GiD-4). The locations of the sampled sections are given in figure 6.1. The bulk samples were crushed, washed and sieved. The 125-250 μm fractions were used for standard magnetic and heavy liquid separations of sanidine, the 250-500 μm fractions for separation of biotite. Density separations ranged from 2.55-2.58 g/cm^3 for sanidine and were $>3.05 \text{ g/cm}^3$ for biotite. Size fractions smaller than 125 μm were considered unsuitable for $^{40}\text{Ar}/^{39}\text{Ar}$ dating. Subsequently, all samples were handpicked and sanidine samples were leached with a 1:5 HF solution in an ultrasonic bath for 5 minutes. The samples were wrapped in Al-foil and loaded in a 5 mm ID quartz vial. Fish Canyon Tuff (FC-2) sanidine and Taylor Creek Rhyolite (TCR2a) were wrapped in Cu-foil and loaded at the top and bottom positions and between each set of 3-5 samples. Samples were irradiated in one irradiation batch (VU42) for 7 hours in the Oregon State University TRIGA reactor in the cadmium shielded extended tube CLICIT facility. After irradiation samples and standards were loaded in 2 mm diameter holes of a copper planchet and placed in an ultra-high vacuum extraction line. After placement of the samples in the extraction line, samples and extraction line were outgassed at 200°C with heating coil and an infrared lamp. Samples and standards were stepwise heated or directly fused. See chapter 1 for details on instrumentation and analytical procedures.

Replicate fusion experiments have been performed on standards after a pre-heating step with a defocused laserbeam with an output of 2 W (samples did not glow and gas was pumped away) to remove undesirable atmospheric argon adsorbed to the crystal surface. From past experience we know that under these conditions only a small fraction (<5%) of ^{39}Ar , equivalent to first incremental heating steps, is affected. Multiple grain fractions of biotite have been measured by stepwise heating. Experiments were replicated up to 5 times. Multiple grain feldspar fractions have been analyzed in two steps. The first "preheating" step contained significant amounts of gas, which has been analyzed. During the second step samples were completely fused. Beam intensities were measured in a peak-jumping mode over the mass range 40-36 on a secondary electron multiplier. For data collection the mass spectrometer is operated with a modified version of standard MAP software (i.e., valve control, laser control and variable

integration times). System blanks were measured every 3 steps. The total system blanks were in the range of 2.9×10^{-14} moles for mass 40, 3.6×10^{-15} moles for mass 39, 1×10^{-15} moles for mass 38, 1.2×10^{-14} moles for mass 37 and 1.3×10^{-15} moles for mass 36. Mass discrimination (1.002-1.0070 per atomic mass unit) was monitored by frequent analysis of $^{40}\text{Ar}/^{38}\text{Ar}$ reference gas pipette aliquots (chapter 1). The irradiation parameter J for each unknown was determined by interpolation using a 2nd order weighted polynomial fitting between the individually measured standards (see chapter 1).

Data reduction is performed using the in-house developed ArArCalc(v2.20c) software (Koppers, 2002). Blanks corrections are performed by subtracting the mean blank values of blank analyses before and after measurement of the unknown. Mass discrimination and interfering nuclear isotope corrections are applied as described in chapter 1. Ages are calculated with the standard age equation relative to FCT of 28.02 Ma (Renne et al., 1998) and with the decay constants of Steiger and Jäger (1977). Errors are reported at the 1σ level and include the analytical error in the unknown and standard. Weighted mean $^{40}\text{Ar}/^{39}\text{Ar}$ ratios or ash-layer/FC intercalibration factors (R) and their standard errors of the mean are used in the age calculations (eq. 1.11 and 1.12). For comparison ages are also calculated with a slightly modified version of the full external error calculation as in Min et al. (2000) with physical parameters and activity data as in table 1.4, column VII. This last approach presents the most realistic age and error estimate. MSWD values are assessed to estimate the reliability of estimated ages and errors.

RESULTS

In table 6.1 the analytical data are given for all experiments (extended data tables are given in the online appendix). Figure 6.4 shows $^{40}\text{Ar}/^{39}\text{Ar}$ age probability distributions, where the vertical dashed line represents the astronomical age for each volcanic ash layer.

MDC RESPIGHI BIOTITE

Three stepwise heating experiments have been performed on biotite (250-500 μm) of the Respighi ash layer. Figures 6.3a-c show the incremental heating spectra. Two experiments are characterized by a younger and an older plateau (plateau I and II), which are significantly different (at the 2σ level). The third experiment does not show this behavior, but the plateau is equivalent in age as the plateau II in the other experiments. Combination of all plateau steps (ignoring plateau I data) results in an age of 13.47 ± 0.03 Ma (1σ analytical error) for the biotite of the Respighi ash layer. We preferred the plateau II age because it comprises a higher amount of the total ^{39}Ar released. Isochrons are poorly constrained due to clustering of the data, but intercepts do not deviate from the atmospheric $^{40}\text{Ar}/^{36}\text{Ar}$ ratio at the 2σ level. Therefore, we prefer the integrated plateau age above the integrated isochron ages. Further, figures 6.4a and b show the probability distribution of the age of the Respighi layer, where 6.4b is more detailed and shows the separate distributions of plateau I and II. Deconvolution of both groups is only based on the data (not on deconvolution software). Plateau I and II separately show normal behavior, where the older peak is the preferred age for the Respighi layer.

Identity (biotite)	F _{unknown}	σ_f	N	MSWD	$^{40}\text{Ar}^*$ %	$^{39}\text{Ar}_k$ %	Normal isochron intercept	Inverse isochron intercept	F _c	$\sigma_{f,c}$	$^{40}\text{Ar}/^{39}\text{Ar}$ age (Ma)
MdC Respighi VU42-A24											
02m0399b, plateau I	3.9643	0.0087	3 (7)	0.06	89.2	50.8	281 ± 48	281 ± 48	8.3929	0.0176	13.29 ± 0.04 (0.19)
02m0399b, plateau II	4.0205	0.0089	3 (7)	0.01	91.1	44.0	286 ± 73	285 ± 72	8.3929	0.0176	13.48 ± 0.04 (0.19)
02m0399b, combined plateau	3.9917	0.0126	6 (4)	4.14	90.1	94.8	207 ± 46	221 ± 47	8.3929	0.0176	13.38 ± 0.05 (0.19)
02m0399c, plateau I	3.9604	0.0108	2 (8)	0.11	87.5	29.8	-	-	8.3929	0.0176	13.28 ± 0.05 (0.19)
02m0399c, plateau II	4.0384	0.0083	4 (6)	0.25	90.9	62.1	268 ± 35	270 ± 35	8.3929	0.0176	13.54 ± 0.04 (0.19)
02m0399c, combined plateau	4.0095	0.0171	6 (4)	6.74	89.8	92.0	207 ± 26	202 ± 26	8.3929	0.0176	13.44 ± 0.06 (0.20)
02m0406a, plateau	4.0116	0.0052	7 (2)	0.32	89.8	88.3	300 ± 25	300 ± 25	8.3929	0.0176	13.45 ± 0.03 (0.19)
Integrated plateau I	3.9628	0.0068	5	0.08	88.5	-	282 ± 28	282 ± 28	8.3929	0.0176	13.28 ± 0.04 (0.19)
Integrated plateau (II)	4.0193	0.0039	14	0.79	90.4	-	277 ± 17	281 ± 17	8.3929	0.0176	13.47 ± 0.03 (0.19)
MdC Ancona VU42-A25/A57											
A25: 02m0400a plateau	3.5397	0.0068	7 (2)	0.36	85.1	87.9	292 ± 12	292 ± 12	8.4019	0.0176	11.86 ± 0.03 (0.17)
A25: 02m0400b plateau I	3.5304	0.0065	4 (5)	0.90	88.4	61.0	245 ± 30	247 ± 28	8.4019	0.0176	11.83 ± 0.03 (0.17)
A25: 02m0400b, plateau II	3.4600	0.0136	3 (6)	0.12	79.2	28.1	294 ± 7	294 ± 7	8.4019	0.0176	11.59 ± 0.05 (0.17)
A25: 02m0400b combined plateau	3.5174	0.0119	7 (2)	4.12	85.3	89.1	284 ± 13	281 ± 12	8.4019	0.0176	11.78 ± 0.05 (0.17)
A57: 02m0400d plateau	3.7637	0.0090	5 (4)	0.68	90.7	61.8	245 ± 49	234 ± 47	8.9649	0.0188	11.82 ± 0.04 (0.17)
A57: 02m0400e plateau	3.7699	0.0081	5 (4)	0.19	91.5	78.4	268 ± 33	277 ± 33	8.9649	0.0188	11.84 ± 0.04 (0.17)
A25: 02m0405a plateau	3.5094	0.0075	6 (3)	0.17	89.8	81.3	293 ± 29	295 ± 30	8.4019	0.0176	11.76 ± 0.04 (0.16)
Integrated plateau (I)	R	σ_R	27	0.58	88.9	-	293 ± 11	294 ± 11	-	-	11.82 ± 0.01 (0.17)

Identity (sanidine / plagioclase)	F_{unknown}	σ_F	N	MSWD	$^{40}\text{Ar}^*$ %	K/Ca	Normal isochron intercept	Inverse isochron intercept	F_{ic}	$\sigma_{F_{\text{ic}}}$	$^{40}\text{Ar}/^{39}\text{Ar}$ age (Ma)	
MdC Ancona VU42-A32												
Step 1	3.5306	0.0040	10	0.35	98.4	13.0	238 ± 35	253 ± 37	8.4839	0.0178	11.71 ± 0.03 (0.16)	
Step 2	3.5195	0.0052	10	0.45	98.1	13.9	242 ± 29	270 ± 34	8.4839	0.0178	11.68 ± 0.03 (0.16)	
Step 1 & 2	3.5264	0.0032	20	0.53	98.3	13.3	257 ± 23	264 ± 25	8.4839	0.0178	11.70 ± 0.03 (0.16)	
MdC Ancona VU42-A29												
Step 1	3.5307	0.0065	7 (3)	0.84	96.7	8.0	308 ± 64	368 ± 80	8.4472	0.0177	11.76 ± 0.03 (0.16)	
Step 2	3.5082	0.0086	7 (3)	0.19	99.1	10.4	114 ± 69	226 ± 69	8.4472	0.0177	11.69 ± 0.04 (0.16)	
Step 1 & 2	3.5226	0.0052	14 (6)	0.81	97.5	8.3	274 ± 30	335 ± 32	8.4472	0.0177	11.74 ± 0.03 (0.16)	
MdC Ancona VU42-A32/A29												
	R	σ_R										
Step 1	0.4167	0.0005	17 (3)	0.61	97.8	9.1	308 ± 26	336 ± 28	-	-	11.73 ± 0.01 (0.16)	
Step 2	0.4150	0.0006	17 (3)	0.28	98.4	12.3	178 ± 27	257 ± 34	-	-	11.68 ± 0.02 (0.16)	
Step 1 & 2	0.4160	0.0004	34 (6)	0.59	98.0	9.7	251 ± 19	332 ± 21	-	-	11.71 ± 0.01 (0.16)	

Table 6.1: Analytical data of biotite experiments on Respighi and Ancona ash layers, of sanidine experiments on Ancona ash layer and of experiments on Gibiliscemi volcanic ash layers.

This table lists the analytical data of all $^{40}\text{Ar}/^{39}\text{Ar}$ experiments on middle Miocene ash layers. Errors are quoted at the 1σ level. Errors in the $^{40}\text{Ar}/^{39}\text{Ar}$ ratios represent standard errors of the mean. Ages and 1σ analytical errors are calculated relative to FCT of 28.02 Ma (Renne et al., 1998, chapter 1; equations 1.11, 1.12). Ages according to equation 1.14 did not yield different ages. Full errors are reported between brackets (chapter 1; equation 1.14).

Identity (sanidine / plagioclase)	F _{unknown}	σ _F	N	MSWD	⁴⁰ Ar* %	K/Ca	Normal isochron intercept	Inverse isochron intercept	F _c	σ _{F_c}	⁴⁰ Ar/ ³⁹ Ar age (Ma)
Gid-4 VU42-A36/A52											
Step 1	R	σ _R									
Step 1	0.5260	0.0392	10	2813	84.4	7.6	(2.8 ± 0.9) × 10 ³	(1.2 ± 0.4) × 10 ³	-	-	14.8 ± 1.1 (1.1)
Step 2	0.4837	0.0472	10	3892	92.9	9.0	467 ± 129	(11 ± 17) × 10 ³	-	-	13.6 ± 1.3 (1.3)
Step 1 & 2	0.5062	0.0303	20	3276	87.5	7.7	562 ± 94	2143 ± 972	-	-	14.2 ± 0.8 (0.8)
A52: Step 1	4.9962	0.4435	6	4897	81.7	7.1	(3.1 ± 1.4) × 10 ³	(4 ± 6) × 10 ³	8.8785	0.0178	15.8 ± 1.4 (1.4)
A52: Step 2	4.9460	0.8355	6	10475	92.6	8.2	575 ± 370	(0.3 ± 12) × 10 ⁶	8.8785	0.0178	15.7 ± 2.6 (2.6)
A52: Step 1 & 2	4.9774	0.4185	12	6989	85.2	7.2	(2.4 ± 0.7) × 10 ³	(7 ± 17) × 10 ³	8.8785	0.0178	15.8 ± 1.3 (1.3)
A36: Step 1	3.4444	0.0129	3 (1)	13.0	93.4	9.0	424 ± 37	429 ± 37	8.5255	0.0179	11.37 ± 0.16 (0.22)
A36: Step 2	3.4715	0.0097	3 (1)	0.54	91.6	10.7	308 ± 14	306 ± 13	8.5255	0.0179	11.46 ± 0.04 (0.16)
A36: Step 1 & 2	3.4618	0.0077	6 (2)	6.0	92.5	9.2	340 ± 29	336 ± 27	8.5255	0.0179	11.43 ± 0.07 (0.17)
Gid-3 VU42-A35											
Step 1	3.4636	0.0051	10	0.30	97.4	11.2	260 ± 81	333 ± 106	8.5255	0.0179	11.44 ± 0.03 (0.16)
Step 2	3.4894	0.0047	10	0.25	96.8	11.7	280 ± 15	293 ± 17	8.5255	0.0179	11.52 ± 0.03 (0.16)
Step 1 & 2	3.4776	0.0035	20	0.98	97.1	11.4	240 ± 24	315 ± 17	8.5255	0.0179	11.48 ± 0.03 (0.16)
Gif-2 VU42-A33											
Step 1	4.4466	0.2287	10	23.6	21.5	2.9	294 ± 23	302 ± 25	8.4977	0.0178	14.7 ± 0.8 (0.8)
Step 2	4.4740	0.2130	10	757	90.2	10.2	39 ± 340	(4.4 ± 3.9) × 10 ³	8.4977	0.0178	14.8 ± 0.7 (0.7)
Step 1 & 2	4.4733	0.1469	20	370	52.4	3.5	272 ± 23	314 ± 19	8.4977	0.0178	14.8 ± 0.5 (0.5)
Step 1	3.6638	0.1411	2 (8)	0.07	15.6	3.0	-	-	8.4977	0.0178	12.1 ± 0.5 (0.5)
Step 2	3.5427	0.0289	2 (8)	0.03	85.9	11.1	-	-	8.4977	0.0178	11.73 ± 0.10 (0.19)
Step 1 & 2	3.5476	0.0283	4 (16)	0.27	42.7	3.3	297 ± 2	297 ± 2	8.4977	0.0178	11.75 ± 0.10 (0.19)
Gif-1 VU42-A37											
Step 1	3.5957	0.0067	9 (1)	0.50	91.4	6.8	271 ± 15	277 ± 16	8.5534	0.0180	11.83 ± 0.03 (0.16)
Step 2	3.6250	0.0042	9 (1)	0.37	94.9	8.8	301 ± 14	292 ± 14	8.5534	0.0180	11.93 ± 0.03 (0.17)
Step 1 & 2	3.6166	0.0039	18 (2)	1.22	93.3	7.3	283 ± 9	274 ± 9	8.5534	0.0180	11.90 ± 0.03 (0.16)

1σ is multiplied by √MSWD when MSWD > 1

Table 6.1: Analytical data of biotite experiments on Respighi and Ancona ash layers, of sanidine experiments on Ancona ash layer and of experiments on Gibliscemi volcanic ash layers (continued from previous page).

MDC ANCONA BIOTITE

For the Ancona ash layer 5 incremental heating experiments on biotite (400-500 μm) have been performed on samples splits obtained during two different field campaigns. Apart from experiment 02m0400b, the experiments all show one straightforward plateau (figure 6.3d-h). 02m0400b can be divided in two significantly different plateaus. However, the plateau containing the higher proportion of the total ^{39}Ar released in the consecutive steps (plateau I) is equivalent in age to the other plateaus. Combination of all plateau steps (excluding plateau II steps of 02m0400b, because it compromises a small amount of total ^{39}Ar released) results in an age of 11.82 ± 0.01 Ma (1σ analytical error) for the biotite of the Ancona ash layer. Isochrons are relatively well defined (normal/inverse isochron age 11.83 ± 0.08 Ma) and intercepts do not deviate from the atmospheric $^{40}\text{Ar}/^{36}\text{Ar}$ ratio. Figure 6.4c shows the cumulative age probability distributions of the Ancona biotite steps, one curve represents all steps, the other only steps included in plateau I and II. In figure 6.4d the data are divided according to steps belonging to respectively plateau I and II. The steps contributing to the accepted plateau age, i.e. the older peak age display a normal behavior.

MDC ANCONA "SANIDINE"

Fusion experiments on two "sanidine" fractions of the Ancona level (VU42-A29: 125-400 μm ; VU42-A32: 200-400 μm) obtained during different field campaigns were performed. Pre-heating steps were done with a defocused laserbeam with an output of 2W to remove undesirable atmospheric argon adsorbed to the crystal surface. In contrast to the experiments on sanidine of the Melilla, Cretan, Ptolemais ash layers and the standards, where no significant amount of gas were released in the pre-heating step, the samples start to glow and gas was released probably due to their more milky appearance. Therefore the released gas was analyzed (step 1). This step was followed by a total fusion step (step 2) and it appeared that both steps produced about the same amount of ^{39}Ar . Also no substantial difference in the radiogenic ^{40}Ar yield between both steps could be detected. The analytical data of the two mineral fractions and the consecutive steps are given in table 6.1. The normal isochron intercept deviates from 295.5 at the 2σ level in a few cases. It appears the normal isochron is dominated by three individual steps; removal of these 3 steps solves the deviation from 295.5 in all cases. From the K/Ca ratios (~ 10) it appeared that we did not analyze a pure sanidine mineral separate. Apparently, the density separation at 2.58 g/cm^3 and picking could not prevent plagioclase to occur in the mineral separate and/or in spite of HF-leaching plagioclase rims around the crystal might still occur. However, the radiogenic ^{40}Ar yields are high ($>95\%$). The combined weighted mean age of all steps (step 1 & 2) results in an age of 11.71 ± 0.01 Ma (MSWD 0.59), the inverse isochron age is 11.68 ± 0.03 (MSWD 0.53). Further, the fraction VU42-A29 shows some heterogeneity (figure 6.4e). Removal of the clearly outlying data results in a normal age probability distribution. Splitting this distribution into the step 1 and step 2 data shows the slightly younger age of 11.68 Ma for step 2 as compared to 11.73 Ma for step 1 potentially implying minor effects of excess argon in the first step.

GIBLISCEMI GID-4 AND GIF-2

The same two step procedure as for the Ancona feldspar was applied to feldspar fractions of the volcanic layers in Gibilscemi, i.e. 10 multigrain feldspar fractions were analyzed in two steps. However, the $^{40}\text{Ar}/^{39}\text{Ar}$

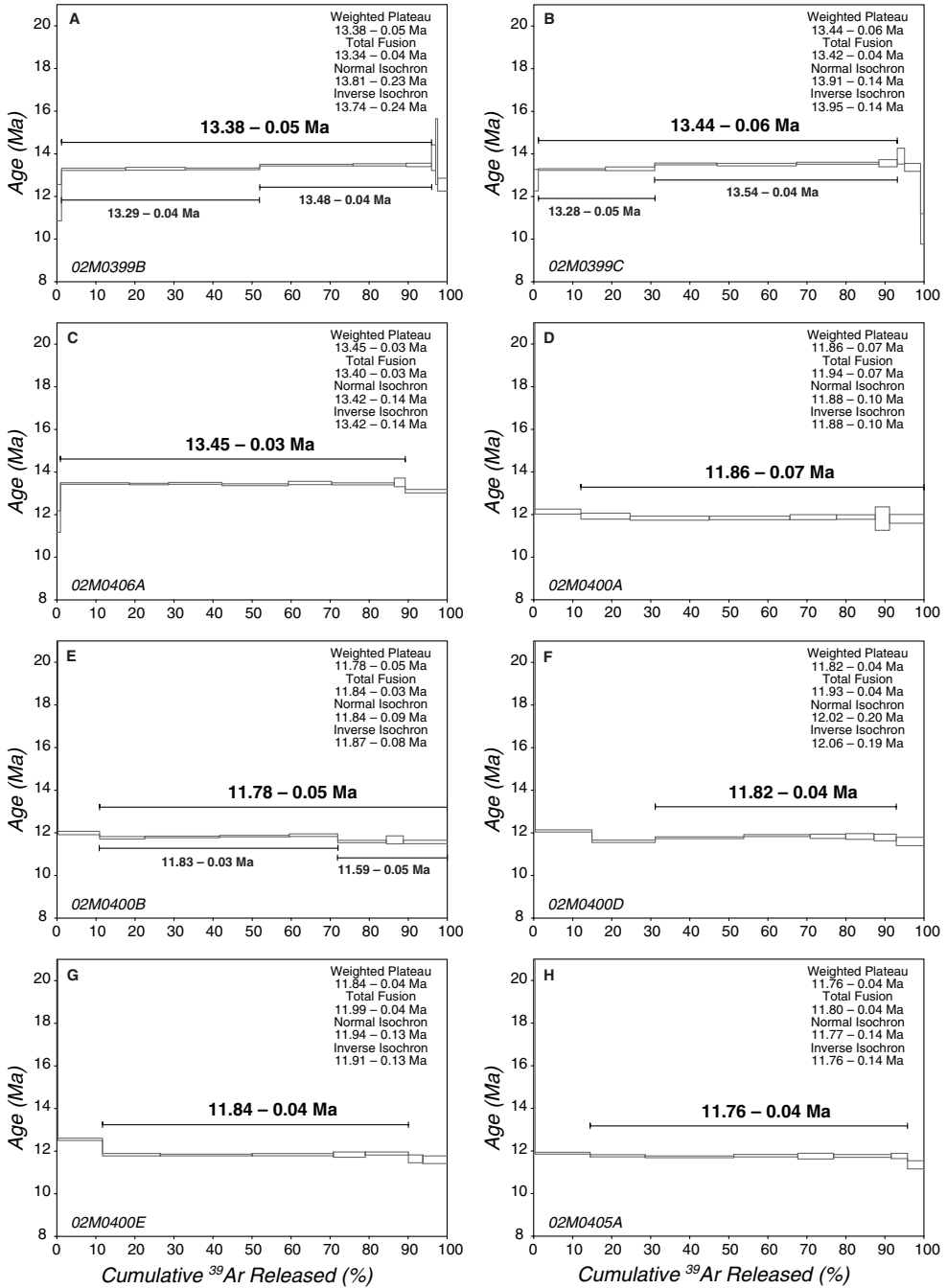


Figure 6.3: Incremental heating spectra of experiments on biotite of the Respighi and Ancona ash layers. Incremental heating spectra for biotite experiments are shown. Plateau steps are shown with their 1σ analytical errors.

data for the volcanic layers GiD-4 and GiF-2 appeared to be extremely heterogeneous (table 6.1 and figure 6.4g, i). The step 1 data of GiF-2 contain low amounts of radiogenic ^{40}Ar (14-25%), the step 2 data contain 85-94% $^{40}\text{Ar}^*$. Associated analytical errors of individual experiments are therefore higher (~5 times) in step 1. Removal of 8 out of 10 of the analyzed fractions (age range 12.8-19.7 Ma, see distribution in figure 6.4i) leaves the two youngest fractions (table 6.1, figure 6.4j is a detail of the youngest peak in 6.4i). The combined age of both steps is 11.75 ± 0.10 Ma (MSWD, 0.27, $n = 4$) with an isochron $^{40}\text{Ar}/^{36}\text{Ar}$ intercept of 297 ± 2 , or omitting the low radiogenic steps 11.73 ± 0.10 Ma (MSWD 0.03, $n = 2$), which is the "accepted" age. However, due to the observed heterogeneity it is not possible to regard this age as reliable.

GiD-4 shows no difference in radiogenic ^{40}Ar yields between the two steps, also the K/Ca ratio is fairly constant. The fraction VU42-A36 shows more consistent results than VU42-A52, which can be explained by the better quality and the somewhat larger grain size of the handpicked material in VU42-A36. Removal of the more heterogeneous VU42-A52 data and 1 analyses of VU42-A36 leaves an age of 11.43 ± 0.07 Ma (step 1 and 2 data combined, MSWD 6.0) and 11.46 ± 0.04 Ma for step 2 data only (MSWD 0.54) (see also figure 6.4h). Isochron ages are $11.43 / 11.44 \pm 0.06$ Ma for respectively the normal and inverse isochron, but the intercept does not deviate from 295.5 at 2σ level. This is the best $^{40}\text{Ar}/^{39}\text{Ar}$ age estimate for this ash layer, but considering the observed heterogeneity, also this age must be regarded with caution.

GIBLISCEMI GIF-1

Ash layer GiF-1 is stratigraphically the oldest ash in the Gibilscemi section. The already described two step analytical procedure has been applied on 10 multi-grain fractions. This sample is more homogeneous than the previous Gibilscemi samples and only one fraction (2 steps) has been omitted from interpretation. K/Ca ratios and radiogenic ^{40}Ar yields are slightly smaller in step 1 than in step 2. The combined age for this sample is 11.90 ± 0.03 Ma (1σ analytical error), normal and inverse isochron ages are respectively 11.92 ± 0.04 Ma and 11.93 ± 0.03 Ma. The age probability distribution of the combined data deviates slightly from normality due to the small difference in age in both steps (figure 6.4l), although the separate steps show more or less normal distributions. Nevertheless, the step 2 distribution is less broad and does not show an asymmetrical distribution and is therefore the preferred age (11.93 ± 0.03 Ma).

GIBLISCEMI GiD-3

For this ash layer none of the 20 steps is excluded to produce MSWD values <1 and more or less normal age probability distributions (table 6.1, figure 6.4m). However, the step 1 data are slightly younger than the step 2 data (statistically not different at the 2σ level). The combined age of both steps is 11.48 ± 0.03 Ma and the inverse isochron age is 11.46 ± 0.03 Ma. The normal isochron intercept deviates from the atmospheric $^{40}\text{Ar}/^{36}\text{Ar}$ ratio at the 2σ level, but appeared to be dominated by two data points. Removal of those two data indeed results in an intercept not statistically different from 295.5.

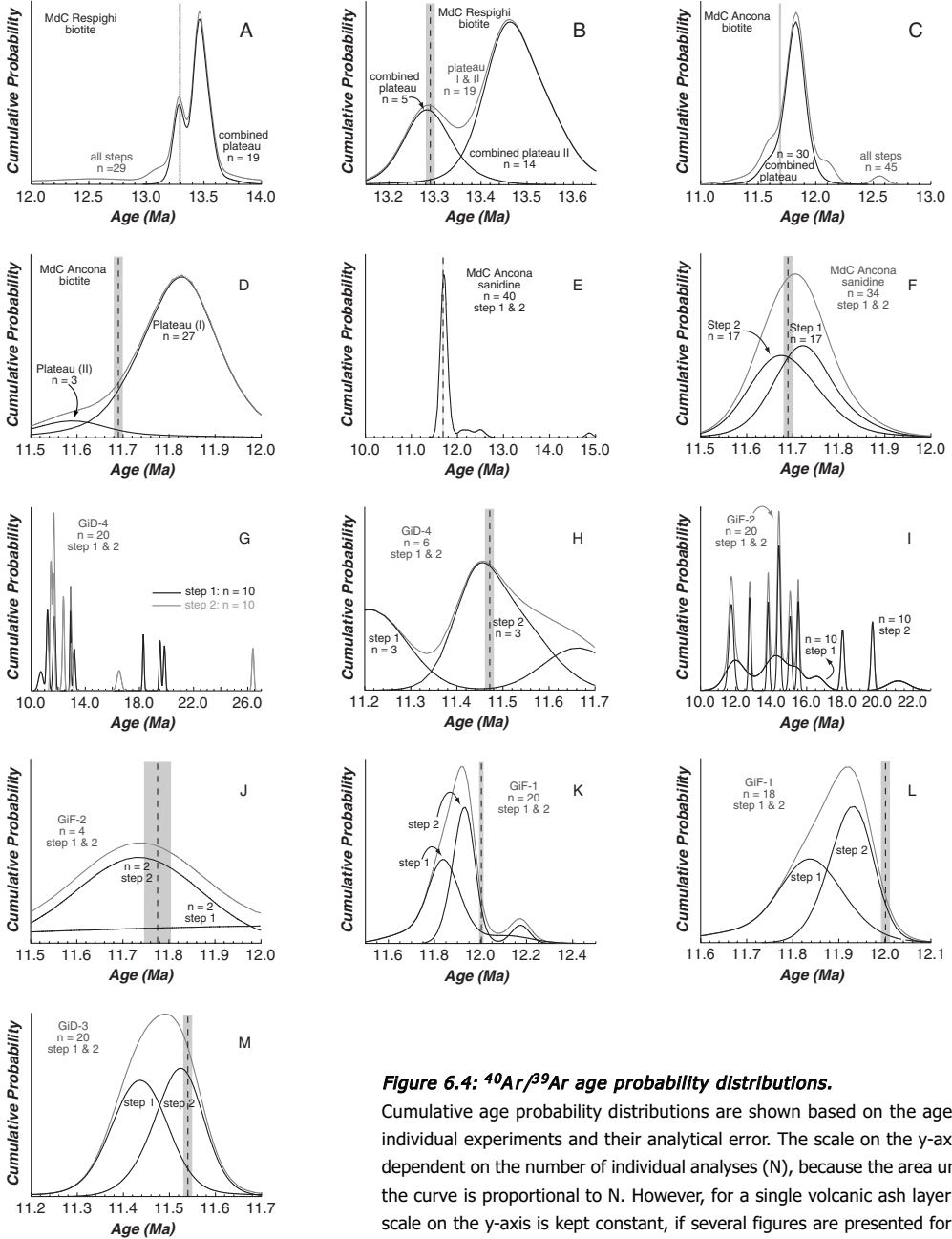


Figure 6.4: $^{40}\text{Ar}/^{39}\text{Ar}$ age probability distributions.

Cumulative age probability distributions are shown based on the ages of individual experiments and their analytical error. The scale on the y-axis is dependent on the number of individual analyses (N), because the area under the curve is proportional to N. However, for a single volcanic ash layer the scale on the y-axis is kept constant, if several figures are presented for the different figures. The vertical dashed line is the astronomical age, the surrounding shade represents the error in the astronomical age.

DISCUSSION

COMPARISON WITH PREVIOUS ISOTOPIC STUDIES

Montanari et al. (1997) performed 4 incremental heating experiments on biotite from the Respighi ash layer and 1 incremental heating experiment on biotite from the Ancona ash layer. Ages as reported in the original publication are listed in table 6.2. The ages have been recalculated relative to FC-2 sanidine of 28.02 Ma to be able to compare the data of Montanari et al. (1997) directly with our new data. Montanari et al. (1997) preferred the inverse isochron above the mean plateau age of the combined steps included in three plateaus for Respighi. The fourth plateau is significantly older and is omitted from the integrated isochron age. The isochron age is preferred because “the isochron analysis technique is a better approach to performing the “trapped” ⁴⁰Ar/³⁶Ar correction”, although they stated that the trapped ⁴⁰Ar/³⁶Ar compositions were indistinguishable from atmospheric argon. The integrated plateau age for Respighi (table 6.2) is calculated with the analytical data reported in Montanari et al. (1997). This results in an integrated plateau age of 12.91 ± 0.07 Ma for their data. Only analytical errors are reported, because ages are calculated with the same values for the decay constants and standard age. Therefore, potential systematic errors in these parameters will introduce the same systematic error in both ages. Comparing this integrated plateau age with our age of 13.47 ± 0.03 Ma results in a large discrepancy (~ 0.5 Ma) between both studies. Integrated isochron ages are 12.94 ± 0.16 Ma (Montanari et al., 1997) versus 13.56 ± 0.09 Ma or 13.54 ± 0.09 Ma for respectively the normal and reversed isochrons (this study). It must however be remarked that the discrepant age of 13.36 ± 0.11 Ma (Montanari et al., 1997) is statistically equivalent to the age we obtained.

Montanari et al. (1997) performed one incremental heating experiment on biotite of the Ancona ash layer, resulting in an isochron age of 10.95 ± 0.38 Ma or an plateau age of 11.50 ± 0.10 Ma (analytical errors only). Their plateau shows the same two step behavior as our sample O2m0400b, but in Montanari et al. (1997) the two plateaus overlap. Again our biotite age obtained for this ash layer (11.82 ± 0.01 Ma) is significantly older. The initial lower temperature steps show more atmospheric contamination than the later steps. Montanari et al. (1997) indicate that after only 14% of the cumulative ³⁹Ar release the higher radiogenic yields are reached. In our study this occurs exactly at the same point. Lower radiogenic yields in the first step(s) in combination with a slightly older age might be indicative for some alteration of the biotite. However, the argon isotope signature in the mineral is apparently not significantly disturbed, since the incremental heating spectra are flat (apart from O2m0400b).

The age difference of ~ 0.5 Ma for the Respighi level and of ~ 0.3 Ma for the Ancona level between Montanari et al. (1997) dataset and ours cannot be explained easily, because both studies show reliable plateaus, isochrons and isochron intercepts equivalent to the atmospheric ⁴⁰Ar/³⁶Ar ratio of 295.5. As stated before the observed age difference in both studies cannot be due to systematic errors in decay constants and standard ages, because ages have been calculated with the same values for the decay constant and both studies used the same standard and standard age. Therefore, the Ancona and Respighi volcanic levels are either heterogeneous or some other sort of systematic errors between the two laboratories (BGC and VUA) must occur. Montanari et al. (1997) irradiated their samples in the central thimble of the Omega West reactor without Cd shielding (in contrast to our irradiation in the Cd-shielded CLICIT facility). No Cd-

	Published age (Ma)	Isochron intercept	Recalculated age (Ma)
MdC Respighi			
Plateau 5804/2 01 (n = 8)	12.83 ± 0.08	297.8 ± 3.8	12.91 ± 0.08 (± 0.19)
Plateau 5804/2 02 (n = 6)	12.85 ± 0.08	278.0 ± 4.0	12.93 ± 0.08 (± 0.19)
Plateau 5804/2 01 (n = 6) ^a	13.27 ± 0.11	301.5 ± 6.4	13.36 ± 0.11 (± 0.20)
Plateau 5809/2 02 (n = 5)	12.74 ± 0.09	283.0 ± 14	12.82 ± 0.09 (± 0.19)
Integrated isochron age (n = 19)	12.86 ± 0.16		12.94 ± 0.16 (± 0.24)
Integrated plateau age (n = 19)	-		12.91 ± 0.07 (± 0.18)
MdC Ancona			
Isochron age (n = 7)	10.88 ± 0.38	417 ± 93	10.95 ± 0.38 (± 0.41)
Plateau age (n = 7)	11.43 ± 0.10		11.51 ± 0.10 (± 0.17)

^a) Excluded from integrated isochron/plateau age.

Table 6.2: Previously published data on the Monte dei Corvi ash layers (Montanari et al., 1997).

Previously published data compared to our new data. Ages as reported in original publication are calculated relative to FCT of 27.84 Ma. Recalculated ages are calculated relative to FCT 28.02 Ma of Renne et al. (1998) with decay constants of Steiger and Jäger (1977). 1σ analytical errors are reported. Ages calculated according to equation 1.14 with parameters for activities and physical parameters as reported in table 1.4, column VII, do not differ from standard age calculations and are not reported separately. Full error estimates (based on equation 1.14) are given between brackets.

shielding increases the requirement of an accurate ($^{40}\text{Ar}/^{39}\text{Ar}$)_κ correction factor. If this correction factor was not accurately determined, a major systematic error in the measured age could be the result, especially when young samples are measured (McDougall and Harrison, 1999). However, inspection of the applied correction factors and its influence on the final ages indicated that potential uncertainties could not explain the observed discrepancy. Therefore, an obvious reason for the age difference in both studies can not be given.

DISCREPANCY BETWEEN $^{40}\text{Ar}/^{39}\text{Ar}$ AND ASTRONOMICAL AGES

In the previous chapters (3 and 5) a systematic discrepancy between $^{40}\text{Ar}/^{39}\text{Ar}$ and astronomical ages was found. This discrepancy disappeared mostly when full and realistic errors of the absolute age of the standards and the decay constant were taken into account. However, to reduce the influence of decay constant errors and absolute standard ages an astronomically dated standard was proposed, resulting in an age of 28.24 ± 0.01 Ma (standard error of the mean) for FCT based on ash layers of the Melilla Basin and 28.21 ± 0.03 Ma based on ash layer A1 on Crete.

The data in table 6.1, table 6.2 and figure 6.4 were all calculated relative to FC-2 sanidine of 28.02 Ma, which age is based on intercalibration the primary standard GA1550 (Renne et al., 1998). As can be seen visually in figure 6.4 (where only is accounted for analytical errors) the Respighi and Ancona biotite ages are older than the astronomical age. The 1σ uncertainty (standard deviation) is the 68% area under a normal distribution curve, so it is clear that the step 1, step 2 and combined feldspar ages do not statistically deviate from the astronomical age for the Ancona ash layer. The more reliable Gibilscemi ages of volcanic ash layers GiF-1 and GiD-3 are slightly younger than the astronomical age and the less reliable Gibilscemi samples GiF-2 and GiD-4 can also be interpreted as slightly younger or equivalent to the astronomical ages. For all samples the probability

distributions overlap with the astronomical within 1σ and the distributions are relatively broad compared to the distributions of the Melilla, Cretan or Ptolemais samples (chapter 3 and 5), indicating less precise analyses. In table 6.1 the ages are also calculated with uncertainties including improved estimates of uncertainties in decay constants and absolute ages of primary and secondary standards (modified from Min et al., 2000, chapter 1). Comparing the astronomical ages with the $^{40}\text{Ar}/^{39}\text{Ar}$ full error ages (because we compare two independent dating methods, the full error must be taken into account) there is no discrepancy observed at the 1σ level for any of the samples.

Two of the dated ash layers (GiF-2 and GiD-4) appeared to be extremely heterogeneous in age. Contamination with older grains might also be possible in the other samples and might have averaged out over the analyzed gas fractions due to the analysis of multigrain fractions. The occurrence of this effect can indeed cause broadening of cumulative age probability distributions, which is observed here. Broadening should occur when the age difference between the “real” ages and contaminating material is smaller than the analytical error. When this age difference is larger than the analytical uncertainty skewed (multi modal) distributions are expected, which do not observe. Therefore, we assume that if contamination with older material occurred, this material can only be slightly older (<60 kyr, the analytical error of individual analyses) still regard the single crystal experiments as performed on the Melilla samples as the most reliable.

WHY TENDS BIOTITE TO BE OLDER THAN SANIDINE?

We have seen in several cases, i.e. for the Ancona layer (this chapter), for a.1.1 and a.1.2 in Sorbas (chapter 5), for SLM3T in Ptolemais and Fan-A1 on Crete (chapter 3), that biotite ages tend to be older than sanidine ages from the same sample. Also $^{40}\text{Ar}/^{39}\text{Ar}$ age of biotite from FCT is older than the sanidine $^{40}\text{Ar}/^{39}\text{Ar}$ age (e.g., Dazé et al., 2003), where the authors stated that the biotite was inclusion rich. We do not have convincing evidence that might provide an explanation for this age difference. However, models show that K-feldspar will only exhibit excess argon in the most extreme circumstances whereas minerals with higher partitioning coefficients between mineral and fluids/melt like biotite may more commonly yield erroneous old ages (Kelley, 2002). Stepwise heating experiments prove to be a very effective technique to detect excess argon originating from fluid inclusions. Excess argon from melt inclusions is more difficult to recognize in age spectra. However, isochron ages of step heating experiments circumvent the requirement to know the exact amount excess argon at least when the isotope ratio of the contaminating component is homogeneous. “Unfortunately”, our biotite ages do not show indications for excess argon (isochron intercepts are not statistically deviating from the atmospheric $^{40}\text{Ar}/^{36}\text{Ar}$ ratios), although the isochrons are not excellently defined in this study (due to clustering of data points). Isochron ages hardly differ from weighted mean plateau ages. To obtain the best quality of biotite all sample have undergone density separation at 3.05 g/cm^3 . This indeed might remove the slightly weathered fraction, but probably increased the more inclusion rich fraction. However, we do not find compelling evidence to point to excess argon as the main cause for the observed discrepancy.

Recoil of $^{39}\text{Ar}_K$ can also affect age spectra of samples. This is likely to occur when potassium is mainly located in fine-grained phases adjacent to potassium poor areas. This can cause more than one apparent

Ash layer	Astronomical age (Ma)	Apparent FCT age (Ma)
Respighi biotite	~13.296	27.65 ± 0.07
Respighi biotite (Montanari et al., 1997)	~13.296	28.86 ± 0.15
Ancona biotite	~11.688	27.71 ± 0.02
Ancona biotite (Montanari et al., 1997)	~11.688	28.44 ± 0.16
Ancona feldspar (step 2)	~11.688	28.04 ± 0.02
Ancona feldspar (step 1 & 2)	~11.688	27.97 ± 0.02
GiD-4 (step 2, n=3)	~11.443	28.26 ± 0.12
GiD-3 (step 1 & 2, n=20)	~11.54	28.16 ± 0.07
GiF-2 (step 2, n=2)	~11.778	28.12 ± 0.25
GiF-1 (step 2, n=9)	~12.006	28.20 ± 0.07

Table 6.3: Intercalibration between FCT and the astronomically dated ash layers of the middle Miocene.

An astronomically calibrated age for FCT is derived according to equation 1.15 using the $^{40}\text{Ar}^*/^{39}\text{Ar}_K$ ratios of FCT and the ash layers and the astronomical age of the ash layers. Errors are reported at the 1σ level.

age spectra in some cases (McDougall and Harrison, 1999). However, ^{39}Ar recoil artifacts in age spectra of coarse-grained (diameter >100 μm) appear to be unimportant (Huneke and Smith, 1974).

INTERCALIBRATION BETWEEN ASTRONOMICAL AND $^{40}\text{Ar}/^{39}\text{Ar}$ SYSTEM?

In spite of the lesser quality of the data presented here, we decided to apply the same procedure for intercalibration of these middle Miocene ash layer and the FCT standard as in chapter 3 and 5, i.e. we used the $^{40}\text{Ar}/^{39}\text{Ar}$ ratios of the ashes (= in this case the standard) and of FCT (= in this case the unknown) and the astronomical age of the ash to calculate the age for FCT (including a proper error propagation). Table 6.3 shows the results. The error propagation methods were described in detail in chapter 1. We can conclude from this table that the Gibliscemi ashes at least do not contradict the proposed intercalibration of chapter 5. From the biotite ages of Respighi and Ancona in our study in combination with the astronomical age, we calculate ages for FCT that are significantly younger, i.e. closer to the age of ~27.5 Ma proposed by Lanphere and Baadsgaard (2001) and disputed by Schmitz et al. (2003). FCT intercalibrated with the feldspar of the Ancona ash layer results in an age of 27.97 ± 0.02 Ma contradicting the age proposed in the previous chapter. We are inclined to explain this due to the poorer quality of the $^{40}\text{Ar}/^{39}\text{Ar}$ age of the Ancona ash layer, which might be slightly heterogeneous.

CONCLUSIONS

The data for the middle Miocene do not straightforward support the ideas as established on basis of the $^{40}\text{Ar}/^{39}\text{Ar}$ and astronomical ages of the late Miocene in Crete and Melilla. However, the Gibliscemi data do not contradict (i.e., is in agreement with) the observed discrepancy in chapters 3 and 5. Further, biotite ages show the similar tendency to be older than the sanidine ages from the same ash layer. We conclude on basis of the quality of the middle Miocene data, that the intercalibration between both methods as proposed in chapter 3 and 5 is not opposed by the data presented here. Future work should be focussed on $^{40}\text{Ar}/^{39}\text{Ar}$ experiments on minerals of higher quality intercalated in middle Miocene astronomically tuned sections. So

far, no land-based sections have been found fulfilling both criteria (high quality volcanic ash layers and a good astrochronological time control). ODP cores might provide a solution to this problem, but comparison of both methods is only useful if there is no doubt about astronomical time control in these cores. Another solution might be the comparison of middle Miocene astronomical ages with ages based on supplementary isotopic (U/Pb) system. The Ancona ash layer does contain zircon, allowing U/Pb experiments. However, the next chapter focuses first on the potential of intercalibration of the U/Pb system with the K/Ar system and the astronomical method for the Pliocene time interval.

CHAPTER 7

**DIRECT INTERCALIBRATION OF THE $^{40}\text{Ar}/^{39}\text{Ar}$ AND U/Pb
ISOTOPE SYSTEMS WITH ASTRONOMICAL TIME: A FIRST
EXAMPLE FROM THE PLIOCENE PTOLEMAIS FORMATION,
N-GREECE.**

INTRODUCTION

In chapters 3 and 5 we showed a systematic difference between $^{40}\text{Ar}/^{39}\text{Ar}$ and astronomical ages, where the $^{40}\text{Ar}/^{39}\text{Ar}$ ages tended to be younger by $\sim 1\%$. We argued that this discrepancy probably is caused by a bias in the age for the standard used in $^{40}\text{Ar}/^{39}\text{Ar}$ dating. In chapter 5 following a systematic evaluation of all parameters involved we proposed a new age (28.24 ± 0.01 Ma) for the commonly used standard FCT sanidine based on intercalibration of single crystal $^{40}\text{Ar}/^{39}\text{Ar}$ and astronomical ages for several astronomically dated ash layers in the Melilla Basin. However, intercalibration of the astronomical and $^{40}\text{Ar}/^{39}\text{Ar}$ methods for the upper five ash layers in Ptolemais (chapter 3, 28.60 Ma) deviated from the proposed intercalibration for Melilla (chapter 5). We decided to extend our research to the U/Pb system, although we realized that the young ages of our samples explore the limits of the U/Pb dating technique. The zircon of the upper Ptolemais ash layer SR3M seemed the most suitable for U/Pb experiments (pristine, pink magmatic crystals) after microscopic inspection of heavy mineral fractions of ash layers from Melilla, Crete and Ptolemais in spite of the somewhat larger uncertainty in the astronomical tuning of Ptolemais. Zircon of the A1 ash layer from Crete has also been assessed. In this chapter we describe the results of the

U/Pb experiments on the upper Ptolemais ash layer SR3M and compare these results with the available $^{40}\text{Ar}/^{39}\text{Ar}$ data and astronomical ages.

GEOLOGICAL SETTING

The geological setting of the Ptolemais Basin was already described in Steenbrink et al. (1999) and in chapter 3 and is briefly repeated here (figure 7.1). The Basin is part of a 250 km long NNW-SSE trending graben system filled with Neogene to Quaternary sediments. The basin formed in response to a late Miocene NE-SW extension. NW-SW extension during the Pleistocene resulted in the development of a series of sub-basins. The pre-Neogene rocks of the basin and surrounding area consist of Paleozoic metamorphic rocks, Mesozoic carbonate cover and ophiolites (Pavlidis and Mountrakis, 1987). The basin fill is divided into three lithostratigraphic units: the Lower Formation, Ptolemais Formation and Upper Formation. All units are of continental origin and mainly deposited under lacustrine conditions. The Ptolemais Formation with a thickness of ~ 110 m consists of cyclic

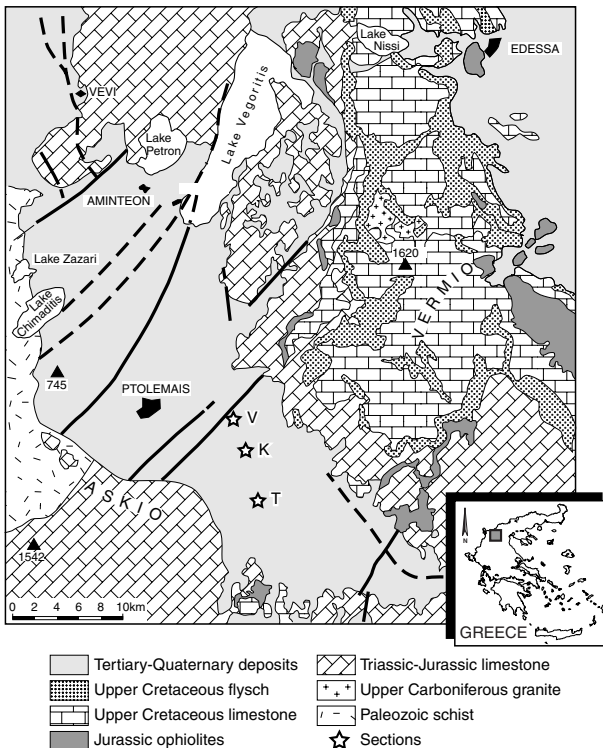


Figure 7.1: Location and geological setting of Ptolemais Basin. Locations of the studied sections containing ash layer SR3M are shown (modified from Steenbrink et al., 1999). V = Vorio, K = Komanos, T = Tomea Eksi. The volcanic center of Edessa is located north of the Ptolemais Basin, the Voras mountains north of Edessa (not shown).

alternations of lignite and lacustrine marl which are controlled by precession (Van Vugt et al, 1998; Steenbrink et al., 1999). The volcanic ash layer SR3M studied here is intercalated in the Ptolemais Formation.

The volcanic ash layers in the Ptolemais most probably originate from the volcanism in the Voras Mountains or the volcanic areas near Aridea and Edessa. Volcanic rocks directly NE of Edessa predominantly consist of volcanic tuffs of latite-andesite, latite or trachyte composition, but their age is not determined directly (Marakis and Sideris, 1973). The Voras volcanic rocks consist predominantly of a "shoshonitic" group (mainly trachyte) and a "calc-alkaline" group (mainly low-K trachyte) (Kolios et al., 1980). K/Ar experiments on samples of the Voras volcanic rocks showed that the "shoshonitic" volcanism took place from 2.5 to 1.8 Ma and the "calc-alkaline" volcanism from 5.0 to 4.0 Ma (Kolios et al., 1980). Bellon et al. (1979) obtained four K/Ar ages between 4.0 to 2.65 Ma for samples from the area south of Aridea (north of Edessa). These samples showed the same geochemical and petrological characteristics as the "shoshonitic" series of the Voras Mountains, suggesting that the volcanism spanned the Pliocene completely.

ASTRONOMICAL TIME CONTROL IN THE PTOLEMAIS BASIN

The astronomical time frame for the lacustrine sediments of the Ptolemais formation was described in detail by Van Vugt et al. (1998) and Steenbrink et al. (1999) and was summarized in chapter 3. The ash layer SR3M studied in this chapter was one of the upper five $^{40}\text{Ar}/^{39}\text{Ar}$ dated ash layers showing a systematic divergence from astronomical ages for the same layers where the astronomical ages tend to be older. But this inconsistency is significantly larger (~2% versus ~1%) than the inconsistency found for the lower Ptolemais ash layers and ash layers from the Melilla Basin and Crete. This suggests that the astronomical tuning in Ptolemais previously described by Van Vugt et al. (1997), Steenbrink et al. (1997) and in chapter 3

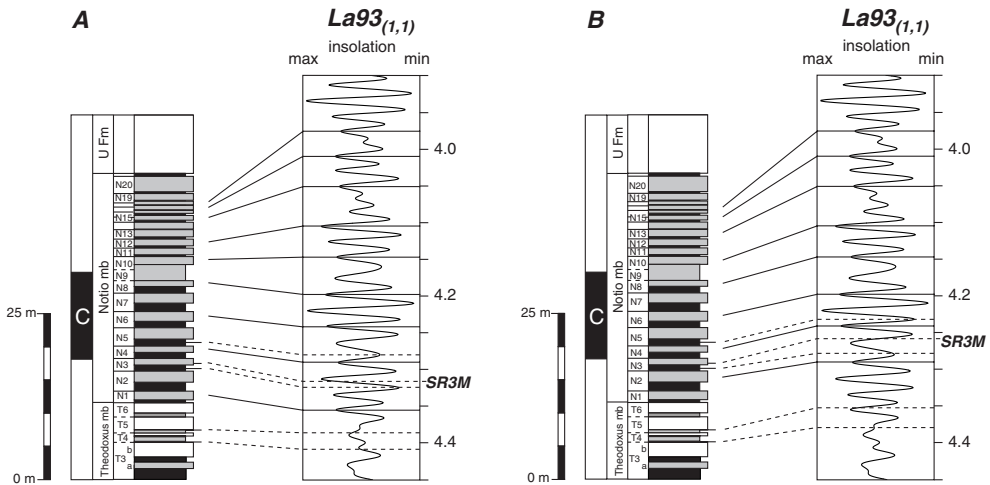


Figure 7.2 a and b: Astronomical tuning of ash layer SR3M. Astronomical tuning of the upper part of the Ptolemais Formation is shown based on (a) Van Vugt et al. (1998) and Steenbrink et al. (1999) and (b) shifted two cycles upward based on the intercalibration between $^{40}\text{Ar}/^{39}\text{Ar}$ and astronomical ages in the Melilla Basin.

might not be correct. Although the sedimentary cycle pattern in the Ptolemais composite fits well with the insolation pattern, especially for the interval in which ash layer SR3M is intercalated, it appeared that the sedimentary cycle pattern was not identical in parallel sections due to local effects. This might indicate that although the sedimentary cycles are orbitally controlled local (tectonic) processes obscure the characteristic cycle patterns. Figure 7.2a shows the tuning as was described in chapter 3.

MATERIALS AND METHODS

About 30 kg of ash layer SR3M intercalated in the lacustrine sediments of the Ptolemais Basin has been sampled. The sample was washed (no crushing was required) and sieved in size fractions <125 μm , 125-250 μm and 250-500 μm . The size fraction 250-500 μm was used for heavy liquid density (lithium heteropolytungstate) separations at 2.55 g/cm^3 and 2.58 g/cm^3 using an overflow centrifuge to obtain sanidine for $^{40}\text{Ar}/^{39}\text{Ar}$ dating. The size fraction <125 μm underwent heavy liquid density separations at ~ 2.8 g/cm^3 (lithium heteropolytungstate) and 3.30 g/cm^3 (diiodomethane) to obtain zircon for U/Pb dating.

$^{40}\text{Ar}/^{39}\text{Ar}$ METHOD

The detailed analytical procedures for $^{40}\text{Ar}/^{39}\text{Ar}$ experiments on ash layer SR3M were already described in chapters 1 and 3. Several sample splits have been analyzed, i.e. one split in irradiation VU16, one in VU32 (also analyzed in irradiation VU37) and the sample split from which the zircon was separated in irradiation VU37. In all cases samples were irradiated in the Oregon State Reactor in the CLICIT facility for 7 hours. TCR sanidine (85G003) was loaded as "main" standard; additionally FCT sanidine was loaded in VU32 and VU37 for intercalibration purposes with TCR sanidine.

Multiple grain fractions of samples and standards were preheated using a defocused laser beam with an output of 2W to remove undesirable atmospheric argon, followed by total fusion. The gas was analyzed on a MAP215-50 mass spectrometer operated with a modified version of standard MAP software (i.e., adjustable integration cycles and valve control). Beam intensities were measured in a peak-jumping mode over the 40-36 mass range on a secondary electron multiplier (Johnston MM1) operated at a gain of 500 with respect to the faraday collector system. System blanks were measured every 3 steps. The total system blanks were in the range of 5.0×10^{-14} moles for mass 40, 4.0×10^{-15} moles for mass 39, 2.6×10^{-15} moles for mass 38, 2.6×10^{-14} moles for mass 37 and 2.0×10^{-15} moles for mass 36. Mass discrimination (1.002-1.0100 per atomic mass unit) was monitored by frequent analysis of $^{40}\text{Ar}/^{38}\text{Ar}$ reference gas or $^{40}\text{Ar}/^{36}\text{Ar}$ air pipette aliquots (see chapter 1).

Regressions of the individual isotopes, blank corrections, corrections for nuclear interference reactions and mass discrimination corrections have been performed with the in-house developed ArArCalc (v2.20c) software (Koppers, 2002). Ages and uncertainties have been calculated according to standard age equations (equation 1.11; chapter 1) using the consensus decay constants of Steiger and Jäger (1977) and an absolute age of 28.34 ± 0.16 Ma (or ± 0.28 Ma when decay constant errors are included) for TCR sanidine (Renne et al., 1998). Further, age and error estimates are calculated following the slightly modified procedure of Min et al. (2000) with activities and physical parameters as in table 1.4, column VII (see chapter 1; equation 1.14). Intercalibration factors between FCT, TCR and GA1550 as well as K content of

the primary standard GA1550 were used from Renne et al. (1998), while the radiogenic ^{40}Ar content of primary standard GA1550 is taken from McDougall and Roksandic (1974). Recently, Spell and McDougall (2003) compiled potassium data for GA1150 over a period from 1968 to 2001 resulting in a potassium content of 7.646 ± 0.006 wt%. Additionally, they established a FC / GA1550 intercalibration factor of 0.2797 ± 0.0004 resulting in FCT age of 28.10 ± 0.04 Ma. For the moment we decided to use the commonly applied Renne et al. (1998) data to avoid further confusion about absolute ages of standards. The background dataset (intensities of all isotopes for individual experiments) is given in the online appendix (<http://www.geo.vu.nl/users/kuik>). All errors are quoted at the 1σ significance level.

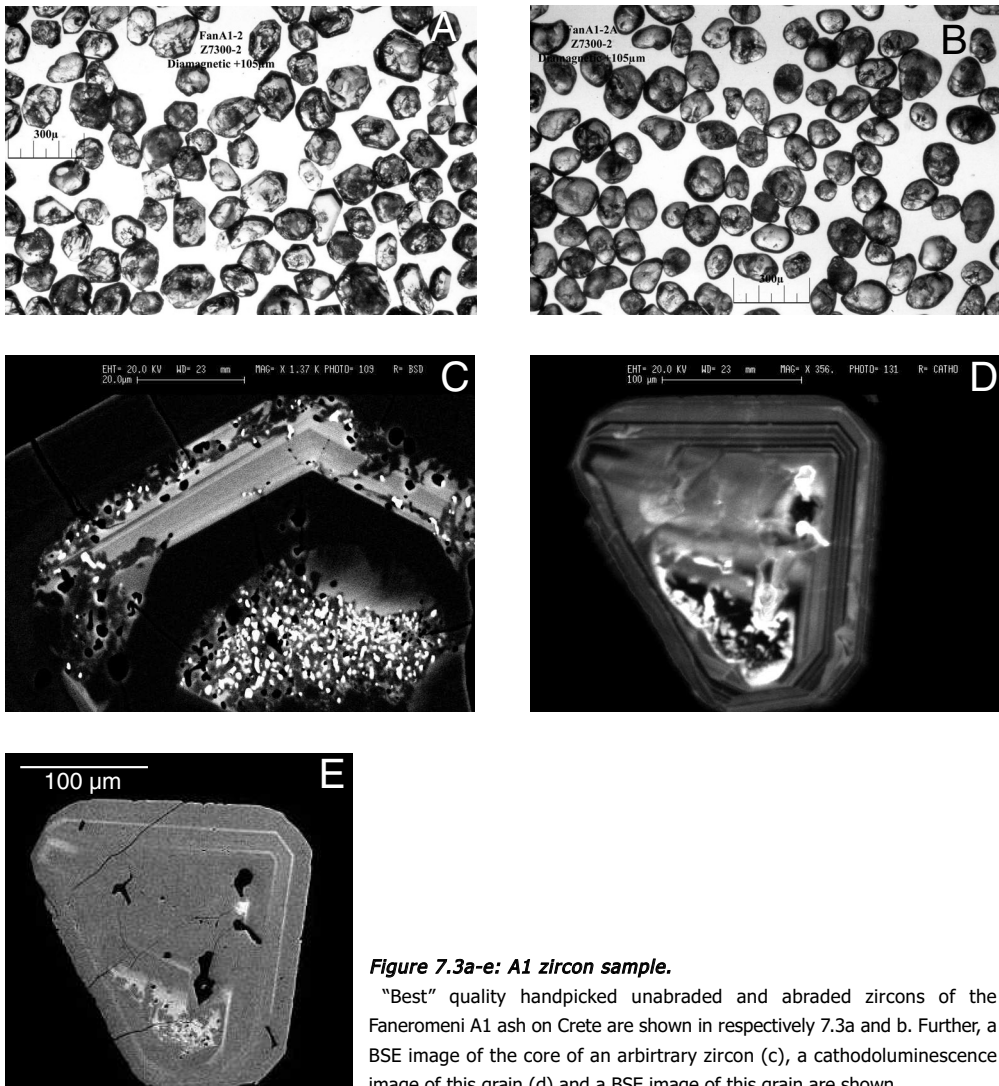


Figure 7.3a-e: A1 zircon sample.

“Best” quality handpicked unabraded and abraded zircons of the Faneromeni A1 ash on Crete are shown in respectively 7.3a and b. Further, a BSE image of the core of an arbitrary zircon (c), a cathodoluminescence image of this grain (d) and a BSE image of this grain are shown.

U/Pb TIMS METHOD

Thermal Ionization Mass Spectrometry (TIMS) analyses were performed at the Geological Survey of Canada. Detailed laboratory procedures are described in e.g. Roddick et al. (1987) and Parrish et al. (1987) and are summarized here. After the heavy liquid separation, the heavy mineral fraction was subjected to standard magnetic techniques using a Frantz™ LB-1 separator. The least magnetic (or diamagnetic) fraction was sieved in ethyl alcohol in size fractions of <60 μm , 60-90 μm and 90-120 μm . Zircon grains of the 90-120 μm fraction were selected for analyses by handpicking in ethyl alcohol under a binocular microscope. Due to the very young age of the sample >500 grains from the 90-120 μm fraction had to be picked for one experiment in order to have sufficient yields for U/Pb dating. The zircon fractions were abraded using pyrite following the technique of Krogh (1982) (Figures 7.3a,b and 7.4). Minerals were washed in high purity 3N HNO_3 and then rinsed in water and acetone. After drying the samples were weighted on a microbalance with a reproducibility of $\pm 0.2 \mu\text{g}$ (Parrish et al., 1987). The samples were then loaded into TFE Teflon® 0.35 ml capacity microcapsules. Subsequently, mineral fractions are spiked with a small amount ($\sim 8\text{-}10 \mu\text{g}$) of mixed ^{205}Pb - ^{233}U - ^{235}U tracer. To dissolve the zircon fractions ~ 0.2 ml 48% HF and ~ 0.02 ml 16N HNO_3 are added to the microcapsules. Microcapsules are loaded in a 125 ml TFE Teflon® dissolution vessel to which 5 ml 48% HF and approximately 200 μl 16N HNO_3 are added. This Teflon® liner is placed in a metal bomb (Parr®), which is sealed and placed in an oven at 240-245 $^\circ\text{C}$ for 36 hours. After dissolution of the zircon the liquid is first evaporated to form fluoride salts and then transformed into chloride salts by addition of 1 ml 3.1N HCl followed by heating for 14 hours at 210 $^\circ\text{C}$ and subsequent evaporation (Parrish, 1987).

U and Pb are purified by anion exchange chemistry (Roddick et al., 1987) using 0.25 ml Dowex* 1 \times 8 anion resin, 200-400 mesh (75-175 μm). The column was first washed with the following sequence of reagents: 2 \times 1 ml H_2O , 1 ml 6N HCl, 1 ml H_2O , 2 \times 1 ml 6.2 N HCl, 1 ml H_2O , 1 ml 3.1 N HCl. Then the samples are added to the column and washed with 2 \times 0.5 ml 3.1N HCl. Pb was collected with the addition of 3 \times 0.5 ml 6.2 HCl and U was collected with 1 ml H_2O , 0.5 ml H_2O . Two drops of H_3PO_4 were added to the Pb-solution and the solution is evaporated to dryness at 135 $^\circ\text{C}$, for the U-solution two drops of H_3PO_4 and 1 drop of HNO_3 are added and the solution is evaporate to dryness at 135 $^\circ\text{C}$.

Isotopic compositions of Pb were measured on a Finnigan MAT 261 variable multicollector mass spectrometer by static measurement of ^{208}Pb , ^{207}Pb , ^{206}Pb and ^{205}Pb on Faraday cups and ^{204}Pb on a secondary electron multiplier (SEM). The lead fraction is loaded on degassed rhenium filaments with silica gel and phosphoric acid. Gain calibration between the Faraday and the SEM is performed by magnetically switching the ^{205}Pb beam into the SEM before and after each data block and simultaneous measurement of the ^{205}Pb (in the multiplier) and ^{206}Pb in a Faraday cup. The gain can be determined by comparing this $^{205}\text{Pb}/^{206}\text{Pb}$ ratio with the ratio obtained in the Faraday cups and this gain is then applied to the $^{205}\text{Pb}/^{204}\text{Pb}$ ratio (Roddick et al., 1987; Parrish et al., 1987). Mass fractionation factors for the Pb isotopes are based on periodic analyses of common lead standard NIST SRM 981 (and is determined at $0.09 \pm 0.03\%$ per AMU). The U concentration and isotopic compositions were measured on the newly installed Thermo Finnigan Triton mass spectrometer. Uranium is loaded as nitrate on a double rhenium filament pair and is ionized as a metal ion. Uranium is measured in a static mode with the three isotopes (^{233}U , ^{235}U and ^{238}U) measured simultaneously in Faraday cups. The isotopic U ratios are corrected for fractionation using the $^{233}\text{U}/^{235}\text{U}$. Procedural blanks were <1 pg for U and 10 pg for Pb. Residual common Pb was subtracted using the model

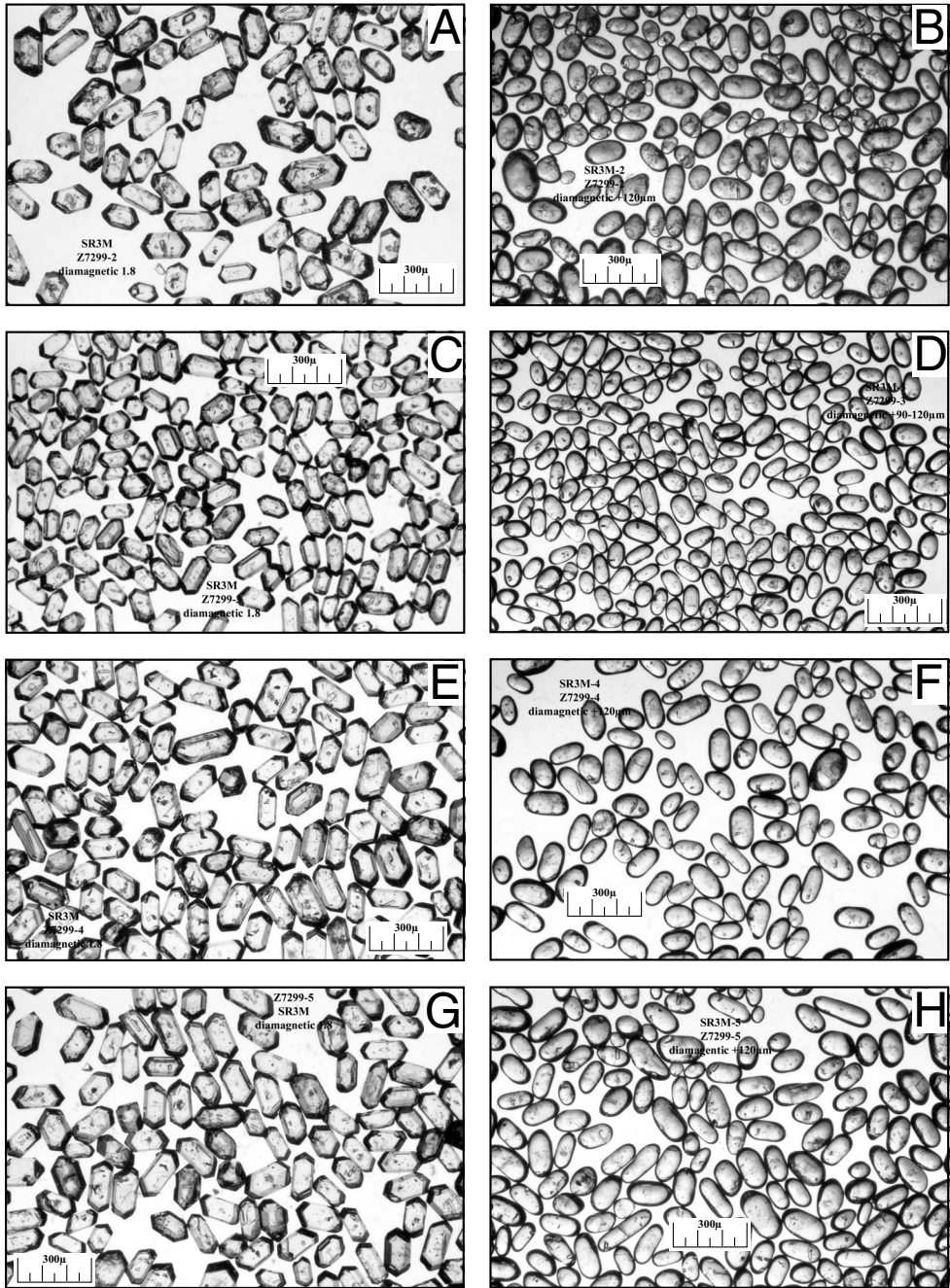


Figure 7.4: Transmitted light photos of unabrased and abrased fractions for ID-TIMS.

Analyzed ID-TIMS fractions before (a, c, e, and g) and after (b, d, f, h) abrasion. The abrased fractions are used for TIMS analyses. The scale bar is 300 μm.

Pb isotopic composition derived from the growth curve of Stacey and Kramers (1975). Decay constants were 1.55125×10^{-10} (^{238}U) and 9.8485×10^{-10} (^{235}U) (Steiger and Jäger, 1977). Data reduction for TIMS U-Pb data follow the error propagation techniques as outlined in Roddick (1987).

U/Pb SHRIMP METHOD

Sensitive High Resolution Ion Microprobe (SHRIMP) analyses were performed on the SHRIMP II ion microprobe at the Geological Survey of Canada, Ottawa. For SHRIMP analyses ~150 arbitrary grains of the 90-120 μm diamagnetic fraction were mounted in an epoxy resin 25 mm diameter mount including a few fragments of the zircon standard BR266 ($^{206}\text{Pb}/^{238}\text{U}$ age 559.0 ± 0.02 Ma; Stern, 2001). Polishing with 9 μm , 6 μm and finally 1 μm diamond polishing compounds exposed the grain centers of the zircons. The zircons were photographed in transmitted light. Then the mount was cleaned and coated with 4.0 nm of high purity Au to provide sufficient surface charge dissipation for cathodoluminescence (CL) and back scattered electron (BSE) imaging (Stern, 1997). Subsequently, the mount was coated with additional Au, loaded into the sample lock of the SHRIMP and kept under high vacuum for at least 24 hours before transfer into the sample chamber.

A mass-resolved O^- primary ion beam was focused into a roughly spherical spot of ca. 30 μm diameter of uniform beam density, with a sputtering rate of ~ 5 $\mu\text{m}/\text{h}$. Under these operating conditions, the mass resolution was >5000 when applying a 1% criterion and Pb sensitivity for zircon about 20 cps/ppm/nA O^- (following the procedures discussed in Stern and Amelin, 2003). Approximately 0.3% of all sputtered Pb atoms arrive at the detector (Stern, 1997).

Error analysis is described in detail in Stern (1997) and includes errors due to the standard calibration, counting errors, common and background Pb corrections, composition of the common Pb, mass fractionation of Pb isotopes and isobaric interferences. Samples are corrected for common lead using the ^{207}Pb method.

RESULTS

This chapter describes the results of U/Pb experiments for Ptolemais ash layers SR3M. In addition we attempted to obtain good quality zircon of the A1 ash layer on Crete. This ash layer indeed contained zircons, but we decided not to analyze this sample based on inspection of transmitted light, BSE and CL images (figure 7.3). Figure 7.3a shows the "best" handpicked diamagnetic zircon grains, which exist of broken, rounded, cloudy and/or cracked grains. Abrasion does not improve the quality of the grains (figure 7.3b). Figures 7.3c-e show respectively a BSE (back scattered electron), a BSE of the core and CL (cathodoluminescence) image of an A1 zircon grain.

$^{40}\text{Ar}/^{39}\text{Ar}$ RESULTS

Detailed description of the $^{40}\text{Ar}/^{39}\text{Ar}$ data is given in chapter 3 and is briefly summarized here (table 7.1). Steenbrink et al. (1999) already showed the excellent age spectra of sanidine from Ptolemais tephra and pure sanidine separates have been analyzed (most K/Ca >30) in a single fusion step (table 7.1). SR3M

SR3M	F _{unknown}	σ_{Funknown}	N	MSWD	K/Ca	F _{Tc}	σ_{Tc}	Age	Apparent $^{40}\text{Ar}/^{39}\text{Ar}$ age (Ma)				Published age (Ma)	
									I	II	III	IV		
VU32 C21	1.3734	0.0022	5	1.50	54.9	9.1945	0.0267	4.261	0.007	0.014	0.028	0.045	4.260	0.059
VU32 C22	1.3784	0.0018	5	1.00	33.7	9.2428	0.0268	4.255	0.006	0.014	0.028	0.045	4.253	0.059
VU37 C27	1.3325	0.0022	3	0.09	37.1	8.9654	0.0224	4.240	0.007	0.013	0.027	0.045	4.239	0.058
VU37 C30	1.3460	0.0016	3	0.14	27.7	9.0370	0.0226	4.249	0.005	0.012	0.027	0.045	4.248	0.058
VU37 C31	1.3414	0.0020	3	0.32	28.5	9.0629	0.0227	4.223	0.006	0.012	0.027	0.044	4.221	0.058
VU37 C32	1.3509	0.0015	3	0.48	40.2	9.0889	0.0227	4.241	0.005	0.012	0.027	0.044	4.239	0.058
VU37 C34	1.3593	0.0021	3	0.25	42.7	9.1414	0.0229	4.242	0.007	0.012	0.027	0.045	4.241	0.058
VU37 C44	1.3961	0.0018	3	0.31	34.7	9.3964	0.0216	4.239	0.005	0.011	0.027	0.044	4.238	0.058
VU37 C45	1.4036	0.0018	3	0.94	35.3	9.4300	0.0226	4.247	0.006	0.012	0.027	0.044	4.245	0.058
VU37 C16	1.3076	0.0034	2 (3)	0.01	55.7	8.7426	0.0227	4.267	0.011	0.016	0.029	0.046	4.266	0.059
VU37 C17	1.3064	0.0017	4 (1)	0.32	52.7	8.7620	0.0228	4.254	0.006	0.012	0.027	0.045	4.252	0.058
VU16 D4	4.4673	0.0108	5	2.35	35.5	30.462	0.0914	4.184	0.010	0.016	0.029	0.045	4.183	4.122 ± 0.026
VU16 D4 ^a	4.5107	0.0129	8 (2)	0.66	45.0	30.462	0.0914	4.225	0.012	0.018	0.030	0.046	4.223	4.162 ± 0.029
	R	σ_{R}												
VU32/VU37	6.7186	0.0041	37	0.68	37.2			4.246	0.003	0.024	0.042	0.042	4.245	0.057
VU37	6.7232	0.0046	27	0.54	33.5			4.244	0.003	0.024	0.042	0.042	4.242	0.057

^{a)} Incremental heating experiment

Table 7.1. $^{40}\text{Ar}/^{39}\text{Ar}$ data of volcanic ash layer SR3M.

Summary of the $^{40}\text{Ar}/^{39}\text{Ar}$ data of ash layer SR3M. For details the reader is referred to chapter 3 and the appendix. Errors are presented with increasing hierarchy as the analytical error of the sample (I), analytical error of the sample and standard (II), analytical error plus errors in $^{40}\text{Ar}/^{39}\text{Ar}$ of primary standard and intercalibration of primary and secondary standards (III) and the foregoing uncertainties and decay constant errors (IV). Decay constants are used from Steiger and Jäger (1977), TCR standard age and error are from Renne et al. (1998). The age according to equation 1.14 concerns a slightly modified method as presented in Min et al. (2000) and chapter 1 with activities and physical parameters as in table 1.4, column VII. The astronomical age of the volcanic ash layer is given in **bold italic**. All errors are quoted at the 1 σ level.

showed normal probability distribution based on data of two irradiations (VU32 and VU37, figure 7.7a). The VU16 data show a younger age peak and therefore add a population to the probability distribution. One explanation for the deviation of the VU16 data might be a systematic error in the behavior of the analytical system. From VU32, but especially from VU37 onwards mass discrimination was monitored more frequently and peak shapes were assessed more regularly. Therefore we regard, the VU37 data as the best age estimates, although problems due to sample heterogeneity cannot completely be excluded.

U/Pb ID-TIMS RESULTS

Figures 7.4a-h show the transmitted light photographs of (part of) the analyzed fractions before and after abrasion. The picked grains exclude any cracked and cloudy grains, but the grains are not completely inclusion free. Analyzed fractions consisted of more than 500 grains in the size range (90-120 μm) and the results are presented in table 7.2. It appeared that the zircons contained (unexpectedly) very high amounts of uranium that exacerbated the underspiking of the samples for U. Additionally corrections for Th and common lead were significant. Figure 7.5 shows a concordia diagram. The bulk zircon fractions plot below

Fraction	Wt (mg)	U (ppm)	Th/U	Th (ppm)	Pb* (ppm)	$^{206}\text{Pb}/^{204}\text{Pb}$	Common Pb (pg)	$^{208}\text{Pb}/^{206}\text{Pb}$	Discordance %
2 (Z)	2722	2243	0.37	821	2	642.3	428	0.22	97.52
3 (Z)	2837	2413	0.36	858	2	920.2	335	0.21	97.55
4B (Z)	1620	2261	0.34	777	2	824.6	216	0.20	97.75
5A (Z)	1618	2108	0.36	757	2	824.0	190	0.21	96.58

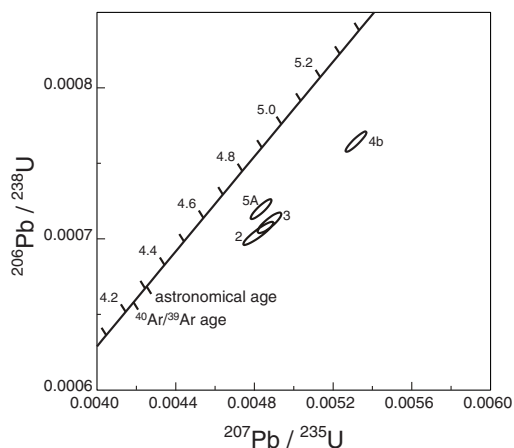
Fraction	$^{206}\text{Pb}/^{238}\text{U}$	$^{207}\text{Pb}/^{235}\text{U}$	$^{207}\text{Pb}/^{206}\text{Pb}$	$^{207}\text{Pb}/^{206}\text{Pb}$ age (Ma)	$^{206}\text{Pb}/^{238}\text{U}$ age (Ma)	$^{207}\text{Pb}/^{235}\text{U}$ age (Ma)
2 (Z)	0.0007 \pm <0.00005	0.005 \pm <0.0005	0.04968 \pm 0.00019	180.1 \pm 17.3	4.5 \pm <0.05	4.9 \pm 0.01
3 (Z)	0.0007 \pm <0.00005	0.005 \pm <0.0005	0.04977 \pm 0.00016	184.4 \pm 15.2	4.6 \pm <0.05	4.9 \pm 0.01
4B (Z)	0.0008 \pm <0.00005	0.005 \pm <0.0005	0.05044 \pm 0.0001	215.5 \pm 9.4	4.9 \pm <0.05	5.4 \pm 0.01
5A (Z)	0.0007 \pm <0.00005	0.005 \pm <0.0005	0.04872 \pm 0.00012	134.2 \pm 11.8	4.6 \pm <0.05	4.9 \pm 0.01

Table 7.2: Analytical data of ID-TIMS analyses.

Standard errors of the mean are reported at the 68% confidence level for the isotopic ratios and at 95% confidence level for the ages. Errors are calculated by numerical propagation including tracer calibration uncertainties, but excluding errors in decay constants. Pb* is the amount of radiogenic lead. $^{206}\text{Pb}/^{204}\text{Pb}$ ratio is corrected for mass fractionation and spike. Common Pb (pg) refers to the total amount of common Pb measured in the analysis corrected for fractionation and spike. Th/U ratios are calculated from radiogenic $^{208}\text{Pb}/^{206}\text{Pb}$ and $^{207}\text{Pb}/^{206}\text{Pb}$. Th abundance is calculated from Th/U and U. Atomic ratios are corrected for Pb and U blank, fractionation and initial common Pb (Stacey and Kramers, 1975). The % discordance refers to the percent discordance along a line to zero age.

Figure 7.5: U/Pb concordia diagram.

Concordia diagram based on the ID-TIMS analyses. The $^{40}\text{Ar}/^{39}\text{Ar}$ (relative to FCT 28.02 Ma) and astronomical ages of SR3M are indicated on the concordia line. Ellipses represent the 2σ errors.



the concordia line at older ages than the expected age of ~ 4.31 Ma and are slightly discordant ($\sim 97\%$). Applying different methods of Th and common Pb correction does not result in a shift of the data onto the concordia line.

U/Pb SHRIMP RESULTS

An important benefit of the use of an ion microprobe to analyze zircons is the ability to avoid and/or resolve inherited radiogenic Pb. As the TIMS data indicated that inherited components might indeed be present in the SR3M zircons, SHRIMP analyses were performed on the zircons, even though errors in SHRIMP techniques are at least $\pm 2\%$ ($\pm 1\sigma$) for an individual analysis on young zircons (Stern, 1997). It should also be noted that Stern and Amelin (2003) have indicated that internal variability inherent in HR-SIMS analysis may limit attainable precision (external) to a minimum of $\pm 1\%$ ($\pm 1\sigma$) for $^{206}\text{Pb}/^{238}\text{U}$ ages. In addition, the extremely young age of the zircons necessitates a significant extrapolation from the comparative standard's data, warranting some caution because of the possibility for systematic bias during data reduction. Before analyses SHRIMP mounts are first assessed using transmitted light photography (figure 7.6a, d, g, i and l), back scattered electron images (figure 7.6a, c, e, f and g) and cathodoluminescence images (figure 7.6b and d). All BSE and CL images reveal magmatic growth zoning. The bright CL areas indicate low U zones and vice versa, because in CL imaging luminosity is primarily caused by the REE Dy^{3+} , but also by Sm^{3+} , Eu^{2+} , Tb^{3+} , and Y^{3+} and suppressed by U and Th (Hanchar and Miller, 1993 and references therein). Sharp edged magmatic zonation might imply that intracrystalline diffusion did not occur at any significant scale (Connelly, 2000). Chemical zonation does not undermine U/Pb experiments on zircon since each chemical zone might represent a closed system yielding identical ratios of U and Pb, and thus yield the same age. Zonation in combination with crystal shape suggests evidence for a primary magmatic origin of the zircon crystals.

Further, it appeared that dark areas in transmitted light microscopy and bright, white areas on BSE images were thorite (ThSiO_4). This was unexpected, because in spite of the fact that the mineral thorite is isostructural with zircon (and like zircon, is frequently found to be metamict) the lack of intermediate compositions between zircon and thorite suggests a relatively wide miscibility gap (Speer, 1980). Although the occurrence of thorite in zircon is rare, evidence has been accumulating for the existence of mineral phases of intermediate composition (e.g., Pointer et al., 1988; Rubin et al., 1989).

Table 7.3 gives an overview of the analytical data of all SHRIMP analyses. SHRIMP data are all corrected using ^{207}Pb correction for the common Pb. This assumes concordance of the points (fairly reasonable for this dataset) and corrects common Pb by using the excess ^{207}Pb (i.e. above and beyond that accounted for by the necessary decay of ^{235}U) to correct the $^{206}\text{Pb}/^{238}\text{U}$ ratio. As such there is no concordia diagram, but

rather the weighted average of the $^{206}\text{Pb}/^{238}\text{U}$ ages is used. Further it should be noticed that U and Th contents are high.

It would appear that Th is endemic in the zircon, which may lead to excess ^{206}Pb . Therefore, most spots of the SHRIMP analyses avoid the thorite bearing areas in the center of the grains. The SHRIMP data form a good Gaussian distribution, indicating no significant inheritance or Pb loss (figure 7.7). The weighted mean

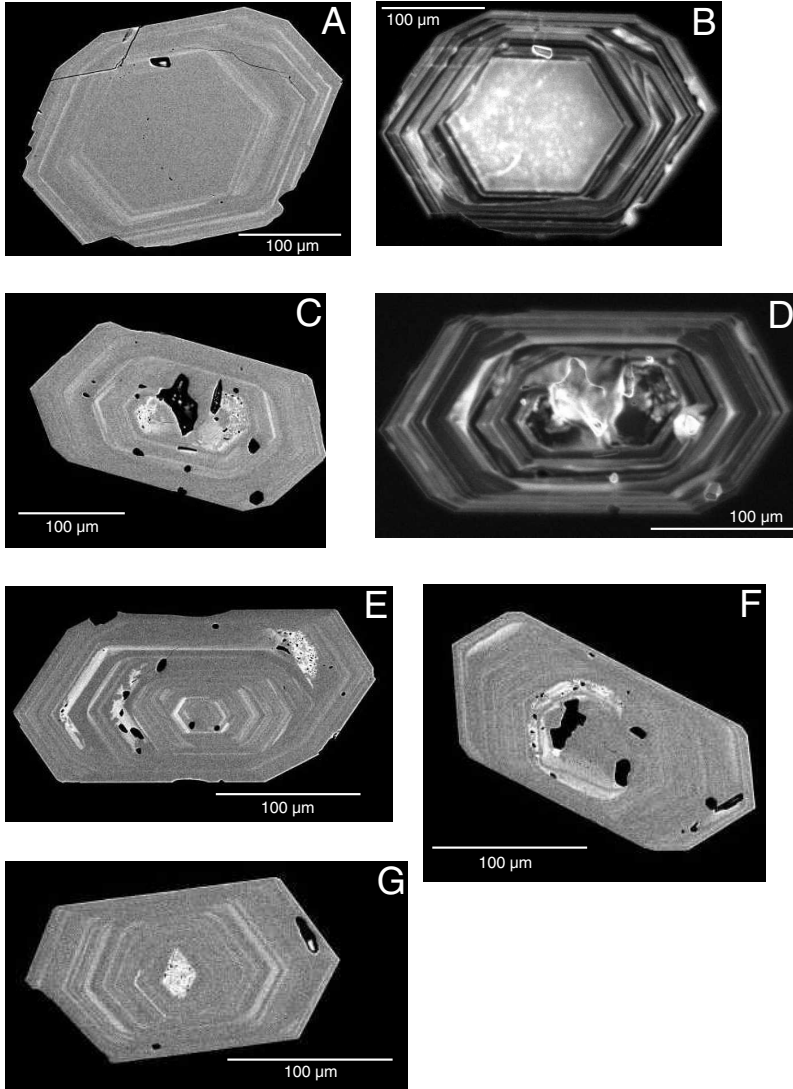


Figure 7.6a-g: BSE and CL images of five zircon grains. BSE and CL images of arbitrary (not handpicked) zircons of the diamagnetic 90-120 μm size fraction. Zonation is visible and bright white spots in BSE images are thorite. Figures 7.6b and d are cathodoluminescence images of respectively zircons a and c showing the zonation even more clearly.

Labels	U (ppm)	Th (ppm)	Th/U ± 1se	Pb* (ppm)	²⁰⁶ Pb _c (ppb)	²⁰⁴ Pb/ ²⁰⁶ Pb × 10 ⁻⁴ ± 1se	²⁰⁶ Pb/ ²⁰⁴ Pb	f ²⁰⁶ Pb _c / ²⁰⁶ Pb _t ± 1se	f ²⁰⁷ Pb _c / ²⁰⁷ Pb _t	f ²⁰⁸ Pb _c / ²⁰⁸ Pb _t
7299-1.1	2162	874	0.417 ± 0.003	1	<0.5	10.9 ± 3.2	920	0.0038 ± 0.0017	0.0038	0.0017
7299-1.2	3382	1290	0.394 ± 0.005	2	<0.5	7.7 ± 1.9	1294	0.0036 ± 0.0028	0.0036	0.0028
7299-2.1	1561	1965	1.301 ± 0.011	1	<0.5	3.7 ± 6.6	2668	0.0019 ± 0.0027	0.0019	0.0027
7299-3.1	2047	1293	0.653 ± 0.005	2	<0.5	0.1 ± 0.1	100000	0.0064 ± 0.0018	0.0064	0.0018
7299-4.1	1482	485	0.338 ± 0.003	1	<0.5	4.8 ± 5.4	2069	0.0073 ± 0.0029	0.0073	0.0029
7299-5.1	1383	410	0.306 ± 0.003	1	<0.5	7.1 ± 5.9	1409	0.0065 ± 0.0050	0.0065	0.0050
7299-6.1	546	282	<i>0.534 ± 0.608</i>	0	<0.5	<i>26.7 ± 13.1</i>	<i>374</i>	<i>0.0193 ± 0.0156</i>	<i>0.0193</i>	<i>0.0156</i>
7299-7.1	3102	1996	0.665 ± 0.004	2	1	4.4 ± 2.7	2279	0.0089 ± 0.0018	0.0089	0.0018
7299-8.1	3218	1398	0.449 ± 0.002	2	<0.5	8.7 ± 2.5	1149	0.0031 ± 0.0014	0.0031	0.0014
7299-9.1	2750	1366	0.513 ± 0.004	2	<0.5	4.6 ± 2.6	2191	0.0040 ± 0.0015	0.0040	0.0015
7299-9.2	<i>1107</i>	<i>261</i>	<i>0.243 ± 0.263</i>	<i>1</i>	<0.5	<i>18.6 ± 12.4</i>	<i>539</i>	<i>0.0009 ± 0.0102</i>	<i>0.0009</i>	<i>0.0102</i>
7299-10.1	1596	949	0.614 ± 0.007	1	<0.5	3.0 ± 8.0	3320	0.0020 ± 0.0032	0.0020	0.0032
7299-11.1	4955	4758	0.992 ± 0.006	4	<0.5	5.4 ± 1.5	1867	0.0031 ± 0.0012	0.0031	0.0012
7299-12.1	1986	531	0.276 ± 0.003	1	1	19.4 ± 10.2	515	0.0209 ± 0.0056	0.0209	0.0056
7299-13.1	1400	1011	0.746 ± 0.006	1	<0.5	7.0 ± 5.3	1430	0.0084 ± 0.0030	0.0084	0.0030
7299-14.1	3050	1500	0.508 ± 0.003	2	1	4.0 ± 2.6	2490	0.0058 ± 0.0016	0.0058	0.0016
7299-15.1	2756	1064	0.399 ± 0.003	2	1	10.0 ± 5.8	999	0.0068 ± 0.0018	0.0068	0.0018
7299-16.1	2725	1096	0.415 ± 0.002	2	<0.5	0.1 ± 0.1	100000	0.0020 ± 0.0015	0.0020	0.0015
7299-17.1	2553	1469	0.595 ± 0.004	2	<0.5	11.2 ± 3.1	891	0.0046 ± 0.0016	0.0046	0.0016
7299-18.1	1492	2492	1.725 ± 0.019	1	<0.5	5.7 ± 7.9	1756	0.0067 ± 0.0024	0.0067	0.0024
7299-19.1	927	1324	1.476 ± 0.030	1	<0.5	14.2 ± 8.8	705	0.0130 ± 0.0046	0.0130	0.0046
7299-20.1	1950	2878	1.524 ± 0.010	2	<0.5	13.7 ± 6.4	729	0.0061 ± 0.0033	0.0061	0.0033
7299-21.1	4258	2395	0.581 ± 0.004	3	<0.5	9.0 ± 3.3	1113	0.0035 ± 0.0013	0.0035	0.0013
7299-22.1	2619	979	0.386 ± 0.004	2	<0.5	2.4 ± 2.8	4106	0.0054 ± 0.0033	0.0054	0.0033
7299-23.1	2735	4353	<i>1.644 ± 0.028</i>	2	<0.5	<i>5.7 ± 2.7</i>	<i>1740</i>	<i>0.0062 ± 0.0017</i>	<i>0.0062</i>	<i>0.0017</i>

Table 7.3: Analytical data of SHRIMP analyses.

Standard errors of the mean are reported at the 68% confidence level for the analytical data and at the 95% confidence level for the ages. The data omitted from interpretation are shown in *italic*.

Labels	$^{208}\text{Pb}/^{206}\text{Pb} \pm 1\text{se}$	$^{208}\text{Pb}/^{232}\text{Th} \times 10^{-4} \pm 1\text{se}$	$^{206}\text{Pb}/^{238}\text{U} \pm 1\text{se}$	$^{238}\text{U}/^{206}\text{Pb} \pm 1\text{se}$	$^{208}\text{Pb}/^{232}\text{Th}$ age (Ma) $\pm 2\text{se}$	$^{206}\text{Pb}/^{238}\text{U}$ age (Ma) $\pm 2\text{se}$
7299-1.1	0.1539 \pm 0.0063	2.5 \pm 0.1	6.7 \pm 0.01	1489 \pm 30	5.01 \pm 0.23	4.33 \pm 0.09
7299-1.2	0.1423 \pm 0.0069	2.6 \pm 0.1	7.1 \pm 0.01	1414 \pm 30	5.16 \pm 0.28	4.56 \pm 0.10
7299-2.1	0.4299 \pm 0.0129	2.2 \pm 0.1	6.8 \pm 0.01	1480 \pm 32	4.51 \pm 0.17	4.35 \pm 0.09
7299-3.1	0.2080 \pm 0.0057	2.2 \pm 0.1	6.8 \pm 0.01	1465 \pm 31	4.39 \pm 0.16	4.40 \pm 0.09
7299-4.1	0.1255 \pm 0.0074	2.5 \pm 0.2	6.7 \pm 0.02	1490 \pm 34	5.03 \pm 0.32	4.32 \pm 0.10
7299-5.1	0.1111 \pm 0.0111	2.4 \pm 0.2	6.7 \pm 0.01	1494 \pm 32	4.91 \pm 0.50	4.31 \pm 0.09
7299-6.1	0.1592 \pm 0.0478	2.0 \pm 2.4	6.7 \pm 0.09	1503 \pm 206	4.01 \pm 4.76	4.29 \pm 0.59
7299-7.1	0.2157 \pm 0.0063	2.1 \pm 0.1	6.4 \pm 0.02	1573 \pm 38	4.17 \pm 0.16	4.10 \pm 0.10
7299-8.1	0.1638 \pm 0.0051	2.4 \pm 0.1	6.5 \pm 0.01	1538 \pm 32	4.80 \pm 0.18	4.19 \pm 0.09
7299-9.1	0.1737 \pm 0.0060	2.3 \pm 0.1	6.8 \pm 0.01	1476 \pm 30	4.63 \pm 0.19	4.36 \pm 0.09
7299-9.2	0.1198 \pm 0.0299	3.2 \pm 4.5	6.5 \pm 0.57	1528 \pm 1332	6.51 \pm 9.16	4.22 \pm 3.68
7299-10.1	0.2095 \pm 0.0101	2.2 \pm 0.1	6.6 \pm 0.02	1517 \pm 38	4.54 \pm 0.25	4.25 \pm 0.11
7299-11.1	0.3357 \pm 0.0058	2.4 \pm 0.1	7.1 \pm 0.02	1402 \pm 33	4.88 \pm 0.14	4.60 \pm 0.11
7299-12.1	0.0807 \pm 0.0149	2.1 \pm 0.4	7.2 \pm 0.02	1389 \pm 33	4.25 \pm 0.79	4.64 \pm 0.11
7299-13.1	0.2507 \pm 0.0084	2.2 \pm 0.1	6.7 \pm 0.01	1500 \pm 32	4.53 \pm 0.18	4.30 \pm 0.09
7299-14.1	0.1816 \pm 0.0045	2.5 \pm 0.1	7.1 \pm 0.01	1412 \pm 29	5.11 \pm 0.17	4.56 \pm 0.09
7299-15.1	0.1361 \pm 0.0061	2.3 \pm 0.1	6.8 \pm 0.02	1462 \pm 33	4.71 \pm 0.24	4.41 \pm 0.10
7299-16.1	0.1564 \pm 0.0046	2.5 \pm 0.1	6.7 \pm 0.01	1502 \pm 31	5.07 \pm 0.18	4.29 \pm 0.09
7299-17.1	0.2058 \pm 0.0054	2.4 \pm 0.1	6.8 \pm 0.01	1465 \pm 31	4.78 \pm 0.16	4.40 \pm 0.09
7299-18.1	0.5880 \pm 0.0103	2.3 \pm 0.1	6.7 \pm 0.01	1501 \pm 31	4.59 \pm 0.13	4.29 \pm 0.09
7299-19.1	0.4715 \pm 0.0299	2.1 \pm 0.2	6.5 \pm 0.02	1539 \pm 50	4.19 \pm 0.31	4.19 \pm 0.14
7299-20.1	0.5262 \pm 0.0103	2.3 \pm 0.1	6.6 \pm 0.02	1505 \pm 36	4.64 \pm 0.15	4.28 \pm 0.10
7299-21.1	0.1968 \pm 0.0053	2.3 \pm 0.1	6.8 \pm 0.01	1474 \pm 32	4.64 \pm 0.16	4.37 \pm 0.09
7299-22.1	0.1411 \pm 0.0092	2.5 \pm 0.2	6.8 \pm 0.01	1463 \pm 31	5.05 \pm 0.35	4.41 \pm 0.09
7299-23.1	0.5330 \pm 0.0075	2.0 \pm 0.1	6.3 \pm 0.01	1582 \pm 35	4.14 \pm 0.13	4.07 \pm 0.09

Table 7.3: Analytical data of SHRIMP analyses (continued).

Standard errors of the mean are reported at the 68% confidence level for the analytical data and at the 95% confidence level for the ages. The data omitted from interpretation are shown in *italic*.

$^{206}\text{Pb}/^{238}\text{U}$ age and error are 4.359 ± 0.056 Ma ($\pm 2\sigma$, weighted by data point errors, MSWD 1.8, $n = 22$). The probability distribution is broad however due to the large 1σ error for individual SHRIMP data points (on the order of $\pm 2\%$).

DISCUSSION

ERRORS IN ASTRONOMICAL TIME CONTROL?

As briefly stated before the astronomical tuning of ash layer SR3M as proposed by Van Vugt et al. (1998) and Steenbrink et al. (1999) might not be correct. On basis of the intercalibration between $^{40}\text{Ar}/^{39}\text{Ar}$ and astronomical time as proposed for the Melilla Basin, the cycles for the younger part of the Ptolemais section should be tuned 2.5 cycles younger to be exactly in agreement with the Melilla intercalibration. This would indicate also that the inferred phase relation (which was based on the best pattern fit between sediments and target curve) between the lignite / marl sediments and the insolation minima and maxima might be wrong. However, Kloosterboer-Van Hove (2000) confirmed the phase relation as proposed by Van Vugt et al. (1998) on basis of pollen data. Therefore we estimate that the tuning might be shifted upward with 2 or 3 cycles for the upper part (above the possible hiatus) of the Ptolemais Formation. The revised astronomical age for ash layer SR3M is then $\sim 4.27 \pm 0.025$ Ma (was 4.318 Ma). Figure 7.2a shows the tuning as was described in chapter 3; figure 7.2b is the tuning when cycles are tuned 2 cycles higher.

This also has implications for the magnetostratigraphy, because the Cochiti normal polarity interval is located in this part of the stratigraphic section and a shift in the tuning will affect the location of the reversals with respect to the APTS. Table 7.4 list the locations of the Cochiti polarity reversals in the Rossello and Ptolemais Composites with respect to the nearest insolation peaks (i-codes after Lourens et al., 1996). The Cochiti reversal horizon in the original tuning of Van Vugt et al. (1998) and the APTS (= Rossello

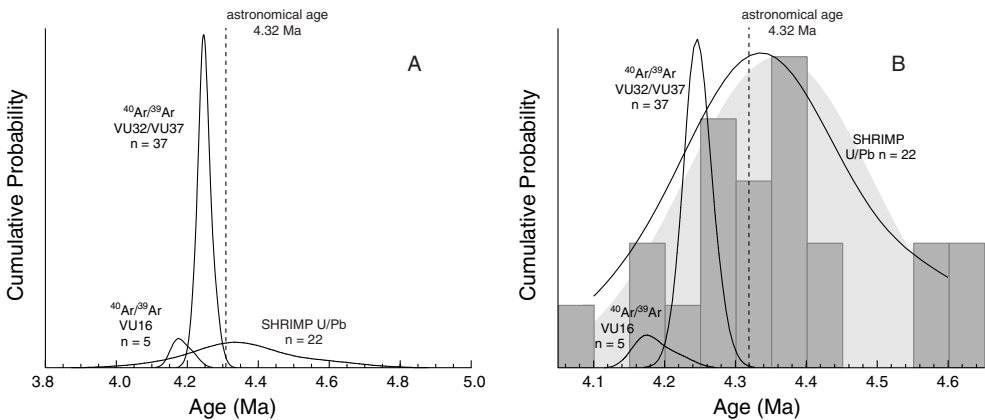


Figure 7.7: Cumulative age probability distributions for U/Pb SHRIMP and $^{40}\text{Ar}/^{39}\text{Ar}$ data.

Age probability distributions for the $^{40}\text{Ar}/^{39}\text{Ar}$ data of Steenbrink et al. (1999) (VU16), the $^{40}\text{Ar}/^{39}\text{Ar}$ data reported in this thesis (VU32/VU37) and the U/Pb SHRIMP data. The area below the curve is proportional to the number of experiments in 7.7a. In 7.7b the distribution of the SHRIMP data is stretched to better visualize the normal behavior and optimum age of the SHRIMP data. The gray area in 7.7b indicates a normal distribution for the U/Pb data. Histogram of SHRIMP data is presented as gray bars.

	Upper Cochiti	Lower Cochiti
i-cycle and age (Ma) Rossello Composite	403 / 4.188	413 / 4.300
i-cycle and age (Ma) Ptolemais (Van Vugt et al., 1998)	403 / 4.188	414 / 4.313
i-cycle and age (Ma) Ptolemais shifted 2 cycles upwards	399 / 4.137	410 / 4.264

Table 7.4: i-codes and ages of Cochiti reversal.

i-codes after Lourens et al. (1996) and non-lagged astronomical ages corresponding to the insolation peaks for reversals are given for the Cochiti normal polarity interval as recorded in the Rossello Composite (Lourens et al., 1996), in the Ptolemais composite (Van Vugt et al., 1998) and in the Ptolemais composite after shifting the tuning two precession cycles upward (see figure 7.2b).

Composite) typically deviate less than one i-code cycle (i.e., less than half a lithological cycle). The shifted tuning results in deviations of 3-4 i-code cycles for the Cochiti interval (i.e., 1.5-2 lithological cycles). Since the ages of the Ptolemais reversals in the shifted tuning are too young compared to the APTS, delayed acquisition in Ptolemais cannot explain the discrepancy. However, inspection of the results in the three subsections of Van Vugt et al. (1998) indicate the locations of the Cochiti reversals might be located 2 lithological cycles lower in Vorio as well Tomea Eksi (Komanos does not show a reliable magnetostratigraphy for the Notio member). This would agree excellently with the APTS. Therefore, it might be justified to tune the upper part of the Ptolemais section two cycles upwards. This will result in an astronomical age of 4.27 Ma for the SR3M ash layer.

INTERCALIBRATION OF ISOTOPIC AND ASTRONOMICAL TIME

Different dating methods should ideally produce equivalent absolute ages when the same geological event is dated. Within this frame our attention was focussed on $^{40}\text{Ar}/^{39}\text{Ar}$ and astronomical dating methods in the previous chapters. The purpose of the U/Pb experiments presented in this chapter was to further intercalibrate the $^{40}\text{Ar}/^{39}\text{Ar}$ and astronomical dating methods with the U/Pb system. Previous studies focussed either directly on the intercalibration between the astronomical and $^{40}\text{Ar}/^{39}\text{Ar}$ system (e.g., Renne et al, 1994; this thesis), or on intercalibration between different isotopic methods (e.g., Baadsgaard et al., 1993; Min et al., 2000). In addition, a lot of work was (and still is) done on the isotope systematics of the commonly used dating standard Fish Canyon Tuff (FCT). A discrepancy between the $^{40}\text{Ar}/^{39}\text{Ar}$ sanidine mineral age (e.g., 28.02 ± 0.16 Ma relative to K/Ar dated GA1550 biotite, Renne et al., 1998) and the U/Pb mineral age (e.g., 28.46 ± 0.06 Ma zircon crystallization age, Schmitz and Bowring, 2001) emphasize a substantial systematic error in the application in one or both of these methods (e.g., decay constant and/or standard age errors in $^{40}\text{Ar}/^{39}\text{Ar}$ and residence time in U/Pb). As outlined in chapter 5 the FCT sanidine age proposed on basis of intercalibration with astronomically dated ash layers in the Melilla Basin is 28.24 ± 0.01 Ma. This indicates that systematic errors indeed might have occurred in both methods to estimate the FCT eruption age. U/Pb data for the astronomically and $^{40}\text{Ar}/^{39}\text{Ar}$ dated volcanic ash layer SR3M aimed to get more insight in the intercalibration systematics and potential for all systems.

Unfortunately, the difficulties introduced by inheritance for the bulk zircon analysis (more than 500 crystals have been analyzed simultaneously) were clearly illustrated by the discordant TIMS data in figure 7.5. TIMS data are therefore inadequate for establishing the true crystallization age of SR3M zircon (and also excludes the possibility to make statements about potential residence times). Further, young minerals might also be affected by disequilibrium of intermediate isotopes in the U decay chains (^{230}Th and ^{234}U in the $^{238}\text{U}/^{206}\text{Pb}$

and ^{231}Pa in the $^{235}\text{U}/^{207}\text{Pb}$ decay chain) (Mattinson, 1973; Schärer, 1984). However, ^{234}U is not substantially differentiated from ^{238}U during mineral formation, therefore only a correction for the ^{230}Th disequilibrium must be applied in the $^{238}\text{U}/^{206}\text{Pb}$ decay chain. ^{230}Th disequilibrium in zircon is expected to be much smaller than in e.g. monazite, but correction will affect the current data due to the high amounts of Th in the SR3M zircons. For example mineral fraction 5A has a Th/U ratio in the mineral of 0.6 and to move the datapoint in the direction of the concordia disequilibrium correction requires a Th/U ratio in the rock on the order of 0.1-0.2. This ratio is extremely low and likely unrealistic, but additionally the corrected $^{206}\text{Pb}/^{238}\text{U}$ age is increasingly sensitive to the chosen value for $[\text{Th}/\text{U}]_{\text{rock}}$ (4.0 Ma for 0.1 versus 4.4 Ma for 0.2). However, in all cases the $^{207}\text{Pb}/^{235}\text{U}$ age is 4.9 to 5.4 Ma and this will not change by excess ^{206}Pb correction. Considering the distance to the concordia line it is therefore clear that inheritance plays a role and can not be avoided for the large fractions necessary for TIMS analysis.

Assuming that the memory observed in the zircons originated from the 320 Ma old Hercynian crystalline basement (upper intercept with concordia line) results in a lower intercept age of 2.2 ± 0.5 Ma (MSWD 32). Clearly, this does not have any geological significance. Pinning the lower intercept at 4.3 Ma (astronomical age), an upper intercept of ~ 1.4 Ga is derived. Once again, this clearly points to evidence for inheritance, probably of multiple ages.

The SHRIMP data were corrected for common Pb using the ^{207}Pb common lead method. This assumes a precise concordance of the $^{206}\text{Pb}^*/^{238}\text{U}$ and $^{207}\text{Pb}^*/^{235}\text{U}$ ages, using the common-Pb $^{207}\text{Pb}/^{206}\text{Pb}$ calculated from the $^{206}\text{Pb}/^{204}\text{Pb}$ and $^{207}\text{Pb}/^{204}\text{Pb}$. This might not be completely true (see TIMS data). Further, the weighted mean SHRIMP U/Pb age of 4.36 ± 0.03 Ma ($\pm 1\sigma$) compared to the $^{40}\text{Ar}/^{39}\text{Ar}$ age of 4.24 ± 0.06 Ma ($\pm 1\sigma$, full external error) or the astronomical age of ~ 4.32 Ma (Steenbrink et al., 1999; in this chapter revised to ~ 4.27 Ma) is slightly too old to represent the eruption age of the event responsible for volcanic ash layer SR3M. Therefore, it seems that the SHRIMP fractions have some inherited component as well or that residence times >60 kyr play a role. Table 7.5 summarizes several methods that have been applied to determine an eruption age for FCT by (inter)calibration with U/Pb, $^{40}\text{Ar}/^{39}\text{Ar}$ or astronomical ages of secondary standards or FCT itself. What can be seen from this table is that apart from the lack of consensus between the data, the FCT age of 28.79 Ma based on intercalibration with SR3M SHRIMP U/Pb data produces an erroneous old age. It must however be remarked that this age is (coincidentally?) not different from the FCT age based on astronomical intercalibration with the younger Ptolemais ash layers (chapter 3) with the astronomical ages for these ash layers as in the original tuning of Van Vugt et al. (1998) and Steenbrink et al. (1999).

The information gained from the U/Pb data can be placed in a somewhat broader perspective. Our older U/Pb SHRIMP age compared to the astronomical and $^{40}\text{Ar}/^{39}\text{Ar}$ ages for the same sample supports the U/Pb dating by Schmitz and Bowring (2001) of magmatic sphene and zircon for the FC tuff, in that all results point to slightly but significantly older ages for U/Pb (note that the single grain approach of Schmitz and Bowring (2001) excluded the inheritance problem as observed in this chapter). Taking this one step further, the ages of 28.48 ± 0.06 Ma for magmatic zircon, 28.40 ± 0.05 Ma for magmatic sphene, and our result of 28.24 ± 0.01 Ma for astronomically tuned $^{40}\text{Ar}/^{39}\text{Ar}$ age of sanidine can be interpreted as mutually consistent taking into account the differences in temperature of isotopic closure between the U/Pb systems of zircon and sphene and K/Ar in sanidine. If this interpretation is correct, then we may conclude that the

Apparent SR3M Age (Ma)	Apparent FCT age (Ma)	Comment
4.24 ± 0.06	28.02 ± 0.28	$^{40}\text{Ar}/^{39}\text{Ar}$ SR3M sanidine relative to FCT sanidine relative to K/Ar age of GA-1550 (Renne et al., 1998)
4.27 ± 0.02	28.20 ± 0.17	$^{40}\text{Ar}/^{39}\text{Ar}$ FCT sanidine relative to shifted astronomical age SR3M (this chapter)
4.32 ± 0.02	28.52 ± 0.17	$^{40}\text{Ar}/^{39}\text{Ar}$ FCT sanidine relative to original astronomical age SR3M (Van Vugt et al. 1998; Steenbrink et al., 1999; chapter 3)
4.36 ± 0.03	28.79 ± 0.20	$^{40}\text{Ar}/^{39}\text{Ar}$ FCT sanidine relative to SHRIMP U/Pb age SR3M (this chapter)
-	28.40 ± 0.08	FCT $^{206}\text{Pb}/^{238}\text{U}$ titanite age (Schmitz and Bowring, 2001)
-	28.48 ± 0.06	FCT U/Pb zircon concordia age (Schmitz and Bowring, 2001)
-	28.32 ± 0.14	$^{40}\text{Ar}/^{39}\text{Ar}$ FCT sanidine relative to $^{207}\text{Pb}/^{206}\text{Pb}$ zircon dated Pallsade rhyolite alkali feldspar (Min et al., 2000)
-	27.98 ± 0.15	$^{40}\text{Ar}/^{39}\text{Ar}$ FCT sanidine relative to $^{207}\text{Pb}/^{204}\text{Pb}$ monazite dated MAC-83 biotite (Villeneuve et al., 2000)
-	28.24 ± 0.01	$^{40}\text{Ar}/^{39}\text{Ar}$ FCT sanidine relative to astronomical sanidine ages in Melilla Basin (chapter 5, weighted standard error)

Table 7.5 Age determinations of FCT.

The apparent age of FCT is calibrated relative to several standards which ages are based on different methods. The ages of Schmitz and Bowring (2001) reported in this table concern direct age determinations on minerals from the FCT. Errors are reported at the 1 σ level.

best age for the eruption of the FC tuff is likely to be the sanidine age of 28.24 ± 0.01 Ma, whereas the U/Pb data of sphene and zircon yield highly relevant information as to magma chamber processes, such as magma generation and residence before eruption.

CONCLUSION AND PERSPECTIVES

The U/Pb data presented here are a first attempt to directly intercalibrate the U/Pb and $^{40}\text{Ar}/^{39}\text{Ar}$ isotope systems with the astronomical dating method. Unfortunately, the TIMS U/Pb data seem to be affected by an inherited component causing the data to plot slightly off-concordia. The SHRIMP data show better near concordant data, but are less precise inherent to the technique. Therefore, we were not able to make firm statements on basis of the current data set about e.g. our preferred astronomical tuning option for the upper part of the Ptolemais formation. We can however conclude that the SR3M zircons (like FCT zircons) do not show a simple magmatic history and residence times of zircon in the magma chamber might occur. In the future, this research might be extended to zircons for ash layers in the Melilla Basin (chapter 5), or the Ancona ash layer (chapter 6). The ash layers of the Melilla Basin have the advantage of reliable $^{40}\text{Ar}/^{39}\text{Ar}$ isotopic ages and astronomical time control, although so far the quality of zircons found in these ash layers is moderate. The isotopic $^{40}\text{Ar}/^{39}\text{Ar}$ ages for the Ancona ash layer are less straightforward (chapter 6), but its middle Miocene (~ 11.7 Ma) age, might improve the quality of U/Pb data due to the exponential nature of radioactive decay and therefore higher amounts of radiogenic Pb.

CHAPTER 8

**DIRECT INTERCALIBRATION OF ISOTOPIC AND
ASTRONOMICAL TIME IN THE MEDITERRANEAN NEOGENE:
A SYNTHESIS.**

SYNTHESIS

The standard geological time scale of Berggren et al. (1995) is calibrated with different dating techniques, i.e. the Plio – Pleistocene relies on astronomical tuning, and older parts of the time scale are mainly based on radio-isotopic ($^{40}\text{Ar}/^{39}\text{Ar}$ and U/Pb) calibration methods. In the new edition of the standard geological timescale (Lourens et al., to be published in 2004) the entire Neogene will rely on astronomical dating. Therefore, it is of crucial importance that all dating methods produce equivalent absolute ages when the same geological event is dated. The Mediterranean Neogene provides the opportunity to compare three different dating methods by isotopic dating ($^{40}\text{Ar}/^{39}\text{Ar}$, U/Pb) of volcanic ash layers intercalated in astronomically tuned sediments. Here we show that in spite of potential errors in all methods, we can intercalibrate the $^{40}\text{Ar}/^{39}\text{Ar}$ and astronomical methods and propose an astronomically calibrated age for the in $^{40}\text{Ar}/^{39}\text{Ar}$ geochronology commonly used standard FCT sanidine.

The age models of earlier versions of the Geomagnetic Polarity Time Scale (e.g., La Brecque et al., 1977) were based on a few radio-isotopic calibration points (which were in turn based on more extended background data sets) assuming constant spreading rates between calibration points. These radio-isotopic data consisted predominantly of K/Ar ages for the Cenozoic part of the time scale. With the development of astronomical dating as useful tool to date the younger part of the time scale K/Ar ages of reversals soon turned out to be younger than astronomical ages of the ages of the same reversals (e.g., Hilgen, 1991b). Meanwhile new technical developments in the $^{40}\text{Ar}/^{39}\text{Ar}$ dating technique (e.g., single crystal laser fusion) started an avalanche of studies focusing on the comparison of astronomical ages of reversals and their equivalent $^{40}\text{Ar}/^{39}\text{Ar}$ ages (e.g., Baksi, 1993; Baksi et al., 1992, 1993, 1995; Clement et al., 1997; Hall and Farrell, 1995; Izett and Obradovich, 1994; Renne et al., 1993; Singer and Pringle, 1996; Spell and McDougall, 1992; Tauxe et al., 1992; Turrin et al., 1994). All these studies showed a remarkable agreement between $^{40}\text{Ar}/^{39}\text{Ar}$ and astronomical ages, and therefore the younger K/Ar ages were discarded as erroneous. However, none of these studies involved direct astronomical and isotopic dating on the same sample as performed in this thesis. The applied methods ranged from $^{40}\text{Ar}/^{39}\text{Ar}$ dating of whole rock or groundmass of lava flows in or bracketing polarity reversals (Baksi, 1993; Baksi et al., 1992, 1993; Singer and Pringle, 1996; Singer et al., 1999), single crystal dating on sanidine from rhyolitic domes (Spell and McDougall, 1992; Izett and Obradovich, 1994; Turrin et al., 1994), to dating of minerals from volcanic layers intercalated in sediments with a reliable magnetostratigraphy (Hall and Farrell, 1995; Clement et al., 1997; Renne et al., 1993; Tauxe et al., 1992). All these studies assume an excellently defined magnetostratigraphy, both in the studied section and the astronomically tuned reference section and a correct correlation between the studied section and the APTS. In addition, part of the studies required linear inter- or extrapolation assuming constant sedimentation rates. Moreover, three different secondary standards (FCT biotite, FCT sanidine and TCR sanidine) have been used with age ranges of respectively 27.95-27.99 Ma, 27.55-27.9 Ma and 27.92 Ma contrasting with the currently common used age of 28.02 Ma for FCT sanidine, 28.34 Ma for TCR sanidine (Renne et al., 1998) and 28.16 Ma for FCT biotite (using the intercalibration factor between FCT sanidine and biotite 1.005 ± 0.009 of Dazé et al., 2003). The first intercalibration study between the astronomical and $^{40}\text{Ar}/^{39}\text{Ar}$ system with the purpose to derive an astronomically calibrated $^{40}\text{Ar}/^{39}\text{Ar}$ standard resulted in an age of 28.03 ± 0.09 Ma for FCT sanidine (Renne et al., 1994). This study was based on $^{40}\text{Ar}/^{39}\text{Ar}$ and polarity data of some of the studies mentioned before (Renne et al., 1993; Spell and McDougall, 1992; Tauxe et al., 1992; Turrin et al., 1994).

To compare astronomical and $^{40}\text{Ar}/^{39}\text{Ar}$ ages directly (without assumptions about reliable magnetostratigraphies in all relevant sections and sedimentation rates) Hilgen et al. (1997) dated volcanic ash layers intercalated in astronomically tuned deep marine late Miocene sections on Crete. Unfortunately, the assumption of undisturbed plateaus underlying the total fusion biotite ages of Hilgen et al. (1997) could not be met (chapter 3). Steenbrink et al. (1999) directly dated sanidine of several volcanic ash layers of the astronomically tuned lacustrine, Pliocene Ptolemais Basin. The $^{40}\text{Ar}/^{39}\text{Ar}$ data showed excellent sanidine plateau ages, but the astronomical tuning in the Ptolemais Basin depends on a reliable magnetostratigraphy. As shown in chapter 3 and 7 the astronomical tuning in Ptolemais has to be treated with caution. However, the observed discrepancy between $^{40}\text{Ar}/^{39}\text{Ar}$ and astronomical ages, where the last tended to be older by $\sim 4\%$, could not be explained by considering potential uncertainties in the magnetostratigraphy only.

Therefore, we decided to study the volcanic ash layers in Ptolemais and Crete again and put a lot of effort in obtaining the most precise $^{40}\text{Ar}/^{39}\text{Ar}$ ages (e.g., by installation of a new reference gas for monitoring of mass fractionation, by intercalibration of TCR and FCT sanidine supporting the intercalibration data of Renne et al., 1998, see chapter 1). In contrast to Hilgen et al. (1997) we were able to obtain pure sanidine mineral splits for ash layer A1 on Crete. Multigrain fusion experiments were performed on the Cretan and Ptolemais volcanic ash layers and measured $^{40}\text{Ar}/^{39}\text{Ar}$ ratios of standard and samples in combination with the astronomical ages of ash layers were used to calculate an astronomically calibrated age for FCT sanidine (chapter 3). It appeared that the upper Ptolemais ash layers would produce an FCT age of 28.61 ± 0.20 Ma equivalent to the U/Pb zircon age for FCT (28.48 ± 0.06 Ma, Schmitz and Bowring, 2001). The lower Ptolemais ash layers and the A1 ash layers produced an FCT age of respectively 28.28 ± 0.21 Ma and 28.21 ± 0.04 Ma. Comparison of these data with the first intercalibration study of Renne et al. (1994, FCT sanidine 28.03 ± 0.09 Ma) points to slightly older ages for FCT. On the basis of the Cretan and Ptolemais ash layers alone we were not able to make a clear statement on the "true" age of FCT sanidine. All analyses involved multigrain experiments where xenocrystic contamination might go unnoticed. Further the lower Ptolemais ash layers, although yielding an equivalent FCT age as A1 on Crete, were either bimodal, contained sometimes excess argon or yielded relatively low K/Ca ratios and are therefore not regarded as the "best" age estimates (chapter 3). The upper Ptolemais ash layers yielded an FCT age almost equivalent to the zircon age for FCT. However, recent studies showed potential complications in the magmatic history of the Fish Canyon Tuff (e.g., Bachmann et al., 2002), which especially might affect U/Pb ages of zircon. Therefore, we decided to extend our studies to the western Mediterranean, where volcanic ash layers are intercalated in marine sediments of the Melilla Basin, Morocco and Sorbas and Nijar Basins, SE Spain.

The astronomical time control in these basins is good, although the tuning in Melilla is based on the occurrence of synchronous bio-events throughout the Mediterranean (category 2 ash layer, chapter 2, and chapter 4). The advantage of the Melilla Basin lies in the proximity of the volcanic centers responsible for the volcanic tephra intercalated in the sediments. Therefore, sanidine (and biotite) crystals have grainsizes up to 2 mm. Intercalibration of 185 single crystal experiments from 16 ash layers resulted in an astronomically calibrated FCT sanidine age of 28.24 ± 0.01 Ma (weighted standard error), which is in agreement with the intercalibration based on A1. Single crystal dating provided the possibility to remove xenocrystic contamination, which happened for 16 out of 19 ash layers (chapter 5). This aspect in combination with the reliable tuning convinced us that most reliable age based on direct intercalibration

with astronomical time is the apparent FCT sanidine age of 28.24 ± 0.01 Ma. The concordant results of the mainly Messinian marine sections of Crete, Spain and Morocco strongly support the internal consistency throughout the Mediterranean basin of the astronomical dating technique for this time period.

However, not all ash layers studied in this thesis produced $^{40}\text{Ar}/^{39}\text{Ar}$ ages that are consistent with the excellent results from the reliably tuned Messinian marine sections from Crete and Melilla. The fact that sanidine either from Crete and/or Melilla was always included in the irradiations used in this thesis, excluded the occurrence of systematic errors due to irradiation circumstances and performance of the analytical system. In this way we were able to evaluate potential causes for the less consistent results from the Pliocene lacustrine Ptolemais basin, and the middle Miocene sections of Giblem (Sicily) and Monte dei Corvi (northern Italy). The deviating results based on direct intercalibration with the Ptolemais ash layers (28.61 ± 0.20 Ma for FCT based on the upper ashes, 28.28 ± 0.20 Ma based on the lower ashes) might be explained by an error in the tuning (chapters 3 and 7). The lower and upper Ptolemais ash layers are separated by a thick stratigraphic interval, which might contain a hiatus. Consequently, a possible error in the tuning might not be identical for the lower and upper parts of the Ptolemais Formation in which the two clusters of ash layers are intercalated. But this error will most likely be the same for ash layers in either of the two clusters because they are intercalated in parts of the Ptolemais Formation in which the succession of individual cycles is evident. In contrast the astronomical tuning for the older middle Miocene sections in Italy is considered reliable. Moreover, as mentioned earlier internal intercalibration with sanidine from Crete and/or Melilla excludes any error and/or bias from the technical side of the dating procedure. This internal intercalibration is confirmed by intercalibration of TCR and FCT based on data of 4 different irradiations including a total of 7 vials (chapter 1). Additionally, this FCT/TCR intercalibration also supports the intercalibration factor of 1.0112 ± 0.0010 proposed by Renne et al. (1998) pointing towards negligible interlaboratory errors. This still leaves xenocrystic admixture with older minerals as the most logical explanation for the deviating ages of the middle Miocene ash layers. This explanation is supported by the sometimes complex age distributions. Further, potential problems of re-deposition of the ash material in its final position have to be considered before we would come to a conclusion that the tuning of these middle Miocene sedimentary cycles might be wrong. Clearly, more research is required in the intercalibration of the system in the direction of middle Miocene and older time.

Further, we made a first attempt in a reliable intercalibration of a third method (U/Pb) with the other two methods. The accurate measurement of radiogenic lead in zircons of this young age using ID-TIMS is difficult due to the effects of inherited older lead in large multigrain (>500) fractions. Further the corrections for common lead and ^{230}Th disequilibrium are critical under these extreme conditions. Some of these drawbacks could be overcome by using SHRIMP spot analysis on 'best' zircon fragments rather than full dissolution of many zircons for the TIMS approach. Unfortunately, the SHRIMP results had an analytical uncertainty that precluded the intended intercalibration due to the young age of the sample and therefore low amounts of radiogenic lead.

Still the information gained from the U/Pb data can be placed in a somewhat broader perspective. Our older U/Pb age compared to the astronomical and $^{40}\text{Ar}/^{39}\text{Ar}$ ages for the same sample (SR3M) supports the U/Pb dating by Schmitz and Bowring (2001) of magmatic sphene and zircon for the FC tuff, in that all results point to slightly but significantly older ages for U/Pb (note that the single grain approach of Schmitz and

Bowring (2001) excluded the inheritance problem as observed in chapter 7). Taking this one step further, the apparent ages of 28.48 ± 0.06 Ma for magmatic zircon, 28.40 ± 0.05 Ma for magmatic sphene, and our result of 28.24 ± 0.01 Ma for astronomically tuned $^{40}\text{Ar}/^{39}\text{Ar}$ age of sanidine can be interpreted as mutually consistent taking into account the differences in temperature of isotopic closure between the U/Pb systems of zircon and sphene and K/Ar in sanidine. If this interpretation is correct, then we may conclude that the best age for the eruption of the FC tuff is likely to be the sanidine age of 28.24 ± 0.01 Ma, whereas the U/Pb data of sphene and zircon yield highly relevant information as to magma chamber processes, such as magma generation and residence before eruption.

The entire Neogene in the new version of the standard geological time scale (Lourens et al., in prep.) will most likely rely on astronomical dating using the Laskar 2003 solution (Laskar et al., in prep.). Astronomical tuning in this thesis is based on the identical La90 or La93 solutions with present day values for dynamical ellipticity and tidal dissipation. During writing of this final chapter the Laskar 2003 astronomical solution became available. Therefore, the implications for astronomical ages of ash layers using the new solution have been assessed, but only for the ash layers relevant for the direct intercalibration between the $^{40}\text{Ar}/^{39}\text{Ar}$ and astronomical system (i.e., Melilla and A1 on Crete). Intercalibration of radio-isotopic and astronomical time tuned to the La2003_(1,1) solution results in a FCT age of 28.24 ± 0.01 Ma for the Melilla Basin, and 28.21 ± 0.04 Ma for A1 and is thus identical to the previously proposed intercalibration.

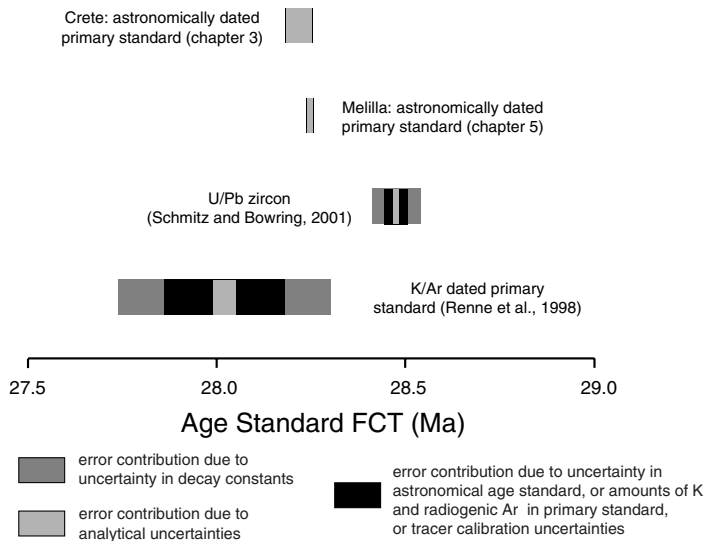


Figure 8.1 Apparent age of Fish Canyon Tuff (FCT).

Visualization of apparent FCT age including contribution of several sources of uncertainty (i.e. analytical uncertainties, decay constant errors, tracer calibration errors for U/Pb, uncertainties in astronomical age of "primary" standards (=ash layers) for astronomically calibrated FCT, and uncertainties in the amounts of ^{40}K and radiogenic ^{40}Ar of the K/Ar dated primary standards. The FCT age relative to a primary K/Ar dated standard is from Renne et al. (1998). The U/Pb age of Schmitz and Bowring (2001) is shown for comparison, indicating a high precision, but lower accuracy due to potential complications of magma chamber processes.

In summary, the direct intercalibration between astronomical and $^{40}\text{Ar}/^{39}\text{Ar}$ dating methods provided an astronomically calibrated age for the commonly used FCT sanidine standard. The ash layers intercalated in sedimentary sequences in the Melilla Basin appeared to be the most reliable for this purpose. The advantage of an astronomically calibrated FCT sanidine standard above the commonly used K/Ar calibrated FCT age of 28.02 Ma (Renne et al., 1998) is visualized in figure 8.1, where decay constant errors and ^{40}K and radiogenic ^{40}Ar contents in primary standard dominate the total uncertainty in the value of Renne et al. (1998). Instead of using the astronomically calibrated age for FCT sanidine, we can also use sanidine of volcanic layers in combination with their astronomical age directly as neutron fluence monitors. Based on the (lack of) detection of xenocrystic contamination or the (lack of) occurrence of multi-modal age populations, we suggest the ash layers Mes-17, Mes-16, Mes-9 or Mes-4 (figure 5.5 in chapter 5) as good candidates for a new standard, because they show no or little contamination and normal age distributions. Mes-9 and Mes-4 both can easily be recognized in the Messadit section due to their thickness of respectively 0.6 m and 5.0 m. Mes-17 and Mes-16 can also easily be recognized, but require inspection of the cyclostratigraphic framework as proposed in chapter 4. To avoid any confusion about the location of the ash layers we propose either Mes-9 or Mes-4 as a $^{40}\text{Ar}/^{39}\text{Ar}$ dating standard.

REFERENCES

REFERENCES

- Abdul Aziz, H.**, Hilgen, F., Krijgsman, W., Sanz, E. and Calvo, J.P., 2000. Astronomical forcing of sedimentary cycles in the middle to late Miocene continental Calatayud Basin (NE-Spain). *Earth Planet. Sci. Lett.*, 177: 9-22.
- Abdul Aziz, H.**, Krijgsman, W., Hilgen, F.J., Wilson, D.S. and Calvo, J.P., 2003. An astronomical polarity timescale for the late middle Miocene based on cyclic continental sequences. *J. Geophys. Res.*, 108: 2159, doi: 10.1029/2002JB001818.
- Adhémar, J.A.**, 1842. Révolutions des mers; déluges périodiques. *Publication privée*, Paris.
- Aparico, A.**, Mitjavila, J., Arana, V. and Villa, I.M., 1991. La edad del volcanismo de las islas Columbretes Grande Alboran (Mediterraneo occidental). *Bol. Geol. Min.*, 102: 562-570.
- Arias, C.**, Bigazzi, G., Bonadonna, F.P., Morlotti, E., Radicati di Brozolo, F., Rio, D., Torelli, L., Brigatti, M.F., Giuliani, O. and Tirelli, G., 1976. Chronostratigraphy of the Izarôrene section in the Melilla basin (Northeastern Morocco). *Bol. Soc. Geol. It.*, 95: 1681-1694.
- Audi, G.**, Bersillon, O., Blachot, J. and Wapstra, A.H., 1997. The NUBASE evaluation of nuclear and decay properties. *Nucl. Phys. A*, 624: 1-124.
- Baadsgaard, H.**, Lerbekmo, J.F., Wijbrans, J.R., Swisher III, C.C. and Fanning, M., 1993. Multimethod radiometric age for a bentonite near the top of the Baculites reesidei Zone of southwestern Saskatchewan (Campanian-Maastrichtian stage boundary?). *Can. J. Earth Sci.*, 30: 769-775.
- Bachmann, O.**, Dungan, M.A. and Lipman, P.W., 2000. Voluminous lava-like precursor to a major ash-flow tuff; low-column pyroclastic eruption of the Pagosa Peak Dacite, San Juan volcanic field, Colorado. *J. Volcanol. Geotherm. Res.*, 98: 153-171.
- Bachmann, O.**, Dungan, M.A. and Lipman, P.W., 2002. The Fish Canyon Tuff magma body, San Juan volcanic field, Colorado: rejuvenation and eruption of an upper crustal batholith. *J. Petrol.*, 43: 1469-1503.
- Baksi, A.**, Hsu, V., McWilliams, M.O. and Farrar, E., 1992. $^{40}\text{Ar}/^{39}\text{Ar}$ dating of the Brunhes-Matuyama geomagnetic field reversal. *Science*, 256: 356-357.
- Baksi, A.**, Hoffman, K. and McWilliams, M., 1993. Testing the accuracy of the geomagnetic polarity time-scale (GPTS) at 2-5 Ma, utilizing $^{40}\text{Ar}/^{39}\text{Ar}$ incremental heating data on whole-rock basalts. *Earth Planet. Sci. Lett.*, 118: 135-144.
- Baksi, A.**, 1993. A geomagnetic polarity time scale for the period 0-17 Ma, based on $^{40}\text{Ar}/^{39}\text{Ar}$ plateau ages for selected field reversals. *Geophys. Res. Lett.*, 20: 1607-1610.
- Baksi, A.**, 1995. Fine tuning the radiometrically derived geomagnetic polarity time scale (GPTS) for 0-10 Ma. *Geophys. Res. Lett.*, 22: 457-460.
- Baksi, A.**, Archibald, D. and Farrar, E., 1996. Intercalibration of $^{40}\text{Ar}/^{39}\text{Ar}$ dating standards. *Chem. Geol.*, 129: 307-324.
- Barbiéri, F.**, Morlotti, E., Palmieri, G., Rio, D. and Torelli, L., 1976. Biostratigraphy of the Izarôrene section in the Melilla basin. *VII African Micropaleontol. Colloquium ILE-IFE*, Nigeria.
- Barbiéri, R.** and Ori, G.G., 2000. Neogene palaeoenvironmental evolution in the Atlantic side of the Rifian Corridor, Morocco. *Palaeogeogr., Palaeoclim., Palaeoecol.*, 163: 1-31.
- Beckinsale, R.D.** and Gale, N.H., 1969. A reappraisal of the decay constants and branching ratio of ^{40}K . *Earth Planet. Sci. Lett.*, 6: 289-294.
- Begemann, F.**, Ludwig, K., Lugmair, G., Min, K., Nyquist, L., Patchett, P., Renne, P., Shih, C., Villa, I. and Walker, R., 2001. Call for an improved set of decay constants for geochronological use. *Geochim. Cosmochim. Acta*, 65: 111-121.
- Bellon, H.**, Jarrige, J. and Sorel, D., 1979. Les activités magmatiques éeennes de l'Oligocene a nos jours, et leurs cadres geodynamiques; donnees nouvelles et synthese. *Rev. Géol. Dynam. Géogr. Phys.*, 21: 41-55.
- Bellon, H.**, Buù, N.Q., Chaumont, J., Philippet, J.-C., 1981. Implantation ionique d'argon dans une cible support. Application au traçage isotopique de l'argon contenu dans les minéraux et les roches. *C. R. Acad. Sci.*, 292: 977-980.
- Bellon, H.**, Bordet, P. and Montenat, C., 1983. Chronologie du magmatisme neogene des Cordilleres Betiques (Espagne meridionale). *Bull. Soc. Géol. Fance.*, 25: 205-217.
- Benammi, M.**, Calvo, M., Prévot, M. and Jaeger, J.J., 1996. Magnetostratigraphy and paleontology of Ait Kandoula Basin (High Atlas) and African-European late Miocene terrestrial fauna exchanges. *Earth Planet. Sci. Lett.*, 145: 15-29.
- Benmoussa, A.**, Demarcq, G. and Lauriat, R., 1987. Pectinides messiniens du Bassin de Melilla (NE Maroc); comparaisons interregionales et interêts paleobiologiques. *Rev. Paleobiol.*, 6: 111-129.
- Benson, R.H.**, Krana, R.-E.B. and Bonaduce, G., 1991. An important current reversal (influx) in the Rifian Corridor (Morocco) at the Tortonian-Messinian boundary; the end of Tethys Ocean. *Paleoceanography*, 6: 165-192.
- Berger, A.L.**, 1977. Support for the astronomical theory of climatic change. *Nature*, 269: 44-45.
- Berger, A.L.**, 1988. Milankovitch theory and climate. *Reviews of Geophysics*, 26: 624-657.
- Berger, A.L.** and Loutre, M.F., 1991. Insolation values for the climate of the last 10 million years. *Quat. Sci. Rev.*, 10: 297-317.
- Berggren, W.A.**, Kent, D.V., Swisher, C.C., III and Aubry, M.P., 1995. A revised Cenozoic geochronology and chronostratigraphy. *SEPM Spec. Publ.*, 54: 129-212.
- Bernini, M.**, Boccaletti, M., El Mokhtari, J., Gelati, R., Iaccarino, S., Moratti, G. and Papani, G., 1992. Données

REFERENCES

- stratigraphiques nouvelles sur le Miocène supérieur du bassin de Taza-Guercif (Maroc nord-oriental). *Bull. Soc. Geol. France*, 163: 73-76.
- Cande, S.C.** and Kent, D.V., 1995. Revised calibration of the geomagnetic timescale for the Late Cretaceous and Cenozoic. *J. Geophys. Res.*, 100: 6093-6095.
- Carpéna, J.** and Mailhé, D., 1987. Fission-track dating calibration of the Fish Canyon Tuff standard in French reactors. *Chem. Geol.*, 66(1-2): 53-59.
- Cebula, G.T.**, Kunk, M.J., Mehnert, H.H., Naeser, C.W., Obradovich, J.D. and Sutter, J.F., 1986. The Fish Canyon Tuff, a potential standard for the $^{40}\text{Ar}/^{39}\text{Ar}$ and fission-track dating methods. *Terra Cognita*, 6: 139-140.
- Choubert, G.**, Faure, M.A., Hottinger, L. and Lecointre, G., 1966. Le Néogène du bassin de Melilla (Maroc septentrional) et sa signification pour définir la limite Mio-Pliocène au Maroc. *Proceedings of Int. Union Geol. Sci.*, Comm. Mediter. Neogene Stratigr., Sess. 3: 238-249.
- Choubert, G.**, Charlot, R., Faure-Muret, A., Hottinger, L., Marçais, J., Tisserant, D., Vidal, P., 1968. Note préliminaire sur le volcanisme messinien-«sontien» au Maroc. *C. R. Acad. Sci.*, 266: 197-199.
- Clement, B.M.**, Swisher, C.C. and Rodda, P., 1997. New magnetostratigraphic and $^{40}\text{Ar}/^{39}\text{Ar}$ dating results from the Suva Marl, Fiji: Calibration of the Early Pliocene geomagnetic polarity time scale. *Earth Planet. Sci. Lett.*, 151: 107-115.
- Cohen, E.R.** and Taylor, B.N., 1987, The 1986 CODATA recommended values of the fundamental physical constants. *J. Res. Natl. Bureau. Stand.*, 92: 85-95.
- Comas, M.C.**, García-Dueñas, V. and Jurado, M.J., 1992. Neogene tectonic evolution of the Alboran basin from MCS data. *Geo-Marine Letters*, 12: 157-164.
- Connelly, J.N.**, 2000. Degree of preservation of igneous zonation in zircon as a signpost for concordancy in U/Pb geochronology. *Chem. Geol.*, 172: 25-39.
- Cornée, J.-J.**, Saint Martin, J., Conesa, G., André, J., Muller, J. and Ben Moussa, A., 1996. Anatomie de quelques plates-formes carbonatées progradantes messiniennes de Méditerranée occidentale. *Bull. Soc. Géol. France*, 167: 495-507.
- Cornée, J.-J.**, Roger, S., Münch, P., Saint Martin, J.P., Feraud, G., Conesa, G., Pestrea-Saint Martin S., 2002. Messinian events: new constraints from sedimentological investigations and new $^{40}\text{Ar}/^{39}\text{Ar}$ ages in the Melilla-Nador Basin (Morocco). *Sediment. Geol.*, 151: 127-147.
- Correia, A.**, Laskar, J. and Néron de Surgy, O., 2003. Long term evolution of the spin of Venus -Theory. Icarus, in press.
- Cramp, A.**, Vitaliano, C. and Collins, M., 1989. Identification and dispersion of the Campanian ash layer (Y-5) in the sediments of the Eastern Mediterranean. *Geo-Marine Letters*, 9: 19-25.
- Croll, J.**, 1866. On the reason why the change of climate in Canada since the glacial epoch has been less complete than in Scotland. *Trans. Geol. Soc. Glasgow*: 138-141.
- Culler, T.S.**, Becker, T.A., Muller, R.A. and Renne, P.R., 2000. Lunar impact history from $^{40}\text{Ar}/^{39}\text{Ar}$ dating of glass spherules. *Science*, 287: 1785-1788.
- Cunningham, K.J.**, Farr, M.R. and Rakic-El Bied, K., 1994. Magnetostratigraphic dating of an Upper Miocene shallow-marine and continental sedimentary succession in north-eastern Morocco. *Earth Planet. Sci. Lett.*, 127: 77-93.
- Cunningham, K.J.**, Benson, R.H., Rakic-El Bied, K. and McKenna, L.W., 1997. Eustatic implications of late Miocene depositional sequences in the Melilla Basin, northeastern Morocco. *Sediment. Geol.*, 107: 147-165.
- Cunningham, K.J.** and Collins, L.S., 2002. Controls on facies and sequence stratigraphy of an upper Miocene carbonate ramp and platform, Melilla Basin, NE Morocco. *Sediment. Geol.*, 146: 285-304.
- Dalrymple, G.B.** and Lanphere, M.A., 1971. $^{40}\text{Ar}/^{39}\text{Ar}$ technique of K-Ar dating: a comparison with the conventional technique. *Earth Planet. Sci. Lett.*, 12: 300-308.
- Dalrymple, G.B.**, Alexander Jr., E.C., Lanphere, M.A. and Kraker, G.P., 1981. Irradiation of samples for $^{40}\text{Ar}/^{39}\text{Ar}$ dating using the Geological Survey TRIGA reactor. *U.S.G.S. Prof. Paper*, 1167: 55.
- Dalrymple, G.B.** and Duffield, W.A., 1988. High precision $^{40}\text{Ar}/^{39}\text{Ar}$ dating of Oligocene rhyolites from the Mogollon-Datil volcanic field using a continuous laser system. *Geophys. Res. Lett.*, 15: 463-466.
- Dalrymple, G.**, Izett, G., Snee, L. and Obradovich, J., 1993. $^{40}\text{Ar}/^{39}\text{Ar}$ age spectra and total-fusion ages of tektites from Cretaceous-Tertiary boundary sedimentary rocks in the Beloc Formation, Haiti. *U.S.G.S Bull.*, 20 pp.
- Dazé, A.**, Lee, J. and Villeneuve, M., 2003. An intercalibration study of the Fish Canyon sanidine and biotite $^{40}\text{Ar}/^{39}\text{Ar}$ standards and some comments on the age of the Fish Canyon Tuff. *Chem. Geol.*, 199: 111-127.
- Dickin, A.P.**, 1997. Radiogenic isotope geology. Cambridge University Press, 490 pp.
- Duffield, W.A.**, Richter, D.H. and Priest, S.S., 1987. Preliminary geologic map of the Taylor Creek Rhyolite, Catron and Sierra counties, New Mexico. *Open-file report U.S.G.S.*: 1 sheet.
- Duffield, W.A.** and Dalrymple, G.B., 1990. The Taylor Creek Rhyolite of New Mexico; a rapidly emplaced field of lava domes and flows. *Bull. Volcanol.*, 52(6): 475-487.
- Duffield, W.A.** and Du Bray, E.A., 1990. Temperature, size, and depth of the magma reservoir for the Taylor Creek

REFERENCES

- Rhyolite, New Mexico. *Am. Mineralogist*, 75: 1059-1070.
- El Bakkali, S.**, Bourdier, J.-L. and Gourgaud, A., 1998. Caractérisation et stratigraphie de dépôts volcanoclastiques marqueurs dans le Miocène supérieur du bassin de Melilla-bas Kert (Rif oriental, Maroc). *C. R. Acad. Sci.*, 327: 93-100.
- Elston, W.E.**, Damon, P.E., Coney, P.J., Rhodes, R.C., Smith, E.I. and Bikerman, M., 1973. Tertiary Volcanic Rocks, Mogollon-Datil Province, New Mexico, and Surrounding Region; K-Ar Dates, Patterns of Eruption, and Periods of Mineralization. *Bulletin Geol. Soc. Am.*, 84: 2259-2273.
- Endt, P.M.** and Van der Leun, C., 1973. Energy levels of A = 21-44 nuclei (V). *Nucl. Phys. A*, 214: 1-625.
- Esteban, M.**, 1979. Significance of the upper Miocene coral reefs of the western Mediterranean. *Palaeogeogr., Palaeoclim., Palaeoecol.*, 29: 169-188.
- Faure, G.**, 1986. Principles of isotope geology. John Wiley & Sons, Inc., New York, 589 pp.
- Fleck, R.J.**, Sutter, J.F. and Elliot, D.H., 1977. Interpretation of discordant $^{40}\text{Ar}/^{39}\text{Ar}$ age-spectra of Mesozoic tholeiites from Antarctica. *Geochim. Cosmochim. Acta*, 41: 15-32.
- Foland, K.A.**, 1983. $^{40}\text{Ar}/^{39}\text{Ar}$ incremental heating plateaus for biotites with excess argon. *Chem. Geol.*, 41: 3-21.
- Foland, K.A.**, Gilbert, L.A., Sebring, C.A. and Jiang-Feng, C., 1986. $^{40}\text{Ar}/^{39}\text{Ar}$ ages for plutons of the Monteregian Hills, Quebec: Evidence for a single episode of Cretaceous magmatism. *Bulletin Geol. Soc. Am.*, 97: 966-974.
- Forte, A.M.** and Mitrovica, J.X., 1997. A resonance in the Earth's obliquity and precession over the past 20 Myr driven by mantle convection. *Nature*, 390: 676-680.
- Fortuin, A.R.** and Krijgsman, W., 2003. The Messinian of the Nijar basin (SE Spain): sedimentation, depositional environments and paleogeographic evolution. *Sediment. Geol.*, 160: 213-242.
- Fytikas, M.**, Innocenti, F., Manetti, P., Mazzuoli, R., Peccerillo, A. and Villari, L., 1984. Tertiary to Quaternary evolution of volcanism in the Aegean region. *Geol. Soc. Spec. Publ.*, 17: 687-699.
- Garcés, M.**, Krijgsman, W. and Agustí, J., 1998. Chronology of the late Turolian deposits of the Fortuna basin (SE Spain): implications for the Messinian evolution of the eastern Betics. *Earth Planet. Sci. Lett.*, 163(1-4): 69-81.
- Garner, E.L.**, Murphy, T.J., Gramlich, J.W., Paulsen, P.J. and Barnes, I.L., 1975. Absolute isotopic abundance ratios and the atomic weight of a reference sample of potassium. *J. Res. Natl. Bureau Stand.*, 79A: 713-725.
- Gaudant, J.**, Saint Martin, J.P., Benmoussa, A., Cornée, J.J., El Hajjaji, K. and Muller, J., 1994. L'ichthyofaune messienne à la périphérie de la plate-forme carbonatée de Melilla-Nador (Nord-Est du Maroc). *Géol. Méd.*, 21: 25-35.
- Gelati, R.**, Moratti, G. and Papani, G., 2000. The Late Cenozoic sedimentary succession of the Taza-Guercif Basin, South Rifian Corridor, Morocco. *Marine and Petroleum Geology*, 17: 373-390.
- Gilbert, G.**, 1895. Sedimentary measurement of Cretaceous time. *J. Geol.*, 3: 121-127.
- Gomez, F.**, Barazangi, M. and Demnati, A., 2000. Structure and evolution of the Neogene Guercif Basin at the junction of the Middle Atlas Mountains and the Rif thrust belt, Morocco. *AAPG Bulletin*, 84: 1340-1364.
- Guillemin, M.** and Houzay, J.P., 1982. Etudes géologiques sur la Chaîne du Rif; III, Le Neogene post-nappes et le Quaternaire du Rif nord-oriental; stratigraphie et tectonique des bassins de Mellila, du Kert, de Boudinar et du piedmont des Kbdana. *Notes Mém. Serv. Géol. Maroc*, 314: 7-238.
- Hahn, G.J.** and Saphiro, S.S., 1969. Statistical models in engineering. J. Wiley and Sons, 355 pp.
- Hall, C.M.** and Farrell, J.W., 1995. Laser $^{40}\text{Ar}/^{39}\text{Ar}$ ages of tephra from Indian Ocean deep-sea sediments: Tie points for the astronomical and geomagnetic polarity time scales. *Earth Planet. Sci. Lett.*, 133: 327-338.
- Hanchar, J.M.** and Miller, C.F., 1993. Zircon zonation patterns as revealed by cathodoluminescence and backscattered electron images; implications for interpretation of complex crustal histories. *Chem. Geol.*, 110: 1-13.
- Hays, J.D.**, Imbrie, J. and Shackleton, N.J., 1976. Variations in the Earth's orbit; pacemaker of the ice ages. *Science*, 194: 1121-1132.
- Hernandez, J.**, Bellon, H., 1985. Chronologie K-Ar du volcanisme miocène du Rif oriental (Maroc): implications tectoniques et magmatologiques. *Rev. Géol. Dynam. Géogr. Phys.*, 26: 85-98.
- Hilgen, F.J.**, 1991a. Extension of the astronomically calibrated (polarity) time scale to the Miocene/Pliocene boundary. *Earth Planet. Sci. Lett.*, 107(2): 349-368.
- Hilgen, F.J.**, 1991b. Astronomical calibration of Gauss to Matuyama sapropels in the Mediterranean and implication for the geomagnetic polarity time scale. *Earth Planet. Sci. Lett.*, 104: 226-244.
- Hilgen, F.J.**, Krijgsman, W., Langereis, C.G., Lourens, L.J., Santarelli, A. and Zachariasse, W.J., 1995. Extending the astronomical (polarity) time scale into the Miocene. *Earth Planet. Sci. Lett.*, 136: 495-510.
- Hilgen, F.J.**, Krijgsman, W. and Wijbrans, J.R., 1997. Direct comparison of astronomical and $^{40}\text{Ar}/^{39}\text{Ar}$ ages of ash beds: potential implications for the age of mineral dating standards. *Geophys. Res. Lett.*, 24: 2043-2046.
- Hilgen, F.J.** and Krijgsman, W., 1999. Cyclostratigraphy and astrochronology of the Tripoli diatomite formation (pre-

REFERENCES

- evaporite Messinian, Sicily, Italy). *Terra Nova*, 11: 16-22.
- Hilgen, F.J.**, Krijgsman, W., Raffi, I., Turco, E. and Zachariasse, W.J., 2000a. Integrated stratigraphy and astronomical calibration of the Serravallian/Tortonian boundary section at Monte Gibliscemi (Sicily, Italy). *Mar. Micropaleontol.*, 38: 181-211.
- Hilgen, F.J.**, Iaccarino, S., Krijgsman, W., Langereis, C.G., Villa G. and Zachariasse, W.J., 2000b. The Global Boundary Stratotype Section and Point (GSSP) of the Messinian Stage (uppermost Miocene). *Episodes*, 23: 172-178.
- Hilgen, F.J.**, Bissoli, L., Iaccarino, S., Krijgsman, W., Meijer, R., Negri, A. and Villa, G., 2000c. Integrated stratigraphy and astrochronology of the Messinian GSSP at Oued Akrech (Atlantic Morocco). *Earth Planet. Sci. Lett.*, 182: 237-251.
- Hilgen, F.J.**, Abdul Aziz, H., Krijgsman, W., Raffi, I. and Turco, E., 2003. Integrated stratigraphy and astronomical tuning of the Serravallian and lower Tortonian at Monte dei Corvi (Middle-Upper Miocene, northern Italy). *Palaeogeogr., Palaeoclim., Palaeoecol.*, 199: 229-264.
- Hodell, D.A.**, Benson, R.H., Kennett, J.P. and Rakic-El Bied, K., 1989. Stable isotope stratigraphy of latest Miocene sequences in northwest Morocco: The Bou Regreg section. *Paleoceanography*, 4: 467-482.
- Hodell, D.A.**, Benson, R., Kent, D., Boersma, A. and Rakic-El Bied, K., 1994. Magnetostratigraphic, biostratigraphic, and stable isotope stratigraphy of an upper Miocene drill core from Salé Briqueterie (Northwestern Morocco). A high resolution chronology for the Messinian stage. *Paleoceanography*, 9: 835-855.
- Hodell, D.A.**, Curtis, J., Sierro, F. and Raymo, M., 2001. Correlation of late Miocene to early Pliocene sequences between the Mediterranean and North Atlantic. *Paleoceanography*, 16: 164-178.
- Holden, N.E.**, 1990. Total half-lives for selected nuclides. *Pure and Applied Chemistry*, 62: 941-958.
- Holmes, A.**, 1911. The association of lead with uranium in rock minerals and its application to the measurement of geological time. *Proc. R. Soc. London*, 85A: 248-256.
- Hughes, S.S.**, 1989. The OSTR Cd-lined epithermal neutron activation facility CLICIT: N-flux gradient, operating temperature and experimental recommendations, Oregon State University TRIGA Reactor Operations Committee.
- Huneke, J.** and Smith, S., 1976. The realities of recoil; ^{39}Ar recoil out of small grains and anomalous age patterns in $^{40}\text{Ar}/^{39}\text{Ar}$ dating. In: R. Merrill, R. Morris, J. Rhodes and T. Usselman (Eds.), Proceedings of the Seventh lunar science conference; Volume 2, Petrogenetic studies of mare and highland rocks. pp. 1987-2008.
- Hurfurd, A.** and Hammerschmidt, K., 1985. $^{40}\text{Ar}/^{39}\text{Ar}$ and K/Ar dating of Bishop and Fish Canyon tuffs; calibration ages for fission-track-dating standards. *Chem. Geol.*, 58: 23-32.
- Imbrie, J.**, Hays, J., Martinson, D., McIntyre, A., Mix, A., Morley, J., Pisias, N., Prell, W. and Shackleton, N., 1984. The orbital theory of Pleistocene climate: support from a revised chronology of the marine $\delta^{18}\text{O}$ record. In: A. Berger et al. (Ed.), Milankovitch and Climate, pp. 269-305.
- Izett, G.** and Obradovich, J., 1994. $^{40}\text{Ar}/^{39}\text{Ar}$ age constraints for the Jaramillo Normal Subchron and Matuyama-Brunhes geomagnetic boundary. *J. Geophys. Res.*, 99: 2925-2934.
- Karner, D.B.** and Renne, P.R., 1998. $^{40}\text{Ar}/^{39}\text{Ar}$ geochronology of Roman volcanic province tephra in the Tiber River valley: Age calibration of middle Pleistocene sea-level changes. *Bulletin Geol. Soc. Am.*, 110: 740-747.
- Keller, J.**, Ryan, W.B.F., Ninkovich, D. and Altherr, R., 1978. Explosive volcanic activity in the Mediterranean over the past 200,000 yr as recorded in deep-sea sediments. *Bulletin Geol. Soc. Am.*, 89: 591-604.
- Kelley, S.**, 2002. Excess argon in K-Ar and Ar-Ar geochronology. *Chem. Geol.*, 188: 1-22.
- Kelvin, L.**, 1897. The age of the earth as an abode fitted for life. *Annual Report - Smithsonian Institution*: 337-357.
- Kloosterboer-Van Hoeve, M.**, 2000. Cyclic changes in the late Neogene vegetation of northern Greece: a palynological study. *Thesis*, Utrecht University, p131.
- Knesel, K.**, Davidson, J. and Duffield, W., 1999. Evolution of silicic magma through assimilation and subsequent recharge; evidence from Sr isotopes in sanidine phenocrysts, Taylor Creek Rhyolite, NM. *J. Petrol.*, 40: 773-786.
- Köppen, W.** and Wegener, A.L., 1924. Die Klimate der geologischen Vorzeit. Berlin, Gebr. Borntraeger, 255 pp.
- Kolios, N.**, Innocenti, F., Manetti, P., Peccerillo, A. and Giuliani, O., 1980. The Pliocene Volcanism of the Voras Mts. (Central Macedonia, Greece). *Bull. Volcanol.*, 43: 553-568.
- Koppers, A.A.P.**, 2002. ArArCALC-software for $^{40}\text{Ar}/^{39}\text{Ar}$ age calculations. *Computers & Geosciences*, 28: 605-619.
- Krijgsman, W.**, Hilgen, F., Langereis, C., Santarelli, A. and Zachariasse, W., 1995. Late Miocene magnetostratigraphy, biostratigraphy and cyclostratigraphy in the Mediterranean. *Earth Planet. Sci. Lett.*, 136: 475-494.
- Krijgsman, W.**, Hilgen, F., Negri, A., Wijbrans, J. and Zachariasse, W., 1997. The Monte del Casino section (Northern Apennines, Italy): a potential Tortonian/Messinian stratotype? *Palaeogeogr., Palaeoclim., Palaeoecol.*, 133: 27-47.
- Krijgsman, W.**, Hilgen, F., Raffi, I., Sierro, F. and Wilson, D., 1999a. Chronology, causes and progression of the Messinian salinity crisis. *Nature*, 400: 652-655.
- Krijgsman, W.**, Langereis, C., Zachariasse, W., Boccaletti, M., Moratti, G., Gelati, R., Iaccarino, S., Papani, G. and Villa,

REFERENCES

- G., 1999b. Late Neogene evolution of the Taza-Guercif Basin (Rifian Corridor, Morocco) and implications for the Messinian salinity crisis. *Mar. Geol.*, 153: 147-160.
- Krijgsman, W.**, Fortuin, A.R., Hilgen, F.J. and Sierro, F.J., 2001. Astrochronology for the Messinian Sorbas Basin (SE Spain) and orbital (precessional) forcing for evaporite cyclicity. *Sediment. Geol.*, 140: 43-60.
- Krijgsman, W.**, Blanc-Valleron, M., Flecker, R., Hilgen, F., Kouwenhoven, T., Merle, D., Orszag-Sperber, F. and Rouchy, J., 2002. The onset of the Messinian salinity crises in the Eastern Mediterranean (Pissouri Basin, Cyprus). *Earth Planet. Sci. Lett.*, 194: 299-310.
- Krogh, T.E.**, 1982. Improved accuracy of U-Pb zircon ages by the creation of more concordant systems using an air abrasion technique. *Geochim. Cosmochim. Acta*, 46: 637-649.
- Kunk, M.J.**, Sutter, J.F. and Naeser, C.W., 1985. High-precision $^{40}\text{Ar}/^{39}\text{Ar}$ ages of sanidine, biotite, hornblende, and plagioclase from the Fish Canyon Tuff, San Juan volcanic field, south-central Colorado. *Abstracts with Programs - Geol. Soc. Am.*, 17: 636.
- Kutzbach, J.E.**, 1981. Monsoon climate of the early Holocene; climate experiment with the Earth's orbital parameters for 9000 years ago. *Science*, 214: 59-61.
- LaBrecque, J.L.**, Kent, D.V. and Cande, S.C., 1977. Revised magnetic polarity time scale for late Cretaceous and Cenozoic time. *Geology*, 5: 330-335.
- Lanphere, M.A.**, Dalrymple, G.B., Fleck, R.J. and Pringle, M.S., 1990. Intercalibration of mineral standards for K-Ar and $^{40}\text{Ar}/^{39}\text{Ar}$ age measurements. *EOS Transactions*, 71: 1658.
- Lanphere, M.A.** and Dalrymple, G.B., 2000. First-principles calibration of ^{38}Ar tracers: implications for the ages of $^{40}\text{Ar}/^{39}\text{Ar}$ fluence monitors. *U.S.G.S. Prof. Paper*, 1621: 1-10.
- Lanphere, M.** and Baadsgaard, H., 2001. Precise K-Ar, $^{40}\text{Ar}/^{39}\text{Ar}$, Rb-Sr and U/Pb mineral ages from the 27.5 Ma Fish Canyon Tuff reference standard. *Chem. Geol.*, 175: 653-671.
- Laplace, S.P.**, 1799-1825. *Traité de mécanique céleste*. Mémoires or volumes of the Academy, 5 volumes.
- Laskar, J.**, 1988. Secular evolution of the solar system over 10 million years. *Astron. Astroph.*, 198: 341-362.
- Laskar, J.**, 1989. A numerical experiment on the chaotic behaviour of the Solar System. *Nature*, 338: 237-238.
- Laskar, J.**, 1990. The chaotic motion of the solar system: a numerical estimate of the size of the chaotic zones. *Icarus*, 88: 226-291.
- Laskar, J.**, Quinn, T. and Tremaine, S., 1992. Confirmation of resonant structure in solar system. *Icarus*, 95: 148-152.
- Laskar, J.**, Joutel, F. and Boudin, F., 1993a. Orbital, precessional, and insolation quantities for the Earth from -20Myr to +10Myr. *Astron. Astroph.*, 270: 522-533.
- Laskar, J.**, Joutel, F. and Robutel, P., 1993b. Stabilization of the Earth's obliquity by the Moon. *Nature*, 361: 615-617.
- Laskar, J.**, 1999. The limits of Earth orbital calculations for geological time-scale use. *Philos. Trans. R. Soc. Math., Phys. and Engin. Sci.*, 357: 1735-1759.
- Laskar, J.**, Robutel, P., Joutel, F., Gastineau, M., Correia, A. and Levrard, B., 2003. A numerical solution for the insolation quantities for the Earth from -100 Ma to +50 Ma. Manuscript in preparation.
- Laurenzi, M.A.**, Tateo, F., Villa, I.M. and Vai, G.B., 1997. New radiometric datings bracketing the Tortonian/Messinian boundary in the Romagna potential stratotype sections (Northern Apennines, Italy). In: A. Montanari, G.S. Odin and R. Coccioni (Editors), *Miocene Stratigraphy: an integrated approach*, pp. 493-520.
- Le Verrier, U.J.J.**, 1856. *Recherches astronomiques*. Ann. Observ. Imp. Paris, II.
- Levrard, B.**, and Laskar, J., 2003. Climate friction and the Earth's obliquity. *Geoph. J. Intern.*, submitted.
- Lelieveldt, S.**, 1995. Determination of Ca- and K-correction factors for $^{40}\text{Ar}/^{39}\text{Ar}$ dating for OSU TRIGA and ECN Petten reactors. *Internal report*, Department of Petrology and Isotope Geology, Vrije Universiteit, Amsterdam.
- Lipman, P.**, Steven, T. and Mehnert, H., 1970. Volcanic history of the San Juan mountains, Co., as indicated by potassium-argon dating. *Bulletin Geol. Soc. Am.*, 81: 2329-2351.
- Lourens, L.J.**, Antonarakou, A., Hilgen, F.J., Van Hoof, A.A.M., Vergnaud-Grazzini, C. and Zachariasse, W.J., 1996. Evaluation of the Plio-Pleistocene astronomical timescale. *Paleoceanography*, 11: 391-413.
- Lourens, L.J.**, Wehausen, R., Brumsack, H.J., 2001. Geological constraints on tidal dissipation and dynamical ellipticity of the Earth over the past three million years. *Nature*, 409: 1029-1033.
- Lourens, L.J.**, Hilgen, F.J., Laskar, J., Shackleton, N.J., and Wilson, D., 2004. The Neogene Period. In: *A Geological Timescale 2004*, edited by Felix Gradstein, Jim Ogg and Alan Smith, submitted
- Mansour, B.** and Saint-Martin, J.-P., 1999. Conditions de dépôt des diatomites messiniennes en contexte de plateforme carbonatée d'après l'étude des assemblages de diatomées: exemple du Djebel Murdjadjo (Algérie). *Geobios*, 32: 395-408.
- Marakis, G.** and Sideris, C., 1973. Petrology of the Edessa Area Volcanic Rocks, Western Macedonia, Greece. *Bull. Volcanol.*, 36: 462-472.
- Martin, J.M.** and Braga, J.C., 1994. Messinian events in the Sorbas Basin in southeastern Spain and their implications in

REFERENCES

- the Recent history of the Mediterranean. *Sediment. Geol.*, 90(3-4): 257-268.
- McDougall, I.** and Roksandic, Z., 1974. Total fusion $^{40}\text{Ar}/^{39}\text{Ar}$ age using HIFAR reactor. *J. Geol. Soc. Austr.*, 21: 81-89.
- McDougall, I.** and Harrison, M.T., 1999. Geochronology and thermochronology by the $^{40}\text{Ar}/^{39}\text{Ar}$ method. Oxford University Press, Inc., 269 pp.
- McIntosh, W.C.**, Sutter, J.F., Chapin, C.E. and Kedzie, L.L., 1990. High-precision $^{40}\text{Ar}/^{39}\text{Ar}$ sanidine geochronology of ignimbrites in the Mogollon-Datil volcanic field, southwestern New Mexico. *Bull. Volcanol.*, 52: 584-601.
- Merrihue, C.** and Turner, G., 1966. Potassium-argon dating by activation with fast neutrons. *J. Geophys. Res.*, 71: 2852-2857.
- Meulenkamp, J.E.** and Hilgen, F., 1986. Event stratigraphy, basin evolution and tectonics of the Hellenic and Calabro-Sicilian arcs. In: F. Wezel (Ed.), *Origin of arcs*, pp. 327-350.
- Meulenkamp, J.E.**, Wortel, M.J.R., van, W.W.A., Spakman, W. and Hoogerduyn, S.E., 1988. On the Hellenic subduction zone and the geodynamic evolution of Crete since the late middle Miocene. *Tectonophysics*, 146: 203-215.
- Min, K.**, Mundil, R., Renne, P. and Ludwig, K., 2000. A test for systematic errors in $^{40}\text{Ar}/^{39}\text{Ar}$ geochronology through comparison with U/Pb analysis of a 1.1-Ga rhyolite. *Geochim. Cosmochim. Acta*, 64: 73-98.
- Montanari, A.**, Carey, S., Coccioni, R. and Deino, A., 1994. Early Miocene tephra in the Apennine pelagic sequence; an inferred Sardinian provenance and implications for western Mediterranean tectonics. *Tectonics*, 13: 1120-1134.
- Montanari, A.**, Beaudoin, B., Chan, L., Coccioni, R., Deino, A., DePaolo, D., Emmanuel, L., Fornaciari, E., Kruge, M., Lundblad, S., Mozzato, C., Portier, E., Renard, M., Rio, D., Sandroni, P. and Stankiewicz, A., 1997. Integrated stratigraphy of the Middle to Upper Miocene pelagic sequence of the Cònero Riviera (Marche region, Italy). In: A. Montanari, G. Odin and R. Coccioni (Eds.), *Miocene Stratigraphy: an integrated approach*, pp. 409-450.
- Münch, P.**, Roger, S., Cornée, J., Saint Martin, J., Féraud, G. and Ben Moussa, A., 2001. Restriction des communications entre l'Atlantique et la Méditerranée au Messinien: apport de la téphrochronologie dans la plate-forme carbonatée et le bassin de Melilla-Nador (Rif nord-oriental, Maroc). *C. R. Acad. Sci.*, 332: 569-576.
- Näser, C.W.**, Zimmerman, R.A. and Cebula, G.T., 1981. Fission-track dating of apatite and zircon: an interlaboratory comparison. *Nuclear Tracks*, 5: 65-72.
- Néron de Surgy, O.** and Laskar, J., 1996. On the long term evolution of the spin of the Earth. *Astron. Astrophys.*, 318: 975-989.
- Newton, I.**, 1687. Principia.
- Nier, A.**, 1950. A redetermination of the relative abundances of the isotopes of carbon, nitrogen, oxygen, argon, and potassium. *Phys. Rev.*, 77: 789-793.
- Oberli, F.**, Fischer, H. and Meier, M., 1990. High resolution ^{238}U - ^{206}Pb zircon dating of tertiary bentonites and Fish Canyon Tuff: a test for age "concordance" by single crystal analysis, Abstracts - Geol. Soc. Austr., 27: 74.
- Oberli, F.**, Bachmann, O., Meier, M. and Dungan, M., 2002. The Fish Canyon Tuff: Ar-Ar versus U-Pb age discrepancy reassessed. Goldschmidt, Davos, A565.
- Odin, G.S.**, Montanari, A., Deino, A., Drake, R., Guise, P., Kreuzer, H. and Rex, D., 1991. Reliability of volcano-sedimentary biotite ages across the Eocene-Oligocene boundary (Apennines, Italy). *Chem. Geol.*, 86: 203-224.
- Odin, G.S.**, Takahashi, M. and Cosca, M., $^{40}\text{Ar}/^{39}\text{Ar}$ geochronology of Middle Miocene calcareous nannofossil biohorizons in Central Japan, *Chem. Geol.* 171, 239-252, 2001.
- Pälike, H.**, Shackleton, N. and Roehl, U., 2001. Astronomical forcing in late Eocene marine sediments. *Earth Planet. Sci. Lett.*, 193(3-4): 589-602.
- Parrish, R.R.**, Roddick, J., Loveridge, W. and Sullivan, R., 1987. Uranium-lead analytical techniques at the geochronology laboratory, Geol. Surv. Can. Radiogenic age and isotopic studies; 1, *Geol. Surv. Can.*, 87-2: 3-7.
- Parrish, R.**, 1987. An improved micro-capsule for zircon dissolution in U-Pb geochronology, in: New developments and applications in isotope geoscience. *Chem. Geol.*, 66: 99-102.
- Pavlidis, S.B.** and Mountrakis, D.M., 1987. Extensional tectonics of northwestern Macedonia, Greece, since the late Miocene. *J. Struct. Geol.*, 9: 385-392.
- Penck, A.** and Brückner, E., 1909. Die Alpen im Eiszeitalter. Tauchnitz, Leipzig.
- Pestrea, S.**, Al Hajjaji, K. and Ben-Moussa, A., 1997. Diatomites du Messinien d'Afrique du Nord (Algérie, Maroc): Principeaux enseignements. *Cryptogam Algol*, 20: 109-110.
- Pisias, N.G.** and Moore, T.C., Jr., 1981. The evolution of Pleistocene climate; a time series approach. *Earth Planet. Sci. Lett.*, 52: 450-458.
- Poincaré**, 1890. Sur les problème des trois corps et les équations de la dynamique, *Acta Mathematica*, Oeuvres, tome VII, pages 262-479.
- Pointer, C.M.**, Ashworth, J.R. and Ixer, R.A., 1988. The zircon-thorite mineral group in metasomatized granite, Ririwai, Nigeria 2. Zoning, alteration and exsolution in zircon. *Mineralogy and petrology*, 39: 21-37.
- Prell, W.L.** and Kutzbach, J., 1987. Monsoon variability over the past 150,000 years. *J. Geophys. Res.*, 92: 8411-8425.
- Quinn, T.**, Tremaine, S. and Duncan, M., 1991. A three

REFERENCES

- million year integration of the Earth's orbit. *Astr. J.*, 100(6): 2287-2305.
- Rachid, A.**, El Hajjaji, K. and Ben Moussa, A., 1997. Les associations de foraminifères benthiques des séries marnodiatomitiques messiniennes du bassin de Nador-Melilla (Maroc nord oriental). *Géol. Méd.*, XXIV: 29-49.
- Ratté, J.C.**, Marvin, R.F. and Naeser, C.W., 1984. Calderas and ash flow tuffs of the Mogollon Mountains, southwestern New Mexico. *J. Geophys. Res.*, 89: 8713-8732.
- Raymo, M.E.**, Ruddiman, W.F., Backman, J., Clement, B.M. and Martinson, D.G., 1989. Late Pliocene variation in Northern Hemisphere ice sheets and North Atlantic Deep Water circulation. *Paleoceanography*, 4: 413-446.
- Renne, P.**, Walter, R., Verosub, K., Sweitzer, M. and Aronson, J., 1993. New data from hadar (ethiopia) support orbitally tuned time scale to 3.3 Ma. *Geophys. Res. Lett.*, 20: 1067-1070.
- Renne, P.R.**, Deino, A.L., Walter, R.C., Turrin, B.D., Swisher, C.C., Becker, T.A., Curtis, G.H., Sharp, W.D. and Jaouni, A.-R., 1994. Intercalibration of astronomical and radioisotopic time. *Geology*, 22: 783-786.
- Renne, P.R.**, Sharp, W., Deino, A.L., Orsi, G. and Civetta, L., 1997. $^{40}\text{Ar}/^{39}\text{Ar}$ dating into the historical realm: calibration against Pliny the Younger. *Science*, 277: 1279-1280.
- Renne, P.R.**, Swisher, C.C., Deino, A.L., Karner, D.B., Owens, T.L. and DePaolo, D.J., 1998. Intercalibration of standards, absolute ages and uncertainties in $^{40}\text{Ar}/^{39}\text{Ar}$ dating. *Chem. Geol.*, 145: 117-152.
- Renne, P.R.** and Min, K., 1998. $^{40}\text{Ar}/^{39}\text{Ar}$ dating of the 79 AD of Vesuvius: An ab initio basis for improved accuracy in $^{40}\text{Ar}/^{39}\text{Ar}$ geochronology, Goldschmidt Conference. *Mineral. Mag.*, pp. 1255-1256.
- Roddick, J.C.**, 1987. Generalized numerical error analysis with applications to geochronology and thermodynamics. *Geochim. Cosmochim. Acta*, 51: 2129-2135.
- Roddick, J.C.**, Loveridge, W.D. and Parrish, R.R., 1987. Precise U/Pb dating of zircon at the sub-nanogram Pb level. *Chem. Geol.*, 66: 111-121.
- Roger, S.**, Münch, P., Cornée, J.J., Saint Martin, J.P., Féraud, G., Pestrea, S., Conesa, G. and Ben Moussa, A., 2000. $^{40}\text{Ar}/^{39}\text{Ar}$ dating of the pre-evaporitic Messinian Marine sequences of the Melilla basin (Morocco): A proposal for some bio-sedimentary events as isochrons around the Alboran sea. *Earth Planet. Sci. Lett.*, 179: 101-113.
- Rossignol-Strick, M.**, Nesteroff, W., Olive, P. and Vergnaud, G.C., 1982. After the deluge; Mediterranean stagnation and sapropel formation. *Nature*, 295: 105-110.
- Rossignol-Strick, M.**, 1985. Mediterranean Quaternary sapropels, and immediate response of the African monsoon to variation of insolation. *Palaeogeogr., Palaeoclim., Palaeoecol.*, 49: 237-263.
- Rossignol-Strick, M.**, 1987. Rainy periods and bottom water stagnation initiating brine accumulation and metal concentrations; 1, The late Quaternary. *Paleoceanography*, 2: 333-360.
- Rubin, J.N.**, Henry, C. and Price, J., 1989. Hydrothermal zircons and zircon overgrowths, Sierra Blanca Peaks, Texas. *Am. Mineralogist*, 74: 865-869.
- Ruddiman, W.**, Raymo, M., Martinson, D., Clement, B. and Backman, J., 1989. Pleistocene evolution; Northern Hemisphere ice sheets and North Atlantic Ocean. *Paleoceanography*, 4: 353-412.
- Saint Martin, J.P.** and Rouchy, J.M., 1986. Intérêt du complexe récifal du Cap des Trois Fourches (Bassin de Nador, Maroc septentrional) pour l'interprétation paléogéographique des événements messiniens en Méditerranée occidentale. *C. R. Acad. Sci.*, 302: 957-962.
- Saint Martin, J.P.**, Cornée, J., Muller, J., Camoin, G., André, J., Rouchy, J. and Ben-Moussa, A., 1991. Contrôles globaux et locaux dans l'édification d'une plateforme carbonatée messinienne (Bassin de Melilla, Maroc); apport de la stratigraphie séquentielle et de l'analyse tectonique. *C. R. Acad. Sci.*, 312: 1573-1579.
- Saint Martin, J.-P.** and Cornée, J.-J., 1996. The Messinian reef complex of Melilla, Northeastern Rif, Morocco. *In: Concepts in Sedimentology and Paleontology Series*, 5: 227-237.
- Sani, F.**, Zizi, M. and Bally, A., 2000. The Neogene-Quaternary evolution of the Guercif Basin (Morocco) reconstructed from seismic line interpretation. *Marine and Petroleum Geology*, 17: 343-357.
- Sanz de Galdeano, C.** and Vera, J., 1992. Stratigraphic record and palaeogeographical context of the Neogene basins in the Betic Cordillera, Spain. *Basin Research*, 4: 21-36.
- Scaillet, S.**, 2000. Numerical error analysis in $^{40}\text{Ar}/^{39}\text{Ar}$ dating. *Chem. Geol.*, 162: 269-298.
- Schärer, U.**, 1984. The effect of initial ^{230}Th disequilibrium on young U-Pb ages; the Makalu case, Himalaya. *Earth Planet. Sci. Lett.*, 67: 191-204.
- Schenau, S.**, Antonarakou, A., Hilgen, F., Lourens, L., Nijenhuis, I., Van der Weijden, C. and Zachariasse, W., 1999. Organic-rich layers in the Metochia section (Gavdos, Greece); evidence for a single mechanism of sapropel formation during the past 10 My. *Marine Geology*, 153: 117-135.
- Schmitz, M.** and Bowring, S., 2001. U-Pb zircon and titanite systematics of the Fish Canyon Tuff; an assessment of high-precision U-Pb geochronology and its application to young volcanic rocks. *Geochim. Cosmochim. Acta*, 65: 2571-2587.
- Schmitz, M.**, Bowring, S., Ludwig, K. and Renne, P., 2003.

REFERENCES

- Comment on "Precise K-Ar, ^{40}Ar - ^{39}Ar , Rb-Sr and U-Pb mineral ages from the 27.5 Ma Fish Canyon Tuff reference standard" by M. Lanphere, H. Baadsgaard. *Chem. Geol.*, 199: 277-280.
- Shackleton, N.J.**, Berger, A. and Peltier, W.A., 1990. An alternative astronomical calibration of the lower Pleistocene timescale based on ODP Site 677. *Trans. R. Soc. Edinburgh: Earth Sciences*, 81: 251-261.
- Shackleton, N.J.**, Crowhurst, S., Hagelberg, T., Pisias, N.G. and Schneider, D.A., 1995. A new late Neogene time scale: application to leg 138 sites. *Proc. ODP, Scientific Results*, 138: 73-101.
- Shackleton, N.J.**, Crowhurst, S.J., Weedon, G.P. and Laskar, J., 1999. Astronomical calibration of Oligocene-Miocene time. *Philos. Trans. R. Soc. Math. Phys. Engin. Sci.*, 357: 1907-1929.
- Shackleton, N.J.**, Hall, M.A., Vincent, E., 2000. Phase relationships between millennial-scale events 64,000-24,000 years ago. *Paleoceanography*, 15: 565-569.
- Sierro, F.**, Flores, J., Zamarrano, I., Vázquez, A., Utrilla, R., Francés, G., Hilgen, F. and Krijgsman, W., 1999. Messinian pre-evaporite sapropels and precession-induced oscillations in western Mediterranean climate. *Mar. Geol.*, 153: 137-146.
- Sierro, F.**, Ledesma, S., Flores, J., Torrecusa, S. and del Martinez, O., 2000. Sonic and gamma-ray astrochronology; cycle to cycle calibration of Atlantic climatic records to Mediterranean sapropels and astronomical oscillations. *Geology*, 28: 695-698.
- Sierro, F.J.**, Hilgen, F.J., Krijgsman, W., Flores, J.A., 2001. The Abad composite (SE Spain): a Messinian reference section for the Mediterranean and the APTS. *Palaeogeogr., Palaeoclim., Palaeoecol.*, 168: 141-169.
- Sierro, F.J.**, Flores, J.A., Frances, G., Vazquez, A., Utrilla, R., Zamarrano, I., Erlenkeuser, H. and Barcena, M.A., 2003. Orbitally-controlled oscillations in planktic communities and cyclic changes in western Mediterranean hydrography during the Messinian. *Palaeogeogr., Palaeoclim., Palaeoecol.*, 190: 289-316.
- Singer, B.S.** and Pringle, M., 1996. Age and duration of the Matuyama-Brunhes geomagnetic polarity reversal from $^{40}\text{Ar}/^{39}\text{Ar}$ incremental heating analyses of lavas. *Earth Planet. Sci. Lett.*, 139: 47-61.
- Singer, B.S.**, Hoffman, K.A., Chauvin, A., Coe, R.S. and Pringle, M.S., 1999. Dating transitionally magnetized lavas of the late Matuyama Chron: Toward a new $^{40}\text{Ar}/^{39}\text{Ar}$ timescale of reversals and events. *J. Geophys. Res.*, 104: 679-693.
- Sparks, R.**, Bursik, M., Ablay, G., Thomas, R. and Carey, S., 1992. Sedimentation of tephra by volcanic plumes. Part 2: controls on thickness and grain-size variations of tephra fall deposits. *Bull. Volcanol.*, 54: 685-695.
- Speer, J.A.**, 1980. Zircon. In: P. Ribbe (Ed.), *Orthosilicates*. Reviews in Mineralogy. Mineral. Soc. Am., Washington, DC, United States, pp. 67-112.
- Spell, T.L.** and McDougall, I., 1992. Revisions to the age of Brunhes-Matuyama boundary and the Pleistocene geomagnetic polarity timescale. *Geophys. Res. Lett.*, 19: 1181-1184.
- Spell, T.L.** and McDougall, I., 2003. Characterization and calibration of $^{40}\text{Ar}/^{39}\text{Ar}$ dating standards. *Chem. Geol.*, 198: 189-211.
- Stacey, J.S.** and Kramers, J.D., 1975. Approximation of terrestrial lead isotope evolution by a two-stage model. *Earth Planet. Sci. Lett.*, 26: 207-221.
- Steenbrink, J.**, Van Vugt, N., Hilgen, F.J., Wijbrans, J.R. and Meulenkamp, J.E., 1999. Sedimentary cycles and volcanic ash beds in the Lower Pliocene lacustrine succession of Ptolemais (NW Greece): discrepancy between $^{40}\text{Ar}/^{39}\text{Ar}$ and astronomical ages. *Palaeogeogr., Palaeoclim., Palaeoecol.*, 152: 283-303.
- Steiger, R.** and Jäger, E., 1977. Subcommission on geochemistry: convention on the use of decay constants in geo- and cosmochronology. *Earth Planet. Sci. Lett.*, 36: 359-362.
- Stern, R.A.**, 1997. The GSC sensitive high resolution ion microprobe (SHRIMP): analytical techniques of zircon U-Th-Pb age determinations and performance evaluation. Radiogenic age and isotopic studies; 10, *Geol. Surv. Can.*: 1-31.
- Stern, R.A.**, 2001. A new isotopic and trace-element standard for the ion microprobe: preliminary thermal ionization mass spectrometry (TIMS) U-PB and electron-microprobe data. Radiogenic age and isotopic studies; 14; *Geol. Surv. Can.*, Current Research, p10.
- Stern, R.A.** and Amelin, Y., 2003. Assessment of errors in SIMS zircon U-Pb geochronology using a natural zircon standard and NIST SRM 610 glass. *Chem. Geol.*, 197: 111-142.
- Steven, T.A.**, Mehnert, H.H. and Obradovich, J.D., 1967. Age of volcanic activity in the San Juan Mountains, Colorado, Geological Survey research 1967, Chap. D., *U.S.G.S. Prof. Paper*, Reston, pp. D47-D55.
- Stimac, J.A.** and Wark, D.A., 1992. Plagioclase mantles on sanidine in silicic lavas, Clear Lake, California; implications for the origin of rapakivi texture. *Bulletin Geol. Soc. Am.*, 104: 728-744.
- Sussman, G.J.** and Wisdom, J., 1988. Numerical evidence that the motion of Pluto is chaotic. *Science*, 241: 433-437.
- Tauxe, L.**, Deino, A.D., Behrensmeier, A.K. and Potts, R., 1992. Pinning down the Brunhes/Matuyama and upper Jaramillo boundaries: a reconciliation of orbital and isotopic time scales. *Earth Planet. Sci. Lett.*, 109: 561-572.
- Taylor, J.R.**, 1997. An introduction to error analysis, the study of uncertainties in physical measurements. University

REFERENCES

Science Books, 327 pp.

- Torres-Roldan, R.L.**, Poli, G. and Peccerillo, A., 1986. An early Miocene arc-tholeiitic magmatic dike event from the Alboran Sea; evidence for precollisional subduction and back-arc crustal extension in the westernmost Mediterranean. *Geologische Rundschau*, 75: 219-234.
- Troelstra, S.R.**, Van de Poel, H.M., Huisman, C.H.A., Geerlings, L.P.A. and Dronkert, H., 1980. Paleocological changes in the latest Miocene of the Sorbas Basin, SE Spain. *Geol. Medit.*, 7: 115-126.
- Tuenter, E.**, Weber, S.L., Hilgen, F.J. and Lourens, L.J., 2003. The response of the African summer monsoon to remote and local forcing due to precession and obliquity. *Global and Planetary Change*, 36: 219-235.
- Turner, G.**, 1971. Argon 40 - argon 39 dating: the optimization of irradiation parameters. *Earth Planet. Sci. Lett.*, 10: 227-234.
- Turrin, B.D.**, Donnelly-Nolan, J.M. and Carter Hearn Jr, B., 1994. $^{40}\text{Ar}/^{39}\text{Ar}$ ages from the rhyolite of Alder Creek, California: Age of Cobb Mountain Normal-Polairty Subchron revisited. *Geology*, 22: 251-254.
- Van Assen, E.**, Kuiper, K.F., Krijgsman, W., Sierro, F.J. and Barhoun, N., Messinian astrochronology of the Melilla Basin: stepwise restriction of the Mediterranean-Atlantic connection through Morocco. *Palaeogeogr., Palaeoclim., Palaeoecol.*, in press.
- Van den Bogaard, P.**, 1995. $^{40}\text{Ar}/^{39}\text{Ar}$ ages of sanidine phenocrysts from Laacher See Tephra (12,900 yr BP): Chronostratigraphic and petrological significance. *Earth Planet. Sci. Lett.*, 133: 163-174.
- Van Hoof, A.A.M.** and Langereis, C.G., 1992. The upper and lower Thvera sedimentary geomagnetic reversal records from southern Sicily. *Earth Planet. Sci. Lett.*, 114: 59-75.
- Van Hoof, A.A.M.**, Van Os, B.J.H., Rademakers, J.G., Langereis, C.G. and de, L.G.J., 1993. A paleomagnetic and geochemical record of the upper Cochiti reversal and two subsequent precessional cycles from southern Sicily (Italy). *Earth Planet. Sci. Lett.*, 117: 235-250.
- Van Vugt, N.**, Steenbrink, J., Langereis, C., Hilgen, F. and Meulenkamp, J., 1998. Magnetostratigraphy-based astronomical tuning of the early Pliocene lacustrine sediments of Ptolemais (NW Greece) and bed-to-bed correlation with the marine record. *Earth Planet. Sci. Lett.*, 164: 535-551.
- Villeneuve, M.**, Sandeman, H.A. and Davis, W.J., 2000. A method for intercalibration of U-Th-Pb and $^{40}\text{Ar}/^{39}\text{Ar}$ in the Phanerozoic. *Geochim. Cosmochim. Acta*, 64: 4017-4030.
- Walker, G.**, 1971. Grain-size characteristics of pyroclastic deposits. *Journal of Geology*, 79: 696-714.
- Watkins, N.**, Sparks, R., Sigurdsson, H., Huang, T., Feder-
man, A., Carey, S. and Ninkovich, D., 1978. Volume and extent of the Minoan tephra from Santorini Volcano: new evidence from deep-sea sediment cores. *Nature*, 271: 122-126.
- Wendt, I.** and Carl, C., 1991. The statistical distribution of the mean squared weighted deviation. *Chem. Geol.*, 86: 275-285.
- Whitney, J.** and Stormer, J., 1985. Mineralogy, petrology, and magmatic conditions from the Fish Canyon Tuff, central San Juan volcanic field, Colorado. *J. Petr.*, 26: 726-762.
- Wijbrans, J.R.** and McDougall, I., 1987. On the metamorphic history of an Archaean granitoid greenstone terrane, East Pilbara, Western Australia, using the $^{40}\text{Ar}/^{39}\text{Ar}$ age spectrum technique. *Earth Planet. Sci. Lett.*, 84: 226-242.
- Wijbrans, J.R.**, Pringle, M.S., Koppers, A.A.P. and Scheveers, R., 1995. Argon geochronology of small samples using the Vulkan argon laserprobe. *Proc. Kon. Ned. Akad. v, Wetensch.*, 98: 185-218.
- Williams, D.**, Kasting, J. and Frakes, L., 1998. Low-latitude glaciation and rapid changes in the Earth's obliquity explained by obliquity-oblateness feedback. *Nature*, 396: 453-455.
- Wilson, D.S.**, 1993. Confirmation of the astronomical calibration of the magnetic polarity timescale from sea-floor spreading rates. *Nature*, 364: 788-790.
- WoldeGabriel, G.**, White, T.D., Suwa, G., Renne, P., de Heinzelin, J., Hart, W.K. and Heiken, G., 1994. Ecological and temporal placement of early Pliocene hominids at Aramis, Ethiopia. *Nature*, 371: 330-333.
- York, D.**, 1969. Least squares fitting of a straight line with correlated errors. *Earth Planet. Sci. Lett.*, 5: 320-324.

ACKNOWLEDGEMENTS / DANKWOORD

Allereerst wil ik Frits Hilgen en Jan Wijbrans bedanken voor het het schrijven van het onderzoeksvoorstel dat uiteindelijk geresulteerd heeft in dit proefschrift. De techniek en achtergronden van $^{40}\text{Ar}/^{39}\text{Ar}$ dateringen heeft Jan mij bijgebracht. Gedurende de vele (nachtelijke) meeturen heb ik Jan (en ook zijn familie) altijd lastig mogen vallen met vragen en telefoontjes over "wat en hoe in het argon lab". Frits heeft me tijdens de diverse veldwerken de toepassing van de astronomische dateringstechniek geleerd. Zijn kennis en enthousiasme over cyclostratigrafie in het algemeen, maar ook over dit onderzoek in combinatie met de extreem korte tijd waarin ik zijn (nuttige) commentaar op de verschillende versies van de hoofdstukken terug kreeg, maakten de tot standkoming van dit proefschrift aanzienlijk makkelijker. Mijn promotoren Johan Meulenkamp en Paul Andriessen ben ik zeer erkentelijk voor alle vrijheid die ze mij gegeven hebben.

The members of the reading committee Dick Kroon, Cor Langereis, Paul Renne, Mike Villeneuve and Bert van der Zwaan are acknowledged for their useful contributions and comments on the manuscript. Paul R. (Berkeley Geochronology Center) is especially thanked for sharing his expertise in the field in Morocco as is Al Deino from the same institute during fieldworks in Greece and Morocco. On the last day of the Moroccan fieldwork we finally discovered a(n) (obscure) place where they sold beer! Further, I greatly appreciated the hospitality and expertise of Mike V. during my stay at the Geological Survey in Ottawa, Canada and in spite of the boring work of picking all those zircons I learned a lot about U/Pb dating techniques. It was fun to join the celebrations of the 2002 Olympic gold medals for both Canadian (ice-)hockey teams (too bad for the Americans...). Thanks also to the other staff, post-docs and PhD's at GSC for all their help and support. Cor wil ik tevens bedanken voor de mogelijkheid die hij mij heeft geboden om mijn proefschrift te kunnen schrijven in de schitterende en rustige omgeving van het Fort: ideaal voor het schrijven van een proefschrift. Verder wil ik graag Wout Krijgsman bedanken voor het opstarten van het onderzoek en veldwerk in Marokko (samen met Paco Sierro), waar voor dit onderzoek zeer belangrijke secties gedateerd zijn, maar ook voor de stimulans om resultaten op te schrijven en te publiceren.

Het laboratoriumwerk van mijn onderzoek heb ik uitgevoerd aan de Vrije Universiteit. Dit werk was nooit tot een goede einde gekomen zonder de ondersteuning van het technische personeel. Dank ben ik verschuldigd aan Roel en Lodewijk voor al hun hulp en advies bij de scheiding van de mineralen. Vooral Roel heeft zijn best gedaan om het pikken van mineralen zo aangenaam en comfortabel mogelijk te maken. Onno stond (en staat) bij elk probleem aan de argon laser probe meteen klaar om te helpen, wat regelmatig leek te gebeuren als Jan ver weg in Australië zat. Ditzelfde geldt ook voor Wim die soms de meest mysterieuze problemen kon oplossen door het schoonmaken en controleren van de talloze contacten in massaspectrometer en klepsturing. Nico (en Wim) ben ik zeer erkentelijk voor de ontwikkeling van de programmatuur voor het automatisch meten, waardoor mijn laatste meetserie zeer vlotjes verliep. In the first years of my PhD Lawrence was always willing to help, if Jan was not around. Thanks! Mijn "buren" Coos en Richard wil ik bedanken voor de hulp die zij hebben geboden bij het leachen van de mineralen.

Verder wil ik alle VU-ers uit heden en verleden bedanken voor de gezellige tijd: Arnd, Barbara (I liked our collaboration in the lab and the good appointments we could make about schedules, air measurements, etc...), Bart, Bert, Bin, Catherine, Eduardo (biertje?), Fenny, Gareth, Glen (thanks for turning on the

automatic runs of my last batch of measurements, it saved me a lot of time), Huaning, Igor, Joaquim, John O'C., John K., Jurgen, Karen B., Karen de B., Lieselotte, Linda, Margo (bedankt voor de lunches in Zeist), Marim, Marlies, Melanie, Nina, Pieter van H., Pieter V., Thijs, Tineke, Tibor, Valentina and Yvette (even lekker bijkleppen). Met Govert Koetsier deelde ik de eerste twee jaar van mijn onderzoek met veel plezier mijn kamer.

De Utrechtse component in het onderzoek bestond vooral uit veldwerk, later gevolgd door de "schrijffase". Ik heb genoten van de verschillende veldwerken met Elena, Esther, Frits, Hayfaa, Jan W. Joris, Nadia Barhoun, Paco Sierro, Rink en Wout. Verder wil ik alle collega's op het Fort bedanken: Cor, Cristine, Fatima, Esther, Geert, Guillaume, Hans, Hayfaa (bedankt voor alle praktische info over proefschriften, promoties, etc.), Hiro, Iuliana, Mark, Piet-Jan, Tanja Z, Tom, Wanda en Willy en van Strat/Pal: Erik, Erwin, Hemmo, Luc (bedankt voor het commentaar op hoofdstuk 2), Marjolein, Rink en Tanja K. De AV-dienst (Paul, Fred en Jaco) heeft mij allerlei hulp geboden bij het opmaken van het proefschrift. Bedankt!

Buiten het werk waren er natuurlijk mijn familie en vrienden. Hoewel je familie niet voor het uitkiezen hebt, heb ik het met jullie goed getroffen: Papa, mama, Melanie en Falentijn, bedankt! Mijn paranympfen Claudia (theetjes, treinen, effe zeuren...) en Babs (katten, Casa, ons "mooie" Overvecht...) ook jullie bedankt voor jullie steun. En Martijn zonder jou was dit proefschrift misschien wel gelukt, maar was het leven heel wat minder leuk geweest.

CURRICULUM VITAE

Klaudia Finette Kuiper werd geboren op 29 april 1974 te Steenwijkerwold. Hier volgde zij de lagere school. In 1986 ging zij naar de RSG Jan Hendrik Tromp Meesters te Steenwijk, waar zij in 1992 haar Gymnasium B diploma behaalde. In datzelfde jaar ging zij Geologie studeren aan de Universiteit Utrecht. In 1993 behaalde zij haar propaedeuse en begon aan de bovenbouw studie Geochemie. Zij liep stage bij het NITG-TNO en werkte aan een onderzoek naar (de)nitrificatie processen in bodems onder leiding van Dr. J. Griffioen. In 1997 studeerde zij af in de richting exogene geochemie. Haar afstudeeronderzoek onder leiding van Dr. S.P. Vriend bestond uit een geïntegreerde geochemische studie naar de water- en bodemkwaliteit in relatie tot de geologie in een natuurpark in Espírito Santo, Brazilië. Na haar studie werkte zij onder andere gedurende 4 maanden als toegevoegd onderzoeker bij de projectgroep Geochemie van de faculteit Aardwetenschappen aan de Universiteit Utrecht. Vanaf 1998 werkte zij als onderzoeker in opleiding (OIO) bij de projectgroepen Isotopen Geochemie van de faculteit Aard- en Levenswetenschappen aan de Vrije Universiteit Amsterdam en Stratigrafie en Paleontologie van de faculteit Geowetenschappen aan de Universiteit Utrecht. De resultaten van dit door de Nederlandse Organisatie voor Wetenschappelijk Onderzoek gefinancierde onderzoek zijn beschreven in dit proefschrift.

APPENDICES

All original data reported in this thesis can be found at <http://www.geo.vu.nl/users/kuik>

APPENDIX: CALCULATION OF F-RATIO AND ITS UNCERTAINTY

$$F = \frac{\frac{(40_u - 40_b)}{(39_u - 39_b)} \times \left(\frac{C\lambda_{39} e^{\lambda_{39} B}}{1 - e^{-\lambda_{39} C}} \right) \times \frac{1}{D} - A \times \frac{(36_u - 36_b) \times \left(\frac{4}{D} - 3 \right)}{(39_u - 39_b) \times \left(\frac{C\lambda_{39} e^{\lambda_{39} B}}{1 - e^{-\lambda_{39} C}} \right) \times \frac{1}{D}} + A \times Z_{Ca} \times \frac{(37_u - 37_b) \times \left(\frac{C\lambda_{37} e^{\lambda_{37} B}}{1 - e^{-\lambda_{37} C}} \right) \times \left(\frac{3}{D} - 2 \right)}{(39_u - 39_b) \times \left(\frac{C\lambda_{39} e^{\lambda_{39} B}}{1 - e^{-\lambda_{39} C}} \right) \times \frac{1}{D}}}{1 - Y_{Ca} \times \frac{(37_u - 37_b) \times \left(\frac{C\lambda_{37} e^{\lambda_{37} B}}{1 - e^{-\lambda_{37} C}} \right) \times \left(\frac{3}{D} - 2 \right)}{(39_u - 39_b) \times \left(\frac{C\lambda_{39} e^{\lambda_{39} B}}{1 - e^{-\lambda_{39} C}} \right) \times \frac{1}{D}} - X_K} - X_K$$

This equation is simplified to

$$F = \frac{(P - Q)D - A(T - U)(4 - 3D) + AZF(V - W)(3 - 2D)}{(R - S)E - YF(V - W)(3 - 2D)} - X = \frac{J - K + L}{M} - X = \frac{N}{M} - X$$

with

P = 40_u = measured ⁴⁰Ar intensity (in Volt)

R = 39_u = measured ³⁹Ar intensity (in Volt)

V = 37_u = measured ³⁷Ar intensity (in Volt)

T = 36_u = measured ³⁶Ar intensity (in Volt)

Q = 40_b = measured blank ⁴⁰Ar intensity (in Volt)

S = 39_b = measured blank ³⁹Ar intensity (in Volt)

W = 37_b = measured blank ³⁷Ar intensity (in Volt)

U = 36_b = measured blank ³⁶Ar intensity (in Volt)

A = atmospheric ⁴⁰Ar/³⁶Ar ratio

D = mass discrimination factor

Y = Y_{Ca} = (³⁹Ar/³⁷Ar)_{Ca} correction factor

Z = Z_{Ca} = (³⁶Ar/³⁷Ar)_{Ca} correction factor

X = X_K = (⁴⁰Ar/³⁹Ar)_K correction factor

C = duration of irradiation

B = time elapsed between irradiation and measurement

λ₃₉ = the decay constant of ³⁹Ar

λ₃₇ = the decay constant of ³⁷Ar

J = (P-Q)D

K = A(T-U)(4-3D) L = AZF(V-W)(3-2D)

N = J - K + L

M = (R-S)E - YF(V-W)(3-2D)

E =

F =

$$\left(\frac{C\lambda_{39} e^{\lambda_{39} B}}{1 - e^{-\lambda_{39} C}} \right)$$

$$\left(\frac{C\lambda_{37} e^{\lambda_{37} B}}{1 - e^{-\lambda_{37} C}} \right)$$

APPENDICES

The total variance can be calculated with

$$\sigma_F^2 = \left(\frac{\partial F}{\partial P}\right)^2 \sigma_P^2 + \left(\frac{\partial F}{\partial R}\right)^2 \sigma_R^2 + \left(\frac{\partial F}{\partial V}\right)^2 \sigma_V^2 + \left(\frac{\partial F}{\partial T}\right)^2 \sigma_T^2 + \left(\frac{\partial F}{\partial Q}\right)^2 \sigma_Q^2 + \left(\frac{\partial F}{\partial S}\right)^2 \sigma_S^2 + \left(\frac{\partial F}{\partial W}\right)^2 \sigma_W^2 + \left(\frac{\partial F}{\partial U}\right)^2 \sigma_U^2 + \left(\frac{\partial F}{\partial A}\right)^2 \sigma_A^2 + \left(\frac{\partial F}{\partial D}\right)^2 \sigma_D^2 + \left(\frac{\partial F}{\partial Y_{Ca}}\right)^2 \sigma_{Y_{Ca}}^2 + \left(\frac{\partial F}{\partial Z_{Ca}}\right)^2 \sigma_{Z_{Ca}}^2 + \left(\frac{\partial F}{\partial X_K}\right)^2 \sigma_{X_K}^2 + \left(\frac{\partial F}{\partial \lambda_{37}}\right)^2 \sigma_{\lambda_{37}}^2 + \left(\frac{\partial F}{\partial \lambda_{39}}\right)^2 \sigma_{\lambda_{39}}^2 + \left(\frac{\partial F}{\partial B}\right)^2 \sigma_B^2 + \left(\frac{\partial F}{\partial C}\right)^2 \sigma_C^2$$

It is assumed that σ_B and σ_C are 0 and these two terms can thus be omitted from the total variance equations. The partial derivatives of the other parameters are given by

$$\left(\frac{\partial F}{\partial P}\right) = \frac{D}{M}$$

$$\left(\frac{\partial F}{\partial Q}\right) = \frac{-D}{M}$$

$$\left(\frac{\partial F}{\partial R}\right) = \frac{-J + K - L}{M^2} = \frac{-NE}{M^2}$$

$$\left(\frac{\partial F}{\partial S}\right) = \frac{J - K + L}{M^2} = \frac{NE}{M^2}$$

$$\left(\frac{\partial F}{\partial T}\right) = \frac{-4A}{M} + \frac{3AD}{M} = \frac{A(3D - 4)}{M}$$

$$\left(\frac{\partial F}{\partial U}\right) = \frac{4A}{M} - \frac{3AD}{M} = \frac{-A(3D - 4)}{M}$$

$$\left(\frac{\partial F}{\partial V}\right) = \frac{AZF(3 - 2D) \times M - N \times YF(2D - 3)}{M^2}$$

$$\left(\frac{\partial F}{\partial W}\right) = \frac{-AZF(3 - 2D) \times M + N \times YF(2D - 3)}{M^2}$$

$$\left(\frac{\partial F}{\partial Z}\right) = \frac{A(V - W)F(3 - 2D)}{M} = \frac{L}{ZM}$$

$$\left(\frac{\partial F}{\partial Y}\right) = \frac{N(V - W)F(3 - 2D)}{M^2} = \frac{NL}{AZM^2} \quad \left(\frac{\partial F}{\partial X}\right) = -1$$

$$\left(\frac{\partial F}{\partial A}\right) = \frac{-(T - U)(4 - 3D) + Z(V - W)F(3 - 2D)}{M^2} = \frac{-K/A + L/A}{M^2} = \frac{L - K}{AM^2}$$

$$\begin{aligned} \left(\frac{\partial F}{\partial D}\right) &= \frac{(P - Q + 3AT - 3AU - 2AZFV + 2AZFW) \times M - N \times (2YFV - 2YFW)}{M^2} \\ &= \frac{\{P - Q + 3A(T - U) - 2AZF(V - W)\}M - 2NYF(V - W)}{M^2} \end{aligned}$$

$$\left(\frac{\partial F}{\partial \lambda_{37}}\right) = \frac{MAZ(V-W)(3-2D)\left\{\left(Ce^{\lambda_{37}B} + BC\lambda_{37}e^{\lambda_{37}B}\right)\left(1-e^{-\lambda_{37}C}\right) - \left(C^2\lambda_{37}e^{\lambda_{37}B}e^{-\lambda_{37}C}\right)\right\}}{\left(1-e^{-\lambda_{37}C}\right)^2M^2} -$$

$$\frac{NY(V-W)(3-2D)\left\{\left(Ce^{\lambda_{37}B} + BC\lambda_{37}e^{\lambda_{37}B}\right)\left(1-e^{-\lambda_{37}C}\right) - \left(C^2\lambda_{37}e^{\lambda_{37}B}e^{-\lambda_{37}C}\right)\right\}}{\left(1-e^{-\lambda_{37}C}\right)^2M^2} =$$

$$\frac{(MAZ-NY)(V-W)(3-2D)\left\{\left(Ce^{\lambda_{37}B} + BC\lambda_{37}e^{\lambda_{37}B}\right)\left(1-e^{-\lambda_{37}C}\right) - \left(C^2\lambda_{37}e^{\lambda_{37}B}e^{-\lambda_{37}C}\right)\right\}}{\left(1-e^{-\lambda_{37}C}\right)^2M^2}$$

$$\left(\frac{\partial F}{\partial \lambda_{39}}\right) = \frac{-N(R-S)\left\{\left(Ce^{\lambda_{39}B} + BC\lambda_{39}e^{\lambda_{39}B}\right)\left(1-e^{-\lambda_{39}C}\right) - \left(C^2\lambda_{39}e^{\lambda_{39}B}e^{-\lambda_{39}C}\right)\right\}}{\left(1-e^{-\lambda_{39}C}\right)^2M^2}$$

APPENDIX: CALCULATION OF A $^{40}\text{Ar}/^{39}\text{Ar}$ AGE RELATIVE TO A PRIMARY K/Ar STANDARD

with use of TCR as secondary standard (see chapter 1 for explanation of parameters)

$$T_u = \frac{fN_0}{(A_e + A_\beta)WS} \ln \left(\frac{A_e + A_\beta}{A_e} \times \frac{F_u}{F_{TC}} \times R_{FC}^{TC} \times R_{GA1550}^{FC} \times \frac{{}^{40}\text{Ar}_p^* \times W \times 100}{K_p f} + 1 \right) = Z \ln(X)$$

$$\begin{aligned} \sigma_{T_u}^2 = & \left(\frac{\partial T_u}{\partial f} \right)^2 \sigma_f^2 + \left(\frac{\partial T_u}{\partial N_0} \right)^2 \sigma_{N_0}^2 + \left(\frac{\partial T_u}{\partial A_e} \right)^2 \sigma_{A_e}^2 + \left(\frac{\partial T_u}{\partial A_\beta} \right)^2 \sigma_{A_\beta}^2 + \left(\frac{\partial T_u}{\partial W} \right)^2 \sigma_W^2 + \left(\frac{\partial T_u}{\partial S} \right)^2 \sigma_S^2 + \left(\frac{\partial T_u}{\partial F_u} \right)^2 \sigma_{F_u}^2 + \\ & \left(\frac{\partial T_u}{\partial F_{TC}} \right)^2 \sigma_{F_{TC}}^2 + \left(\frac{\partial T_u}{\partial R_{FC}^{TC}} \right)^2 \sigma_{R_{FC}^{TC}}^2 + \left(\frac{\partial T_u}{\partial R_{GA1550}^{FC}} \right)^2 \sigma_{R_{GA1550}^{FC}}^2 + \left(\frac{\partial T_u}{\partial {}^{40}\text{Ar}_p^*} \right)^2 \sigma_{{}^{40}\text{Ar}_p^*}^2 + \left(\frac{\partial T_u}{\partial K_p} \right)^2 \sigma_{K_p}^2 \end{aligned}$$

$$\left(\frac{\partial T_u}{\partial f} \right) = \frac{Z \ln(X)}{f} + \frac{Z(1-X)}{Xf}$$

$$\left(\frac{\partial T_u}{\partial N_0} \right) = \frac{Z \ln(X)}{N_0}$$

$$\left(\frac{\partial T_u}{\partial A_e} \right) = \frac{Z \ln(X)}{A_e + A_\beta} + \frac{ZA_\beta(1-X)}{XA_e(A_e + A_\beta)}$$

$$\left(\frac{\partial T_u}{\partial A_\beta} \right) = \frac{Z \ln(X)}{A_e + A_\beta} + \frac{Z(X-1)}{X(A_e + A_\beta)}$$

$$\left(\frac{\partial T_u}{\partial W} \right) = \frac{-Z \ln(X)}{W} + \frac{Z(X-1)}{XW}$$

$$\left(\frac{\partial T_u}{\partial S} \right) = \frac{-Z \ln(X)}{S}$$

$$\left(\frac{\partial T_u}{\partial F_u} \right) = \frac{Z(X-1)}{XF_u}$$

$$\left(\frac{\partial T_u}{\partial F_{TC}} \right) = \frac{Z(1-X)}{XF_{TC}}$$

$$\left(\frac{\partial T_u}{\partial R_{FC}^{TC}} \right) = \frac{Z(X-1)}{XR_{FC}^{TC}}$$

$$\left(\frac{\partial T_u}{\partial R_{GA1550}^{FC}} \right) = \frac{Z(X-1)}{XR_{GA1550}^{FC}}$$

$$\left(\frac{\partial T_u}{\partial {}^{40}\text{Ar}_p^*} \right) = \frac{Z(X-1)}{X{}^{40}\text{Ar}_p^*}$$

$$\left(\frac{\partial T_u}{\partial K_p} \right) = \frac{Z(1-X)}{XK_p}$$

APPENDIX: CALCULATION OF A $^{40}\text{Ar}/^{39}\text{Ar}$ AGE RELATIVE TO A PRIMARY K/Ar STANDARD

with use of FCT as secondary standard (see chapter 1 for explanation of parameters)

$$T_u = \frac{fN_0}{(A_e + A_\beta)WS} \ln \left(\frac{A_e + A_\beta}{A_e} \times \frac{F_u}{F_{FC}} \times R_{\text{GA1550}}^{\text{FC}} \times \frac{{}^{40}\text{Ar}_p^* \times W \times 100}{K_p f} + 1 \right) = Z \ln(X)$$

$$\begin{aligned} \sigma_{T_u}^2 = & \left(\frac{\partial T_u}{\partial f} \right)^2 \sigma_f^2 + \left(\frac{\partial T_u}{\partial N_0} \right)^2 \sigma_{N_0}^2 + \left(\frac{\partial T_u}{\partial A_e} \right)^2 \sigma_{A_e}^2 + \left(\frac{\partial T_u}{\partial A_\beta} \right)^2 \sigma_{A_\beta}^2 + \left(\frac{\partial T_u}{\partial W} \right)^2 \sigma_W^2 + \left(\frac{\partial T_u}{\partial S} \right)^2 \sigma_S^2 + \left(\frac{\partial T_u}{\partial F_u} \right)^2 \sigma_{F_u}^2 + \\ & \left(\frac{\partial T_u}{\partial F_{FC}} \right)^2 \sigma_{F_{FC}}^2 + \left(\frac{\partial T_u}{\partial R_{\text{GA1550}}^{\text{FC}}} \right)^2 \sigma_{R_{\text{GA1550}}^{\text{FC}}}^2 + \left(\frac{\partial T_u}{\partial {}^{40}\text{Ar}_p^*} \right)^2 \sigma_{{}^{40}\text{Ar}_p^*}^2 + \left(\frac{\partial T_u}{\partial K_p} \right)^2 \sigma_{K_p}^2 \end{aligned}$$

$$\left(\frac{\partial T_u}{\partial f} \right) = \frac{Z \ln(X)}{f} + \frac{Z(1-X)}{Xf}$$

$$\left(\frac{\partial T_u}{\partial N_0} \right) = \frac{Z \ln(X)}{N_0}$$

$$\left(\frac{\partial T_u}{\partial A_e} \right) = \frac{Z \ln(X)}{A_e + A_\beta} + \frac{ZA_\beta(1-X)}{XA_e(A_e + A_\beta)}$$

$$\left(\frac{\partial T_u}{\partial A_\beta} \right) = \frac{Z \ln(X)}{A_e + A_\beta} + \frac{Z(X-1)}{X(A_e + A_\beta)}$$

$$\left(\frac{\partial T_u}{\partial W} \right) = \frac{-Z \ln(X)}{W} + \frac{Z(X-1)}{XW}$$

$$\left(\frac{\partial T_u}{\partial S} \right) = \frac{-Z \ln(X)}{S}$$

$$\left(\frac{\partial T_u}{\partial F_u} \right) = \frac{Z(X-1)}{XF_u}$$

$$\left(\frac{\partial T_u}{\partial F_{FC}} \right) = \frac{Z(1-X)}{XF_{FC}}$$

$$\left(\frac{\partial T_u}{\partial R_{\text{GA1550}}^{\text{FC}}} \right) = \frac{Z(X-1)}{XR_{\text{GA1550}}^{\text{FC}}}$$

$$\left(\frac{\partial T_u}{\partial {}^{40}\text{Ar}_p^*} \right) = \frac{Z(X-1)}{X{}^{40}\text{Ar}_p^*}$$

$$\left(\frac{\partial T_u}{\partial K_p} \right) = \frac{Z(1-X)}{XK_p}$$

APPENDIX: CALCULATION OF $^{40}\text{Ar}/^{39}\text{Ar}$ AGE RELATIVE TO AN ASTRONOMICAL STANDARD

$$\begin{aligned}
T_u &= \frac{fN_0}{(A_e + A_\beta)WS} \ln \left[1 + \left(e^{\frac{(A_e + A_\beta)WS}{fN_0} T_0} - 1 \right) \prod_{i=1}^n R_{i-1}^i \right] \\
&= \frac{fN_0}{(A_e + A_\beta)WS} \ln \left[1 + \prod_{i=1}^n R_{i-1}^i e^{\frac{(A_e + A_\beta)WS}{fN_0} T_0} - \prod_{i=1}^n R_{i-1}^i \right] = Z \ln \left[1 + \prod_{i=1}^i R_{i-1}^i e^{\frac{1}{Z} T_0} - \prod_{i=1}^n R_{i-1}^i \right] \\
&= Z \ln \left[1 + C e^{\frac{1}{Z} T_0} - C \right] = Z \ln [X]
\end{aligned}$$

$$\begin{aligned}
\sigma_{T_u}^2 &= \left(\frac{\partial T_u}{\partial f} \right)^2 \sigma_f^2 + \left(\frac{\partial T_u}{\partial N_0} \right)^2 \sigma_{N_0}^2 + \left(\frac{\partial T_u}{\partial A_e} \right)^2 \sigma_{A_e}^2 + \left(\frac{\partial T_u}{\partial A_\beta} \right)^2 \sigma_{A_\beta}^2 + \left(\frac{\partial T_u}{\partial W} \right)^2 \sigma_W^2 + \left(\frac{\partial T_u}{\partial S} \right)^2 \sigma_S^2 \\
&\quad + \left(\frac{\partial T_u}{\partial T_0} \right)^2 \sigma_{T_0}^2 + \sum_{i=1}^n \sum_{j=1}^n \left(\frac{\partial T_u}{\partial R_{i-1}^j} \right)^2 \sigma_{R_{i-1}^j}^2
\end{aligned}$$

where the partial derivatives in this equation are:

$$\begin{aligned}
\left(\frac{\partial T_u}{\partial f} \right) &= \frac{Z}{f} \ln[X] + \frac{-CT_0}{Xf} e^{\frac{1}{Z} T_0} & \left(\frac{\partial T_u}{\partial N_0} \right) &= \frac{Z}{N_0} \ln[X] + \frac{-CT_0}{XN_0} e^{\frac{1}{Z} T_0} \\
\left(\frac{\partial T_u}{\partial A_e} \right) &= \frac{-Z}{A_e + A_\beta} \ln[X] + \frac{CT_0}{X(A_e + A_\beta)} e^{\frac{1}{Z} T_0} & \left(\frac{\partial T_u}{\partial A_\beta} \right) &= \frac{-Z}{A_e + A_\beta} \ln[X] + \frac{CT_0}{X(A_e + A_\beta)} e^{\frac{1}{Z} T_0} \\
\left(\frac{\partial T_u}{\partial W} \right) &= \frac{-Z}{W} \ln[X] + \frac{CT_0}{XW} e^{\frac{1}{Z} T_0} & \left(\frac{\partial T_u}{\partial S} \right) &= \frac{-Z}{S} \ln[X] + \frac{CT_0}{XS} e^{\frac{1}{Z} T_0} \\
\left(\frac{\partial T_u}{\partial T_0} \right) &= \frac{C}{X} e^{\frac{1}{Z} T_0} & \left(\frac{\partial T_u}{\partial R_{i-1}^j} \right) &= \frac{Z \left(e^{\frac{1}{Z} T_0} - 1 \right) \Pi R_{i-1}^j}{XR_j}
\end{aligned}$$

APPENDICES

Or for the specific case where one standard (in this case FCT) is directly calibrated to an astronomically dated standard, (this can be changed to any arbitrary standard):

$$T_{Fc} = \frac{fN_0}{(A_e + A_\beta)WS} \ln \left[R_{ash}^{Fc} \times \left(e^{\frac{(A_e + A_\beta)WS}{fN_0} t_{ash}} - 1 \right) + 1 \right] = Z \ln \left[R_{ash}^{Fc} \times \left(e^{\frac{t_{ash}}{Z}} - 1 \right) + 1 \right] = Z \ln(X)$$

$$\sigma_{T_{Fc}}^2 = \left(\frac{\partial T_{Fc}}{\partial f} \right)^2 \sigma_f^2 + \left(\frac{\partial T_{Fc}}{\partial N_0} \right)^2 \sigma_{N_0}^2 + \left(\frac{\partial T_{Fc}}{\partial A_e} \right)^2 \sigma_{A_e}^2 + \left(\frac{\partial T_{Fc}}{\partial A_\beta} \right)^2 \sigma_{A_\beta}^2 + \left(\frac{\partial T_{Fc}}{\partial W} \right)^2 \sigma_W^2 + \left(\frac{\partial T_{Fc}}{\partial S} \right)^2 \sigma_S^2 +$$

$$\left(\frac{\partial T_{Fc}}{\partial R} \right)^2 \sigma_R^2 + \left(\frac{\partial T_{Fc}}{\partial T_{ash}} \right)^2 \sigma_{T_{ash}}^2$$

where the partial derivatives in this equation are:

$$\left(\frac{\partial T_u}{\partial f} \right) = \frac{Z}{f} \ln[X] + \frac{-R_{tephra}^{FC} t_{tephra}}{Xf} \times e^{\frac{t_{tephra}}{Z}}$$

$$\left(\frac{\partial T_u}{\partial N_0} \right) = \frac{Z}{N_0} \ln[X] + \frac{-R_{tephra}^{FC} t_{tephra}}{XN_0} \times e^{\frac{t_{tephra}}{Z}}$$

$$\left(\frac{\partial T_u}{\partial A_e} \right) = \frac{-Z}{A_e + A_\beta} \ln[X] + \frac{R_{tephra}^{FC} t_{tephra}}{X(A_e + A_\beta)} \times e^{\frac{t_{tephra}}{Z}}$$

$$\left(\frac{\partial T_u}{\partial A_\beta} \right) = \frac{-Z}{A_e + A_\beta} \ln[X] + \frac{R_{tephra}^{FC} t_{tephra}}{X(A_e + A_\beta)} \times e^{\frac{t_{tephra}}{Z}}$$

$$\left(\frac{\partial T_u}{\partial W} \right) = \frac{-Z}{W} \ln[X] + \frac{R_{tephra}^{FC} t_{tephra}}{XW} \times e^{\frac{t_{tephra}}{Z}}$$

$$\left(\frac{\partial T_u}{\partial S} \right) = \frac{-Z}{S} \ln[X] + \frac{R_{tephra}^{FC} t_{tephra}}{XS} \times e^{\frac{t_{tephra}}{Z}}$$

$$\left(\frac{\partial T_u}{\partial t_{tephra}} \right) = \frac{R_{tephra}^{FC}}{X} \times e^{\frac{t_{tephra}}{Z}}$$

$$\left(\frac{\partial T_u}{\partial R_{tephra}^{FC}} \right) = \frac{Z \left(e^{\frac{t_{tephra}}{Z}} - 1 \right)}{X}$$

APPENDICES

APPENDIX: MASS DISCRIMINATION FACTORS

Mass discrimination factor during analysis of VU32

Date	Factor	± 1σ %	Date	Factor	± 1σ %	Date	Factor	± 1σ %
31-May-99	1.0070	0.20	24-Aug-99	1.0033	0.22	06-Sep-99	1.0032	0.32
01-Jun-99	1.0076	0.20	25-Aug-99	1.0044	0.22	07-Sep-99	1.0026	0.32
02-Jun-99	1.0081	0.20	26-Aug-99	1.0040	0.22	08-Sep-99	1.0021	0.32
03-Jun-99	1.0085	0.20	27-Aug-99	1.0029	0.22	09-Sep-99	1.0017	0.32
04-Jun-99	1.0088	0.20	28-Aug-99	1.0017	0.22	10-Sep-99	1.0015	0.32
05-Jun-99	1.0090	0.20	29-Aug-99	1.0010	0.22	11-Sep-99	1.0013	0.32
06-Jun-99	1.0090	0.20	30-Aug-99	1.0017	0.22	12-Sep-99	1.0012	0.32
07-Jun-99	1.0090	0.20	31-Aug-99	1.0043	0.22	13-Sep-99	1.0012	0.32
08-Jun-99	1.0089	0.20				14-Sep-99	1.0012	0.32
09-Jun-99	1.0087	0.20				15-Sep-99	1.0012	0.32
10-Jun-99	1.0085	0.20				16-Sep-99	1.0013	0.32
11-Jun-99	1.0083	0.20				17-Sep-99	1.0014	0.32
12-Jun-99	1.0079	0.20				18-Sep-99	1.0015	0.32
13-Jun-99	1.0076	0.20				19-Sep-99	1.0016	0.32
14-Jun-99	1.0072	0.20				20-Sep-99	1.0017	0.32
15-Jun-99	1.0068	0.20				21-Sep-99	1.0018	0.32
16-Jun-99	1.0064	0.20				22-Sep-99	1.0018	0.32
17-Jun-99	1.0060	0.20				23-Sep-99	1.0017	0.32
18-Jun-99	1.0056	0.20				24-Sep-99	1.0017	0.32
19-Jun-99	1.0052	0.20				25-Sep-99	1.0015	0.32
20-Jun-99	1.0049	0.20				26-Sep-99	1.0012	0.32
21-Jun-99	1.0046	0.20				27-Sep-99	1.0009	0.32
22-Jun-99	1.0043	0.20				28-Sep-99	1.0005	0.32
23-Jun-99	1.0041	0.20				29-Sep-99	0.9999	0.32
24-Jun-99	1.0039	0.20				30-Sep-99	0.9992	0.32
25-Jun-99	1.0039	0.20				01-Oct-99	0.9983	0.32
26-Jun-99	1.0039	0.20						
27-Jun-99	1.0039	0.20				11-Nov-99	1.0034	0.30
28-Jun-99	1.0041	0.20				12-Nov-99	1.0037	0.30
29-Jun-99	1.0044	0.20				18-Nov-99	1.0057	0.30
30-Jun-99	1.0048	0.20				19-Nov-99	1.0060	0.30
01-Jul-99	1.0053	0.20						

APPENDICES

Mass discrimination factor during analysis of VU37-I

Date	Factor	± 1σ %	Date	Factor	± 1σ %	Date	Factor	± 1σ %
31-Jul-00	1.0089	0.16	23-Aug-00	1.0085	0.16	16-Oct-00	1.0077	0.0033
1-Aug-00	1.0090	0.16	24-Aug-00	1.0085	0.17	17-Oct-00	1.0078	0.0033
2-Aug-00	1.0091	0.16	25-Aug-00	1.0086	0.16	18-Oct-00	1.0079	0.0033
3-Aug-00	1.0092	0.16	26-Aug-00	1.0088	0.16	19-Oct-00	1.0080	0.0033
4-Aug-00	1.0092	0.16	27-Aug-00	1.0089	0.16	20-Oct-00	1.0081	0.0033
5-Aug-00	1.0092	0.16	28-Aug-00	1.0091	0.16	21-Oct-00	1.0082	0.0033
6-Aug-00	1.0092	0.16	29-Aug-00	1.0093	0.17	22-Oct-00	1.0083	0.0033
7-Aug-00	1.0092	0.16	30-Aug-00	1.0096	0.16	23-Oct-00	1.0084	0.0033
8-Aug-00	1.0092	0.16	31-Aug-00	1.0099	0.17	24-Oct-00	1.0085	0.0033
9-Aug-00	1.0091	0.16	1-Sep-00	1.0103	0.16	25-Oct-00	1.0086	0.0033
10-Aug-00	1.0090	0.17	2-Sep-00	1.0107	0.16	26-Oct-00	1.0086	0.0033
11-Aug-00	1.0090	0.16	3-Sep-00	1.0112	0.16	27-Oct-00	1.0087	0.0033
12-Aug-00	1.0089	0.16	4-Sep-00	1.0117	0.16	28-Oct-00	1.0087	0.0033
13-Aug-00	1.0088	0.16	5-Sep-00	1.0123	0.16	29-Oct-00	1.0087	0.0033
14-Aug-00	1.0088	0.16				30-Oct-00	1.0087	0.0033
15-Aug-00	1.0087	0.16				31-Oct-00	1.0086	0.0033
16-Aug-00	1.0086	0.16				01-Nov-00	1.0086	0.0033
17-Aug-00	1.0085	0.17				02-Nov-00	1.0084	0.0033
18-Aug-00	1.0085	0.16				03-Nov-00	1.0083	0.0033
19-Aug-00	1.0085	0.16				04-Nov-00	1.0081	0.0033
20-Aug-00	1.0084	0.16				05-Nov-00	1.0079	0.0033
21-Aug-00	1.0084	0.16				06-Nov-00	1.0076	0.0033
22-Aug-00	1.0084	0.17				07-Nov-00	1.0073	0.0033

Mass discrimination factor during analysis of VU37-II

Date	Factor	± 1σ %	Date	Factor	± 1σ %	Date	Factor	± 1σ %
16-Jan-01	1.0061	0.10	03-Feb-01	1.0060	0.10	21-Feb-01	1.0045	0.10
17-Jan-01	1.0063	0.10	04-Feb-01	1.0059	0.10	22-Feb-01	1.0045	0.10
18-Jan-01	1.0064	0.10	05-Feb-01	1.0058	0.10	23-Feb-01	1.0046	0.10
19-Jan-01	1.0065	0.10	06-Feb-01	1.0056	0.10	24-Feb-01	1.0047	0.10
20-Jan-01	1.0066	0.10	07-Feb-01	1.0055	0.10	25-Feb-01	1.0048	0.10
21-Jan-01	1.0067	0.10	08-Feb-01	1.0054	0.10	26-Feb-01	1.0049	0.10
22-Jan-01	1.0067	0.10	09-Feb-01	1.0053	0.10	27-Feb-01	1.0050	0.10
23-Jan-01	1.0067	0.10	10-Feb-01	1.0052	0.10	28-Feb-01	1.0052	0.10
24-Jan-01	1.0067	0.10	11-Feb-01	1.0051	0.10	01-Mar-01	1.0054	0.10
25-Jan-01	1.0067	0.10	12-Feb-01	1.0050	0.10	02-Mar-01	1.0056	0.10
26-Jan-01	1.0067	0.10	13-Feb-01	1.0049	0.10	03-Mar-01	1.0059	0.10
27-Jan-01	1.0066	0.10	14-Feb-01	1.0048	0.10	04-Mar-01	1.0061	0.10
28-Jan-01	1.0066	0.10	15-Feb-01	1.0047	0.10	05-Mar-01	1.0065	0.10
29-Jan-01	1.0065	0.10	16-Feb-01	1.0046	0.10	06-Mar-01	1.0068	0.10
30-Jan-01	1.0064	0.10	17-Feb-01	1.0046	0.10	07-Mar-01	1.0072	0.10
31-Jan-01	1.0063	0.10	18-Feb-01	1.0045	0.10	08-Mar-01	1.0076	0.10
01-Feb-01	1.0062	0.10	19-Feb-01	1.0045	0.10	09-Mar-01	1.0081	0.10
02-Feb-01	1.0061	0.10	20-Feb-01	1.0045	0.10			

APPENDICES

Mass discrimination factor during analysis of VU41

Date	Factor	$\pm 1\sigma$ %	Date	Factor	$\pm 1\sigma$ %	Date	Factor	$\pm 1\sigma$ %
26-Oct-01	1.0045	0.27	14-Nov-01	1.0064	0.27	3-Dec-01	1.0058	0.27
27-Oct-01	1.0049	0.27	15-Nov-01	1.0063	0.27	4-Dec-01	1.0061	0.27
28-Oct-01	1.0053	0.27	16-Nov-01	1.0062	0.27	5-Dec-01	1.0063	0.27
29-Oct-01	1.0056	0.27	17-Nov-01	1.0060	0.27	6-Dec-01	1.0066	0.27
30-Oct-01	1.0059	0.27	18-Nov-01	1.0059	0.27			
31-Oct-01	1.0062	0.27	19-Nov-01	1.0058	0.27	16-Dec-01	1.0105	0.24
1-Nov-01	1.0064	0.27	20-Nov-01	1.0057	0.27	17-Dec-01	1.0089	0.24
2-Nov-01	1.0066	0.27	21-Nov-01	1.0056	0.27	18-Dec-01	1.0073	0.25
3-Nov-01	1.0067	0.27	22-Nov-01	1.0055	0.27	19-Dec-01	1.0057	0.25
4-Nov-01	1.0068	0.27	23-Nov-01	1.0054	0.27			
5-Nov-01	1.0069	0.27	24-Nov-01	1.0053	0.27	03-Jan-02	1.0045	0.08
6-Nov-01	1.0069	0.27	25-Nov-01	1.0053	0.27			
7-Nov-01	1.0069	0.27	26-Nov-01	1.0053	0.27	22-Jan-02	1.0065	0.16
8-Nov-01	1.0069	0.27	27-Nov-01	1.0053	0.27	25-Jan-02	1.0062	0.16
9-Nov-01	1.0068	0.27	28-Nov-01	1.0053	0.27	31-Jan-02	1.0059	0.16
10-Nov-01	1.0068	0.27	29-Nov-01	1.0053	0.27	01-Feb-02	1.0060	0.16
11-Nov-01	1.0067	0.27	30-Nov-01	1.0054	0.27	02-Feb-02	1.0061	0.16
12-Nov-01	1.0066	0.27	1-Dec-01	1.0055	0.27			
13-Nov-01	1.0065	0.27	2-Dec-01	1.0057	0.27			

APPENDICES

Mass discrimination factor during analysis of VU42

Date	Time	Factor	$\pm 1\sigma$ %	Date	Time	Factor	$\pm 1\sigma$ %
30-Mar-02	0.00u	1.0035	0.26	06-Jul-02	0.00u	1.0061	0.14
30-Mar-02	12.00u	1.0032	0.26	06-Jul-02	12.00u	1.0061	0.14
31-Mar-02	0.00u	1.0029	0.26	07-Jul-02	0.00u	1.0062	0.14
31-Mar-02	12.00u	1.0027	0.26	07-Jul-02	12.00u	1.0062	0.14
01-Apr-02	0.00u	1.0025	0.26	08-Jul-02	0.00u	1.0062	0.14
01-Apr-02	12.00u	1.0023	0.26	08-Jul-02	12.00u	1.0062	0.14
02-Apr-02	0.00u	1.0022	0.26	09-Jul-02	0.00u	1.0062	0.14
02-Apr-02	12.00u	1.0022	0.26	09-Jul-02	12.00u	1.0062	0.14
03-Apr-02	0.00u	1.0021	0.26	10-Jul-02	0.00u	1.0062	0.14
03-Apr-02	12.00u	1.0022	0.26	10-Jul-02	12.00u	1.0062	0.14
04-Apr-02	0.00u	1.0022	0.26	11-Jul-02	0.00u	1.0062	0.14
04-Apr-02	12.00u	1.0023	0.26	11-Jul-02	12.00u	1.0062	0.14
05-Apr-02	0.00u	1.0024	0.26	12-Jul-02	0.00u	1.0062	0.14
05-Apr-02	12.00u	1.0026	0.26	12-Jul-02	12.00u	1.0062	0.14
06-Apr-02	0.00u	1.0028	0.26	13-Jul-02	0.00u	1.0062	0.14
06-Apr-02	12.00u	1.0031	0.26	13-Jul-02	12.00u	1.0062	0.14
08-Apr-02	0.00u	1.0045	0.15	14-Jul-02	0.00u	1.0062	0.14
08-Apr-02	12.00u	1.0046	0.15	14-Jul-02	12.00u	1.0062	0.14
09-Apr-02	0.00u	1.0047	0.15	15-Jul-02	0.00u	1.0062	0.14
09-Apr-02	12.00u	1.0047	0.15	15-Jul-02	12.00u	1.0062	0.14
10-Apr-02	0.00u	1.0048	0.15	16-Jul-02	0.00u	1.0062	0.14
10-Apr-02	12.00u	1.0048	0.15	16-Jul-02	12.00u	1.0062	0.14
11-Apr-02	0.00u	1.0049	0.15	17-Jul-02	0.00u	1.0062	0.14
11-Apr-02	12.00u	1.0050	0.15	17-Jul-02	12.00u	1.0062	0.14
12-Apr-02	0.00u	1.0050	0.15	18-Jul-02	0.00u	1.0062	0.14
12-Apr-02	12.00u	1.0051	0.15	18-Jul-02	12.00u	1.0062	0.14
13-Apr-02	0.00u	1.0051	0.15	19-Jul-02	0.00u	1.0062	0.14
15-Apr-02	0.00u	1.0026	0.12	19-Jul-02	12.00u	1.0062	0.14
15-Apr-02	12.00u	1.0012	0.12	20-Jul-02	0.00u	1.0062	0.14
16-Apr-02	0.00u	1.0001	0.12	20-Jul-02	12.00u	1.0062	0.14
18-Apr-02	0.00u	1.0023	0.09	21-Jul-02	0.00u	1.0061	0.14
18-Apr-02	12.00u	1.0026	0.09	21-Jul-02	12.00u	1.0061	0.14
19-Apr-02	0.00u	1.0028	0.09	22-Jul-02	0.00u	1.0061	0.14
19-Apr-02	12.00u	1.0029	0.09	22-Jul-02	12.00u	1.0061	0.14
20-Apr-02	0.00u	1.0030	0.09	23-Jul-02	0.00u	1.0061	0.14
20-Apr-02	12.00u	1.0031	0.09	23-Jul-02	12.00u	1.0061	0.14
21-Apr-02	0.00u	1.0032	0.09	24-Jul-02	0.00u	1.0060	0.14
21-Apr-02	12.00u	1.0032	0.09	24-Jul-02	12.00u	1.0060	0.14
22-Apr-02	0.00u	1.0031	0.09	25-Jul-02	0.00u	1.0060	0.14
22-Apr-02	12.00u	1.0030	0.09	25-Jul-02	12.00u	1.0060	0.14
23-Apr-02	0.00u	1.0029	0.09	26-Jul-02	0.00u	1.0059	0.14
23-Apr-02	12.00u	1.0027	0.09	26-Jul-02	12.00u	1.0059	0.14
24-Apr-02	0.00u	1.0025	0.09	27-Jul-02	0.00u	1.0059	0.14
24-Apr-02	12.00u	1.0023	0.09	27-Jul-02	12.00u	1.0059	0.14
25-Apr-02	0.00u	1.0020	0.09	28-Jul-02	0.00u	1.0058	0.14
25-Apr-02	12.00u	1.0016	0.09	28-Jul-02	12.00u	1.0058	0.14
31-May-02	0.00u	1.0043	0.06	29-Jul-02	0.00u	1.0058	0.14
31-May-02	12.00u	1.0043	0.06	29-Jul-02	12.00u	1.0057	0.14
21-Jun-02	0.00u	1.0060	0.06	30-Jul-02	0.00u	1.0057	0.14
21-Jun-02	12.00u	1.0060	0.06	30-Jul-02	12.00u	1.0057	0.14
21-Jun-02	0.00u	1.0062	0.06	31-Jul-02	0.00u	1.0057	0.14
21-Jun-02	12.00u	1.0063	0.06	31-Jul-02	12.00u	1.0056	0.14
04-Jul-02	0.00u	1.0061	0.14	01-Aug-02	0.00u	1.0056	0.14
04-Jul-02	12.00u	1.0061	0.14	01-Aug-02	12.00u	1.0055	0.14
05-Jul-02	0.00u	1.0061	0.14	02-Aug-02	0.00u	1.0055	0.14
05-Jul-02	12.00u	1.0061	0.14	02-Aug-02	12.00u	1.0055	0.14

APPENDICES

APPENDIX: GPS-COORDINATES OF STUDIED SECTIONS

Crete Agios Ioannis	N 35° 03.725' E 24° 53.738'
Crete Kastelli	N 35° 04.065' E 24° 55.011'
Crete Faneromeni	N 35° 13.298' E 26° 03.980'
Ptolemais Tomea Eksi (SR3M, SR3L)	N 40° 21.124' E 21° 47.641'
Ptolemais Tomea Eksi (SR5L)	N 40° 21.139' E 21° 47.704'
Ptolemais Tomea Eksi (SLM3T)	N 40° 26.186' E 21° 47.519'
Ptolemais Tomea Eksi (SLM2T)	N 40° 27.029' E 21° 47.116'
Ptolemais Komanos (older ash layers)	N 40° 21.021' E 21° 46.439'
Ptolemais Anargyri	N 40° 35.805' E 21° 37.351'
Morocco, Messâdit	N 35° 21.075' W 03° 10.349'
Morocco, Izarorene	N 35° 13.051' W 03° 07.893'
Morocco, Ifounassene	N 35° 20.999' W 03° 07.893'
Italy, Monte dei Corvi	N 43° 35.277' E 13° 33.828'

Due to the nature of the open pit mines, which are still in use, it might not be possible to resample the Ptolemais ash layers at the exact locations listed above.

